On the Determination of Absolute Nuclear Charge Radii for Elements without Stable Isotopes via Precision X-ray Spectroscopy of Lithium-like Ions

by

Andrew S. M. Senchuk

A Thesis Submitted to
the Faculty of Graduate Studies
in Partial Fulfillment of the Requirements of the Degree of

DOCTOR OF PHILOSOPHY

Department of Physics and Astronomy
University of Manitoba
Winnipeg, Manitoba

Abstract

There is currently no method to experimentally determine the absolute charge radius of nuclei for elements that have no stable or extremely long-lived isotope: The standard methods, electron scattering and muonic atom spectroscopy, require macroscopic amounts of the isotope under investigation. Thus, for nuclei with charge $Z > 83$, (uranium is the exception), there are no experimental data for the absolute nuclear charge radius. We are currently developing a technique to measure the absolute charge radius of any heavy isotope of sufficient half-life (order of seconds) using precise x-ray spectroscopy of the electronic 2s-2p transition in lithium-like ions. The finite nuclear size shifts the transition energy by more than 10 eV in these systems, whereas experimentally, the transition energy can be measured absolutely with an accuracy below 100 meV (Beiersdorfer et al. (1998)). In addition, recent progress in QED theory allows us to account for radiative corrections at a comparable level as well (Yerokhin et al. (2006)). As a result, the contribution by the finite nuclear charge distribution can be extracted at the 100 meV level. In this thesis, we will develop a computational approach that allows us to obtain general relationships between the nuclear charge radius of a particular ion, and its 2s-2p transition energy. This is done for every element between lead (Z = 82, A = 208) and uranium (Z = 92, A = 238). Some conclusions are made about the future prospects of the method as experimental and theoretical techniques improve.

Acknowledgements

I would like to express my sincerest gratitude to my advisor Prof. Gerald Gwinner for his continuous support of my Ph.D studies, and for his patience, motivation, and knowledge. His guidance was instrumental in completing this thesis. I would also like to thank my co-advisor Prof. Khodr Shamseddine for his constant encouragement and helpful comments in preparing this thesis.

I would also like to thank the rest of my thesis committee: Profs. George Tabisz, Michael Gericke, and Georg Schrekenbach, for their insightful comments and encouragement. In addition, I would like to thank my external examiner Prof. Gordon Drake for agreeing to read my manuscript and for asking challenging but constructive questions during the defence.

My sincere thanks goes to Dr. Charlotte Froese-Fischer and Dr. Jonathan Sapirstein, for their assistance in critical portions of this thesis, and their willingness to help me when I reached out to them. Without their insights it would not have been possible to complete this research.

I would like to thank my family: my parents and siblings on both sides, for supporting me throughout the research and then writing phases of the thesis.

Most importantly, I would like to thank my wife Kathrine Basarab for sticking with me for the duration of this project and for giving me the strength to continue despite the many times I was tempted to walk away. Words cannot express the gratitude I feel for her support and encouragement.

I dedicate this thesis to my family.

Contents

List of Tables

List of Figures

Chapter 1

Introduction

> ... Unfortunately, the atomic wave functions are not known with sufficient precision to do this – ΔE is a very small difference, perhaps 10^{-4} of E, and the simple hydrogenic-like 1s wave functions are not good enough to calculate E to a precision of 1 part in 10^4 (relativistic effects and the presence of other electrons are two factors that also influence the 1s energy). Thus a single measurement of the energy of a K x-ray cannot be used to deduce the nuclear radius.
> *Krane (1988)* [49]

The nuclei of atoms are still somewhat mysterious objects; while contributing overwhelmingly to the mass of the atom, their size is on average only one ten thousandth of that of the atom. Ever since their discovery by Rutherford in the early twentieth century, they have been the objects of intense study. The goals of that study are two-pronged: fundamental physical knowledge and applications such as power generation and medicine. To that end, the most fundamental properties of nuclei have been found to be the nuclear charge radius and the nuclear mass. These, for example, give crucial information for understanding nucleosynthesis in cosmology.

With the advent of powerful radioactive beam facilities, such as the Isotope Separator and ACcelerator (ISAC) at the Tri-University Meson Facility (TRIUMF) in British Columbia, several high-profile experiments have been proposed to study the fundamental symmetries of nature such as mirror symmetry and time reversal symmetry and their violation in heavy atoms [12]. In these systems, the experimental

signatures of the aforementioned effects are enormously enhanced due to the strong electric field of the nucleus. Candidates for such experiments are francium, radon, and radium – all elements with no stable isotopes and hence no nuclear charge radius information. The Manitoba group working at TRIUMF is leading a mirror symmetry experiment in francium, which requires reliable knowledge of the nuclear charge radius in francium.

1.1 Parity Violation in Atomic Systems

In this section, for completeness, we will briefly outline the theory of parity violation in atomic systems. Our treatment will follow that given in Commins and Bucksbaum [27], and no claim of originality is made. Other standard treatments include Derevianko and Porsev [30] and Khriplovich [46].

The standard mode of interaction between an electron and nucleus is electromagnetic, where a virtual photon is exchanged. However, after electroweak unification was achieved, we know that there is a non-zero probability that a Z^0, the weak-neutral force carrier, can also be exchanged virtually. Although parity is strictly conserved by electromagnetic interactions, the same is not true for the exchange of weak gauge bosons.

The total scattering amplitude for the interaction (at tree-level) consists of two parts:

$$A = A_{EM} + A_{weak}, \tag{1.1}$$

where A_{EM} is the amplitude for the electromagnetic interaction and A_{weak} is the amplitude for the weak interaction. The cross-section for scattering is proportional to the absolute-square of the amplitude:

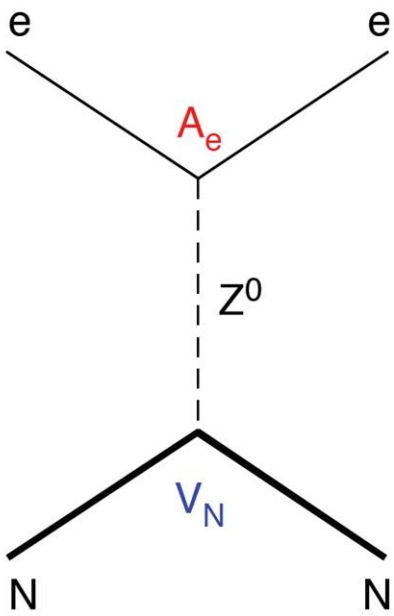

Figure 1.1: Z boson exchange between a bound electron and nucleus

$$
\begin{aligned}
|A|^2 &= |A_{EM} + A_{weak}|^2 \\
&= (A_{EM} + A_{weak})^*(A_{EM} + A_{weak}) \\
&= |A_{EM}|^2 + A^*_{EM}A_{weak} + A_{EM}A^*_{weak} + |A_{weak}|^2 \\
&= |A_{EM}|^2 \left(1 + \frac{A^*_{EM}A_{weak} + A_{EM}A^*_{weak}}{|A_{EM}|^2} + \frac{|A_{weak}|^2}{|A_{EM}|^2}\right).
\end{aligned} \tag{1.2}
$$

At laboratory energies, the amplitude for the electromagnetic interactions is many of orders greater than the weak amplitude, thus we can take $|A_{weak}|^2/|A_{EM}|^2 \to 0$. Therefore, A_{weak} must be detected via the electromagnetic-weak interference in the second term:

$$
|A_{int}|^2 = A^*_{EM}A_{weak} + A_{EM}A^*_{weak}. \tag{1.3}
$$

Now, the weak amplitude contains both scalar and pseudoscalar components,

$$A_{weak} = A_{weakS} + A_{weakP} \tag{1.4}$$

where the scalar portion has no observable effects in electron-nucleon interactions, but the pseudoscalar component can be detected since its sign depends on whether the experimental coordinate system is right or left-handed. Practically this is achieved by comparing cross-sections of otherwise identical processes of opposite handedness:

$$\begin{aligned} \delta &= \frac{\sigma_R - \sigma_L}{\sigma_R + \sigma_L} \\ &= \frac{|A_R|^2 - |A_L|^2}{|A_R|^2 + |A_L|^2} \\ &\approx \frac{A^*_{EM} A_{weak} + A_{EM} A^*_{weak}}{|A_{EM}|^2} \\ &= 2Re(A^{odd}_W / A_{em}). \end{aligned} \tag{1.5}$$

For many years it was felt that the prospect of observing this asymmetry in atomic systems was negligible. This can be made plausible if one takes it as the four-momentum transfer between the lepton and the hadron, then A_{em} is proportional to e^2/k^2 while A_W is proportional to $g^2/(k^2 + M^2_{Z_0}c^2)$. For atoms, the momentum transfer is given by the inverse of the Bohr radius $a_0 \approx \hbar/m_e \alpha c$ [24]. Thus

$$\delta \approx \alpha^2 \frac{m_e^2}{M_Z^2} \approx 10^{-15}, \tag{1.6}$$

so it's clear that this effect should be impossible to see.

This was the situation until the work of Bouchiat and Bouchiat [23] and [21, 22] in 1974 and 1975. They were able to show that the probability amplitude of this interaction has enhancement mechanisms that end up scaling the result with the the third power of the nuclear charge, Z^3. This can be seen by considering the explicit expression for the s-p transition:

$$\left\langle ns_{1/2}|V_{pnc}|n'p_{1/2}\right\rangle \alpha \left[\frac{G_F Z^2 Q_w(Z,N)}{2\sqrt{2}}(1+\delta(\epsilon_n))(1+\delta(\epsilon_{n'}))\right] \times K_r(Z,R), \quad (1.7)$$

where K_r is the relativistic finite nuclear-size correction given by:

$$K_r(Z,R) \approx \left[\frac{\Gamma(3)}{\Gamma(2\sqrt{1-(Z\alpha)^2}+1)} \times \left(\frac{2ZR}{a_0}\right)^{(\sqrt{1-(Z\alpha)^2}-1)}\right]^2. \quad (1.8)$$

Thus we see that two powers of Z come in directly, and another comes in via the expression for the weak charge:

$$Q_w(Z,N) = -[(4sin^2\theta_w - 1)Z + N], \quad (1.9)$$

as well as a contribution from the relativistic factor K_r. Due to these mechanisms, the asymmetry factor enhances to $10^{-6} - 10^{-5}$ in high-Z atoms. The first experimental confirmation of this was claimed by Barkov and Zolotorev [9, 10] in Bismuth. Subsequent measurements claimed not to see the effect. This changed in 1981 when Bucksbaum et al. [26] definitively detected the effect in Thallium. The definitive measurement was carried out by Wieman et al. [87] in 1987.

1.2 The Nuclear Charge Radius

As already stated, the most fundamental properties of nuclei have been found to be the nuclear charge radius and the nuclear mass. The standard method for measuring charge radii, going back to the 1950s, is to scatter GeV electrons off target foils made of the desired element or isotope, as famously carried out by Hofstadter [39], and co-workers.

The problem with this method is that only stable or long-lived isotopes can be fashioned into target foils. Thus for nuclei with charge $Z > 83$, (uranium, Z = 92, is the exception), there is no direct experimental data for the absolute nuclear charge radius. Within the realm of these heavy elements, one has to rely on extrapolations,

which range from simple global formulae that depend only on A, such as, [45]:

$$R = 0.836A^{1/3} + 0.570, \tag{1.10}$$

to much more refined approaches such as the tables by Angeli et al. [4].

In 2017, new life was given to the electron scattering method. Tsukada et al. [84] working at the SCRIT facility showed that one can perform electron scattering experiments, not off of foils, but off of trapped ions from an ion beam, specifically a beam of ^{132}Xe. This nucleus has, up until now, never been studied via electron scattering.

The SCRIT facility consists of a 150 MeV electron beam which is injected and accumulated in the storage ring (SR2). The electron beam is then accelerated to the desired energy, where the maximum available energy is 700 MeV. The Xe ions are produced from natural Xe gas and accelerated and mass separated by an electron-beam-driven RI separator for SCRIT (ERIS) [84]. A continuous ion beam from the ERIS is converted to a pulsed beam with the duration of 370 μs at a fringing-rf-field-activated ion beam compressor (FRAC) [84]. The scattered electrons from confined ions in the SCRIT are then detected by a window-frame spectrometer for electron scattering (WiSES).

The SCRIT itself uses a system of four cylindrical electrodes surrounding the electron beam. The middle two electrodes define the trapping length (50 cm), and they are separated with a gap to provide a space for insertion of a tungsten wire (1 cm), which was used for the study of the spectrometer acceptance [84]. These electrodes form an electrostatic potential that is a few Volts lower than the acceleration voltage of the delivered target ions. This was done to make the ion motion slow and to make the confinement time for the ions longer. Electrodes at both ends make barrier potentials for the longitudinal confinement.

The differential cross-sections obtain are shown in Figure 1.2. Tsukada et al. [84] found experimentally that ^{132}Xe has rms charge radius of $4.79(+0.12)(-0.10)$ fm.

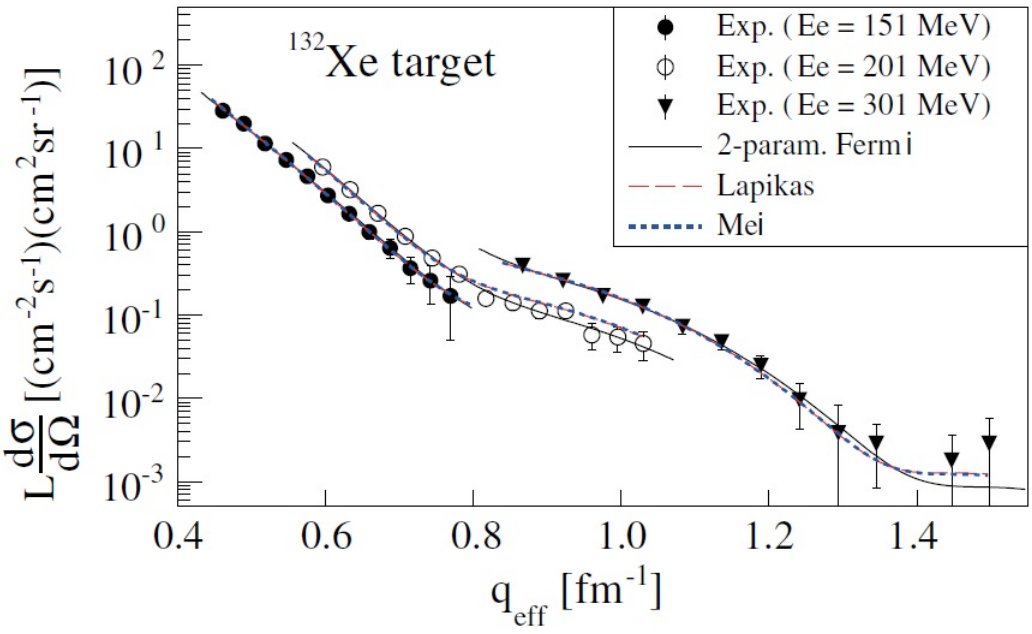

Figure 1.2: Differential cross sections multiplied by luminosity versus effective momentum transfer for E_e = 151 MeV (black filled circles), 201 MeV (open circles), and 301 MeV (filled triangles). The lines are the results of DREPHA calculations assuming nuclear charge density distributions obtained by the two-parameter Fermi distribution (black solid line), the Hartree- Fock + phenomenological calculation (red dashed line), and the beyond-relativistic-mean-field theory (blue dotted line). The parameters of the two-parameter Fermi distribution are best values [84]. Copyright (2017) by the American Physical Society.

1.3 Measuring Nuclear Properties using Atomic Spectroscopy

When considering the nucleus in the studies of atomic structure, simplifying assumptions are often made with regards to its properties to facilitate calculations. That is, the nucleus is treated as an infinitely heavy, point-particle which acts as a source of the Coulomb field that the atomic electrons interact with. The relaxation of these assumptions manifest as corrections in calculations and lead to the so-called isotope shifts in the atomic energy levels [44, 60].

The effect of the finite nuclear mass leads to two sources of isotope shifts, the Normal Mass Shift (NMS) and the Specific Mass Shift (SMS). The NMS manifests simply as a rescaling of the infinite mass results, E_m, by the reduced mass ratio $\mu/m = M_A/(M_A + m)$:

$$\delta E_{NMS} = E_\mu - E_m = \left(\frac{M_A}{M_A + m} - 1 \right) E_m = -\frac{m}{M_A + m} E_m. \tag{1.11}$$

The SMS arises from the effect of the finite nuclear mass on atomic electron correlations:

$$\delta E_{NMS} = \frac{M_A}{2(M_A + m)} \left\langle \sum_{i \neq j} p_i \cdot p_j \right\rangle \tag{1.12}$$

and represents a non-trivial many-body problem [44, 60].

Of greatest interest for this thesis is the third contributor to the isotope shift, the so-called Field Shift (FS) effect. The FS arises from the finite nuclear charge radius, and specifically the small change in charge radius from one isotope to the next. It is standard practice to parametrize the FS as:

$$\delta E = -F \delta \left\langle r^2 \right\rangle, \tag{1.13}$$

where $\delta \langle r^2 \rangle$ is the change in the mean-square radius of the nucleus [44, 60].

To derive the FS parameter, F, we will follow Johnson [44] closely and assume that the nucleus is a uniform charged hard-sphere:

$$V(r) = \begin{cases} -\frac{Z}{2R}\left\{3 - \frac{r^2}{R^2}\right\}, & \text{if } r \leq R; \\ -\frac{Z}{r}. & \text{if } r > R. \end{cases} \tag{1.14}$$

For such a charged distribution, the mean square radius, $\langle r^2 \rangle$ is related to the square radius by

$$\left\langle r^2 \right\rangle = \frac{3}{5} R^2. \tag{1.15}$$

Thus, a change in V induced by a change in R, δR, can be expressed in terms of the mean square radius:

$$\delta V = \frac{5Z}{4R^3}\left(3 - \frac{r^2}{R^2}\right) \delta \left\langle r^2 \right\rangle, \quad r \leq R. \tag{1.16}$$

If we now recall the form of equation (1.13), we can introduce the operator $F(r)$:

$$F(r) = \begin{cases} -\frac{5Z}{4R^3}\left(1 - \frac{r^2}{R^2}\right), & \text{if } r \leq R; \\ = 0, & \text{if } r > R, \end{cases} \tag{1.17}$$

from which we can obtain the FS parameter, F, via perturbation theory:

$$F = \langle n | F(r) | n \rangle . \tag{1.18}$$

The method of isotope shifts, being a relative measurement, is highly accurate, but depends crucially on what could be termed an "anchor isotope". That is, an isotope whose nuclear properties are established via an independent method such as electron scattering. Once a said isotope is established, the isotope shift analysis of an isotopic sequence can be made. At the light end of the periodic table, where the nuclear properties are well known, the method is exquisitely accurate. Lu et al. [52] reviews much of the work in ^{6}He, ^{8}He and ^{11}Li. Recent work for neutral lithium is also discussed in Wang et al. [85].

The isotope shift method has also long been used for heavy isotopes. For example, see the experimental work of Otten [64], Billowes and Campbell [17], Neugart [63],

and Kluge and Nörtershäuser [48]. For theoretical work, in particular in cesium and francium, there is the recent work of Dzuba et al. [32].

As discussed above, the isotope shift method is very accurate provided an anchor isotope is available to anchor the chain. Unfortunately, the heavy elements between bismuth and thorium lack stable isotopes, thus prohibiting the traditional experimental methods of obtaining nuclear information; although the SCRIT facility discussed above is a step in that direction. It is to goal of this thesis to present a new method, using spectroscopy of Li-like heavy ions, of providing the anchor isotope nuclear information upon which isotope shift work can then be based. A similar approach using Na-like ions has been proposed by Gillaspy, Blundell, and coworkers [35].

1.4 Precision X-ray Spectroscopy: A New Approach for determining Nuclear Charge Radii

The quote appearing at the top of this chapter was made by Krane in 1988 [49]. Now, 30 years later, we in this thesis beg to differ. In the intervening decades, the state of the theoretical description (relativistic many-body perturbation theory and bound-state quantum electrodynamics) of the structure of atoms as well as the state of x-ray spectroscopy have reached a sufficiently refined point that this kind of analysis is now possible.

Recently, great progress has been made in the capture and storage of rare, short-lived radioactive isotopes as highly-charged ions in devices known as ion traps (EBITs) so that absolute wavelength X-ray measurements can be made [14, 15]. In heavy, highly charged ions, the correction to electronic transition energies due to the finite nuclear size becomes quite large, of the same order of magnitude as QED corrections. For instance, in Li-like bismuth, the total energy shift due to the finite nuclear size is 1-2 eV as compared to the total transition energy of a few keV (Figure 1.4).

For sufficiently simple systems (H, He, Li-like ions), the atomic energy levels can be calculated with sufficient precision using *ab initio* techniques. In Li-like ions, one has the advantage that the $2s_{1/2} - 2p_{3/2}$ excitation is low in energy, and the p-state

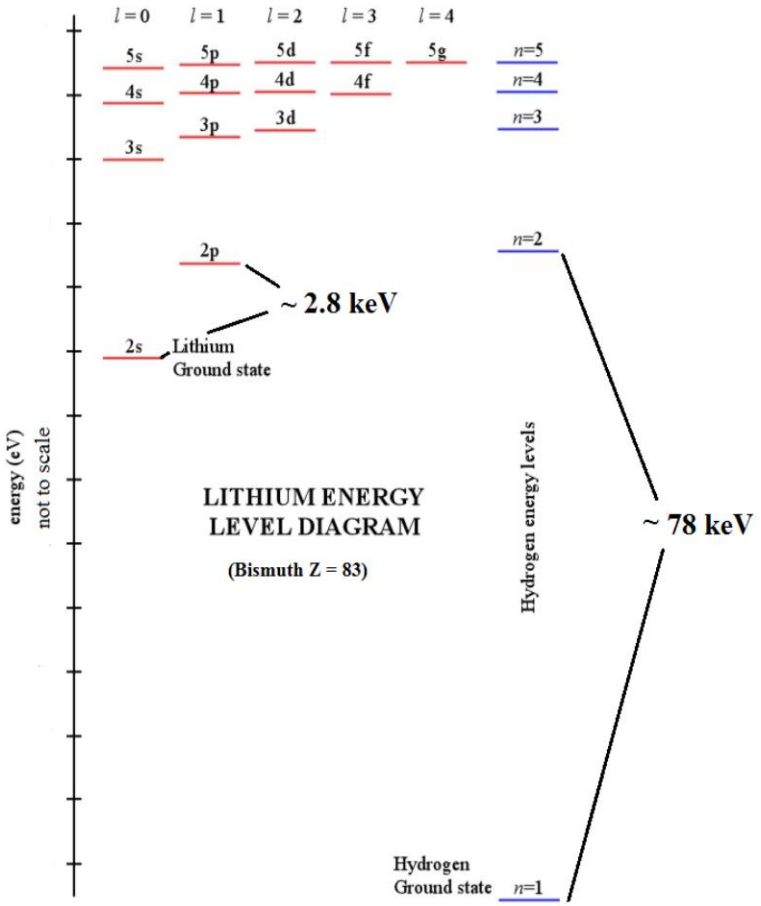

Figure 1.3: Energy levels comparison for H-like and Li-like bismuth

is rather insensitive to the nuclear size compared to the s-state. In addition, typical electron beam ion traps (EBITS) cannot breed H/He-like ions at $Z > 82$, but Li like is possible.

Furthermore, progress made in x-ray spectroscopy has made it possible to determine absolute x-ray energies with meV precision without the need for comparison to reference lines. This together with the ability to calculate the QED correction to the transition energy (roughly same size as nuclear size correction) reliably (50 meV) provides the ability to compare calculated and measured transition energies at the level of a few tens of meV. So far in testing QED the following procedure has been adopted: (a) Measure the experimental value for the $2s_{1/2} - 2p_{3/2}$ x-ray transition in Li-like ions, (b) calculate the Dirac transition energy for a finite-sized nucleus, assuming a nuclear charge radius typically taken from a table (this is no problem, because measurements of $2s_{1/2} - 2p_{3/2}$ x-rays have so far always been done with stable nuclei where the nuclear size is known quite well.), (c) calculate the QED contribution, (d) add finite-size Dirac value and QED correction, compare to the experimental value, then interpret as a test of the QED term. However there is a major problem in this, as mentioned above for certain heavy nuclei, there are no experimental data for the absolute nuclear charge radius.

We propose to turn the above argument around, we take the calculated QED corrections (which have been validated in nearby stable elements) and determine the charge radius that gives agreement with measurement (Figure 1.4).
To that end, we have worked out a new method to extract absolute nuclear charge radii from x-ray transition energies in highly charged ions of heavy, ($Z > 80$) elements. As a way of outline: We know the dependence of the x-ray transition energy on the nuclear charge, this is the famous Mosleys law. We then consider the transition energy of the $2s2p_{3/2}$ transition in lithium-like heavy elements. More specifically: (a) In heavy Li-like ions (Pb, Bi, U) where the nuclear charge radius is known, establish agreement between experiment and theory and determine uncertainty for the calculated QED correction [4, 5]. (b) We could then argue that the QED corrections are a smooth function of the nuclear charge Z, therefore the same calculation in a close-by radioactive nucleus (e.g. Fr) should be similarly reliable. (c) We would then

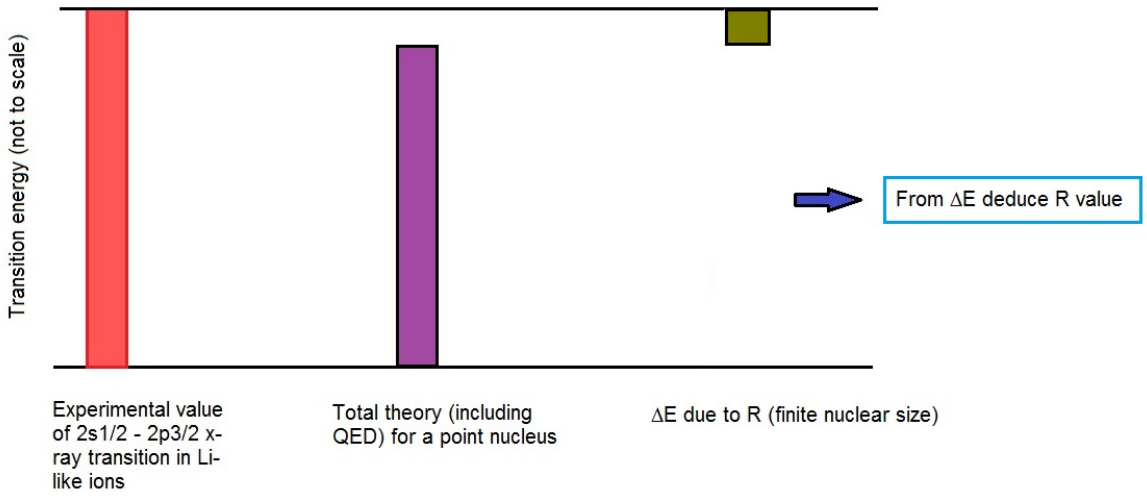

Figure 1.4: Schematic for extracting nuclear charge radius information from the transition energy in Li-like ions.

obtain measurements of the $2s_{1/2} - 2p_{3/2}$ transition in Fr with the highest possible precision, that is, the absolute accuracy should be better than 30 meV. (d) Subtract the calculated QED correction from the experimental value. (e) Perform a relativistic many-body (RMPT) calculation and adjust the value of the nuclear charge radius such that agreement is achieved. (f) Deduce the nuclear charge radius. Thus to determine the nuclear charge radius to the desired accuracy we need to determine the transition energy to about 50 meV. That is 1 part in 100,000.

For francium, the finite nuclear size ($R \approx 5$ fm) shifts the transition by around $E \approx 25$eV, and the shift is quadratic in R. From this we get a sensitivity of

$$\Delta E/\Delta R \approx 10 \text{ (eV/fm)}. \tag{1.19}$$

If the combined uncertainty of the measurement and the the QED calculation is 100 meV, the nuclear charge radius can be determined to 1/100 fm, or 0.2 %

To that end, this thesis produces equations relating the rms nuclear charge radius as a function of transition energy. Thus, when experimental transition energies for a particular isotope are available, one directly has an estimate of the corresponding nuclear charge radius. Of course, at the moment only x-ray data exists for Bi and U as

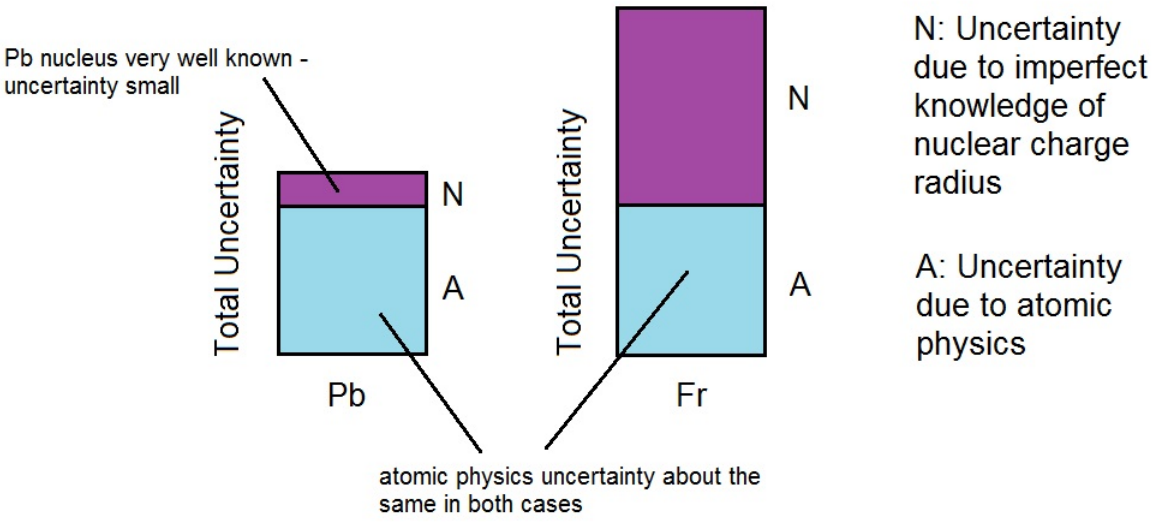

Figure 1.5: Comparison of the uncertainty in transition energy for Pb and Fr. A represents the atomic physics contribution and N represents the nuclear uncertainty contribution. The figure is not to scale.

mentioned above. So these are the cases that will be specifically looked at in chapter 8. However, the theoretical results of charge-radius as a function of the transition energy for all elements between Pb and U will be given as well.

Chapter 2

Theory

2.1 Introduction

The theory of atoms and highly charged ions is contained in the theory of quantum electrodynamics (QED), the relativistic quantum theory of interaction of charged particles and photons. The basic structure of QED is basically the same as that established in the 1940's after the initial formulation of renormalization methods. Applications to bound-state problems occured in the 1950's and since then the theory has been well established. The predictions of the theory are in remarkably good agreement with experiment despite ambiguities associated with renormalization of the charge and mass of the electron [58].

Although QED is one of the most well-tested theories in physics, this regime is the weak-field limit. Less well-tested is the strong-field limit, for example, (a) the electric field at the surface of a uranium nucleus amounts to $|\vec{E}| \backsimeq 2 \times 10^{19}$ V/cm, (b) the magnetic moment of Bi^{209} at the nuclear surface gives a magnetic field strength $|\vec{B}| \backsimeq 10^{12}$ Gauss, (c) electrons in the innermost bound states have the largest overlap with the strong-field domain [58]. Precision measurements of electron binding energies and transition rates are best suited to deduce QED phenomena in the strong-field limit. For example, the binding energy of a single K-shell electron in a Coulomb field of a uranium nucleus is about 132 keV $\backsimeq mc^2/3$ and the radial expectation value of the 1s wave function is of the same order as the electron Compton wavelength (386

fm). In addition, and important for this work, one can consider the overlap of the K-shell electron with the nucleus. Assuming to a first approximation that the nucleus is a homogeneous charged sphere with radius R, the overlap integral with a U nucleus is 2.5×10^{-5}, which can be compared with 1.2×10^{-14} for H [58].

2.2 The Dirac Equation

The solutions of the Dirac equation for the free electron and for hydrogenic atoms are the primary building blocks for calculations on more complex many-electron systems [1], and for highly charged ions ($Z > 82$), contains the largest correction to the $2p - 2s$ transition energy due to the finite nuclear charge radius.

We will start our discussion with the hydrogen atom where the nucleus is a point-particle, this will allow us to lay out the analysis of the interaction of the electron with the nucleus without having to deal with the complication of the structure of the nucleus. Once this has been completed, we will include the effect of a nucleus of finite extent. This will turn out to involve merely changing the form of the nuclear potential [57]. To describe the fine structure of atomic states accurately, it is necessary to treat bound electrons relativistically. Thus we must abandon the Schrödinger description of one electron systems and go over to the Dirac description. Our treatment of these issues will follow Johnson [44] closely, with additional points from Bethe and Salpeter [16], Schiff [80] and Greiner [38]. In the independent particle picture, this is accomplished by using the one-electron Dirac orbital, $\phi(\vec{r})$. The orbital satisfies the single particle Dirac equation

$$h_D \phi = E\phi, \tag{2.1}$$

where h_D is the Dirac Hamiltonian given by (in atomic units):

$$h_D = c\vec{\alpha} \cdot \vec{p} + \beta c^2 + V(r), \tag{2.2}$$

where $\vec{(p)}$ is the momentum operator and $V(r)$ is the electrostatic potential due to the nucleus. The speed of light c, in atomic units is given as $c = 1/\alpha = 137.035999\ldots$,

the inverse of the fine-structure constant. The quantities $\vec{\alpha}$ and β in (2.3) are the 4×4 Dirac matrices

$$\vec{\alpha} = \begin{pmatrix} 0 & \vec{\sigma} \\ \vec{\sigma} & 0 \end{pmatrix}; \quad \vec{\beta} = \begin{pmatrix} \mathrm{I} & 0 \\ 0 & -\mathrm{I} \end{pmatrix}, \tag{2.3}$$

where $\vec{\sigma}$ is the the 2×2 Pauli spin matrix and I, the identity matrix. We can emphasize the covariance of the Dirac equation, and in keeping an eye ahead for when we discuss quantum electrodynamics, we can multiply our Dirac Hamiltonian, ((2.2)), by β/c and introduce the notation [18]:

$$\gamma^0 = \beta \qquad \gamma^i = \beta\alpha_i \qquad i = 1, 2, 3. \tag{2.4}$$

This allows us to write are Dirac Hamiltonian in compact form:

$$h_D = \gamma^\mu p_\mu - c + V(r). \tag{2.5}$$

The total angular momentum of the one-electron system is given by $\vec{J} = \vec{L} + \vec{S}$, where $\vec{L}$ is the orbital angular momentum and $\vec{S}$ is the 4×4 spin angular momentum matrix:

$$\vec{S} = \begin{pmatrix} \vec{\sigma} & 0 \\ 0 & \vec{\sigma} \end{pmatrix}. \tag{2.6}$$

Since $\vec{J}$ commutes with the Dirac Hamiltonian, we can specify simultaneous eigenstates of energy, J^2 and J_Z. The eigenstates of J^2 and J_Z are constructed using the two-component representation of $\vec{S}$, the so-called spherical spinors.

Spherical Spinors

Spherical Spinors (SS) are eigenstates of angular momentum operators J^2 and J_Z, and are formed by combining spherical harmonics, $Y_{lm}(\theta, \phi)$, which are eigenstates of orbital angular momentum, L^2 and L_Z and spinors χ_μ:

$$\Omega_{\rm jlm}(\theta,\phi) = \sum_{\mu} \langle l, m-\mu, 1/2, \mu | jm \rangle \, Y_{l,m-\mu}\chi_{\mu}. \tag{2.7}$$

Explicit formulas for the Clebsch-Gordan coefficients (Table 2.1) lead to explicit formulas for the SS having possible values $j = l + 1/2$:

Table 2.1: Values for Clebsch-Gordan coefficients of type: $C(l, 1/2, j; m - m_s, m_s, m)$.

	$m_s = 1/2$	$m_s = -1/2$
j=l+1/2	$\sqrt{\frac{l+m+1/2}{2l+1}}$	$\sqrt{\frac{l-m+1/2}{2l+1}}$
j=l-1/2	$-\sqrt{\frac{l-m+1/2}{2l+1}}$	$\sqrt{\frac{l+m+1/2}{2l+1}}$

$$\Omega_{l+1/2,l,m} = \begin{pmatrix} \sqrt{\frac{l+m+1/2}{sl+1}} Y_{l,m-1/2}(\theta,\phi) \\ \sqrt{\frac{l-m+1/2}{sl+1}} Y_{l,m+1/2}(\theta,\phi) \end{pmatrix}, \tag{2.8}$$

$$\Omega_{l-1/2,l,m} = \begin{pmatrix} -\sqrt{\frac{l-m+1/2}{sl+1}} Y_{l,m-1/2}(\theta,\phi) \\ \sqrt{\frac{l+m+1/2}{sl+1}} Y_{l,m+1/2}(\theta,\phi) \end{pmatrix}. \tag{2.9}$$

The SS are eigenfunctions of $\vec{\sigma} \cdot \vec{L}$, and thus the operator

$$K = -1 - \vec{\sigma} \cdot \vec{L}, \tag{2.10}$$

which satisfies the eigenvalue equation,

$$K \, \Omega_{jlm} = \kappa \, \Omega_{jlm}. \tag{2.11}$$

The eigenvalues κ are integers with a value given by $\kappa = -l - 1$ when $j = l + 1/2$ and $\kappa = l$ when $j = l - 1/2$. Thus, in summary,

$$\kappa = \mp (j + 1/2) \quad \text{for} \quad j = l \pm 1/2, \tag{2.12}$$

that is, the value of κ determines both j and l. Therefore, we can use the more economic notation $\Omega_{jlm} \to \Omega_{\kappa m}$. We can get a better sense of the economy of the new notation by looking at the spectroscopic notation associated with the states

designated by j and l given in table 2.2

Table 2.2: Table of states given in spectroscopic notation

	$s_{1/2}$	$p_{1/2}$	$p_{3/2}$	$d_{3/2}$	$d_{5/2}$	$f_{5/2}$	$f_{7/2}$	$g_{7/2}$	$g_{9/2}$	$h_{9/2}$	$h_{11/2}$
l	0	1	1	2	2	3	3	3	3	4	4
j	1/2	1/2	3/2	3/2	5/2	5/2	7/2	7/2	9/2	9/2	11/2
κ	-1	1	-2	2	-3	3	-4	4	-5	5	-6

The spherical spinors satisfy the orthogonality conditions

$$\int_0^{\pi} \sin\theta d\theta \int_0^{2\pi} d\phi \; \Omega^{\dagger}_{\kappa' m'}(\theta,\phi)\Omega_{\kappa m}(\theta,\phi) = \delta_{\kappa'\kappa}\delta_{m'm}, \tag{2.13}$$

while under a parity transformation, P, the spherical harmonic portion transforms as

$$\mathrm{P}Y_{lm}(\theta,\phi) = Y_{lm}(\pi-\theta,\phi+\pi) = (-1)^l Y_{lm}(\theta,\phi). \tag{2.14}$$

Thus the spherical spinors are eigenfunctions of P having eigenvalues $p = (-1)^l$. This implies that the spinors $\Omega_{\kappa m}$ and $\Omega_{-\kappa m}$, corresponding to the same value of j and have l differing by 1 have opposite parity.

It is important to study the behavior of the spherical spinors under the operator $\vec{\sigma}\cdot\hat{r}$, as important identities will be obtained for later use. The product of this operator with itself is equal to the identity:

$$(\vec{\sigma}\cdot\hat{r})\;(\vec{\sigma}\cdot\hat{r}) = 1. \tag{2.15}$$

In addition, the operator $\vec{\sigma}\cdot\hat{r}$ commutes with the the total angular momentum operator $\vec{J}$, thus the eigenvalue of $\vec{J}$, j, remains unchanged. Under the parity operation, $\vec{\sigma}\cdot\hat{r}$ changes sign, thus operating on the SS:

$$\vec{\sigma}\cdot\hat{r}\Omega_{\kappa m}(\theta,\phi) = -\Omega_{-\kappa m}(\theta,\phi). \tag{2.16}$$

We can now apply two angular momentum identities, first using (2.15) on the operator $\vec{\sigma}\cdot\vec{p}$ together with the following for Pauli spin matrices

$$\vec{\sigma}\cdot\vec{A}\;\vec{\sigma}\cdot\vec{B}=\vec{A}\cdot\vec{B}+\imath\vec{\sigma}\cdot[\vec{A}\times\vec{B}]. \tag{2.17}$$

This leads to,

$$\vec{\sigma}\cdot\vec{p}=\vec{\sigma}\cdot\hat{r}\;\vec{\sigma}\cdot\hat{r}\;\vec{\sigma}\cdot\vec{p}=-\imath\vec{\sigma}\cdot\hat{r}\left(\imath\hat{r}\cdot\vec{p}-\frac{\vec{\sigma}\cdot[\vec{r}\times\vec{p}]}{r}\right). \tag{2.18}$$

From (2.18) it follows that

$$\vec{\sigma}\cdot\vec{p}\;f(r)\Omega_{\kappa m}(\theta,\phi)=\imath\left(\frac{df}{dr}+\frac{\kappa+1}{r}f\right)\Omega_{-\kappa m}(\theta,\phi). \tag{2.19}$$

Evaluation

With the useful identities (2.14) and (2.19) in hand we can continue our solution of the H-like Dirac equation (2.2). Specifically, wave-function solutions of the form

$$\phi_\kappa(\vec{r})=\frac{1}{r}\begin{pmatrix}\imath P_\kappa(r)\;\Omega_{\kappa m}(\hat{r})\\ Q_\kappa(r)\;\Omega_{-\kappa m}(\hat{r})\end{pmatrix}. \tag{2.20}$$

Applying the above identities, one is led to a set of coupled first-order differential equations for the radial functions $P_\kappa(r)$ and $Q_\kappa(r)$:

$$\left(V+c^2\right)P_\kappa(r)+c\left(\frac{d}{dr}-\frac{\kappa}{r}\right)Q_\kappa(r)=EP_\kappa(r), \tag{2.21a}$$

$$-c\left(\frac{d}{dr}+\frac{\kappa}{r}\right)P_\kappa(r)+\left(V-c^2\right)Q_\kappa(r)=EQ_\kappa(r). \tag{2.21b}$$

And the wave-functions are normalized according to the standard condition

$$\int\phi_\kappa^\dagger(\vec{r})\phi_\kappa(\vec{r})d\vec{r}=1, \tag{2.22}$$

which in terms of the radial functions P and Q can be written as

$$\int_0^\infty\left[P_\kappa^2(r)+Q_\kappa^2(r)\right]dr=1. \tag{2.23}$$

For the point-nuclear case, the potential, V, is given by the classical Coulomb term $V(r) = -Z/r$. Substituting this into (2.21a) and (2.21b) leads to the following two equations:

$$\left(\frac{-Z}{r} + c^2\right) P_\kappa(r) + c\left(\frac{d}{dr} - \frac{\kappa}{r}\right) Q_\kappa(r) = E P_\kappa(r), \tag{2.24a}$$

$$-c\left(\frac{d}{dr} + \frac{\kappa}{r}\right) P_\kappa(r) - \left(\frac{Z}{r} + c^2\right) Q_\kappa(r) = E Q_\kappa(r). \tag{2.24b}$$

With this potential, an analytical solution for P and Q is possible. As a first step in this direction, consider solutions in the regime of large r values (ie. $r \to \infty$). In this case, equations (2.19) and (2.20) reduce to the following simple differential equations

$$c\frac{dQ_\kappa}{dr} = \left(E - c^2\right) P_\kappa, \tag{2.25}$$

and

$$c\frac{dP_\kappa}{dr} = -\left(E + c^2\right) Q_\kappa. \tag{2.26}$$

These can be converted into a single second-order equation first by differentiating equation (2.26):

$$c\frac{d^2P_\kappa}{dr^2} = -\left(E + c^2\right)\frac{dQ_\kappa}{dr}, \tag{2.27}$$

and substituting for dQ_κ/dr by inserting the result from (2.25)

$$c\frac{d^2P_\kappa}{dr^2} = \frac{-\left(E + c^2\right)\left(E - c^2\right)}{c} P_\kappa. \tag{2.28}$$

Simple algebra leads to the final result,

$$c^2\frac{d^2P_\kappa}{dr^2} + \left(E^2 - c^4\right) P_\kappa = 0. \tag{2.29}$$

Equation (2.29) has two linearly independent solutions, $e^{\pm\lambda r}$, where $\lambda = \sqrt{c^2 - E^2/c^2}$. Since it's required of valid radial functions to vanish at infinity, the appropriate solu-

tion is

$$P_\kappa(r) = e^{-\lambda r}, \tag{2.30}$$

with the corresponding result for $Q_\kappa(r)$ given as

$$Q_\kappa(r) = \sqrt{\frac{c^2 - E}{c^2 + E}} e^{-\lambda r}. \tag{2.31}$$

Factoring the wave equations, since two functions of r are required [16], with the ansatz

$$P_\kappa(r) = \sqrt{1 + \frac{E}{c^2}}\; e^{-\lambda r} \left(\phi_1 + \phi_2\right), \tag{2.32}$$

$$Q_\kappa(r) = \sqrt{1 - \frac{E}{c^2}}\; e^{-\lambda r} \left(\phi_1 - \phi_2\right), \tag{2.33}$$

and substituting into equations (2.21a), (2.21b) together with the substitution $x = 2\lambda r$ leads to two coupled equations in the functions ϕ_1 and ϕ_2:

$$\frac{d\phi_1}{dx} = \frac{EZ}{c^2 \lambda x}\phi_1 + \left(\frac{Z}{\lambda x} - \frac{\kappa}{x}\right)\phi_2, \tag{2.34}$$

and

$$\frac{d\phi_2}{dx} = -\left(\frac{Z}{\lambda x} + \frac{\kappa}{x}\right)\phi_1 + \left(1 - \frac{EZ}{c^2 \lambda x}\right)\phi_2. \tag{2.35}$$

Solutions of (2.34) and (2.35) have limiting forms as $\phi_1 = a_1 x^\gamma$ and $\phi_2 = a_2 x^\gamma$ as $x \to 0$. When these are substituted into (2.34) and (2.35), a ratio of the coefficients a_1 and a_2 is obtained:

$$\frac{a_2}{a_1} = \frac{\gamma - EZ/c^2\lambda}{-\kappa + Z/\lambda} = \frac{-\kappa - Z/\lambda}{\gamma + EZ/c^2\lambda}, \tag{2.36}$$

from which an expression for γ is obtained from $\gamma^2 = \kappa^2 - Z^2/c^2 = \kappa^2 - \alpha^2 Z^2$, since $\alpha = 1/c$ in atomic units, by taking the positive square root (i.e. $\gamma = \sqrt{\kappa^2 - \alpha^2 Z^2}$). Using (2.34), we can express ϕ_2 in terms of ϕ_1 as

$$\phi_2 = \frac{1}{-\kappa + Z/\lambda}\left[x\frac{d\phi_1}{dx} - \frac{EZ}{c^2\lambda}\phi_1\right]. \tag{2.37}$$

Equation (2.37) can be used to remove ϕ_2 from (2.34):

$$x\frac{d^2\phi_1}{dx^2} + (1-x)\frac{d\phi_1}{dx} - \left(\frac{\gamma^2}{x^2} - \frac{EZ}{c^2\lambda}\right)\phi_1 = 0; \tag{2.38}$$

by making the substitution: $\phi_1(x) = x^\gamma F(x)$, one is led to Kummer's equation,

$$x\frac{d^2F}{dx^2} + (b-x)\frac{dF}{dx} - aF = 0, \tag{2.39}$$

where $a = \gamma - EZ/c^2\lambda$, and $b = 2\gamma + 1$.

The solutions to (2.39) are regular at the origin and are the confluent hypergeometric functions, thus ϕ_1 becomes

$$\phi_1(x) = x^\gamma F(a, b, x), \tag{2.40}$$

while ϕ_2 can be expressed as

$$\begin{aligned}\phi_2(x) &= \frac{x^\gamma}{(-\kappa + Z/\lambda)}\left(x\frac{dF}{dx} + aF\right) \\ &= \frac{(\gamma - EZ/c^2\lambda)}{(-\kappa + Z/\lambda)}x^\gamma F(a+1, b, x).\end{aligned} \tag{2.41}$$

When these results are combined, the following unnormalized radial functions for the Dirac equation are obtained:

$$\begin{aligned}P_\kappa(r) =& \sqrt{1 + E/c^2}\; e^{-x^2/2}x^\gamma[(-\kappa + Z/\lambda)F(a, b, x) \\ &+ (\gamma - EZ/c^2\lambda)F(a+1, b, x)],\end{aligned} \tag{2.42}$$

$$Q_\kappa(r) = \sqrt{1+E/c^2}\; e^{-x^2/2} x^\gamma [(-\kappa + Z/\lambda) F(a,b,x) - (\gamma - EZ/c^2\lambda) F(a+1,b,x)]. \tag{2.43}$$

To normalize (2.42) and (2.43), one must turn to the eigenvalue problem first. At large values of r, the confluent hypergeometric functions have the following asymptotic form:

$$F(a,b,x) \to \frac{\Gamma(b)}{\Gamma(a)} e^x x^{a-b} [1 + O(|x|^{-1})] \tag{2.44}$$

$$aF(a,b,x) \to \frac{\Gamma(b)}{\Gamma(a)} e^x x^{a+1-b} [1 + O(|x|^{-1})]. \tag{2.45}$$

It follows that the radial wavefunctions are normalizable only if the coefficients in the exponentials above vanish, which occurs when $a = -n_r$, where $n_r = 0, -1, -2, \cdots$. The definition of the principal quantum number, n, is given via the relation, $n = n_r + k$, where k is given as the absolute value of the relativistic angular momentum $|\kappa| = j + 1/2$. The eigenvalue equation, can be written as

$$EZ/c^2\lambda = \gamma + n - k. \tag{2.46}$$

This equation can be solved for E to obtain the Sommerfeld energy

$$E_{n\kappa} = \frac{c^2}{\sqrt{1 + \frac{\alpha^2 Z^2}{(\gamma+n-k)^2}}}. \tag{2.47}$$

The energy levels depend only on k, thus those levels having the same values of n and j, but different l values are degenerate. Thus the $2s_{1/2}$ and $2p_{1/2}$ levels in hydrogen-like ions are degenerate. It must be mentioned that this is only true if the nucleus is point-like, finite nuclear size breaks this degeneracy.

2.3 First-Order QED correction

Quantum electrodynamics (QED), which is the theory for the motions of electrically charged particles (electrons, positrons, charged nuclei) together with their interactions with each other and with the Maxwell photon field, provides the framework for the relativistic theory of atoms and highly-charged ions [37]. During these processes, the number of particles is not necessarily conserved, thus leading one to adopt quantum field theory (QED is an example) as the appropriate tool for investigation. Feynman diagrams are used to clarify the radiative and interaction processes that contribute, and a subset of these diagrams correspond to the familiar self-consistent field theory, which is the starting point for descriptions treating the many-body nature of most atoms (Relativisic Many-body Perturbation Theory is an example). These approaches have successfully led to highly accurate calculations of energy-levels and wavefunctions in many-electron atoms [37]. These ideas will be treated more fully in chapter 4.

The fundamental processes under consideration are depicted in figure 2.1, being the electron self-energy (SE) and vacuum-polarization (VP) respectively. Due to the small mass of the electron, the SE of the bound electron dominates the QED level shift in H-like atoms. As a first indication concerning the importance of the QED radiative processes, consider the associated energy shift for a K-shell electron in H-like U. The sum of both the VP and SE corrections amounts to 266 eV compared to the total 1s binding energy of 132 keV [58].

Traditionally, QED corrections are treated in a perturbation expansion in the fine-structure constant $\alpha \backsimeq 1/137$, representing the number of virtual photons. At the same time, for each order of α one considers an additional expansion in $Z\alpha$ (the coupling constant to the external field with the nuclear charge). However, for the heaviest elements this is not really that small compared to 1 (for U, $Z\alpha \backsimeq 0.67$). Thus an essential aspect of strong-field bound-state QED is the avoidance of any solutions based on $Z\alpha$ expansions.

2.3.1 Bound-state QED (The Furry Picture)

The starting point for considering QED effects in atoms and highly-charged ions is to work in the so-called Furry picture [59]; where instead of using free-particle Dirac wavefunctions, one begins with solutions to a Dirac particle bound in a Coulomb field. Our treatment of this topic will follow Mohr [56, 57] and Grant [37].

We begin by considering the time-dependent solutions of the bound-system Dirac equation:

$$\left(\imath\,\vec{\alpha}\cdot\vec{\bigtriangledown}+\beta+V(\vec{x})\right)\phi_n(\vec{x})=0, \tag{2.48}$$

given as

$$\phi_n(x)=\phi_n(\vec{x})e^{-\imath E_n t}. \tag{2.49}$$

As mentioned above, the potential, $V(\vec{x})$ is assumed to be a nuclear Coulomb field (i.e. H-atom or ion); however the formalism allows an effective potential due to the presence of other electrons in a many-electron atom.

The electron-positron field operator is expanded in terms of electron/positron creation and annihilation operators and solutions to the Dirac equation (2.49):

$$\psi(x)=\sum_{E_n>0}a_n\phi_n(x)+\sum_{E_m<0}b_m^\dagger\phi_m(x), \tag{2.50}$$

where a_n is the electron destruction operator for an electron in state n ($E_n>0$) while $b_m^\dagger$ is the positron creation operator for a positron in state m ($E_m>0$). In summary:

$$\begin{gathered} a_n \text{ and } a_n^\dagger = 0 \text{ if } E_n<0, \\ b_n \text{ and } b_n^\dagger = 0 \text{ if } E_n>0. \end{gathered} \tag{2.51}$$

Furthermore, the creation and annihilation operators obey the standard anti-

commutation relations:

$$\begin{aligned} \left\{a_n, a_m^\dagger\right\} = \delta_{nm} \; ; \; \{a_n, a_m\} = \left\{a_n^\dagger, a_m^\dagger\right\} = 0, \\ \left\{b_n, b_m^\dagger\right\} = \delta_{nm} \; ; \; \{b_n, b_m\} = \left\{b_n^\dagger, b_m^\dagger\right\} = 0. \end{aligned} \tag{2.52}$$

The unperturbed state vectors in this case are of the form:

$$|n\rangle = a_n^\dagger \, |0\rangle \tag{2.53a}$$

$$|n\rangle = a_{1s+}^\dagger a_{1s-}^\dagger a_n^\dagger \, |0\rangle \tag{2.53b}$$

describing one- and three-electron atoms (ions) respectively. For the three-electron case, one usually deals with a single valence electron outside a closed shell, thus this formalism automatically puts those shells into the correct angular momentum eigenstate [74]. This is given in the subscripts for the creation-operators in (2.53b), ($1s+$ represents the one core electron in the 1s state with spin in the positive direction, while $1s-$ represents the other 1s core electron with spin in the opposite direction). In between are, of course, the two-electron ions and the following analysis applies equally to them as well. However, in this thesis our emphasis was on the two former cases exclusively, so for the sake of brevity the analysis of two-electron atoms will be omitted and the interested reader is referred to the literature [56, 58] and references therein.

When considering these states, the unperturbed energy operator is given by the normal-ordered expression:

$$H_0 = \int d^3x N \left[\psi^\dagger(x) H_D \psi(x)\right]$$
$$= \sum_{E_n>0} E_n a_n^\dagger a_n - \sum_{E_m<0} E_m b_m^\dagger b_m, \tag{2.54}$$

where H_D is the Dirac Hamiltonian

$$H_D = -\imath\vec{\alpha}\cdot\vec{\nabla} + \beta + V(x). \tag{2.55}$$

Interactions between the electron-positron and the photon fields are described by the interaction Hamiltonian

$$H_I(x) = j^\mu(x) A_\mu(x) - \delta M(x), \tag{2.56}$$

where j is the electron-positron current operator given by

$$j^\mu(x) = -\frac{1}{2} e \left[\bar{\psi}(x)\gamma^\mu, \psi(x)\right], \tag{2.57}$$

where $A_\mu(x)$ is the quantized photon field operator, and δM is the mass renormalization counterterm

$$\delta M(x) = \frac{1}{2}\delta m \left[\bar{\psi}(x), \psi(x)\right]. \tag{2.58}$$

The magnitude of the mass counterterm coefficient δm is fixed by the condition

$$\lim_{Z\alpha\to 0} \Delta E_n(Z\alpha) \longrightarrow 0, \tag{2.59}$$

where ΔE_n is the level shift. The commutators in j and δM refer to the creation and destruction operators only. The Dirac wavefunctions and gamma matrices always appear in the order shown:

$$\left[\bar{\psi}(x), \psi(x)\right] = \sum_{mn} \overline{\phi_m}(x)\phi_n(x) \left[\hat{a}_m^\dagger, \hat{a_n}\right] + \cdots. \tag{2.60}$$

In the theory of bound-states with which we are dealing, the perturbation expansion for the S matrix (the usual starting point for level-shift calculations) contains infinities corresponding to the intermediate states degenerate with the state under consideration. These singularities ultimately cancel other terms in the expansion. To begin to see this, it is convenient to introduce the adiabatically damped interaction Hamiltonian

$$H_{\mathrm{I}}^{\epsilon}(t) = e^{-\epsilon|t|} H_{\mathrm{I}}(t), \tag{2.61}$$

where

$$H_{\mathrm{I}}(t) = \int d^3x H_I(x) \tag{2.62}$$

as the basic interaction for level shift calculations. The damping factor, ϵ, makes the terms in the perturbation expansion that are infinite in the limit $\epsilon \to 0$ finite. Thus singularities appearing in separate terms of the level shift expression cancel if appropriate Feynman diagrams are included.

Time development, given by

$$\imath \frac{\partial}{\partial t} U_{\epsilon,\lambda}(t, t_0) = \lambda H_{\mathrm{I}}^{\epsilon}(t) U_{\epsilon,\lambda}(t, t_0) \tag{2.63}$$

has the well known solution

$$U_{\epsilon,\lambda}(t, t_0) = \sum_{j=0}^{\infty} (-\imath\lambda)^j \int_{t_0}^{t} dt_j \int_{t_0}^{t} dt_{j-1} \cdots \int_{t_0}^{t} dt_1 H_{\mathrm{I}}^{\epsilon}(t_j) \cdots H_{\mathrm{I}}^{\epsilon}(t_1), \tag{2.64}$$

or, by employing time-ordering,

$$U_{\epsilon,\lambda}(t, t_0) = \sum_{j=0}^{\infty} \frac{(-\imath\lambda)^j}{j!} \int_{t_0}^{t} dt_j \int_{t_0}^{t} dt_{j-1} \cdots \int_{t_0}^{t} dt_1 \mathrm{T}\left[H_{\mathrm{I}}^{\epsilon}(t_j) \cdots H_{\mathrm{I}}^{\epsilon}(t_1)\right] \tag{2.65}$$

The S-matrix is defined by the equation,

$$S_{\epsilon,\lambda} = \lim_{t\to\infty} U_{\epsilon,\lambda}(t,-t) \tag{2.66}$$

with the perturbation expansion,

$$S_{\epsilon,\lambda} = 1 + \sum_{j=1}^{\infty} S^{(j)}_{\epsilon,\lambda}, \tag{2.67}$$

where

$$S^{(j)}_{\epsilon,\lambda} = \frac{(-\imath\lambda)^j}{j!} \int d^4x_j \cdots \int d^4x_1 e^{-\epsilon|t_j|} \cdots e^{-\epsilon|t_1|} \mathrm{T}\left[H_{\mathrm{I}}(x_j)\cdots H_{\mathrm{I}}(x_1)\right]. \tag{2.68}$$

The prescription of Gell-Mann and Low is now used to obtain the expression for the bound-state level shifts in perturbation theory. The level shift may be defined by

$$\Delta E_n = \lim_{\substack{\epsilon\to 0\\ \lambda\to 1}} \frac{\langle n|U_{\epsilon,\lambda}(\infty,0)[H_0 + \lambda H^{\epsilon}_I(0) - E_n]U_{\epsilon,\lambda}(0,-\infty)|n\rangle}{\langle n|U_{\epsilon,\lambda}(\infty,-\infty)|n\rangle}, \tag{2.69}$$

into which we can apply the identity

$$\langle n|U_{\epsilon,\lambda}(\infty,0)[H_0 + \lambda H^{\epsilon}_I(0) - E_n]U_{\epsilon,\lambda}(0,-\infty)|n\rangle = \frac{i\epsilon\lambda}{2}\frac{\partial\langle n|S_{\epsilon,\lambda}|n\rangle}{\partial\lambda}. \tag{2.70}$$

Thus the level shift formula becomes,

$$\Delta E_n = \lim_{\substack{\epsilon\to 0\\ \lambda\to 1}} \frac{\partial\langle n|S_{\epsilon,\lambda}|n\rangle/\partial\lambda}{\langle n|S_{\epsilon,\lambda}|n\rangle}. \tag{2.71}$$

Factorization of the S-matrix can now be used to isolate only the connected graphs in the perturbation expansion. Connected graphs refer to graphs where all the external lines are connected to each other [67];

$$\langle n|S_{\epsilon,\lambda}|n\rangle = \langle n|S_{\epsilon,\lambda}|n\rangle_c \langle 0|S_{\epsilon,\lambda}|0\rangle, \tag{2.72}$$

where the c subscript indicates the connected graph status. When this factorization

is substituted into equation (2.71), we obtain:

$$\Delta E_n = \lim_{\substack{\epsilon\to 0\\ \lambda\to 1}} \frac{i\epsilon}{2} \frac{\partial \langle n|S_{\epsilon,\lambda}|n\rangle_c / \partial\lambda}{\langle n|S_{\epsilon,\lambda}|n\rangle_c} + C. \tag{2.73}$$

The constant term is the same for all levels and thus does not contribute when considering transition energies.

The leading order corrections are obtained by expanding ((2.73)):

$$\Delta E_n = \lim_{\epsilon\to 0} \frac{i\epsilon}{2} \left[\left\langle S^1_\epsilon \right\rangle_c + \left\langle 2S^2_\epsilon \right\rangle_c - (\left\langle S^1_\epsilon \right\rangle_c)^2 + \dots \right], \tag{2.74}$$

where,

$$\left\langle S^j_\epsilon \right\rangle_c = \left\langle S^1_{\epsilon,\lambda} \right\rangle_c |_{\lambda=1}. \tag{2.75}$$

Since we are interested only in terms of order α, we need to consider only the first two terms in (2.74), where the mass-renormalization operator δM contributes through the first-order matrix element S^1

$$\left\langle S^{(1)}_\epsilon \right\rangle_c = i \int d^4x e^{-\epsilon|t|} \left\langle \delta M(x) \right\rangle_c . \tag{2.76}$$

$$\begin{aligned} \left\langle S^{(2)}_\epsilon \right\rangle_c = -\frac{1}{2} \int d^4x_2 d^4x_1 e^{-\epsilon|t_2|} e^{-\epsilon|t_1|} \\ \times \left\langle \mathrm{T}\left[j^{\mu_2}(x_2) A_{\mu_2}(x_2) j^{\mu_1}(x_1) A_{\mu_1}(x_1) \right] \right\rangle_c + \Theta(\alpha^2). \end{aligned} \tag{2.77}$$

We can now employ the following normal-ordering, (denoted by a :), relations for the mass-renormalization and current operators:

$$\delta M(x) = :\delta M(x): - \delta m \mathrm{Tr}\left[S_F(x,x)\right] \tag{2.78}$$

$$j^\mu(x) = : j^\mu(x) : + e\mathrm{Tr}\left[\gamma^\mu S_F(x,x)\right], \tag{2.79}$$

where $S_F(x,x)$ is the electron propagator given, in integral form, as

$$S_F(x_2,x_1) = \frac{1}{2\pi i}\int_{-\infty}^{\infty} dz \sum_n \frac{\phi_n(\bar{x_2})\bar{\phi_n}(\bar{x_1})}{E_n - z(1+i\delta)} e^{-iz(t_2-t_1)}, \tag{2.80}$$

to obtain, for $\left\langle S_\epsilon^{(1)} \right\rangle_c$, the lowest-order mass term

$$\left\langle S_\epsilon^{(1)} \right\rangle_c = \frac{2i}{\epsilon}\delta m \sum_{nm} \int d^3x \bar{\phi_n}(\bar{x})\phi_m(\bar{x})\delta(E_n,E_m)\left\langle a_n^\dagger a_m \right\rangle + \Theta(\epsilon). \tag{2.81}$$

For the second-order term, we can apply the photon propagator D_F, given in integral form as

$$\begin{aligned} g_{\mu_2\mu_1} D_F(x_2-x_1) &= \langle 0|\mathrm{T}\left[A_{\mu_2}(x_2)A_{\mu_1}(x_1)\right]|0\rangle \\ &= -g_{\mu_2\mu_1}\frac{i}{(2\pi)^4}\int_{-\infty}^{\infty} d^4k \frac{e^{-ik(x_2-x_1)}}{k^2+i\delta}, \end{aligned} \tag{2.82}$$

to obtain

$$\begin{aligned} &\left\langle \mathrm{T}\left[j^{\mu_2}(x_2)A_{\mu_2}(x_2)j^{\mu_1}(x_1)A_{\mu_1}(x_1)\right]\right\rangle_c \\ &= \left\langle \mathrm{T}\left[j^{\mu_2}(x_2)j^{\mu_1}(x_1)\right]\right\rangle_c g_{\mu_2\mu_1} D_F(x_2-x_1). \end{aligned} \tag{2.83}$$

We can now apply equation (2.78) to obtain the expression for the second-order term

$$\left\langle S_\epsilon^{(2)} \right\rangle_c = -e^2 \int d^4x_2 \int d^4x_1 e^{-\epsilon|t_2|} e^{-\epsilon|t_1|} D_F(x_2 - x_1) \tag{2.84}$$
$$\times \left[\frac{1}{2} \sum_{n,m} \bar{\phi}_n(x_2)\gamma_\mu \phi_m(x_2) \sum_{k,l} \bar{\phi}_k(x_1)\gamma^\mu \phi_l(x_1) \left\langle a_n^\dagger a_k^\dagger a_l a_m \right\rangle \right.$$
$$+ \sum_{n,m} \bar{\phi}_n(x_2)\gamma_\mu S_F(x_2, x_1)\gamma^\mu \phi_m(x_1) \left\langle a_n^\dagger a_m \right\rangle$$
$$\left. -\mathrm{Tr}[\gamma_\mu S_F(x_2, x_2] \sum_{n,m} \bar{\phi}_n(x_1))\gamma^\mu \phi_m(x_1) \left\langle a_n^\dagger a_m \right\rangle \right] + \Theta(\alpha^2).$$

Combining (2.81) and (2.84) together with the fact that for small ϵ, the integrations over t_1 and t_2 can be simplified, we obtain the formula for the level shift of order α ($e^2 = 4\pi\alpha$)

$$E^{(2)} = -4\pi i\alpha \int d(t_2 - t_1) \int d^3x_2 \int d^3x_1 D_F(x_2 - x_1) \tag{2.85}$$
$$\times \left[\frac{1}{2} \sum_{n,m} \bar{\phi}_n(x_2)\gamma_\mu \phi_m(x_2) \sum_{k,l} \bar{\phi}_k(x_1)\gamma^\mu \phi_l(x_1) \delta(E_n + E_k, E_l + E_m) \right.$$
$$\times \left\langle a_n^\dagger a_k^\dagger a_l a_m \right\rangle + \sum_{n,m} \bar{\phi}_n(x_2)\gamma_\mu S_F(x_2, x_1)\gamma^\mu \phi_m(x_1) \left\langle a_n^\dagger a_m \right\rangle$$
$$\left. -\mathrm{Tr}[\gamma_\mu S_F(x_2, x_2] \sum_{n,m} \bar{\phi}_n(x_1))\gamma^\mu \phi_m(x_1) \left\langle a_n^\dagger a_m \right\rangle \right]$$
$$+ 2i\delta m \sum_{nm} \int d^3x \bar{\phi}_n(\bar{x})\phi_m(\bar{x})\delta(E_n, E_m) \left\langle a_n^\dagger a_m \right\rangle .$$

The level shift formula applies to any zeroth-order basis state consisting of a well defined number of electrons [56].

In general, the three terms inside the square brackets of (2.85) represent the QED processes, (a) photon-exchange, (b) self-energy and (c) vacuum-polarization. We can now consider cases of specific numbers of electrons to obtain specific formulae for each case.

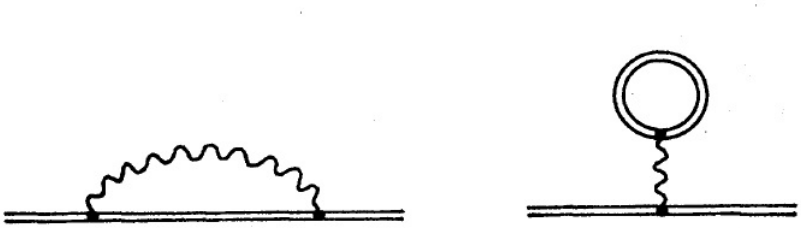

Figure 2.1: Feynman diagrams representing the one-loop SE and VP [56]. Copyright (1985) by the American Physical Society.

One-Electron Atoms

For one-electron atoms, we can consider again the level shift for a single electron in a state i as given above:

$$|i\rangle = a_i^\dagger \, |0\rangle \, . \tag{2.86}$$

In this case, the Fock space matrix elements have the following values:

$$\left\langle a_n^\dagger a_k^\dagger a_l a_m \right\rangle = 0; \tag{2.87}$$

$$\left\langle a_n^\dagger a_m \right\rangle = \delta_{ni}\delta_{mi}. \tag{2.88}$$

Thus we see that for H-like atoms/ions, there is no photon-exchange which is a many-body effect, and only the self-energy and vacuum-polarization contribute.

In this case equation (2.85) reduces to the following two pieces:

$$E^{(2)} = E_{SE}^{(2)} + E_{VP}^{(2)}, \tag{2.89}$$

where,

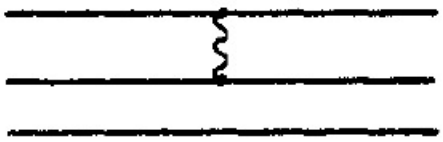

Figure 2.2: Feynman diagram representing the one-photon exchange effect in a three-electron atom/ion [74]. Copyright (1987) by the Institute of Physics.

$$E_{SE}^{(2)} = -4\pi i\alpha \int d(t_2 - t_1) \int d^3x_2 \int d^3x_1 D_F(x_2 - x_1) \times \bar{\phi}_i(x_2)\gamma_\mu S_F(x_2, x_1)\gamma^\mu \phi_i(x_1) - \delta m \int d^3x \bar{\phi}_i(x)\phi_i(x), \tag{2.90}$$

and,

$$E_{VP}^{(2)} = 4\pi i\alpha \int d(t_2 - t_1) \int d^3x_2 \int d^3x_1 D_F(x_2 - x_1) \times \mathrm{Tr}\left[\gamma_\mu S_F(x_2, x_1)\right] \bar{\phi}_i(x_2)\gamma^\mu \phi_i(x_1). \tag{2.91}$$

Three-Electron Atoms

For three-electron atoms, we can consider the level shift for a single electron in a state i above a closed core of 1s electrons, as shown in the Feynman diagram of Figure 2.2. We recall that earlier, (2.53b), we stated that the state representing such an atom is given by:

$$|i\rangle = a_{1s+}^\dagger a_{1s-}^\dagger a_i^\dagger |0\rangle . \tag{2.92}$$

The challenge now is to evaluate the vacuum matrix elements of the creation-annihilation operators using these states. Our task is greatly simplified by the application of Wick's Theorem, excellent standard treatments of which are given in Peskin and Schroder

[67] in the context of quantum field theory and in Lindgren and Morisson [51] in application to atomic structure. This analysis is discussed in Sapirstein [74, 79] and Blundell [20], and only the final results will be stated. Because of the fact that for three-electron atoms, the Pauli exclusion principle ensures that we have one electron sitting above (in terms of energy and distance from the nucleus) the closed 1s shell, to leading-order the Lamb-shift affects the remaining single electron. Thus the formulas for the SE and VP contributions are essentially unchanged from the one-electron case. However, we are actually dealing with a many-electron system, so the first so-called many-body effect now is present. That is, that the valence electron can exchange a virtual photon with each of the electrons in the closed 1s shell leading to the so-called one-photon exchange contribution:

$$E_{PE}^{(2)} = -4\pi i\alpha \int d(t_2 - t_1) \int d^3x_2 \int d^3x_1 D_F(x_2 - x_1) \times \bar{\phi}_i(x_2)\gamma_\mu \phi_i(x_2)\bar{\phi_{1s}}(x_1)\gamma^\mu \phi_{1s}(x_1). \tag{2.93}$$

To lowest-order, this enumerates all the interactions that take place within the framework of QED for both one and three-electron atoms/ions. In higher orders, new effects such as screening will appear, but the basic formalism for treating these effects is the same as what is outlined here. We went in detail over this formalism to set the groundwork for what is to come and to elucidate the effects that will be most important in the context of this thesis; the H-like Dirac-Coulomb, one-loop QED and one photon-exchange effects, because we will find that the finite nuclear size will have the largest effect in these processes. Higher-order processes will be discussed afterwards, but in not as much detail because their inclusion is needed only to complete the energy budget of the transition, to the level that we are interested in.

Chapter 3

The "Dirac" Contribution

3.1 Introduction

In chapter 1, we introduced the various processes that contribute to the 2p-2s transition in highly charged ions. We saw that in general, the largest and most important single contribution comes from the solution of the Dirac equation (DE) for a single electron bound to a heavy, ($Z \geq 80$), nucleus via Coulomb interaction. In Chapter 2, we gave a general presentation of the relativistic description of the electron in a Coulomb potential assuming that the source of the potential was a point-particle. In that case the solutions to the energies and wavefunctions turn out to be analytical. However, in reality atomic nuclei are not points and thus, this nuclear model will eventually lead to discrepancies with experiment. We expect that these discrepancies will become more severe as the charge of the nucleus increases due to the fact that the the nucleus exerts a pull proportional to Z on the bound electron, and thus it displays an increasingly larger probability density close to the origin, where the nucleus itself resides. Consequently, the electron directly senses its nonpoint nature more acutely. Thus in this chapter we will discuss extending the treatment given above to the case where the nuclear charge is a function of radial distance from the origin, (we will assume spherical symmetry here, but this issue will come up again when we discuss the nuclear polarization correction). Thus, the angular component of the solution will remain the same as in the point-nucleus case, however the expressions for the radial

components will, of course, change. Specifically we will consider the hard-sphere, and the Fermi distributions as these distributions are widely used in the literature as models of nuclear charge.

3.2 Spherical charge distribution

As described in Chapter 2, for spherically symmetric potentials, the electron wave-functions for H-like ions follow from the solutions of the radial Dirac equation [44]. Now we replace the point-like Coulomb potential:

$$V(r) = \frac{-Z\alpha}{r}, \tag{3.1}$$

with a more general expression where the charge density is a function of radial distance. To obtain the expression, one solves the 3-d Poisson's equation, which for a spherically symmetric distribution yields

$$V(r) = -4\pi\alpha \left\{ \frac{1}{r} \int_0^r \rho(r') r'^2 dr' + \int_r^\infty \rho(r') r' dr' \right\} \tag{3.2}$$

where $\rho(r)$ has been normalized by means of

$$4\pi \int_0^\infty \rho(r') r'^2 dr' = 1. \tag{3.3}$$

For a homogeneously charged sphere, the charge density is given by the expression,

$$\rho(r) = \frac{3Z}{4\pi R_{sph}^3} \Theta(R_{sph} - r) \tag{3.4}$$

where Θ is the Heaviside step function,

$$\Theta(R - r) = \begin{cases} 1, & \text{if } r \leq R; \\ 0. & \text{if } r > R. \end{cases} \tag{3.5}$$

and R_{sph} is the radius of the sphere expressed in terms of the root-mean-square (rms) nuclear charge radius as $R_{sph} = \sqrt{5/3}R$. We can visualize this distribution

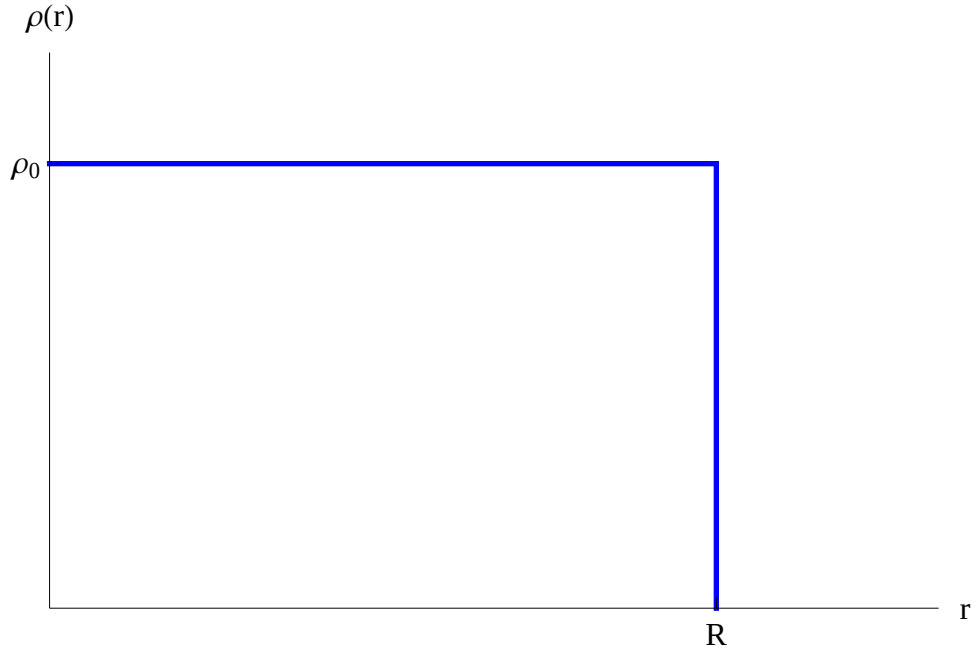

Figure 3.1: Hard-sphere charge density distribution.

graphically as shown in Figure 3.1.

Inserting equation (3.4) into (3.2), upon integration, leads to an analytical expression for the potential,

$$V(r) = \begin{cases} -\frac{Z\alpha}{2R}\left\{3 - \frac{r^2}{R^2}\right\}, & \text{if } r \leq R; \\ -\frac{Z\alpha}{r}. & \text{if } r > R. \end{cases} \tag{3.6}$$

3.3 Fermi charge distribution

Although the hard-sphere distribution is a good first start to modelling the distribution of charge in a nucleus, it suffers from one major drawback. As shown in Figure 3.1, the charge density is constant up to the charge radius and then abruptly drops to zero. In reality, nuclei have a "skin", where the charge density drops off exponentially from the same maximum constant value as the hard-sphere distribution to zero as shown in Figure 3.2 [49]. The distribution that more accurately models this observed behaviour is the Fermi charge distribution, the expression for which is

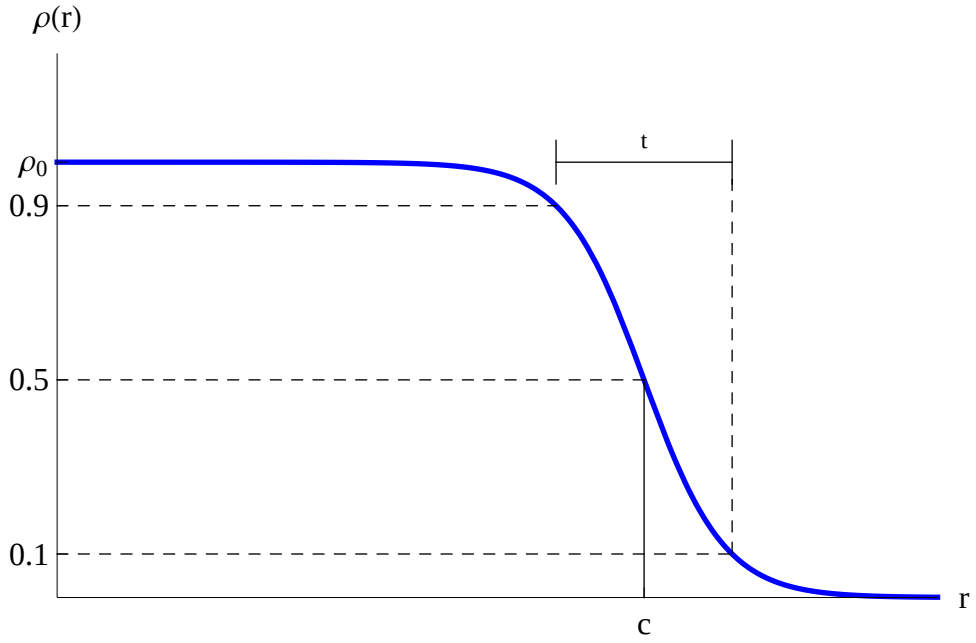

Figure 3.2: Fermi charge density distribution.

given by a two-parameter decaying exponential model:

$$\rho(r) = \frac{\rho_0}{1 + \exp((r-c)/a)}. \tag{3.7}$$

In this formula, c is the 50% fall-off radius of the density, and a is related to the 90%-10% fall-off distance t by $t = 4ln(3)a$. The parameter a is usually fixed by $a = 2.3/(4\ln 3)$ fm, which numerically evaluates to $a \approx 0.5$ fm [97]. For a given value of the rms radius, R, the parameter c is determined through the approximate formula (which for this calculation is fixed exactly)

$$c \approx \sqrt{\frac{5}{3}R^2 - \frac{7}{3}a^2\pi^2}. \tag{3.8}$$

One can now substitute the expression for the Fermi charge density (3.7) into the equation for the potential (3.2), leading to the formula,

$$V_{Fermi}(r) = \begin{cases} 4\pi Z \int_0^r \frac{3r'^2}{(4\pi c^3)\left(\frac{\pi^2 a^2}{c^2}+1\right)\left(e^{\frac{r'-c}{a}}+1\right)}\, dr' \\ +4\pi r Z \int_r^c \frac{3r'}{(4\pi c^3)\left(\frac{\pi^2 a^2}{c^2}+1\right)\left(e^{\frac{r'-c}{a}}+1\right)}\, dr', & \text{for } r \leq c, \\ 4\pi r Z \int_c^\infty \frac{3r'}{(4\pi c^3)\left(\frac{\pi^2 a^2}{c^2}+1\right)\left(e^{\frac{r'-c}{a}}+1\right)}\, dr', & \text{if } r > c,. \end{cases} \tag{3.9}$$

Unlike the hard-sphere distribution, the Fermi distribution leads to a result that is purely numeric. Thus for each point required one needs to evaluate the integrals. The expression can be expressed in terms of two infinite series as given in Johnson [44]:

$$V_{Fermi}(r) = \begin{cases} -\frac{Z}{Nc}\left[\left(\frac{3}{2} - \frac{r^2}{2c^2} + \frac{\pi^2 a^2}{2c^2} + \frac{3a^2}{c^2}P_2\right) + \frac{6a^3}{c^2 r}(S_3 - P_3)\right], & \text{for } r \leq c, \\ -\frac{Z}{Nr}\left[1 + \frac{\pi^2 a^2}{2c^2} + \frac{6a^3}{c^2 r}(S_3 - P_3) - \frac{3ra^2}{c^3}P_2\right], & \text{if } r > c, \end{cases} \tag{3.10}$$

where

$$S_k = \sum_{n=1}^{\infty} \frac{(-1)^{n-1}}{n^k} e^{-nc/a} \tag{3.11}$$

$$P_k = \sum_{n=1}^{\infty} \frac{(-1)^{n-1}}{n^k} e^{-n|r-c|/a}. \tag{3.12}$$

Here,

$$N = 1 + \frac{\pi^2 a^2}{c^2} + \frac{6a^3}{c^3} S_3. \tag{3.13}$$

3.4 Evaluation

The Dirac equation for the bound-states of a hydrogenic ion using both point-like and extended-nuclear cases was evaluated using the freely available Fortran 77 code "Radial" [73]. A brief appendix (Appendix A) is included in this thesis summarizes the information available in [73]. This code was basically used as-is, i.e treated like a

"black-box", with only the form of the potential changed in order to account for the various charge distributions.

The Mathematica feature "MathLink" was used to incorporate "Radial" as a Mathematica function in the package "NRadius" which is the product of this thesis. Incorporated this way, "Radial" can be called on demand when needed [88]. A discussion of the "NRadius" package as a whole is given in Appendix B.

Listing 3.1: Mathematica function that calls Radial using point potential.

```
diracPointEnergy[Ze_,n_,k_]:=Module[{inputdata,energy},
    SetDirectory["c:\\f\\radial"];
    inputdata={{Ze,n,k}};
    Export["inputdata2.dat",inputdata];
    energy=ReadList["!pointdirac<inputdata2.dat",Number];
    SetDirectory["C:\\Users\\Andrew\\Documents"];
    energy [[1]]]
```

Listing 3.2: Mathematica function that calls Radial using a Hard-Sphere potential.

```
diracHSEnergy[Ze_,n_,k_]:=Module[{inputdata,energy},
    SetDirectory["c:\\f\\radial"];
    inputdata={{Ze,n,k}};
    Export["inputdata3.dat",inputdata];
    energy=ReadList["!sphere<inputdata3.dat",Number];
    SetDirectory["C:\\Users\\Andrew\\Documents"];
    energy [[1]]]
```

Listing 3.3: Mathematica function that calls Radial using a Fermi potential.

```
diracEnergy[Ze_,RMS_,n_,k_]:=Module[{inputdata,energy,rms},
    SetDirectory["c:\\f\\radial"];
    rms=RMS*10^-15/bohrRadius;
    inputdata={{Ze,rms,n,k}};
    Export["inputdata.dat",inputdata];
    energy=ReadList["!fermidirac<inputdata.dat",Number];
    SetDirectory["c:\\users\\andrew\\documents"];
    energy [[1]]]
```

The combined Radial and Mathematica functions were used to calculate the Dirac energy for the $2s$ and $2p$ states in H-like heavy ions ($Z = 82 \cdots 92$) using the Fermi nuclear charge distribution. These results are shown in Table 3.1, and are in excellent agreement with previously published results [76, 94]. The uncertainties come from comparing the effects of using a Fermi and a hard-sphere nuclear model as described in [34].

3.4.1 Dirac Nuclear Size Correction

Of particular interest for this thesis is the effect on the 2s-2p transition energy that takes place when one goes from a point nucleus to one of finite radius when calculating the Dirac Energy (DE). This is the first, so-called, nuclear size (NS) correction that one needs to take into account. To leading order, the NS correction to the energy levels of a hydrogen-like atom is defined as the difference of the corresponding eigenvalues of the Dirac equation with the point-Coulomb and the extended-nucleus potentials [97]. It has been known for many years, that although treating a nucleus as a charged sphere is computationally advantageous, a more accurate model of the nucleus is given by the two-parameter Fermi distribution (3.7), [34].

The NS correction can be easily obtained by numerical solution of the Dirac equation using Radial, as summarized above, as a Mathematica function in the NRadius package where the difference is taken between the Fermi distribution result and the point-nucleus result. This method is employed in this thesis, and the results for the range of ions from $Z = 82$ to $Z = 92$ are shown in Table 3.2. We see that the correction size varies between states with the largest correction occurring for the $2s_{1/2}$ state. This can be understood, in general, because for the lowest state, the bound electron tends to be found inside the nucleus with a higher probability, and thus feels the influence of the finite nuclear size most acutely. We also see that the correction size increases, in general, as the value of Z increases. This too can be understood in terms of the strength of the attraction between the nucleus and bound electron being proportional to the nuclear charge. As the nuclear charge increases, the strength of the attraction between nucleus and electron increases, thus the electron will tend to

Table 3.1: Dirac energy for H-like ions using a Fermi nuclear charge distribution.

Z	$\langle r^2 \rangle^{1/2}$ (fm)	State	Dirac (eV)
82	5.501(3)	$2s_{1/2}$	-26048.164(23)
		$2p_{1/2}$	-26058.829(2)
		$2p_{3/2}$	-23407.273
83	5.521(3)	$2s_{1/2}$	-26788.013(27)
		$2p_{1/2}$	-26799.910(2)
		$2p_{3/2}$	-23995.805
84	5.526(13)	$2s_{1/2}$	-27543.17(6)
		$2p_{1/2}$	-27556.385(5)
		$2p_{3/2}$	-24592.196
85	5.539(55)	$2s_{1/2}$	-28313.898(256)
		$2p_{1/2}$	-28328.617(24)
		$2p_{3/2}$	-25196.475
86	5.655(16)	$2s_{1/2}$	-29100.09(9)
		$2p_{1/2}$	-29116.955(9)
		$2p_{3/2}$	-25808.672
87	5.658(13)	$2s_{1/2}$	-29903.179(84)
		$2p_{1/2}$	-29921.911(8)
		$2p_{3/2}$	-26428.815
88	5.670(57)	$2s_{1/2}$	-30723.00(17)
		$2p_{1/2}$	-30743.869(18)
		$2p_{3/2}$	-27056.936
89	5.684(26)	$2s_{1/2}$	-31560.12(38)
		$2p_{1/2}$	-31583.290(44)
		$2p_{3/2}$	-27693.068
90	5.700(57)	$2s_{1/2}$	-32414.70(38)
		$2p_{1/2}$	-32440.634(44)
		$2p_{3/2}$	-28337.237
91	5.710(50)	$2s_{1/2}$	-33287.54(49)
		$2p_{1/2}$	-33316.435(54)
		$2p_{3/2}$	-28989.480
92	5.851(7)	$2s_{1/2}$	-34177.80(10)
		$2p_{1/2}$	-34211.072(11)
		$2p_{3/2}$	-29649.830

be found inside the nucleus with a higher probability and thus feel the effect of the finite NS more strongly.

The NS here is important because it allows us to characterize the effect of the finite NS to the radiative corrections (from QED) that are needed to be made to the transition energy. This topic will be taken up in the next chapter.

Table 3.2: Nuclear size correction to the Dirac energy in H-like ions using a Fermi nuclear charge distribution

Z	$\langle r^2 \rangle^{1/2}$ (fm)	State	ΔEn (eV)
82	5.501(1)	$2s_{1/2}$	11.6636
		$2p_{1/2}$	0.9986
		$2p_{3/2}$	-0.0004
83	5.521(3)	$2s_{1/2}$	13.0509
		$2p_{1/2}$	1.1532
		$2p_{3/2}$	-0.0004
84	5.526(13)	$2s_{1/2}$	14.5442
		$2p_{1/2}$	1.326
		$2p_{3/2}$	-0.0004
85	5.539(55)	$2s_{1/2}$	16.249
		$2p_{1/2}$	1.5287
		$2p_{3/2}$	-0.0004
86	5.655(16)	$2s_{1/2}$	18.6798
		$2p_{1/2}$	1.8136
		$2p_{3/2}$	-0.0003
87	5.658(13)	$2s_{1/2}$	20.8186
		$2p_{1/2}$	2.0847
		$2p_{3/2}$	-0.0003
88	5.670(57)	$2s_{1/2}$	23.2674
		$2p_{1/2}$	2.4033
		$2p_{3/2}$	-0.0002
89	5.684(26)	$2s_{1/2}$	26.0266
		$2p_{1/2}$	2.7728
		$2p_{3/2}$	-0.0003
90	5.700(57)	$2s_{1/2}$	29.1388
		$2p_{1/2}$	3.2017
		$2p_{3/2}$	-0.0003
91	5.710(50)	$2s_{1/2}$	32.5848
		$2p_{1/2}$	3.6926
		$2p_{3/2}$	-0.0003
92	5.851(7)	$2s_{1/2}$	37.6785
		$2p_{1/2}$	4.4055
		$2p_{3/2}$	-0.0000

Chapter 4

One-loop QED Correction

4.1 Introduction

When considering accurate calculations of the transition energies in heavy ions, after considering the Dirac energy contributions one needs to consider the radiative corrections to this effect, that is the the so-called one-loop corrections, the QED corrections of first-order in α. This correction is one of the important contributions to the nuclear-size correction to the transition energy, and has been extensively studied by many authors [13, 40, 47, 66, 83]. Most recently, however, the effect was considered by Yerokhin [97], where the dependence of the one-loop QED radiative correction energy due to both self-energy and vacuum-polarization processes for the three lowest states of H-like ions is given in terms of nuclear charge, Z, and nuclear charge radius. At the end of Chapter 3, we introduced the idea that, just like the one-loop radiative corrections are corrections to the energy obtained from solving the Dirac equation for an electron bound to a nucleus via the Coulomb potential, the nuclear-size correction to the one-loop radiative corrections are corrections to, and thus can be parametrized in terms of, the nuclear-size correction of the bound Dirac term. This chapter will further explore this correction.

The layout of this chapter is the following: A review of the nuclear size effect in the one-loop QED correction will be outlined. This will differ somewhat from the more general material presented in chapter 2 on the one-loop QED correction. Then,

the specific dependencies of the state energies on the nuclear charge and nuclear radius will be presented together with some analysis of these results as well as the technique used to transform the numerical remainders presented as graphs in [97] to mathematical functions. Finally the Mathematica function to calculate this correction will be discussed and results using this function will be compared with published results, such as Yerokhin et. al (2015) [89], to gauge the accuracy of the method.

4.1.1 Self-energy

As we discussed in chapter 2, in lowest order, QED radiative corrections are composed of two contributions, those being the self-energy (SE) and vacuum-polarization (VP). The SE is a correction to the electron, while the VP is a correction to the field that the electron interacts with. The contribution of the SE, the diagram of which is shown in Figure 4.1, combined with the corresponding mass counterterm is given by equation (2.90) [58], reproduced here for convenience:

$$\Delta E_{SE} = 2\imath\,\alpha \int_{-\infty}^{\infty} d\omega \int d^3r_1 \int d^3r_2\, \psi_a^\dagger(\boldsymbol{r_1})\alpha^\mu G\left(E_a-\omega,\boldsymbol{r_1},\boldsymbol{r_2}\right) \times D_{\mu\nu}\left(\omega,\boldsymbol{r_1}-\boldsymbol{r_2}\right)\alpha^\nu\psi_a(\boldsymbol{r_2}) - \delta m \int dx\, \overline{\psi_a}(\boldsymbol{r_1})\,\psi_a(\boldsymbol{r_2}). \tag{4.1}$$

Here $\overline{\psi}(\boldsymbol{r_1}) = \psi^\dagger\gamma_0$ is the Dirac-Coulomb wave function of the state under consideration, $G\left(\omega,\boldsymbol{r_1},\boldsymbol{r_2}\right)$ is the Coulomb Green function, $D_{\mu\nu}\left(\omega,\boldsymbol{r_1}-\boldsymbol{r_2}\right)$ is the photon propagator. In this equation we have used the definition of the γ_μ matrices, given in (2.4), to re-express the equation in terms of α, where $\alpha^\mu = (1,\alpha)$.

This expression can be evaluated in a perturbation theory expansion in a small parameter, $Z\alpha$, where $\alpha \sim 1/137$ is the fine-structure constant, and in fact is particularly well suited because the contributing terms have been well checked independently. We can re-express the energy shift above as

$$\Delta E_{SE} = \frac{\alpha}{\pi}\frac{(Z\alpha)^4}{n^3}F\left(Z\alpha\right)m_e c^2. \tag{4.2}$$

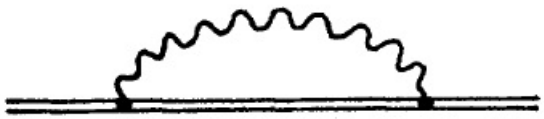

Figure 4.1: Feynman diagram representing the one-loop self-energy [56]. Copyright (1985) by the American Physical Society.

For a particular atomic state, the dimensionless function F depends only on the coupling $Z\alpha$. In general, for light elements where Z is small, the function F can be expanded in a power-series in $Z\alpha$, which can be truncated only after a few terms, to obtain an accurate value for the energy [78]. For heavy atoms/ions, ($Z \geq 80$), the expansion parameter $Z\alpha$ is not a small parameter anymore, and thus the function F must be evaluated, to all orders, numerically and not by a truncated power series. Yerokhin (2011) performed this analysis and showed that the numerical solution can be expressed as a power series expansion plus a numeric remainder [97].

The nuclear-size correction to the self-energy (NSE) was defined in Chapter 3 as the difference between the eigenvalues of the Dirac equation when evaluated with the point-Coulomb potential and the potential of the extended-charge nucleus respectively. In terms of equation 4.2, the dimensionless function F now depends on, in addition to $Z\alpha$, the finite nuclear size radius, R:

$$\Delta E_{NSE} = \frac{\alpha}{\pi}\frac{(Z\alpha)^4}{n^3} F\left(Z\alpha, R\right) m_e c^2. \tag{4.3}$$

As mentioned in the Introduction, we can use the fact that the one-loop QED terms are radiative corrections to the Dirac energy contribution to re-express the NSE in terms of the Dirac energy finite nuclear size correction, where the leading dependence of the NSE correction on R and $Z\alpha$ can be conveniently factorized out

Term	State	Value
a_{01}	np_j	$8/9$
a_{00}	$2p_{1/2}$	$0.808879967(1)$
a_{00}	$np_{3/2}$	$a_{00}(np_{1/2}) - 1$
a_{10}	ns	$\pi(-23/4 + 4\ln 2)$
a_{10}	$np_{1/2}$	$\pi(379/432 - \frac{16}{3}\ln 2)$
a_{10}	$np_{3/2}$	$\pi(559/432 - 4\ln 2)$
$a_{\log}$	$ns,\ np_{1/2}$	$\pi^2/6 - 15/4$
a_{22}	ns	-2/3
a_{21}	$np_{1/2}$	$-2(n^2-1)/n^2$

Table 4.1: Known results for the coefficients of the $Z\alpha$ expansion.

in terms of the first-order NS contribution, that is the nuclear size correction to the Dirac energy result [97]:

$$\Delta E_{NSE}(n,l,j) = \Delta E_N(n,1/2,l)\frac{\alpha}{\pi}G_{NSE}(n,j,l). \tag{4.4}$$

An important feature of this parametrization is that it involves the full NS correction, rather than only the leading term of its $Z\alpha$ expansion:

$$\begin{aligned} G_{NSE}(ns) = (Z\alpha)a_{10} + (Z\alpha)^2 \left[a_{log}\ \ln\left(\frac{b}{R_{sph}}\right)\right] \\ + a_{22}\ \ln^2[(Z\alpha)^{-2}] + O[\ln(Z\alpha)] \end{aligned} \tag{4.5a}$$

$$\begin{aligned} G_{NSE}(npj) = a_{01}\ \ln[(Z\alpha)^{-2}] + a_{00} + (Z\alpha)a_{10} \\ + (Z\alpha)^2 a_{log}\,\delta_{j,1/2}\ \ln\left(\frac{b}{R_{sph}}\right) \\ + (Z\alpha)^2 a_{21}\,\delta_{j,1/2}\ \ln^2[(Z\alpha)^{-2}] + O(1), \end{aligned} \tag{4.5b}$$

where $b = e^{1/(2\gamma)-C-5/6}$, $\gamma = \sqrt{1-(Z\alpha)^2}$ and C is the Euler constant. Known results for the coefficients of the expansion are listed in table 4.1.

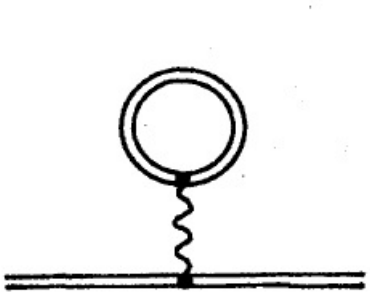

Figure 4.2: Feynman diagrams representing the one-loop vacuum-polarization [56]. Copyright (1985) by the American Physical Society.

We find that the R dependence of our numerical data can be well approximated by a three-parameter fit that includes $\ln(R)$, as suggested by the $Z\alpha$ expansion. We will discuss the numerical evaluation of (4.4) below, after we discuss the vacuum-polarization.

4.1.2 Vacuum-polarization

The vacuum-polarization correction describes the generation of virtual electron-positron pairs out of the vacuum due to the presence of the electron. The expression for the vacuum-polarization is given by

$$\Delta E_{VP} = \frac{\alpha}{2\pi\imath} \int_{-\infty}^{\infty} d\omega \int d^3r_1 \int d^3r_2 \, \psi_a^\dagger(\boldsymbol{r_1}) \frac{1}{|\boldsymbol{r_1} - \boldsymbol{r_2}|} Tr\left[G\left(\omega, \boldsymbol{r_1}, \boldsymbol{r_2}\right)\right] \psi_a(\boldsymbol{r_2}), \quad (4.6)$$

while the Feynman diagram is given in Figure 4.2. This expression is ultraviolet divergent. It can be renormalized by dividing it into two parts. The first part corresponds to the first nonzero term in the potential expansion of the Coulomb Green function in powers of $Z\alpha$ [58]. This is the so-called Uehling portion, which becomes finite due to the charge renormalization and its evaluation causes no problem. The second portion, the so-called Wichmann-Kroll term, accounts for all higher order terms of the $Z\alpha$ expansion [58].

Like in the self-energy case, the nuclear-size vacuum-polarization (NVP) correction is defined as the difference between the one-loop vacuum polarization corrections evaluated with the point-Coulomb potential and the potential of the extended-charge nucleus. The leading dependence of the NVP correction, like the NSE correction, on R and $Z\alpha$ can be conveniently factorized out in terms of the first-order NS contribution ΔE_N, [97]:

$$\Delta E_{VP}(n,l,j) = \Delta E_N(n,1/2,l)\frac{\alpha}{\pi}G_{VP}(n,j,l). \tag{4.7}$$

The $Z\alpha$ expansion of the function G_{NVP} is given by

$$\begin{aligned} G_{NVP}(ns) = (Z\alpha)a_{10} + (Z\alpha)^2 \left[\frac{2}{3\gamma}\ \ln^2\left(\frac{b}{R_{sph}}\right)\right] \\ + (Z\alpha)^2\left[a_{21}\ \ln[(Z\alpha)^{-2}] + f(Z\alpha,R_{sph}) + O(1)\right], \end{aligned} \tag{4.8a}$$

$$\begin{aligned} G_{NVP}(npj) = a_{00} + (Z\alpha)a_{10} + (Z\alpha)^2 \left[\frac{2}{3\gamma}\ \delta_{j,1/2}\ \ln^2\left(\frac{b}{R_{sph}}\right)\right] \\ + (Z\alpha)^2\left[a_{21}\ \delta_{j,1/2}\ f(Z\alpha,R_{sph}) + O(1)\right]. \end{aligned} \tag{4.8b}$$

The expansion coefficients are given as:

$$\begin{aligned} &a_{00}(np_{1/2}) = a_{00}(np_{3/2}) = -8/45, \\ &a_{10}(ns) = 3\pi/4,\ a_{10}(np_{1/2}) = 23\pi/72, \\ &a_{10}(np_{3/2}) = 5\pi/72,\ a_{21}(ns) = 4/15, \end{aligned} \tag{4.9}$$

while,

$$f(Z\alpha, R_{sph}) = \frac{1}{3(Z\alpha)^2}[-2\ln R_{sph} - \frac{5}{3} + \pi\tan(\pi\gamma) + \frac{2}{3+2\gamma} + 2\psi(-1-2\gamma) - \frac{\pi^{3/2}(3+2\gamma)\Gamma(\gamma+1)}{40\sin(2\pi\gamma)(\gamma-1)\Gamma(-1-2\gamma)\Gamma(\gamma+3/2)}(2R_{sph})^{2(1-\gamma)}]. \quad (4.10)$$

4.1.3 The nuclear-size correction

In this section we will look more closely at, and discuss the implications of parameterizing the NSE and NVP correction in terms of the Dirac nuclear-size correction. We saw above that the finite-size nuclear correction to the one-loop QED corrections could be written in factorized form (equations 4.4 and 4.7), where the first term on the right is the finite nuclear size correction to the Dirac energy and G is a dimensionless function incorporating the remaining QED factors. These terms are joined together by the scaling factor α/π. The crucial point is that this factor has a value of approximately 1/400, meaning that if, for instance, the G's are of order unity we would obtain a QED correction effect of 1/400 of the Dirac finite-size effect.

For example if we consider Francium, the Dirac finite size correction for the $2s$ state is approximately 20 eV (Radial calculates it to be 20.18622 eV). Therefore a G of order unity would give a $\Delta E_{NSE/NVP} = 50$ meV. Thus, to keep within the range set out in Chapter 1, we are aiming for a accuracy of 40 % on the value of G. For the VP case, G for the $2s$ case is on order 9, thus the correction to the energy would be about 450 meV, so again we would want to have an accuracy of 4-5% for G. Recall that for a G of order unity would give a $\Delta E \approx 50$ meV, implying a 40% accuracy on G. The $2p_{3/2}$ state gives a correction of about 0.15 meV, which is far below the threshold of concern. Since the form of the G's is given as $Z\alpha$ expansions with a numerical remainder that needs to be added, our ultimate accuracy will rest on how well we can calculate that remainder, since the rest of the expansion is known to machine precision.

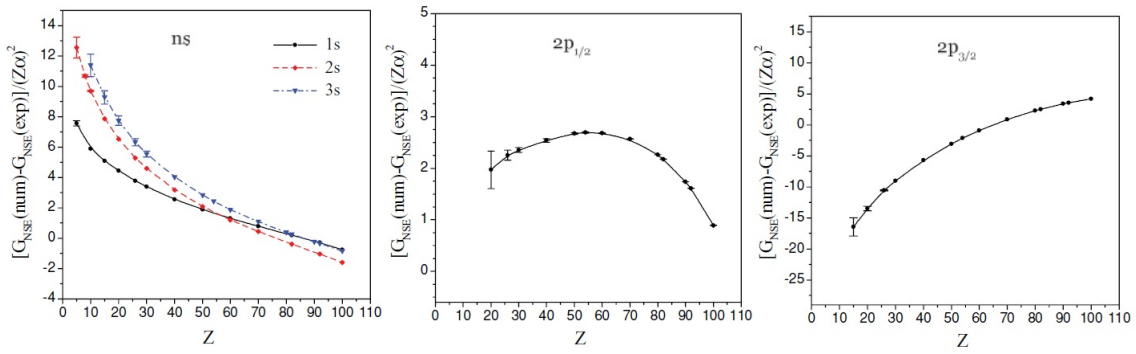

Figure 4.3: Graphs of the remainder terms for the 2s and 2p states for the SE correction [97]. Copyright (2011) by the American Physical Society

Self-Energy

To calculate the remainders to the nuclear-size SE corrections, we used the results given in Yerokhin [97]. In that reference, Yerokhin explicitly gives graphs of the remainder terms, for the $2s$, and $2p$ states as a function of Z, by subtracting the pure $Z\alpha$ expansion results from the full numerical results. These graphs are reproduced in Figure 4.3.

The graphs in Figure 4.3 were digitized using the program "PlotDigitizer", and are shown in Figures 4.4, 4.5 and 4.6. The range that was chosen was Z = 82 - 92 in order to cover the elements under study and to minimize the nonlinearities in the graphs themselves. A least-squares regression was then applied to the digitized points to obtain function that could be implemented in our code. To check the quality of the fit, the residuals were calculated and are shown for each case.

We see from the residual graphs that this procedure introduces an error of approximately 0.000017 of the Dirac value. The results for the NSE is given as:

$$\mathscr{R}(2s) = -110.044 + 3.94841Z - 0.0466387Z^2 + 0.000180466Z^3, \tag{4.11}$$

$$\mathscr{R}(2p_{1/2}) = 141.838 - 4.78895Z + 0.0552297Z^2 - 0.000214623Z^3, \tag{4.12}$$

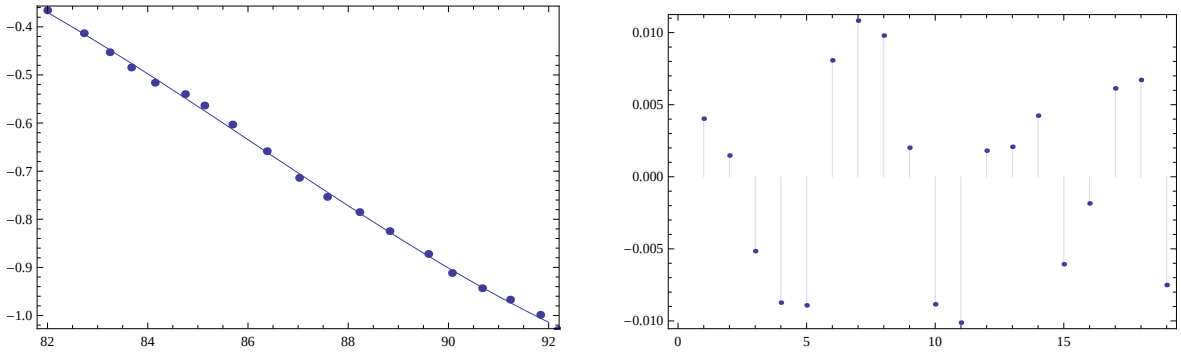

Figure 4.4: Graphs of the digitized remainder and residuals for the 2s state of the NSE correction.

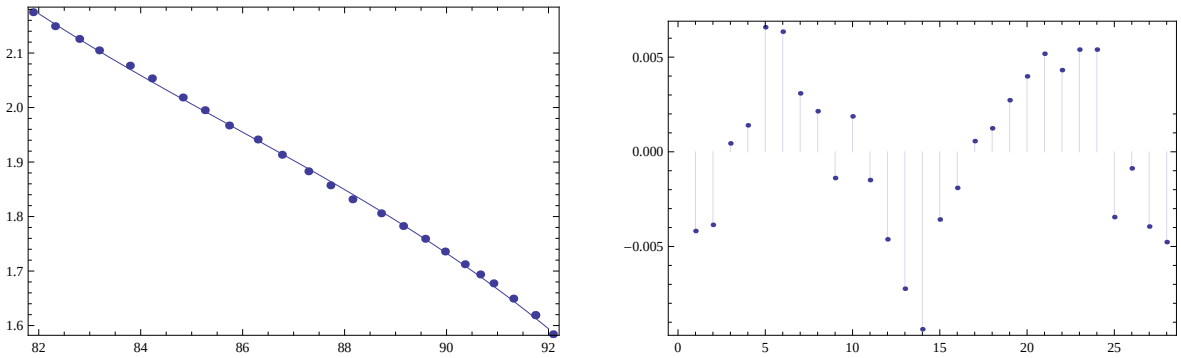

Figure 4.5: Graphs of the digitized remainder and residuals for the $2p_{1/2}$ state of the NSE correction.

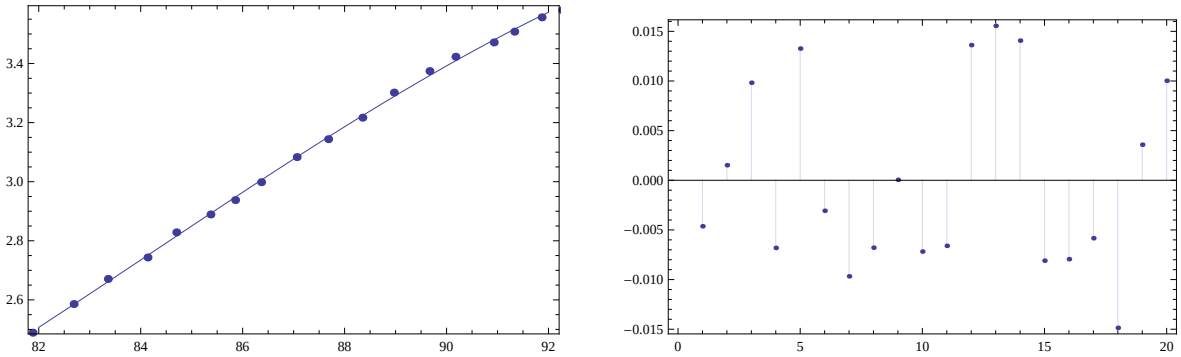

Figure 4.6: Graphs of the digitized remainder and residuals for the $2p_{3/2}$ state of the NSE correction.

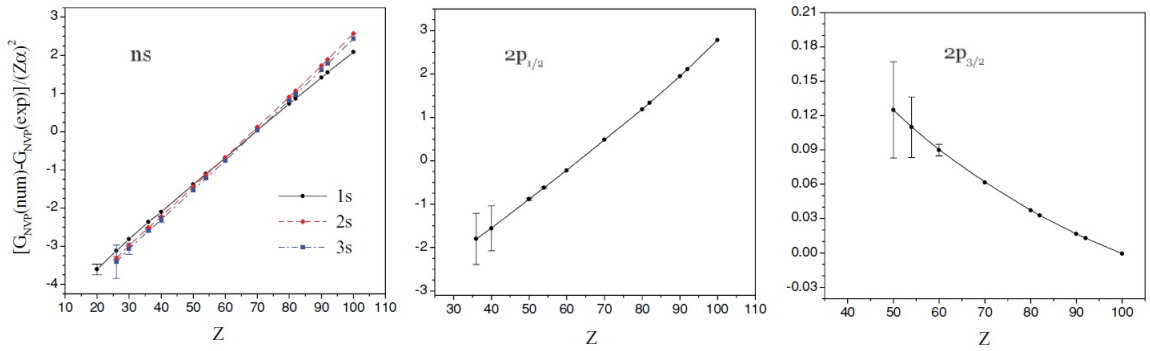

Figure 4.7: Graphs of the remainder terms for the 2s and 2p states for the VP correction [97]. Copyright (2011) by the American Physical Society.

and

$$\mathscr{R}(2p_{3/2}) = 99.7534 - 3.68213Z + 0.0450514Z^2 - 0.00017817Z^3, \tag{4.13}$$

where *Rmd* is the remainder function obtained from the remainder graphs. These equations were incorporated into the expressions the G functions given above.

Vacuum Polarization

The equivalent analysis was performed for the nuclear-size VP corrections. The corresponding graphs are reproduced in Figures 4.7, 4.8, 4.9 and 4.10. The same range was chosen (Z = 82 - 92) as before, again in order to cover the elements under study and to minimize the non-linearities in the graphs themselves. Here we see that the graphs are far more linear in the region of interest as compared to the NSE. Thus we expect a good representation from a linear fit. To check this, again the residuals for each case were plotted.

In this case, we see from the residual graphs that this procedure introduces an error of approximately 0.000009 of the Dirac value. The corresponding formulas for the remainder are given as:

$$\mathscr{R}(2s) = -5.6409 + 0.0818693Z, \tag{4.14}$$

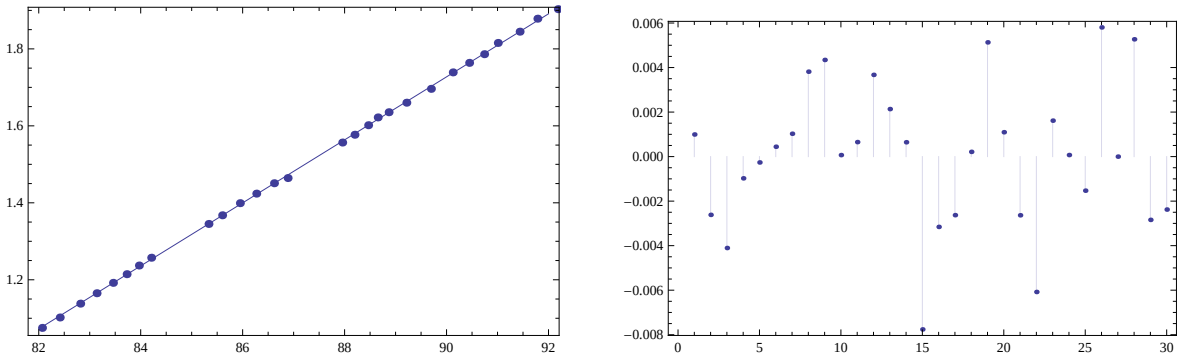

Figure 4.8: Graphs of the digitized remainder and residuals for the 2s state of the NVP correction.

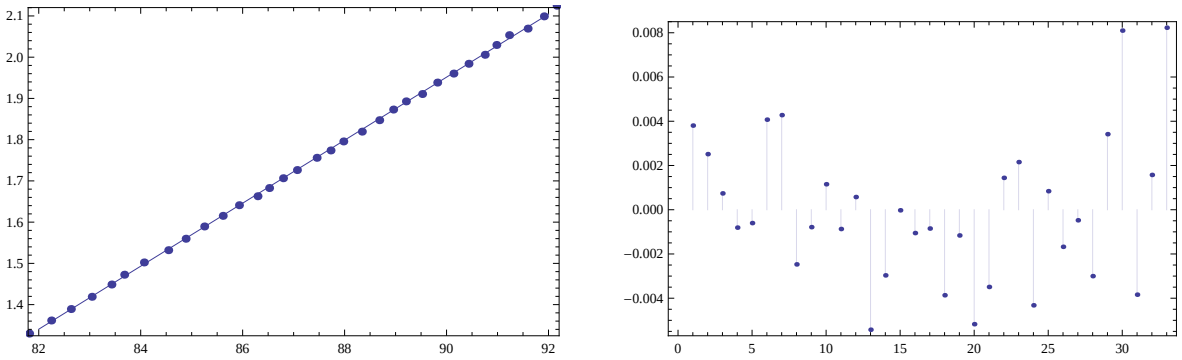

Figure 4.9: Graphs of the digitized remainder and residuals for the $2p_{1/2}$ state of the NVP correction.

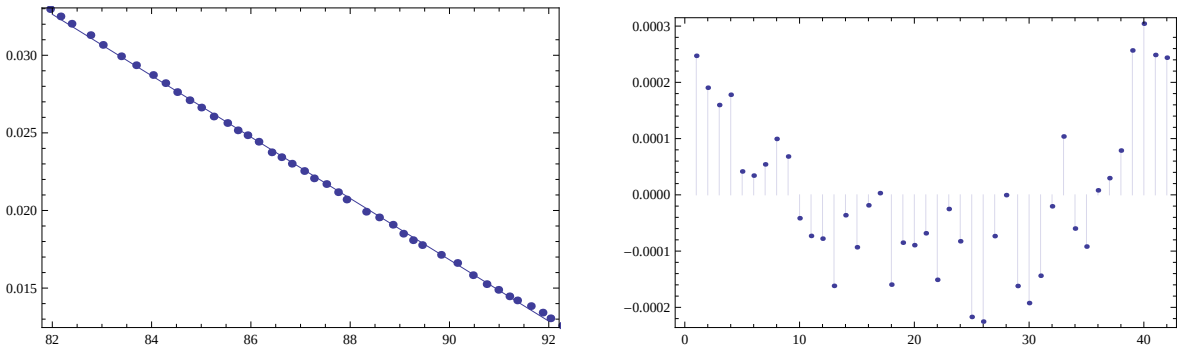

Figure 4.10: Graphs of the digitized remainder and residuals for the $2p_{3/2}$ state of the NVP correction.

$$\mathscr{R}(2p_{1/2}) = -4.92417 + 0.076397Z, \tag{4.15}$$

and

$$\mathscr{R}(2p_{3/2}) = 0.194751 - 0.00197697Z. \tag{4.16}$$

With the remainders in hand, we can now turn to evaluating the corrections numerically.

4.1.4 Numerical Calculations

To obtain the full one-loop QED result, the code evaluates in the following way. First the one-loop QED correction is obtained for the case of a point nucleus. This value was obtained directly from the literature as it has been evaluated recently for all values of Z by Yerokhin and Shabaev [89]. Then the nuclear size correction was applied to the point-nucleus value using the above formalism. This was done in a two-stage process, where the Dirac nuclear-size correction was obtained first using Radial to calculate the energy for a particular level in both the point-nucleus and Fermi nucleus cases and the two values subtracted. The function used is shown below.

Listing 4.1: Dirac nuclear size correction

```
DEND[n_,l_,j_,Ze_,Rsph_]:=((diracEnergy[Ze,Sqrt[3/5]\[Alpha] Rsph,n,(l−j)(2j+1)]−
    diracPointEnergy [Ze,n,(l−j)(2j+1)])∗27.21138386);
```

Listing 4.2: Mathematica calling function used to evaluate one-loop QED term

```
oneLoopQED[Z_, r_, j_] := Module[{DEn, DEpnt, DRsph},

  Rsph = Sqrt[5/3]∗r∗(10^−15)/reducedComptonWavelength;

  DEpnt = ((pointOneLoopQEDSE[Z, 2, 1, j] +
       pointOneLoopQEDVP[Z, 2, 1, j]) − (pointOneLoopQEDSE[Z, 2, 0,1/2] +
           pointOneLoopQEDVP[Z, 2, 0, 1/2])) electronRestEnergy;
  DEn = (DEnseD[2, 1, j, Z, Rsph] +
      DEnvpD[2, 1, j, Z, Rsph]) − (DnseD[2, 0, 1/2, Z, Rsph] +
```

```
9         DEnvpD[2, 0, 1/2, Z, Rsph]);
10
11    Return[DEpnt + DEn]
12    ];
```

These results are then used in conjunction with functions evaluating the Gs to obtain the final result for the one-loop correction. The interested reader is referred to Appendix 2 for the complete listing of the functions.

As in Chapter 3, comparisons were made between the values obtained for Bismuth and Uranium in Yerokhin et al. [93]; these cases are our benchmarks throughout this thesis. The nuclear radii used were those listed in Chapter 3, and the comparisons are shown in table 4.2.

Table 4.2: Table of comparisons for Li-like Bi and U of the one-loop QED correction to the $2p - 2s$ transition energy.

Element	Transition	ΔE	ΔE (published)
Z = 83	$2p_{3/2} - 2s$	-27.4859 eV	-27.48 eV [93]
Z = 92	$2p_{1/2} - 2s$	-42.9291 eV	-42.93 eV [93]

For the case of bismuth, the difference between the published result and our result is 6 meV, well within the expected experimental uncertainty. For the case of uranium the discrepancy is 0.9 meV, again well within the expected error. These results clearly indicate the viability of combining compiled code together with the symbolic and numeric capabilities of Mathematica to deliver results that stack up well to the current standard.

Chapter 5

One-photon Exchange

5.1 Introduction

Up to this point we have been dealing with effects that can be classified as "hydrogenic", that is, effects affecting a single electron bound to a highly-charged nucleus. These have been solutions to the Dirac equation and QED corrections to those solutions. However, our ultimate system of study are lithium-like ions where one valence electron can be found outside a closed $1s$ core. We expect that correlations between these three electrons will be important and must be taken into account. In chapter 1, we saw that the strongest dependence of the transition energy will come in through the lowest order terms, thus we can expect that the most important many-electron effect showing the strongest nuclear charge radius contribution is the one-photon exchange between the two core electrons and the valence electron [94].

In this chapter we will continue our analysis of the one-photon exchange correction, in particular we would like to transform our general expression that we derived in Chapter 2 into a form that can be explicitly evaluated. This will be accomplished by making use of the explicit form of the bound-electron wavefunctions. Then the numerical evaluation of this term will be discussed, in particular the Mathematica program written to evaluate the term. Finally the results obtained for the elements Bismuth and Uranium will be compared to previous work.

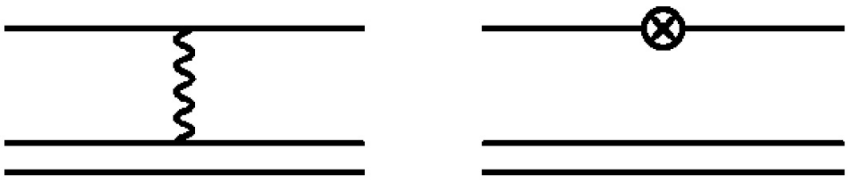

Figure 5.1: Feynman diagram representing the one-photon exchange (left) effect in a three-electron atom/ion together with the mass-counterterm (right)[76]. Copyright (2001) by the American Physical Society.

5.2 Theory

As we have seen in chapter 2, the one-photon exchange correction for Li-like ions is given by the Feynman diagrams shown in Figure 5.1, where the first shows the exchange of a transverse photon, while the second shows the mass counterterm. This latter term can be ignored because it is cancelled when considering the photon exchange together with the self-energy [76].

In this section we will continue our analysis of this term, transforming it into a form that can be evaluated. The energy shift associated with Figure (5.1) was given by equation (2.93). To begin our analysis, we will substitute the expression for the photon propagator to obtain the form:

$$E_v = \Sigma_a \left[g_{vava}(0) - g_{vaav}(\Delta E) \right], \tag{5.1}$$

where

$$g_{ijkl}(z) = \alpha \int d^3x d^3y \frac{e^{z|\bar{x}-\bar{y}|}}{|\bar{x}-\bar{y}|} \bar{\phi}_i(\bar{x}) \gamma_\mu \phi_k(\bar{x}) \bar{\phi}_j(\bar{y}) \gamma^\mu \phi_l(\bar{y}), \tag{5.2}$$

and

$$\Delta E = \epsilon_v - \epsilon_a \text{ (single-particle energies)}. \tag{5.3}$$

The subscript a refers to core electron states, whereas v refers to valence electron states. Thus the sum over a runs over the two spin states of the core $1s$ electrons. Note that the imaginary part of E_v is cancelled by a corresponding term in the self-

energy; this is needed to prevent valence state decay into the core [75].

The form of equations (5.1) and (5.2) is not suitable for direct implementation of numerical evaluation. The usual procedure is to separate the wavefunctions into angular and radial parts, evaluate the angular parts via standard angular momentum reduction techniques and evaluate the radial parts numerically. We will now give an explicit summary of the angular reduction to obtain the forms of (5.1) and (5.2) suitable for evaluation. Our treatment mirrors those given in [42], [44], and [54].

The first g integral can be further transformed in the following way:

$$\begin{aligned} g_{vava}(0) &= \alpha \int d^3x d^3y \frac{1}{|\bar{x}-\bar{y}|} \bar{\phi}_v(\bar{x}) \gamma_\mu \phi_v(\bar{x}) \bar{\phi}_a(\bar{y}) \gamma^\mu \phi_a(\bar{y}) \\ &= \alpha \int d^3x d^3y \frac{1}{|\bar{x}-\bar{y}|} \phi_v^\dagger(\bar{x}) \gamma_0 \gamma_\mu \phi_v(\bar{x}) \phi_a^\dagger(\bar{y}) \gamma_0 \gamma^\mu \phi_a(\bar{y}) \\ &= \alpha \int d^3x d^3y \frac{1}{|\bar{x}-\bar{y}|} \left[\phi_v^\dagger(\bar{x}) \gamma_0 \gamma_0 \phi_v(\bar{x}) \phi_a^\dagger(\bar{y}) \gamma_0 \gamma^0 \phi_a(\bar{y}) \right. \\ &\quad \left. - \phi_v^\dagger(\bar{x}) \gamma_0 \bar{\gamma} \phi_v(\bar{x}) \cdot \phi_a^\dagger(\bar{y}) \gamma_0 \bar{\gamma} \phi_a(\bar{y}) \right], \end{aligned} \tag{5.4}$$

and using the following relations for the products of gamma matrices: $\gamma_0\gamma_0 = \beta\beta = I$ and $\gamma_0\vec{\gamma} = \beta\beta\vec{\alpha} = \vec{\alpha}$ we can rewrite (5.4) as

$$\begin{aligned} g_{vava}(0) = \alpha \int d^3x d^3y \frac{1}{|\bar{x}-\bar{y}|} &\left[\phi_v^\dagger(\bar{x}) \phi_v(\bar{x}) \phi_a^\dagger(\bar{y}) \phi_a(\bar{y}) \right. \\ &\left. - \phi_v^\dagger(\bar{x}) \vec{\alpha} \phi_v(\bar{x}) \cdot \phi_a^\dagger(\bar{y}) \vec{\alpha} \phi_a(\bar{y}) \right]. \end{aligned} \tag{5.5}$$

A similar analysis leads to the exchange term of the following form,

$$\begin{aligned} g_{vaav}(\epsilon) = \alpha \int d^3x d^3y \frac{e^{\imath\epsilon|\bar{x}-\bar{y}|}}{|\bar{x}-\bar{y}|} &\left[\phi_v^\dagger(\bar{x}) \phi_a(\bar{x}) \phi_a^\dagger(\bar{y}) \phi_v(\bar{y}) \right. \\ &\left. - \phi_v^\dagger(\bar{x}) \vec{\alpha} \phi_a(\bar{x}) \cdot \phi_a^\dagger(\bar{y}) \vec{\alpha} \phi_v(\bar{y}) \right]. \end{aligned} \tag{5.6}$$

Collecting the results given above, we see that we have two types of terms; those in-

volving straight products of Dirac spinors ($\phi_v^\dagger(\bar{x})\phi_v(\bar{x})$) for both direct and exchange terms, and those involving products of Dirac spinors and $\vec{\alpha}$ matrices ($\phi_v^\dagger(\bar{x})\vec{\alpha}\phi_a(\bar{x})$), also for both direct and exchange terms. The former gives rise to the so-called Coulomb term, while the latter, the Breit term.

We are now in a position to transform our integrals by separating the angular and radial parts, evaluate the angular momentum parts using standard techniques of angular momentum reduction, and then collect the remaining radial parts together with the results from the angular evaluation. To perform this evaluation, we need explicit expressions for the Dirac wavefunctions,

$$\phi_\kappa(\vec{r}) = \frac{1}{r}\begin{pmatrix} \imath P_\kappa(r)\ \Omega_{\kappa m}(\hat{r}) \\ Q_\kappa(r)\ \Omega_{-\kappa m}(\hat{r}) \end{pmatrix}. \tag{5.7}$$

as well as expressions for the radial Green's functions for both static and frequency-dependent forms:

$$\begin{aligned} \frac{1}{|\bar{x}-\bar{y}|} &= \sum_{kq} \frac{r_<^k}{r_>^{k+1}} (-1)^q C_{-q}^k(\hat{x}) C_q^k(\hat{y}) \\ &= \sum_{kq} g(k,0)(-1)^q C_{-q}^k(\hat{x}) C_q^k(\hat{y}) \end{aligned} \tag{5.8}$$

$$\begin{aligned} \frac{e^{\imath\omega|\bar{x}-\bar{y}|}}{|\bar{x}-\bar{y}|} &= \sum_{kq} \frac{\omega}{c}(2k+1) j_k(\omega r_</c) y_k(\omega r_>/c)(-1)^{q+1} C_{-q}^k(\hat{x}) C_q^k(\hat{y}) \\ &= \sum_{kq} g(k,\omega/c)(-1)^q C_{-q}^k(\hat{x}) C_q^k(\hat{y}), \end{aligned} \tag{5.9}$$

where j and y are the spherical Bessel and Hankel functions respectively, and g will be a convenient shorthand for the radial parts. Using equation (5.7) we can express the product of two Dirac wavefunctions as:

$$\phi_v^\dagger(\vec{x})\phi_v(\vec{x}) = \frac{1}{x}\left[P_v(x)P_v(x) + Q_v(x)Q_v(x)\right]\Omega_{\kappa_v m_v}^\dagger(\hat{x})\Omega_{\kappa_v m_v}(\hat{x}) \tag{5.10}$$

and,

$$\phi_a^\dagger(\vec{y})\phi_a(\vec{y}) = \frac{1}{y}\left[P_a(y)P_a(y) + Q_a(y)Q_a(y)\right]\Omega^\dagger_{\kappa_a m_a}(\hat{y})\Omega_{\kappa_a m_a}(\hat{y}). \tag{5.11}$$

Thus the direct term can now be expressed as:

$$g_{vava}(0) = \alpha\sum_{kq}(-1)^q\left\langle\kappa_v m_v|C^k_{-q}|\kappa_v m_v\right\rangle\left\langle\kappa_a m_a|C^k_q|\kappa_a m_a\right\rangle R(vava;0) \tag{5.12}$$

where

$$\left\langle\kappa_a m_a|C^k_q|\kappa_a m_a\right\rangle = \int d\Omega\ \Omega^\dagger_{\kappa_a m_a}C^k_q\ \Omega_{\kappa_a m_a} \tag{5.13}$$

and

$$\begin{aligned} R(vava;0) = \int dxdy\ g(k,0)\left[P_v(x)P_v(x) + Q_v(x)Q_v(x)\right] \\ \times\left[P_a(y)P_a(y) + Q_a(y)Q_a(y)\right]. \end{aligned} \tag{5.14}$$

Since the spherical spinors are angular momentum eigenstates and the functions C^k_q are spherical tensor operators, the Wigner-Eckhart theorem can be used:

$$\left\langle\kappa_a m_a|C^k_q|\kappa_a m_a\right\rangle = (-1)^{j_a+m_a}\begin{pmatrix} j_a & k & j_a \\ -m_a & q & m_a\end{pmatrix}\left\langle\kappa_a||C^k||\kappa_a\right\rangle, \tag{5.15}$$

and the reduced matrix element $\left\langle\kappa_a||C^k||\kappa_a\right\rangle$ is

$$\left\langle\kappa_a||C^k||\kappa_a\right\rangle = (-1)^{j_a+1/2}(2j_a+1)\begin{pmatrix} j_a & j_a & k \\ -1/2 & 1/2 & 0\end{pmatrix}\Pi(2l_a+1) \tag{5.16}$$

where

$$\Pi(l) = \begin{cases} 1, \ l \text{ is even} \\ 0, \ l \text{ is odd.} \end{cases} \tag{5.17}$$

We can now evaluate the angular momentum portion of the expression, in particular we sum over the magnetic quantum numbers q and m_a:

$$\sum_{m_a q} (-1)^{j_v - m_v + j_a - m_a + k - q} \begin{pmatrix} j_v & k & j_v \\ -m_v & -q & m_v \end{pmatrix} \begin{pmatrix} j_a & k & j_a \\ -m_a & q & m_a \end{pmatrix} = \sqrt{\frac{2j_v+1}{2j_a+1}}\, \delta_{k0}, \tag{5.18}$$

thus we obtain a final expression for the direct term

$$g_{vava}(0) = \sqrt{\frac{2j_v+1}{2j_a+1}} \left\langle \kappa_v || C^0 || \kappa_v \right\rangle \left\langle \kappa_a || C^0 || \kappa_a \right\rangle R(vava; 0). \tag{5.19}$$

Now, since

$$\left\langle \kappa_v || C^0 || \kappa_v \right\rangle = \sqrt{2j_v + 1} \tag{5.20}$$

and,

$$\left\langle \kappa_a || C^0 || \kappa_a \right\rangle = \sqrt{2j_a + 1}. \tag{5.21}$$

So equation 5.19 can be re-expressed as

$$\sum_{m_a} g_{vava}(0) = (2j_v + 1) R(vava; 0), \tag{5.22}$$

which can now be directly programmed for numerical evaluation.

We can now perform an analogous evaluation for the exchange portion given in the first term in (5.6). Thus,

$$\phi_v^\dagger(\vec{x}) \phi_a(\vec{x}) = \frac{1}{x} \left[P_v(x) P_a(x) + Q_v(x) Q_a(x) \right] \Omega^\dagger_{\kappa_v m_v}(\hat{x}) \Omega_{\kappa_a m_a}(\hat{x}) \tag{5.23}$$

and so the radial portion is

$$g_{vaav}(0) = \alpha \sum_{kq} (-1)^q \left\langle \kappa_v m_v | C^k_{-q} | \kappa_a m_a \right\rangle \left\langle \kappa_a m_a | C^k_q | \kappa_v m_v \right\rangle R_k(vaav;\epsilon), \tag{5.24}$$

while the angular momentum terms, summing again over the core-states, are:

$$\begin{aligned} \sum_{m_a q} (-1)^{j_v - m_v + j_a - m_a + k - q} \begin{pmatrix} j_v & k & j_a \\ -m_v & -q & m_a \end{pmatrix} \begin{pmatrix} j_a & k & j_v \\ -m_a & q & m_v \end{pmatrix} \\ = (-1)^{j_v - j_a + k} \frac{1}{2j_a + 1}. \end{aligned} \tag{5.25}$$

Using this result, we find,

$$\begin{aligned} \sum_{m_a} g_{vaav}(\epsilon) &= \sum_k (-1)^{j_v - j_a + 2k} \frac{1}{2j_v + 1} \left\langle \kappa_v || C^k || \kappa_a \right\rangle \left\langle \kappa_a || C^k || \kappa_v \right\rangle R_k(vaav;\epsilon) \\ &= (2j_v + 1) \sum_k \begin{pmatrix} j_v & j_a & k \\ -1/2 & 1/2 & 0 \end{pmatrix}^2 \Pi(l_v + l_a + k) R_k(vaav;\epsilon), \end{aligned} \tag{5.26}$$

which can now, also, be programmed directly to be evaluated numerically.

Now, in considering the Breit terms, the vector portion, or so-called "Gaunt" term involving the $\vec{\alpha}$ matrix, is more complicated, and its reduction into angular and radial parts is straight forward but tedious if one makes use of vector spherical harmonics that are given in Appendix 3. The details are left to the literature Johnson et al. [42], Johnson [44], Mann and Johnson [54]. In general form, for an arbitrary arrangement of states, the Gaunt term is given by:

$$g_{ijkl}(\epsilon) = \sum_L J_L(ijkl) \left[M_L(ijkl;\epsilon) + N_L(ijkl;\epsilon) \right] \tag{5.27}$$

where J is the formula for the angular terms, the general form of equation (5.18)

$$\sum_M (-1)^{j_i - m_i + j_j - m_j + L - M} \begin{pmatrix} j_i & L & j_k \\ -m_i & M & m_k \end{pmatrix} \begin{pmatrix} j_j & L & j_l \\ -m_j & -M & m_l \end{pmatrix}. \tag{5.28}$$

The equations M and N in equation (5.27) are the radial components, and have the following forms,

$$\begin{aligned} M_L(ijkl;0) =& (-1)^L \left\langle \kappa_i || C^L || \kappa_k \right\rangle \left\langle \kappa_j || C^L || \kappa_l \right\rangle \\ & \left[\frac{L+1}{2L+3} \int_0^\infty dx\ dy\ g(L+1;\omega/c) Q_{ik}(x) Q_{jl}(y) \right. \\ & \left. + \frac{L}{2L-1} \int_0^\infty dx\ dy\ g(L-1;\omega/c) P_{ik}(x) P_{jl}(y) \right], \end{aligned} \tag{5.29}$$

and

$$\begin{aligned} N_L(ijkl;0) =& (-1)^{L+1} \left\langle \kappa_i || C^L || \kappa_k \right\rangle \left\langle \kappa_j || C^L || \kappa_l \right\rangle \\ & \frac{(\kappa_i + \kappa_k)(\kappa_j + \kappa_l)}{L(L+1)} \int_0^\infty dx\ dy\ g(L;\omega/c) V_{ik}(x) V_{jl}(y), \end{aligned} \tag{5.30}$$

where

$$P_{ik}(r) = U_{ik}(r) + \frac{\kappa_k - \kappa_i}{L} V_{ik}(r), \tag{5.31}$$

$$Q_{ik}(r) = -U_{ik}(r) + \frac{\kappa_k - \kappa_i}{L+1} V_{ik}(r), \tag{5.32}$$

and

$$U_{ik}(r) = P_i(r) Q_k(r) - Q_i(r) P_k(r), \tag{5.33}$$

$$V_{ik}(r) = P_i(r) Q_k(r) + Q_i(r) P_k(r). \tag{5.34}$$

We note that although the values of the reduced matrix elements depends only on the values of the angular momenta, κ, the selection rules of the reduced matrix elements do depend on the sign of κ.

We can now show that for the Breit term, the direct matrix element vanishes. The angular momentum terms are the same in the Breit term as in the Coulomb term considered above. Hence, we use the result of equation 5.18, since we need to sum over the closed-shell states:

$$\sum_{m_a} g_{vava} = \sqrt{\frac{2j_a+1}{2j_v+1}}(M_0(vava;\epsilon) + N_0(vava;\epsilon)). \tag{5.35}$$

Looking at the individual radial wavefunctions, $P_{aa} = Q_{aa} = 0$, therefore the term $M_0(vava) = 0$ also. The reduced matrix element $\langle -\kappa_a||C^0||\kappa_a\rangle = 0$, thus the term $N_0(vava)$ is also equal to zero. Thus,

$$\sum_{m_a} g_{vava} = 0 \tag{5.36}$$

and only the exchange term, g_{vaav}, contributes to the Breit portion of the one-photon exchange.

5.3 Numerical Evaluation

Now that we have equations that are suitable for numerical implementation in hand, we will proceed with the details of the evaluation. As before, that is in chapters 3 and 4, our starting point will be the the one-electron energies and wavefunctions, thus the backbone of our calculation will be "Radial". In chapters 3 and 4 we saw that Radial provides excellent solutions to H-like ions using a Fermi charge distribution.

Our algorithm will be that for a particular valence state of the Li-like ion, Radial will be called (via a Mathematica wrapper function) to calculate the energy and wavefunction for the H-like ion for the core states (1s) and the valence state (2s or 2p). These, given in the form of matrices will be input into a Mathematica function that implements the theory shown above. To use the built-in integration routines "NInte-

grate[]" the wavefunctions given by Radial must be first fed to the "Interpolation[]" function that generates a "continuous" wavefunction as a function of distance from the nucleus, r. Thus a radial grid is first generated, then using said grid, a potential matrix is generated and then Radial is called. After Radial performs its calculation of the state energy and wavefunction, the result is used to evaluate the one-photon exchange using the formalism developed above. Mathematica has a formalism that can accommodate the mathematical formalism almost directly (see Appendix 2).

To test the accuracy of the code we can calculate the one-photon exchange contribution for the case of Bismuth (Z = 83) which has been investigated by several groups [94] and [76], and thus offers multiple corroboration of the calculation.

Table 5.1: One-photon exchange comparison for Li-like bismuth.

Z=83	ΔE (eV)		
State:	$2s$	$2p_{1/2}$	$2p_{3/2}$
This work	1111.571	1398.249	1135.389
Sapirstein and Cheng [76]	1111.567	1398.245	1135.387
Yerokhin et al. [94]	1111.571	1398.251	1135.389

Table 5.1 shows the comparison between the photon exchange calculated in this work and those calculated by Sapirstein and Cheng [76] and Yerokhin et al. [94]. We see that the agreement is excellent, with differences appearing at the meV scale. This agreement is well within the tolerances that were expressed in the introduction of 10's of meV. Thus, as seen in Chapter 4 already, the strategy of combining a pre-existing pre-compiled code together with native Mathematica functions is vindicated; and is capable of delivering results comparable to the state-of-the art.

Chapter 6

Higher-Order Effects

6.1 Introduction

In this chapter we will consider effects at the next higher order in α. Specifically we will look at the second-order QED correction, the second-order photon exchange, the third-order Photon Exchange and the screened QED effect. We require these contributions to match the level of accuracy of experiment; however as these effects come in at the next level of perturbation theory the effect of the finite nuclear size in these processes is reduced by a further factor of α/π as compared to the first order correction with respect to the Dirac nuclear-size effect, that is, by a factor of $(\alpha/\pi)^2 = 1/160000$), and thus negligible. To that end, all factors here were included by using tables of results from the literature and interpolating when necessary.

6.2 Second-Order QED

The second-order or two-loop QED corrections are the electromagnetic interactions that take place in the next higher order in perturbation theory. These effects have recently become important due to the measurements of the $2p_j - 2s$ transition energies in heavy Li-like ions having recently reached a fractional accuracy of 0.03% with respect to the total QED contribution, thus presenting a 10% sensitivity of the experimental results to the two-loop QED effects [92].

Traditionally, this effect has been studied in the context of an expansion in the nuclear-strength parameter $Z\alpha$, [65, 41, 28]. Such studies, however, do not provide reliable information about the magnitude of the two-loop Lamb shift in heavy ions like uranium, where the parameter $Z\alpha$ approaches unity. Thus theoretical investigations of the two-loop QED effects valid to all orders in the nuclear-strength parameter $Z\alpha$ are required, and such a program has been undertaken by Yerokhin and co-workers[92, 95, 96]. Currently the two-loop QED effects yield the second largest uncertainty in the theoretical prediction for the ground-state Lamb shift in hydrogen (after the proton charge distribution effect)[92].

The complete set of two-loop one-electron QED corrections (also referred to as the two-loop Lamb shift) is graphically represented in Figure 6.1. Specifically, the two-loop self-energy correction represented by diagrams (a)-(c), are evaluated rigorously to all orders in $Z\alpha$ and is described in Yerokhin et al. [92, 95]. While the diagrams that contain fermion loops, that is vacuum-polarization contributions, specifically diagrams (d)-(g), were also be done rigorously and diagrams (h)-(k), within the free-loop approximation, that is only the leading term of the expansion of fermion loops in terms of the binding potential was kept [96]. In the one-loop case, the free-loop approximation corresponds to the Uehling potential and yields the dominant contribution even for high-Z ions like uranium.The assumption was made that the free-loop approximation is reasonably adequate in the two-loop case also.

The two-loop contributions to the energy shift are, like the one-loop case, conveniently represented in terms of the dimensionless function $F(Z\alpha)$ defined by,

$$\Delta E = \left(\frac{\alpha}{\pi}\right)^2 \frac{(Z\alpha)^4}{n^3\alpha^2} F(Z\alpha), \tag{6.1}$$

where we see that there is an extra factor of α/π as compared to the one-loop case (4.2).

The results of the calculation of the two-loop contribution to the Lamb shift are tabulated in Tables 6.1 - 6.5, for the various subsets given in Figure 6.1 for the $2s$ and $2p$ states as a function of Z. Intermediate Z values were interpolated using a 3rd degree polynomial via the Mathematica function "Interpolation[]", (the complete

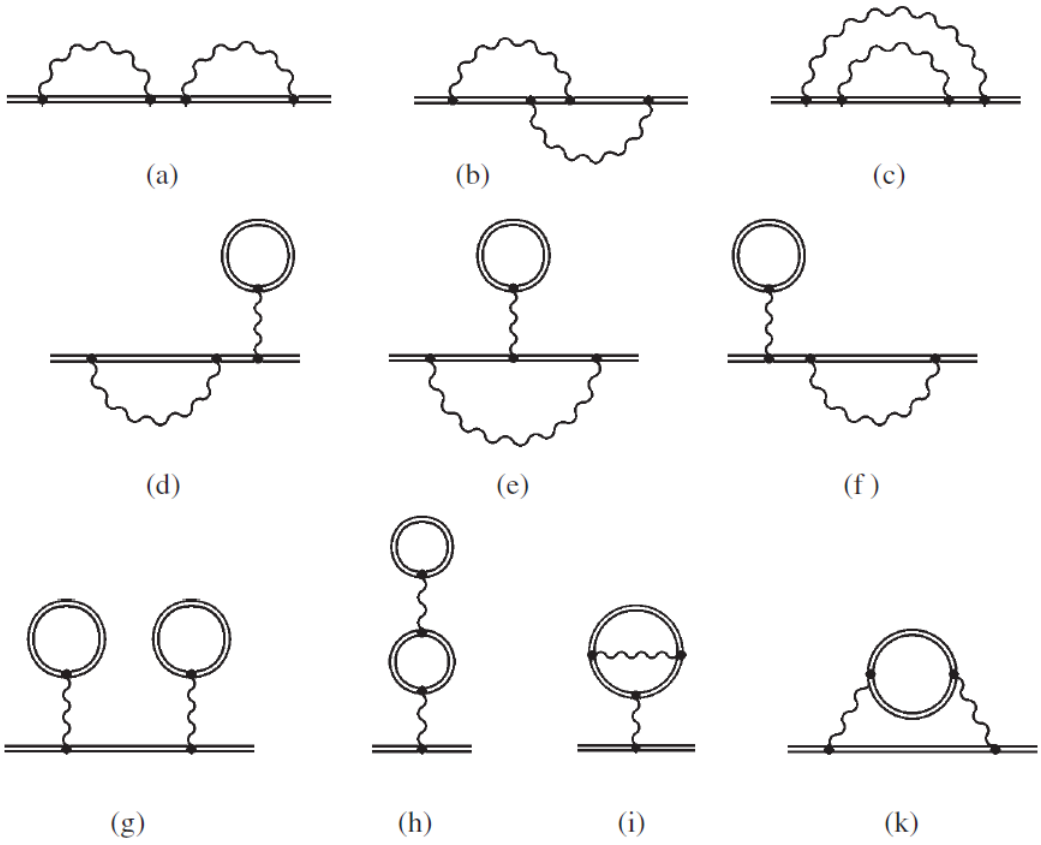

Figure 6.1: Two-loop one-electron QED corrections. The gauge-invariant subsets are referred to as SESE(a-c), SEVP (d-f), VPVP (g-i), and S(VP)E (k) [92]. Copyright (2006) by the American Physical Society.

function is shown in Appendix B).

6.3 Second-Order Photon Exchange

The second-order photon exchange in highly charged ions has, like the two-loop correction, been the subject of intense interest recently, and has been looked at by, Yerokhin et al. [90], Sapirstein and Cheng [76], Artemyev et al. [8], Yerokhin et al. [94]. As with the second-order QED contribution, it is sufficient for us to simply include the results already calculated for a nominal nuclear charge radius because we are concerned with the effect of changes of the charge radius for a particular Z, and

Table 6.1: Values of $F(Z\alpha)$ for the two-loop SESE(a-c) subset [92, 95, 96].

Z	$F(Z\alpha)$		
	$2s$	$2p_{1/2}$	$2p_{3/2}$
60	-1.976(70)	0.222(72)	0.02(14)
70	-2.453(60)	0.192(60)	-0.082(93)
83	-3.296(38)	0.133(38)	-0.175(66)
92	-4.218(34)	0.012(32)	-0.241(48)
100	-5.455(68)	-0.214(32)	-0.282(52)

Table 6.2: Values of $F(Z\alpha)$ for the two-loop SEVP(d-f) subset [92, 95, 96].

Z	$F(Z\alpha)$		
	$2s$	$2p_{1/2}$	$2p_{3/2}$
60	0.9854(4)	0.01477(3)	0.010449(6)
65	1.1463(8)	0.02653(2)	0.015548(8)
70	1.34094(6)	0.04384(4)	0.02171(1)
75	1.5827(2)	0.069408(9)	0.029019(10)
80	1.8834(2)	0.107174(8)	0.037514(4)
83	2.101(2)	0.138236(10)	0.043186(7)
90	2.751(3)	0.2488(2)	0.05798(3)
92	2.9786(8)	0.294(2)	0.06251(1)
100	4.224(8)	0.5871(8)	0.08183(6)

Table 6.3: Values of $F(Z\alpha)$ for the two-loop VPVP(g-i) subset [92, 95, 96].

Z	$F(Z\alpha)$		
	$2s$	$2p_{1/2}$	$2p_{3/2}$
60	-0.10566(6)	-0.003233(2)	-0.000029
65	-0.1342(3)	-0.00518(1)	-0.000039
70	-0.1713(1)	-0.008238(7)	-0.000051
75	-0.2212(2)	-0.01313(1)	-0.000067
80	-0.288(4)	-0.02094(3)	-0.000085
83	-0.3393(5)	-0.02778(4)	-0.000099
90	-0.505(1)	-0.0543(1)	-0.000136
92	-0.566(1)	-0.0658(1)	-0.000149
100	-0.935(4)	-0.1482(6)	-0.000209

Table 6.4: Values of $F(Z\alpha)$ for the two-loop VPVP(ks)(g-i) subset [92, 95, 96].

Z	$F(Z\alpha)$		
	$2s$	$2p_{1/2}$	$2p_{3/2}$
60	-1.04561(2)	-0.069624(1)	-0.008931
65	-1.1053(4)	-0.08862(1)	-0.010259
70	-1.17895(4)	-0.112569(2)	-0.011673
75	-1.27069(9)	-0.143102(5)	-0.013175
80	-1.38369(9)	-0.182409(7)	-0.01477
83	-1.4642(1)	-0.2115(1)	-0.015775
90	-1.6988(8)	-0.30171(8)	-0.018267
92	-1.7791(2)	-0.33488(3)	-0.01902
100	-2.201(2)	-0.5202(3)	-0.022227

Table 6.5: Values of $F(Z\alpha)$ for the two-loop S(VP)E (k) subset [92, 95, 96].

Z	$F(Z\alpha)$		
	$2s$	$2p_{1/2}$	$2p_{3/2}$
60	0.16851(1)	0.00098	0.00226
65	0.18271(1)	0.00314	0.0022
70	0.20042(1)	0.00603	0.00213
75	0.2226(1)	0.00994	0.00205
80	0.25059(2)	0.01528	0.00197
83	0.27097(2)	0.01943	0.00191
90	0.33285(3)	0.03322	0.00177
92	0.35535(3)	0.03863	0.00172
100	0.47842(6)	0.07124(1)	0.00152

such changes will be very small in second order.

The second-order photon exchange correction is composed of three separate effects, each however contains the exchange of two virtual photons. The Feynman diagrams are included in Figure 6.2. The first diagram, (a), is the ladder two-photon exchange effect while the middle diagram, (b), represents the two-photon cross diagram. The diagram on the right, (c), is the three-electron two-photon exchange diagram, which appears because we are dealing with Li-like ions. What occurs here is that the valence electron exchanges one-photon with each of the 1s core electrons.

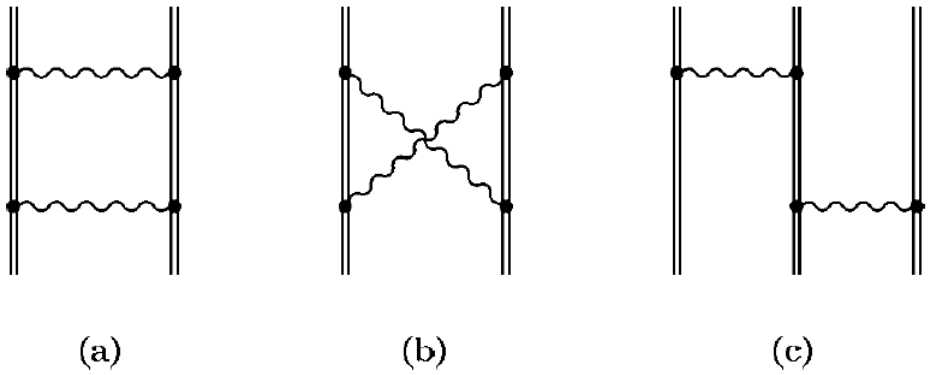

Figure 6.2: Feynman diagrams representing the two-photon exchange corrections [90]. Copyright (2000) by the American Physical Society.

The results of evaluating these diagrams are tabulated in Tables 6.6 and 6.7. These results, just like in the two-loop QED case, were included with an interpolation function to get the missing Z values.

6.4 Screened QED

In this section we complete the inclusion of QED corrections of second order in α; the one-electron QED corrections of this order and the two-photon exchange correction were dealt with above. What remains to be included are the second-order two-electron corrections because we are considering Li-like ions, collectively called the "Screened QED" corrections. The relevant theory has been presented in Blundell

Table 6.6: Two-photon exchange correction for $(1s)^2 2s_{1/2}$ and $(1s)^2 2p_{1/2}$ in eV [90, 76, 8, 94].

Z	$2s$	$2p_{1/2}$
20	-7.02571	-10.5667
30	-7.29673	-11.1861
40	-7.69239	-12.1085
50	-8.23389	-13.3983
60	-8.95336	-15.1576
70	-9.89868	-17.5464
80	-11.1474	-20.8279
83	-11.5978	-22.0461
90	-12.8228	-25.4489
92	-13.2261	-26.5969
100	-15.1456	-32.2447

Table 6.7: Two-photon exchange correction for $(1s)^2 2p_{3/2}$ in eV [90, 76, 8, 94].

Z	$2p_{3/2}$
20	-10.2671
28	-10.438
30	-10.4886
32	-10.5439
40	-10.7983
47	-11.0688
50	-11.1991
54	-11.3842
60	-11.6919
66	-12.0329
70	-12.2813
74	-12.545
79	-12.8998
80	-12.9736
82	-13.1257
83	-13.2027
90	-13.7788
92	-13.9543
100	-14.7107

[20], Artemyev et al. [7], Yerokhin et al. [91]. The Feynman diagrams displaying self-energy correction are shown in Figure 6.3, while that of vacuum-polarization in Figure 6.4. The main difference between these corrections and the corresponding one-electron case is that these involve specifically two electrons. For the electron configuration of Li-like ions, one valence electron above a closed $1s$ core, the screening could be due to either the interaction between the valence electron and either of the core electrons, or between the core electrons in the closed shell.

However, since this correction comes in at the same level as the two-photon exchange correction, the arguments made in terms of the finite-nuclear size effect on the transition energy due to two-photon exchange also apply here. As we saw above, at this level the finite-size correction scales as $(\alpha/\pi)^2$ of the Dirac finite-size correction which is about 30 eV. As we saw above, this scaling factor is about 5.4×10^{-6} giving a finite-size correction of about 0.16 meV. Thus, at this level small variations in the finite-nuclear size will lead to variations in the transition energy due to the screened-QED effect which will be well below the expected uncertainty . Therefore, as before all that is required to include the screened-QED effect is the scaling of the transition energy as a function of Z. This is presented in Figure 6.5 for the $2p_{1/2} - 2s$ transition and in Figure 6.6 for the $2p_{3/2} - 2s$ transition.

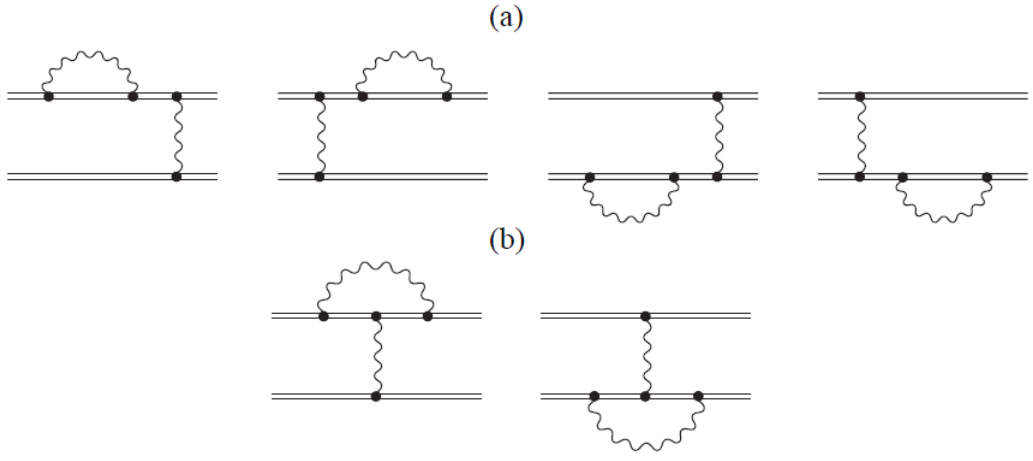

Figure 6.3: Feynman diagrams representing the screened self-energy correction [91]. Copyright (2005) by the American Physical Society.

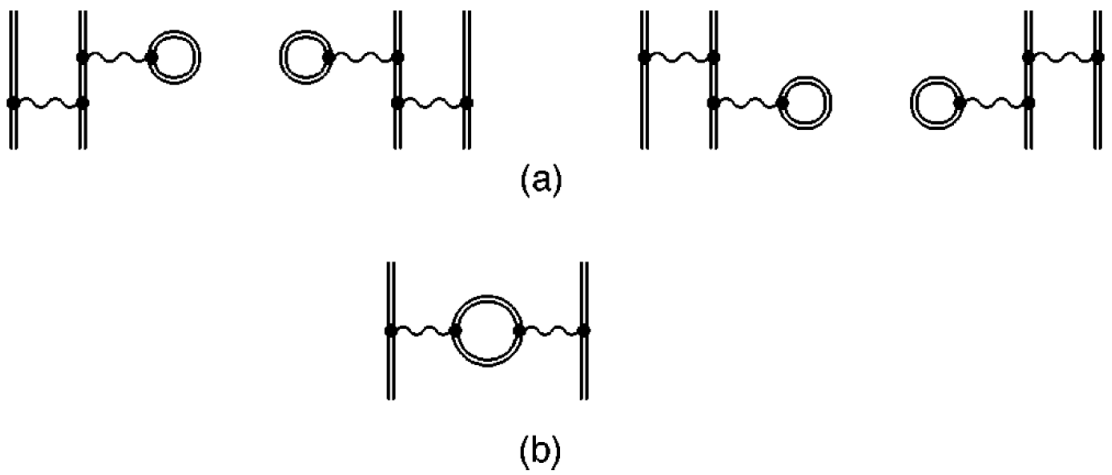

Figure 6.4: Feynman diagrams representing the screened vacuum-polarization correction [7]. Copyright (1999) by the American Physical Society.

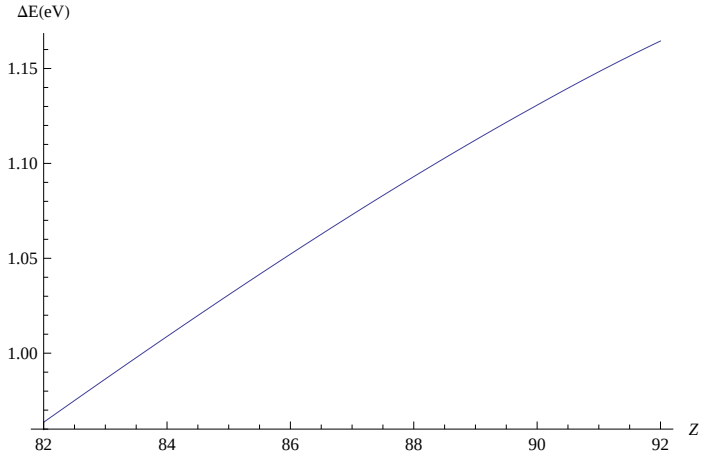

Figure 6.5: Screened QED energy for the $2p_{1/2} - 2s$ transition for $Z = 82 - 92$ [7, 91]

6.5 Third-Order Photon Exchange

The effect of third-order photon exchange must be included in the energy budget in order to match the precision of experiment. However, no appreciable nuclear charge radius information is expected to contribute at this level, thus one only needs to include the energy itself, which is available from Yerokhin et al. [91] for the $2p_{3/2} - 2s$

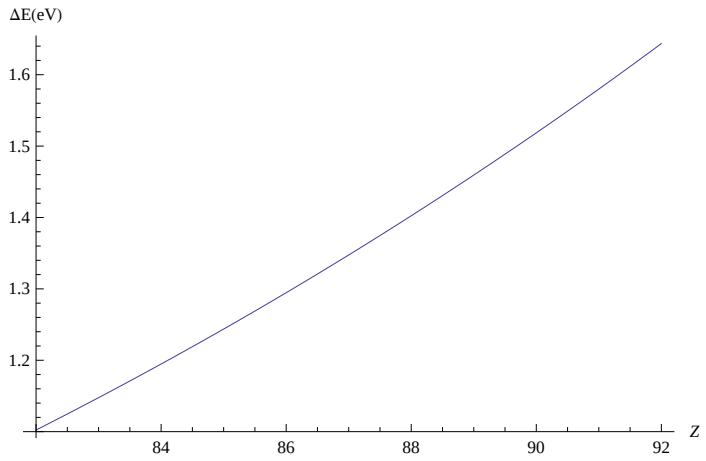

Figure 6.6: Screened QED energy for the $2p_{3/2} - 2s$ transition for $Z = 82 - 92$ [7, 91]

transition and Zherebtsov et al. [98] for the $2p_{1/2} - 2s$ transition. Third-order inter electronic-interaction correction is currently evaluated within the Breit approximation, and is carried out using the framework of perturbation theory as given by the formalism found in Blundell (1987) [19]. The information available therein was extracted and digitized, leading to an interpolated graph for the $2p_{1/2} - 2s$ transition in Li-like ions for the range of $Z = 83 - 92$, as well as for the transition $2p_{3/2} - 2s$. These are shown in Figures 6.7 and 6.8 respectively.

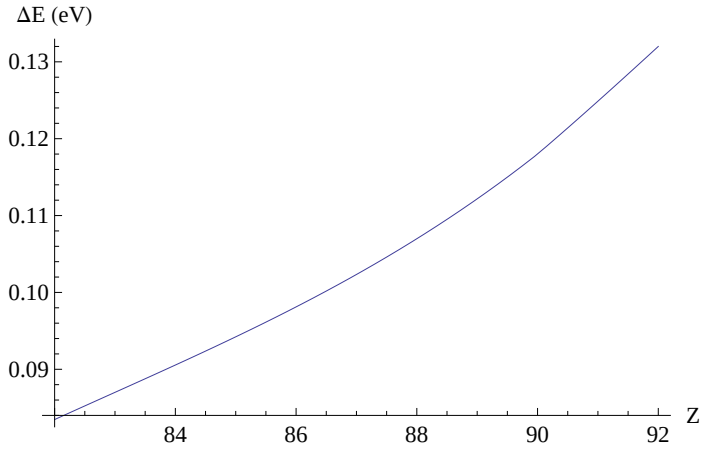

Figure 6.7: Three-photon exchange energy for the $2p_{1/2} - 2s$ transition for $Z = 83 - 92$ [98].

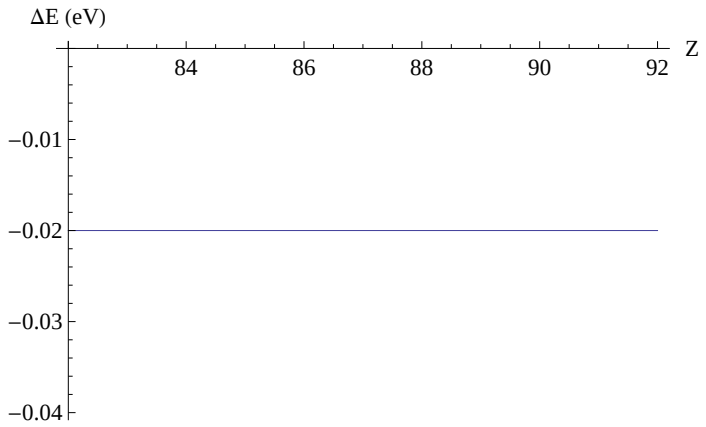

Figure 6.8: Three-photon exchange energy for the $2p_{3/2} - 2s$ transition for $Z = 83 - 92$ [91].

Thus we see that for the Z range of interest, there is no dependence on Z on the result for the three-photon exchange to the accuracy that we are aiming for. However, since the result is $\Delta E_{3PE} = -0.02$ eV, we need to include this effect to match experiment.

Chapter 7

Other Effects

7.1 Introduction

In this final chapter on individual contributions to the 2p-2s Lamb shift in Li-like ions we look at two effects that must be included to match the accuracy currently available in experiment. These are the effects of the nuclear recoil and nuclear polarization.

7.2 Nuclear Recoil

The bound-state QED effects discussed up until now were considered in the presence of a nuclear Coulomb field generated by an infinitely heavy nucleus. However, as mentioned, the accuracy of current experiments requires that one go beyond the static nuclear case. Furthermore, this treatment must be done in an "all-orders" approach as the αZ parameter is not small in the high-Z regime and the aid of an expansion in αZ is not possible. This type of analysis, where the relativistic nuclear recoil corrections to the energy levels of bound electrons which incorporates the external field without an expansion has been carried out by Shabaev and Artemyev [81], and most recently presented by Artemyev et al. [5, 6].

A detailed presentation of this method will not be presented here, only the main results will be summarized together with a few comments about the general thrust of

the approach. Briefly, the nucleus is treated as a Dirac particle of mass M and charge $Z|e|$, which surprisingly is still a good approximation even when complex nuclei are considered [58]. Since this approximation obviously has no nuclear charge radius dependence, all that we require theoretically are the results for the associated energy shifts.

7.2.1 Hydrogenlike Atoms/Ions

For hydrogenlike atoms the nuclear recoil corrections to the energy are given as,

$$\Delta E_{RR} = \Delta E^{(1)} + \Delta E^{(2)}, \tag{7.1}$$

where the two above expressions combine to the simple formula

$$\Delta E^{(1)} = \frac{m}{M}\frac{(\alpha Z)}{2N^2}mc^2, \tag{7.2}$$

and,

$$\Delta E^{(2)} = \frac{m}{M}\frac{(\alpha Z)^5}{\pi n^3}P(\alpha Z)mc^2. \tag{7.3}$$

Here m is the electron mass and the following expressions have been used

$$N^2 = n^2 - 2(n - |\kappa|)(|\kappa| - \gamma), \tag{7.4}$$

$$\gamma = \sqrt{\kappa^2 - (\alpha Z)^2},\ \kappa = (-1)^{j-l+1/2}(j + 1/2). \tag{7.5}$$

The function $P(\alpha Z)$ has been calculated and tabulated in [5] for the states 1s, 2s, $2p_{1/2}$ and $2p_{3/2}$ which is reproduced in Table 7.1.

7.2.2 High-Z Lithiumlike Atoms

The nuclear recoil correction for the case of lithium-like atoms is the sum of two contributions, one- and two-electron corrections. The one-electron contribution is

Table 7.1: One-electron nuclear recoil $P(\alpha Z)$ functions [5]

State	$1s$	$2s$	$2p_{1/2}$	$2p_{3/2}$
Z	$P(\alpha Z)$	$P(\alpha Z)$	$P(\alpha Z)$	$P(\alpha Z)$
1	5.43(2)	6.155(1)	-0.3011(0)	-0.3013(4)
5	4.3033(4)	5.0335(2)	-0.2692(0)	-0.2724(1)
10	3.795(1)	4.5383(1)	-0.2277(0)	-0.2379
15	3.4973(1)	4.2599(0)	-0.1845(0)	-0.2047
20	3.294(1)	4.0825(0)	-0.1393(0)	-0.1726
25	3.1483(1)	3.9691(0)	-0.092(0)	-0.1413
30	3.0437(1)	3.9037(0)	-0.0421(0)	-0.1107
35	2.9714(1)	3.8785(0)	0.0122(0)	-0.0081
40	2.9268(1)	3.89(0)	0.0685(0)	-0.0517
45	2.9077(1)	3.9376(0)	0.131(0)	-0.023
50	2.9137(1)	4.0228(1)	0.2(0)	0.005
55	2.9456(1)	4.1498(1)	0.2774(0)	0.0326
60	3.0061(2)	4.3248(2)	0.3655(0)	0.0597
65	3.0997(2)	4.5584(2)	0.468(0)	0.0863
70	3.2334(4)	4.8656(5)	0.5894(0)	0.1125
75	3.4183(8)	5.2698(8)	0.737(1)	0.1384
80	3.672(1)	5.807(2)	0.9214(2)	0.1638
85	4.022(4)	6.537(4)	1.1598(4)	0.1889
90	4.519(8)	7.557(9)	1.481(1)	0.2138
92	4.77(1)	8.08(2)	1.643(3)	0.2236
95	5.25(3)	9.05(3)	1.937(5)	0.2383
100	6.4(1)	11.4(2)	2.63(2)	0.2623

obtained by summing the one-electron corrections considered in the previous section over all the occupied one-electron states in the Lithium-like ion. The two-electron contribution $\Delta E^{(int)}$ can be expressed in terms of a function $Q(\alpha Z)$ for the transitions $(1s)^2 2p_{1/2}$ and $(1s)^2 2p_{3/2}$ (note that the $(1s)^2 2s$ transition does not contribute):

$$\Delta E^{(int)} = -\frac{2^9}{3^8}\frac{m}{M}(\alpha Z)^2 Q(\alpha Z) mc^2. \tag{7.6}$$

Table 7.2: Values of function $Q(\alpha Z)$ for given Z for lithium-like ions [6].

state	$(1s)^2 2p_{1/2}$	$(1s)^2 2p_{3/2}$
Z	$Q(\alpha Z)$	$Q(\alpha Z)$
5	0.99935	0.99953
10	0.99741	0.9981
15	0.99416	0.99573
20	0.98959	0.99239
25	0.9837	0.98809
30	0.97645	0.98281
35	0.96782	0.97653
40	0.65776	0.96926
45	0.94622	0.96097
50	0.93313	0.95165
55	0.91841	0.94129
60	0.90195	0.92988
65	0.88361	0.91742
70	0.8632	0.9039
75	0.84052	0.8893
80	0.81529	0.87362
85	0.78716	0.85686
90	0.7557	0.83896
92	0.74206	0.83148
95	0.72035	0.81988
100	0.68041	0.79951

7.2.3 Numerical Evaluation

The tabulated values, shown in Tables 7.1 and 7.2, have been interpolated using order=3 to give a value of P and Q for any Z value. The equations given above

were implemented in Mathematica as shown in Appendix B as the function "nuclear-Recoil". Since, by definition, the nucleus is treated as a Dirac point-particle there is no nuclear charge radius information in the nuclear recoil contribution. The results for the transitions $2p_{1/2} - 2s$ and $2p_{3/2} - 2s$ for Li-like ions are collected in Table 7.3.

Table 7.3: Nuclear recoil corrections for Li-like ions

Z	A	$2p_{1/2} - 2s$ (eV)	$2p_{3/2} - 2s$ (eV)
82	208	-0.05	-0.06
83	209	-0.05	-0.07
84	209	-0.06	-0.07
85	210	-0.06	-0.07
86	222	-0.06	-0.07
87	223	-0.06	-0.08
88	226	-0.06	-0.08
89	227	-0.06	-0.08
90	232	-0.07	-0.09
91	231	-0.07	-0.09
92	238	-0.07	-0.09

7.3 Nuclear Polarization

The final effect that one must take into account when considering sensitive tests of QED, is the effect of nuclear polarization (NP). Historically, the interactions between the internal nuclear degrees of freedom with K-shell electrons has been extensively studied in the context of muonic atoms [58], where the binding energies of muons are of the same order as nuclear excitation energies. In the analogous case of electrons, the energy shifts are correspondingly smaller; however the influence of the contribution increases when the interaction with low-lying rotational nuclear states are taken into account. In heavy atoms, on order of $Z \approx 80 - 90$, the electronic transition energies become comparable in magnitude with nuclear excitation energies.

Numerical calculations of nuclear polarization using a relativistic field theoretic approach based on the concept of effective photon propagators have been developed by Plunien et al.[70, 71, 68, 69], applied to the case of heavy even-nuclei, where the

nuclear polarization is due to collective nuclear excitations. The formalism also allows for extension to single-particle valence proton excitations in odd-nuclei as further developed by Nefiodov et al. [50, 62, 61]. We will now summarize this formalism following Mohr et al. [58], Plunien et al. [70].

7.3.1 Theory

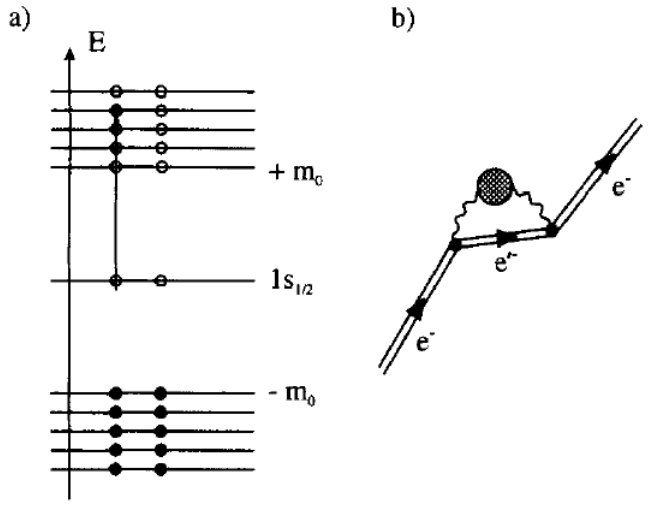

Figure 7.1: The 1s-electron can be virtually excited into an unoccupied state of the positive energy continuum via the interaction with virtual nuclear excitations (a). The corresponding Feymnan diagram (b) represents the first two terms contributing [58]. Copyright (1998) by Elsevier.

In this framework, the nuclear charge is described by an electromagnetic current

$$\hat{j}^{\mu}_{\mathrm{nucl}}(x) = j^{\mu}_{\mathrm{ext}}(\vec{x}) + \hat{j}^{\mu}_{\mathrm{fluc}}(x), \tag{7.7}$$

consisting of a static equilibrium part $j^{\mu}_{\mathrm{ext}}(\vec{x})$ corresponding to the nucleus in the ground state and a second-quantized, time-dependent part $\hat{j}^{\mu}_{\mathrm{fluc}}(x)$ characterizing the intrinsic dynamics of the nuclear charge density. The Dirac current $\hat{j}^{\mu}_{\mathrm{e}}$ interacts with the external electromagnetic field

$$\hat{A}^{\mu}(x) = A^{\mu}_{\mathrm{ext}}(\vec{x}) + \hat{A}^{\mu}_{\mathrm{rad}}(x), \tag{7.8}$$

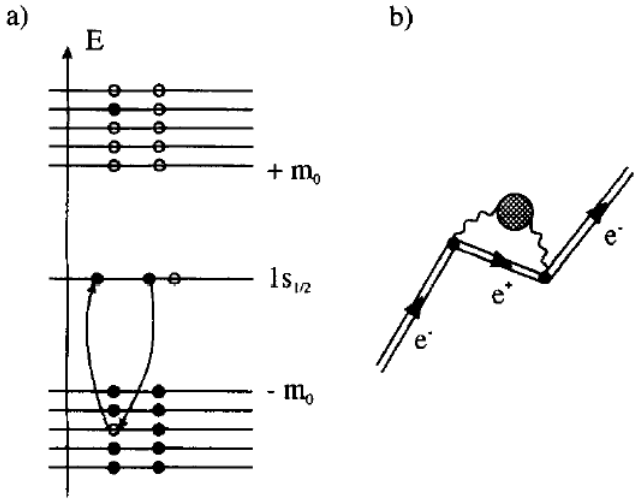

Figure 7.2: An electron from the occupied negative energy continuum can be virtually excited into the occupied $1s_{1/2}$-state at different spacetime points via the interaction with virtual nuclear excitations. The created positron annihilates with the ls-electron, which already had been present (a). The corresponding Feynman diagram of this exchange process (b)represents the vacuum contribution [58]. Copyright (1998) by Elsevier.

where the classical external field $A^{\mu}_{\rm ext}(\vec{x})$ is created by the static nuclear source $j^{\mu}_{\rm ext}$. The total radiation field $A^{\mu}_{\rm rad}$ is written as the sum of the free photon field $A^{\mu}_{\rm free}$ and a fluctuating field $A^{\mu}_{\rm fluc}$ generated by the nuclear-charge fluctuations $\hat{j}^{\mu}_{\rm fluc}$.

The interaction between the electron field and internal nuclear degrees of freedom is described by the interaction Hamiltonian:

$$\hat{H}_{\rm int} = \int d^3x \hat{j}^{\mu}_{\rm e}(x)\hat{A}^{\mu}_{\rm rad}(x). \tag{7.9}$$

In the Furry picture (bound-state interaction picture), described in chapter 3, the energy shift of a given electron bound state $|i\rangle$ is expressed by the Tomanaga-Schwinger equation:

$$e^{-\imath\Delta E_i(t_b-t_a)} = \left\langle i \left| \mathrm{T}\left(e^{-\imath\int_{t_a}^{t_b} dt\, \hat{H}_{\rm int}(t)}\right)\right| i\right\rangle . \tag{7.10}$$

When one performs the perturbation expansion on the above in the standard way,

one is led to Feynman diagrams that contain dressed photon lines that represent an effective photon propagator defined as the time-ordered product

$$\imath\mathscr{D}_{\mu\nu}(x,x') = \left\langle 0 \left| \mathrm{T}\left[\hat{A}^{\mathrm{rad}}_{\mu}(x)\hat{A}^{\mathrm{rad}}_{\nu}(x')\right] \right| 0 \right\rangle, \tag{7.11}$$

where the vacuum expectation value implies that the nucleus is to be considered in its ground state.

We can take equation (7.11) and write it as the sum of the free photon propagator $\mathscr{D}_{\mu\nu}$ and a vacuum polarization correction:

$$\tilde{\mathscr{D}}_{\mu\nu}(x,x') = \int d^4x_1 \int d^4x_2 \mathscr{D}_{\mu\alpha}(x-x_1)\Pi^{\alpha\beta}(x_1,x_2)\mathscr{D}_{\beta\nu}(x_2-x'), \tag{7.12}$$

which defines the reducible nuclear polarization tensor $\Pi^{\mu\nu}$.

The nuclear polarization correction to the Lamb shift can be expressed by

$$\Delta E_i = \imath\ \alpha \int d^3x_1 \int d^3x_2 \psi_i^{\dagger}(\vec{x_i}) \int dE\ S_F(\vec{x_1},\vec{x_2},E_i-E)\tilde{\mathscr{D}}_{00}(\vec{x_1},\vec{x_2},E)\gamma_0\psi_i(\vec{x_i}). \tag{7.13}$$

We can insert the exact electron propagator $S_F(\vec{x_1},\vec{x_2},E_i-E)$ for an electron in the external field of a hard-sphere nucleus (ie. the Furry picture as described in chapter 2):

$$\begin{aligned} S_F(\vec{x},\vec{x'},E) &= \sum_k \frac{\psi_k(\vec{x})\bar{\psi}_k(\vec{x'})}{E-E_k+\mathrm{sgn}(E_k-E_F)\imath\eta} \\ &= \sum_k \frac{\psi_k(\vec{x})\psi_k^{\dagger}(\vec{x'})\gamma_0}{E-E_k+\mathrm{sgn}(E_k-E_F)\imath\eta}, \end{aligned} \tag{7.14}$$

where,

$$\psi_k(\vec{r}) \equiv \psi_{\nu_1\kappa_1\mu_1}(\vec{r}) = \frac{1}{r}\begin{pmatrix} g_{\nu_1\kappa_1}(r)\chi_{\kappa_1\mu_1}(\hat{\Omega}) \\ \imath f_{\nu_1\kappa_1}(r)\chi_{\kappa_1\mu_1}(\hat{\Omega}) \end{pmatrix}, \tag{7.15}$$

and, κ_1 is given by

$$\kappa_1 = \begin{cases} l_1, & \text{if} \quad j_1 = l_1 - 1/2 \\ -(l_1+1), & \text{if} \quad j_1 = l_1 + 1/2 \end{cases}, \tag{7.16}$$

(NB: $i = \nu\kappa\mu$ and $k = \nu_1\kappa_1\mu_1$). The photon propagator above is written as:

$$\tilde{\mathscr{D}}_{00}(\vec{x_1}, \vec{x_2}, E) = \sum_{LM} B(EL; L \to 0) \frac{2E_L}{E^2 - E_L^2 - \imath\eta} F_L(x_1) F_L(x_2) Y_{LM}(\Omega_1) Y^*_{LM}(\Omega_2), \tag{7.17}$$

and can also be inserted to give the following expression for the self-energy:

$$\Delta E_i = \imath\ \alpha \sum_L B(EL; L \to 0) \sum_{\kappa_1} \sum_{M,\mu_1} (\mathscr{W}^{LM}_{\kappa\mu|\kappa_1\mu_1})^2 \int_{\nu_1} \mathscr{E}^L_{\kappa\nu|\kappa_1\nu_1} (\mathscr{R}^L_{\kappa\nu|\kappa_1\nu_1})^2. \tag{7.18}$$

The three corresponding terms are given as,

$$\mathscr{W}^{LM}_{\kappa\mu|\kappa_1\mu_1} = \int d\Omega\ \chi^\dagger_{\kappa\mu}(\Omega) Y^L_M(\Omega) \chi_{\kappa_1\mu_1}(\Omega) = \left\langle \kappa\mu | Y^L_M | \kappa_1\mu_1 \right\rangle, \tag{7.19}$$

$$\mathscr{E}^L_{\nu\kappa|\nu_1\kappa_1} = \int_{-\infty}^{\infty} dE\ (E - E_{\nu_1\kappa_1} + \mathrm{sgn}(E_{\nu_1\kappa_1} - E_F)\imath\eta)^{-1} \frac{2E_L}{(E - E_{\nu\kappa})^2 - E_L^2 - \imath\eta}, \tag{7.20}$$

$$\begin{aligned} \mathscr{R}^L_{\nu\kappa|\nu_1\kappa_1} &= \int_0^\infty dr\ r^2 F_L(r) [g_{\nu\kappa}(r) g_{\nu_1\kappa_1}(r) + f_{\nu\kappa}(r) f_{\nu_1\kappa_1}(r)] \\ &= \left\langle \nu\kappa | F_F | \nu_1\kappa_1 \right\rangle, \end{aligned} \tag{7.21}$$

while the $B(EL; L \to 0)$ term is defined to be

$$B(EL; L \to 0) = \frac{|\left\langle 0 || Q_L || LL \right\rangle|^2}{2L+1}. \tag{7.22}$$

That is, B is the transition probability for exciting a virtual nuclear state and Q_L is the multipole moment operator.

The energy integral can be evaluated by means of contour integration:

$$\begin{aligned}\mathscr{E}^L_{\nu\kappa|\nu_1\kappa_1} &= \int_{-\infty}^{\infty} dE\ (E - E_{\nu_1\kappa_1} + \mathrm{sgn}(E_{\nu_1\kappa_1} - E_F)\imath\eta)^{-1} \\ &\times \left[\frac{1}{(E - E_{\nu\kappa}) - E_L + \imath\eta} - \frac{1}{(E - E_{\nu\kappa}) + E_L + \imath\eta}\right] \\ &= 2\pi\imath\left(\frac{\Theta(E_{\nu_1\kappa_1} - E_F)}{E_{\nu_1\kappa_1} - E_{\nu\kappa} + E_L} + \frac{\Theta(E_F - E_{\nu_1\kappa_1})}{E_{\nu_1\kappa_1} - E_{\nu\kappa} - E_L}\right). \end{aligned} \tag{7.23}$$

Ignoring the contribution from the bound-states, the nuclear polarization contribution can be rewritten, in more compact form as,

$$\Delta E_i = -\alpha \sum_k \sum_{LM} B(EL) |\left\langle k|F_L Y^L_M|i\right\rangle|^2 \left(\frac{\Lambda^{(+)}}{E_k - E_i + E_L} + \frac{\Lambda^{(+)}}{E_k - E_i - E_L}\right), \tag{7.24}$$

where we have made use of lambda operators to project out the positive and negative portions of the energy spectrum. We can separate out the angular variables, and perform an angular momentum reduction to obtain the following expression for the NP correction:

$$\begin{aligned}\Delta E_{\nu lj} &= -\frac{\alpha}{4\pi} \sum_L B(EL)(2L+1) \\ &\times \sum_{\nu_1 j_1} (2j_1 + 1) \begin{pmatrix} j_1 & j & L \\ 1/2 & -1/2 & 0 \end{pmatrix}^2 |\left\langle \nu lj|F_L|\nu_1 l_1 j_1\right\rangle|^2 \\ &\times \left(\frac{\Lambda^{(+)}}{E_k - E_i + E_L} + \frac{\Lambda^{(+)}}{E_k - E_i - E_L}\right), \end{aligned} \tag{7.25}$$

where the the radial matrix is given in (7.21) and ν_1 is actually an integral over the continuous energy states.

The radial dependence in the radial matrix element is given by the functions:

$$F_0(r) = \frac{5\sqrt{\pi}}{2R_0^3}\left[1 - \left(\frac{r}{R_0}\right)^2\right]\Theta(R_0 - r),\ L = 0, \tag{7.26}$$

and,

$$F_L(r) = \frac{4\pi}{(2L+1)R_0^L}\left(\frac{r^L}{R_0^{L+1}}\Theta(R_0 - r) + \frac{R_0^L}{r^{L+1}}\Theta(r - R_0)\right),\ L \geqslant 1. \tag{7.27}$$

The form of the equations reflects the sharp surface approximations that were used in the derivation of the expressions for the nuclear transition charge densities [71]. A hard-sphere extended nuclear charge model of the nucleus was used with a radius R_0 given by $R_0 = 1.2A^{1/3}$ (fm). Again, it should be pointed out that the uncertainties in the nuclear transition parameters completely dominate the discrepancies caused by slightly different nuclear models.

As indicated above, the main contribution to the energy integral comes from the high-energy region. The reason for this can be deduced from the surface character of the effective interaction given in equation (7.17). The function $F_L(r)$ has a sharp peak near the value of the nuclear radius, R_0, thus the bound electron must have a sufficiently high energy to penetrate to the surface of the nucleus. Furthermore, for the $j = 1/2$ electronic states and for the $L \geqslant 2$ multipole excitations, the intermediate state electron energies turn out to be larger than typical nuclear excitation energies. This means that one can neglect E_L in the denominator of equation (7.24), and use a simpler expression for the evaluation of the NP correction.

Analytical Form

For electron states with $j = 1/2$ and for nuclear excitations with $L \geqslant 2$, Labzowsky and Nefiodov [50] have derived an analytical form for the nuclear polarization correction. This is possible because the energies of the intermediate electron states tend to be larger than typical nuclear excitation energies, thus if one considers equation (7.25),

$$\Delta E_{\nu lj} = -2\pi B(EL)\frac{\alpha(\alpha Z)^2 C_{\nu lj}}{(2L+1)R_0^{2L}}\left(\frac{2Z}{Na_0}R_0\right)^{2\gamma} \times \sum_{j_1}(2j_1+1)\begin{pmatrix} j_1 & j & L \\ 1/2 & -1/2 & 0 \end{pmatrix}^2 R_{j_1},\ L \geqslant 2, \tag{7.28}$$

where

$$R_{j_1} = \frac{1}{\mu(\gamma+\mu+L+1)} \times \left(\frac{1}{\gamma+L+1}+\frac{2}{\mu-\gamma+L}\right) + \frac{1}{\mu(\gamma+\mu-L)}\left(\frac{2}{\gamma-\mu-L}+\frac{1}{L-\gamma}\right), \tag{7.29}$$

$$C_{\nu lj} = [n_r^2 - 2\epsilon n_r(N=\kappa) + (N-\kappa)^2] \times \frac{\Gamma(2\gamma+n_r+1)}{\Gamma^2(2\gamma+1)N^2(N=\kappa)n_r!}. \tag{7.30}$$

Here, specifically,

$$N = \sqrt{(n_r+\gamma)^2+(\alpha Z)^2} \tag{7.31a}$$

$$\gamma = \sqrt{\kappa^2-(\alpha Z)^2} \tag{7.31b}$$

$$\kappa = (j+1/2)(-1)^{j+l+1/2} \tag{7.31c}$$

$$n = n_r + |\kappa \tag{7.31d}$$

$$\mu = \sqrt{(j'+1/2)^2-(\alpha Z)^2} \tag{7.31e}$$

In (7.28), a_0 is the Bohr radius, while in (7.30), E_{nj} is the Sommerfeld energy, as given in equation (2.47) [58, 50]. The matrix elements, corresponding to those given

in (7.25), are evaluated with point-nucleus Dirac-electron wave functions and are expanded in a series in powers of ZR_0/a_0 and only the leading term has been retained.

7.3.2 Calculations

To evaluate the nuclear polarization correction we apply equation (7.25) above, using nuclear data for the B-coefficients as given in the tables of Angeli [2], [3] and [4]. The most subtle part of the calculation is that an integration over all virtual continuum states is required. Several possible strategies can be employed, but in this thesis the method of using B-splines to generate a pseudo-spectrum of bound and continuum states was employed. The details of generating the spectrum itself has been placed in Appendix C so as not to interrupt the flow of the discussion. The interested reader can refer there.

For the case of Giant Dipole Resonance (GDR) states, the B-values are estimated via the phenomenological energy-weighted sum rules [71, 62],

$$\langle \omega_0 \rangle \, B(E0) = \frac{25}{4\pi} \frac{Ze^2}{M_p} \left\langle r_p^2 \right\rangle \left(\frac{Z}{A}(1-\tau) + \frac{N}{A}\tau \right), \; L = 0,$$

$$\langle \omega_L \rangle \, B(EL) = \frac{L(2L+1)}{4\pi} \frac{Ze^2}{2M_p} \left\langle r_p^{2L-2} \right\rangle \left(\frac{Z}{A}(1-\tau) + \frac{N}{A}\tau \right), \; L > 0. \tag{7.32}$$

The GDR states are assumed to be single resonant states for each $L\tau$ with the excitation energies given by,

$$\begin{aligned} \langle \omega_L(\tau) \rangle &= [100(1-\tau) + 200\tau](1 - A^{-1/3})A^{-1/3}, \; L = 0, \\ &= 95(1 - A^{-1/3})A^{-1/3}, \; L = 1, \\ &= [75(1-\tau) + 160\tau](1 - A^{-1/3})A^{-1/3}, \; L \geq 2, \end{aligned} \tag{7.33}$$

where M_p denotes the proton mass, τ is the excitation isospin, and $N = A - Z$ is the number of neutrons. The expectation value for protons, $\left\langle r_p^{2L-2} \right\rangle$, in (7.32) is

estimated as,

$$\left\langle r_p^{2L-2} \right\rangle = \frac{3R_0^{2L-2}}{2L+1}, \tag{7.34}$$

, where, again, R_0 is the nuclear charge radius.

The analytical form of the energy, equation (7.28), was used in its range of applicability, that is when the atomic state is $j = 1/2$ and the nuclear state is $L \geqslant 2$. This was done to speed up the entire calculation. Furthermore, states of $j = 3/2$ were not calculated as their contribution would be very small, well within the uncertainty from the nuclear parameters. Below are listed tables for the results of the nuclear polarization correction for $Z = 82 - 92$ for both experimental and GDR states. The sum of all the contributions is quoted, and an uncertainty of 50% of the results is attached to take into account the uncertainty in the nuclear parameters. Many of the elements, because they are unstable, do not have experimentally determined parameters to use. For these cases only the GDR cases are considered and thus an uncertainty of 100% is ascribed to these cases to take into account both the uncertainty in the nuclear parameters and the missing experimental information.

Lead

Table 7.4: Experimental energy states for lead (Z = 82; A = 208)

ω(MeV)	B(E,L)	L	$2s_{1/2}$(eV)	$2p_{1/2}$(eV)
2.615	0.087	3	-0.00014	-0.00001
4.085	0.064	2	-0.00025	-0.00002
5.240	0.019	3	-0.00003	0
6.193	0.010	2	-0.00004	0
		Total	-0.00046	-0.00003

Table 7.5: GBR states for lead (Z = 82; A = 208)

ω (MeV)	B(E,L)	L	τ	$2s_{1/2}$(eV)	$2p_{1/2}$(eV)
10.5218	0.154	2	0	-0.00061	-0.00005
10.5218	0.117	3	0	-0.00019	-0.00002
13.3277	0.120	1	0	-0.00211	-0.00018
14.0291	0.577	0	0	-0.00078	-0.00006
22.4466	0.111	2	1	-0.00044	-0.00004
22.4466	0.084	3	1	-0.00015	-0.00001
28.0582	0.443	0	1	-0.00044	-0.00004
			Total	-0.00472	-0.0004

Bismuth

Table 7.6: Experimental energy states for bismuth (Z = 83; A = 209)

ω(MeV)	B(E,L)	L	$2s_{1/2}$(eV)	$2p_{1/2}$(eV)
0.896	0.003	2	-0.00001	0
1.609	0.052	3	-0.00009	0
2.443	0.014	3	-0.00002	0
2.493	0.147	3	-0.00023	-0.00002
2.6	0.0134	3	-0.00002	0
2.601	0.0154	3	-0.00002	0
2.741	0.011	3	-0.00002	0
		Total	-0.00041	-0.00002

Table 7.7: GDR states for bismuth (Z = 83; A = 209)

ω (MeV)	B(E,L)	L	τ	$2s_{1/2}$(eV)	$2p_{1/2}$(eV)
10.5084	0.158	2	0	-0.00069	-0.00006
10.5084	0.12	3	0	-0.00021	-0.00002
13.3107	0.123	1	0	-0.00236	-0.0002
14.0112	0.591	0	0	-0.0009	-0.00008
22.418	0.112	2	1	-0.00049	-0.00004
22.418	0.085	3	1	-0.00015	-0.00001
28.0225	0.449	0	1	-0.0005	-0.00004
			Total	-0.0053	-0.00045

Polonium

Table 7.8: Experimental energy states for polonium (Z = 84; A = 209)

ω(MeV)	B(E,L)	L	$2s_{1/2}$(eV)	$2p_{1/2}$(eV)
0.545	0.016	2	-0.00008	0
1.418	0.032	2	-0.00015	-0.00001
1.473	0.011	2	-0.00005	0
1.522	0.110	2	-0.00049	-0.00004
2.770	0.027	3	-0.00005	0
		Total	-0.00082	-0.00005

Table 7.9: GDR states for polonium (Z = 84; A = 209)

ω (MeV)	B(E,L)	L	τ	$2s_{1/2}$(eV)	$2p_{1/2}$(eV)
10.5084	0.161	2	0	-0.00078	-0.00007
10.5084	0.123	3	0	-0.00024	-0.00002
13.3107	0.126	1	0	-0.00265	-0.00024
14.0112	0.605	0	0	-0.00103	-0.00009
22.418	0.113	2	1	-0.00054	-0.00005
22.418	0.086	3	1	-0.00017	-0.00001
28.0225	0.450	0	1	-0.00056	-0.00005
			Total	-0.00597	-0.00053

Astatine

Table 7.10: Experimental energy states for astatine (Z = 85; A = 210)

ω(MeV)	B(E,L)	L	$2s_{1/2}$(eV)	$2p_{1/2}$(eV)
1.363	0.022	2	-0.00012	-0.00001
2.550	0.134	3	-0.00028	-0.00003
4.028	0.227	3	-0.00048	-0.00004
		Total	-0.00088	-0.00008

Table 7.11: GDR states for astatine (Z = 85; A = 210)

ω (MeV)	B(E,L)	L	τ	$2s_{1/2}$(eV)	$2p_{1/2}$(eV)
10.4951	0.165	2	0	-0.00087	-0.00008
10.4951	0.126	3	0	-0.00027	-0.00002
13.2938	0.128	1	0	-0.00296	-0.00027
13.9935	0.620	0	0	-0.00118	-0.00011
22.3896	0.114	2	1	-0.00060	-0.00006
22.3896	0.087	3	1	-0.00018	-0.00002
27.9869	0.456	0	1	-0.00063	-0.00006
			Total	-0.0067	-0.00062

Radon

Table 7.12: Experimental energy states for radon (Z = 86; A = 222)

ω(MeV)	B(E,L)	L	$2s_{1/2}$(eV)	$2p_{1/2}$(eV)
0.186	0.463	2	-0.00259	-0.00025
		Total	-0.00259	-0.00025

Table 7.13: GDR states for radon (Z = 86; A = 222)

ω (MeV)	B(E,L)	L	τ	$2s_{1/2}$(eV)	$2p_{1/2}$(eV)
10.3407	0.169	2	0	-0.00094	-0.00009
10.3407	0.133	3	0	-0.00029	-0.00003
13.0983	0.126	1	0	-0.00316	-0.00030
13.7876	0.632	0	0	-0.00129	-0.00012
22.0602	0.125	2	1	-0.00070	-0.00007
22.0602	0.099	3	1	-0.00021	-0.00002
27.5753	0.500	0	1	-0.00074	-0.00007
			Total	-0.0073	-0.0007

Francium

Table 7.14: Experimental energy states for francium (Z = 87; A = 223)

No experimental B's available

Table 7.15: GDR states for francium (Z = 87; A = 223)

ω (MeV)	B(E,L)	L	τ	$2s_{1/2}$(eV)	$2p_{1/2}$(eV)
10.3283	0.172	2	0	-0.00106	-0.00010
10.3283	0.134	3	0	-0.00033	-0.00003
13.0825	0.129	1	0	-0.00353	-0.00035
13.7711	0.647	0	0	-0.00148	-0.00014
22.0337	0.126	2	1	-0.00078	-0.00008
22.0337	0.100	3	1	-0.00024	-0.00002
27.5422	0.505	0	1	-0.00084	-0.00008
			Total	-0.00826	-0.0008

Radium

Table 7.16: Experimental energy states for radium (Z = 88; A = 226)

ω(MeV)	B(E,L)	L	$2s_{1/2}$(eV)	$2p_{1/2}$(eV)
0.896	0.003	2	-0.00001	0
1.609	0.052	3	-0.00009	0
2.443	0.014	3	-0.00002	0
2.493	0.147	3	-0.00023	-0.00002
2.6	0.0134	3	-0.00002	0
2.601	0.0154	3	-0.00002	0
2.741	0.011	3	-0.00002	0
		Total	-0.00041	-0.00002

Table 7.17: GDR states for radium (Z = 88; A = 226)

ω (MeV)	B(E,L)	L	τ	$2s_{1/2}$(eV)	$2p_{1/2}$(eV)
10.2914	0.176	2	0	-0.00119	-0.00012
10.2914	0.141	3	0	-0.00037	-0.00004
13.0358	0.130	1	0	-0.00391	-0.000397
13.7219	0.661	0	0	-0.00168	-0.00017
21.9551	0.130	2	1	-0.00037	-0.00004
21.9551	0.104	3	1	-0.00027	-0.00003
27.4438	0.518	0	1	-0.00096	-0.000096
			Total	-0.00875	-0.00089

Actinium

Table 7.18: Experimental energy states for actinium (Z = 89; A = 227)

No experimental B's available

Table 7.19: GDR states for actinium (Z = 89; A = 227)

ω (MeV)	B(E,L)	L	τ	$2s_{1/2}$(eV)	$2p_{1/2}$(eV)
10.2793	0.180	2	0	-0.00134	-0.00014
10.2793	0.145	3	0	-0.00041	-0.00004
13.0204	0.133	1	0	-0.00438	-0.000458
13.7057	0.676	0	0	-0.00193	-0.000198
21.9291	0.131	2	1	-0.00098	-0.00010
21.9291	0.105	3	1	-0.00030	-0.00003
27.4114	0.524	0	1	-0.00108	-0.00011
			Total	-0.0104	-0.00108

Thorium

Table 7.20: Experimental energy states for thorium (Z = 90; A = 232

ω(MeV)	B(E,L)	L	$2s_{1/2}$(eV)	$2p_{1/2}$(eV)
0.0494	1.840	2	-0.0149	-0.0016
0.7742	0.017	2	-0.0001	-0.00001
0.785	0.029	2	-0.0002	-0.00003
1.106	0.037	3	-0.0001	-0.00001
1.327	0.001	2	-0.0000	-0.0000
1.387	0.002	2	-0.0000	-0.0000
1.553	0.006	2	-0.0000	-0.0000
		Total	-0.0153	-0.00165

Table 7.21: GDR states for thorium (Z = 90; A = 232)

ω (MeV)	B(E,L)	L	τ	$2s_{1/2}$(eV)	$2p_{1/2}$(eV)
10.2194	0.184	2	0	-0.00145	-0.000161
10.2194	0.150	3	0	-0.00046	-0.0000495
12.9445	0.134	1	0	-0.00482	-0.00052
13.6258	0.690	0	0	-0.00218	-0.0002314
21.8013	0.136	2	1	-0.00110	-0.000119
21.8013	0.111	3	1	-0.00034	-0.000037
27.2516	0.544	0	1	-0.00124	-0.000132
			Total	-0.0112	-0.00125

Proactinium

Table 7.22: Experimental energy states for proactinium (Z = 91; A = 231

ω(MeV)	B(E,L)	L	$2s_{1/2}$(eV)	$2p_{1/2}$(eV)
0.0586	1.87	2	-0.01682	-0.00187
		Total	-0.01682	-0.00187

Table 7.23: GDR states for proactinium (Z = 91; A = 231)

ω (MeV)	B(E,L)	L	τ	$2s_{1/2}$(eV)	$2p_{1/2}$(eV)
10.2312	0.188	2	0	-0.00169	-0.000161
10.2312	0.153	3	0	-0.00052	-0.0000495
12.9595	0.137	1	0	-0.00550	-0.00052
13.6416	0.706	0	0	-0.00253	-0.0002314
21.8266	0.136	2	1	-0.00122	-0.000119
21.8266	0.110	3	1	-0.00038	-0.000037
27.2833	0.543	0	1	-0.00140	-0.000132
			Total	-0.0112	-0.00125

Uranium

Table 7.24: Experimental energy states for uranium (Z = 92; A = 238)

ω(MeV)	B(E,L)	L	$2s_{1/2}$(eV)	$2p_{1/2}$(eV)
0.0449	2.46	2	-0.02392	-0.00274
0.732	0.082	3	-0.0003	-0.00003
0.967	0.003	2	-0.00003	0
0.998	0.029	3	-0.00011	-0.00001
1.037	0.013	2	-0.00013	-0.00001
1.06	0.026	2	-0.00025	-0.00003
1.17	0.023	3	-0.00008	0
1.224	0.004	2	-0.00004	0
		Total	-0.02486	-0.00282

Table 7.25: GDR states for uranium (Z = 92; A = 238)

ω(MeV)	B(E,L)	L	τ	$2s_{1/2}$(eV)	$2p_{1/2}$(eV)
10.149	0.192	2	0	-0.00187	-0.00021
10.149	0.159	3	0	-0.00058	-0.00058
12.856	0.218	1	0	-0.00944	-0.00108
13.533	0.721	0	0	-0.00284	-0.00032
21.652	0.143	2	1	-0.00139	-0.00139
21.652	0.119	3	1	-0.00043	-0.00005
27.065	0.572	0	1	-0.00162	-0.00018
			Total	-0.0182	-0.00381

Chapter 8

Extracting the Nuclear Charge Radius

8.1 Introduction

In this penultimate chapter, the results of the use of the method outlined in the previous chapters will be discussed. Mathematica is a functional programming language that stresses symbolic manipulation as well as numerical evaluation. By treating any input (numbers, arrays, characters, entire functions) in the same way, as a "pattern", the user is able to write powerful programs with very few lines of code. Excellent resources exist for novice users to get their feet wet with the language [88, 53, 86]. A Mathematica package was constructed, to bring together in one place all the necessary tools, allowing a user in just a few lines to generate energies as a function of variable nuclear charge radius. Because these tools were themselves written as Mathematica functions, they can be combined with existing built-in functions and display utilities to quickly generate plots showing the relationship between the energy and charge radius. A summary of the Mathematica package listing all the pieces is given in Appendix 2 for convenience.

A brief description of the algorithm used will now be given:

(a) Select an appropriate range to vary the nuclear charge radius over for a particular ion. In general, the uncertainty in the current best value for the nuclear charge radius for a given ion was chosen to be the range [4]. We want this range to be small to aid in step (d) below.

(b) In increments of 0.01 fm, calculate all the contributions to the particular transition energy for the chosen range.

(c) Fit a model to the resultant points calculated in part b) to obtain a model of the transition energy as a function of charge radius. As shown in the Introduction, perturbation theory says that the transition energy depends on the square of the charge radius. However, if we make our observation window small enough, we will be able to use a linear which is easy to work with.

(d) Because the resultant slope is non-zero, invert the linear model to obtain an expression for the charge radius as a function of transition energy.

8.1.1 Can we use a linear fit in our analysis?

In this subsection we will lay out the argument that we can get away with using a linear interpolation to the calculated points using the charge radius uncertainties as observation windows. We will use rough but realistic values for our input parameters.

We know from equation (1.13) in the Introduction that the ultimate dependence of the transition energy on nuclear charge radius is quadratic. For simplicity, assume the dependence to be of the form:

$$|\Delta E| = AR^2, \tag{8.1}$$

in reality the dependence is negative, but for our purposes that does not matter. From our evaluations in Chapter 3, we know that a nuclear charge radius of 5 fm leads to a correction of approximately 20 eV:

$$R \approx 5 \text{ fm} \mapsto \Delta E \approx 20 \text{ eV}. \tag{8.2}$$

Using this information we can extract an approximate value for A:

$$\Delta E(5 \text{ fm}) = A \cdot 25 \text{ fm}^2 \approx 20 \text{ eV}, \tag{8.3}$$

thus,

$$A = \frac{20 \text{ eV}}{25 \text{ fm}^2} \approx 1\text{eV/fm}^2. \tag{8.4}$$

Now that we have the functional form of $\Delta E(R)$ in hand, we can investigate our proposal of looking at a small charge radius window around the nominal value for the isotope by expanding equation (8.1) in a Taylor series and evaluating it at the nominal charge radius value R_0:

$$E(R)|_{R_0} = E(R_0) + (R - R_0)\frac{dE}{dR}\bigg|_{R_0} + \frac{(R - R_0)^2}{2!}\frac{d^2E}{dR^2}\bigg|_{R_0}, \tag{8.5}$$

where,

$$\frac{dE}{dR} = 2AR, \quad \text{and} \quad \frac{d^2E}{dR^2} = 2A. \tag{8.6}$$

We can now consider the linear and quadratic terms in turn to see how much they will contribute to the energy.

The linear term

We begin by making a notational simplification: $\delta R = R - R_0$. Thus the linear term can be expressed as

$$\frac{\delta R}{R_0} \cdot R_0 \cdot 2AR_0. \tag{8.7}$$

If we take a 1% window of R, the width of the typical uncertainty in the nominal radius value, then $\delta R/R = 0.01$, and make the substitutions for the other values, we obtain

$$\frac{\delta R}{R_0} \cdot R_0 \cdot 2AR_0 = 0.02 \cdot 1 \ \frac{\text{eV}}{\text{fm}^2} \cdot 25 \text{ fm}^2 = 0.5 \text{ eV}. \tag{8.8}$$

This result is way above the theoretical and experimental uncertainties ($0.01-0.1$eV), and so must be included in our analysis.

The quadratic term

Performing a similar analysis on the quadratic term:

$$\frac{\delta R^2}{2R_0^2} \cdot R_0 \cdot 2AR_0^2, \tag{8.9}$$

and taking a 1% window again leads to:

$$\frac{\delta R^2}{2R_0^2} \cdot R_0 \cdot 2AR_0^2 = \frac{10^{-4}}{2} \cdot 2 \ \frac{\text{eV}}{\text{fm}^2} \cdot 25 \ \text{fm}^2 = 0.0025 \ \text{eV}. \tag{8.10}$$

This result, unlike the linear term above, is well below the theoretical and experimental uncertainties ($0.01 - 0.1$eV), and thus we are justified in dropping this term from our analysis.

8.2 On the use of the NRadius Package

The NRadius package was used to generate plots of transition energy as a function of varying charge radius for Li-like ions of bismuth to uranium (Z=83-92). In the cases of Bi and U, accurate spectroscopic data exists for the $2s - 2p_{3/2}$ transition in Bi [15] and the $2s - 2p_{1/2}$ transition in U [14]. This allows us to actually extract the nuclear charge radius in these cases. The ultimate goal however is francium, where as yet, spectroscopic data does not exist. All atoms between lead (Z = 82) and uranium (Z = 92) were looked at, and the resulting graphs and radius equations are gathered below, after the cases of Bi and U, in this chapter.

8.2.1 Bismuth (A = 209)

The first case that we will consider is the $2p_{3/2} - 2s$ transition in bismuth; chosen because experimental spectroscopic information is available via the work of Beiersdorfer et al. [15]. Thus, the first step is to select a range of r_{rms} over which to perform

the analysis; for Bi, the range chosen was $5.50 - 5.55$ fm. Below, Table 8.1 shows the results of the the first-order contributions to the transition energy:

Table 8.1: First-order contributions to the transition energy for Bi in eV.

R (fm)	Dirac	PE	QED
5.50	2792.29	23.814	-27.4865
5.51	2792.25	23.816	-27.4862
5.52	2792.21	23.818	-27.4860
5.53	2792.17	23.820	-27.4858
5.54	2792.14	23.822	-27.4856
5.55	2792.10	23.824	-27.4853

The second-order and other processes do not shift with varying the nuclear charge radius, thus their value was calculated once for the particular transition, Table 8.2:

Table 8.2: Second-order contributions to the transition energy for Bi in eV.

Second-order PE	-1.608
Third-order PE	-0.02
Second-order QED	0.12
Screened QED	1.148
Nuclear Recoil	-0.066
Nuclear Polarization	0.005

This information can be combined as points on an radius energy plane, and can subsequently be plotted, as shown in figure 8.1.

Table 8.3: Points for $2p_{3/2} - 2s$ transition in Bi.

R(fm)	E (eV)
5.5	2788.19
5.51	2788.16
5.52	2788.12
5.53	2788.09
5.54	2788.05
5.55	2788.02

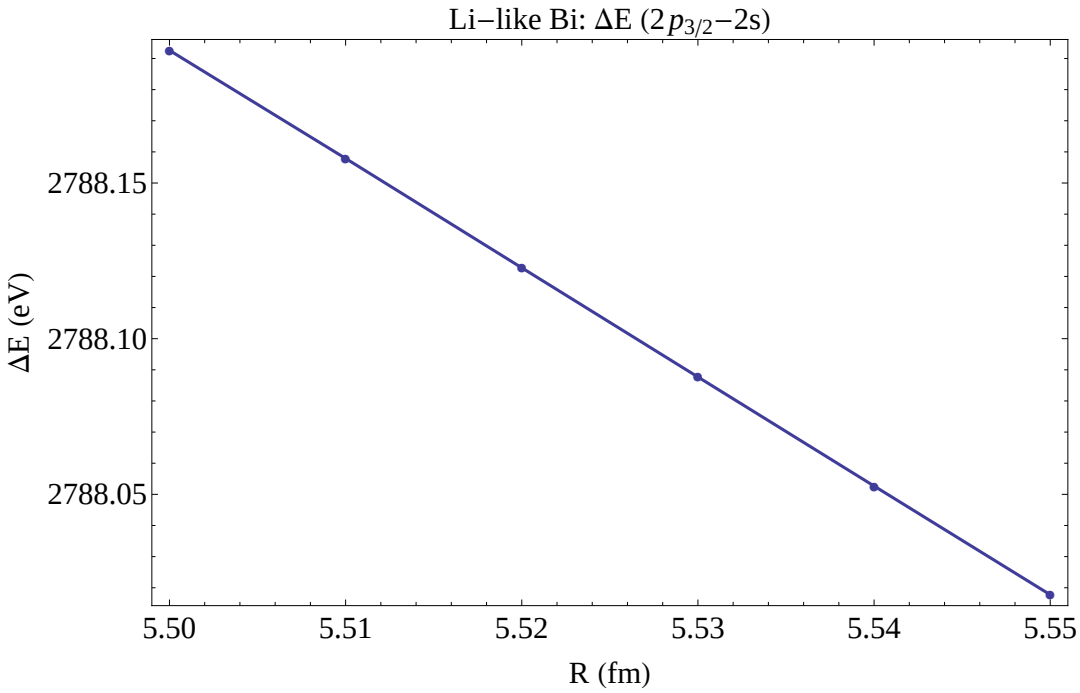

Figure 8.1: Energy variation vs. nuclear charge radius for $2p_{3/2} - 2s$ transition in Bi.

From this, we can perform a linear fit on the data using Mathematica's LinearModelFit function to extract a relationship between the transition energy and the nuclear charge radius. This was performed on the bismuth data, with following equation obtained:

$$\Delta E \text{ (eV)} = 2807.44 - 3.500\ r_{rms} \tag{8.11}$$

where r has units of (fm). To get an idea of how accurate our model is, we can calculate the residuals between the model and the data (Figure 8.2). Thus we see that at most the deviation from the model is 0.00015 eV, well below the accuracy goal of the method. It should be noted here that uncertainty in the calculations, particularly coming from the second-order and higher contributions, are not taken into account during the model building step but combined with the experimental energy uncertainties to obtain an uncertainty in the r_{rms} from the model at the end, (see below).

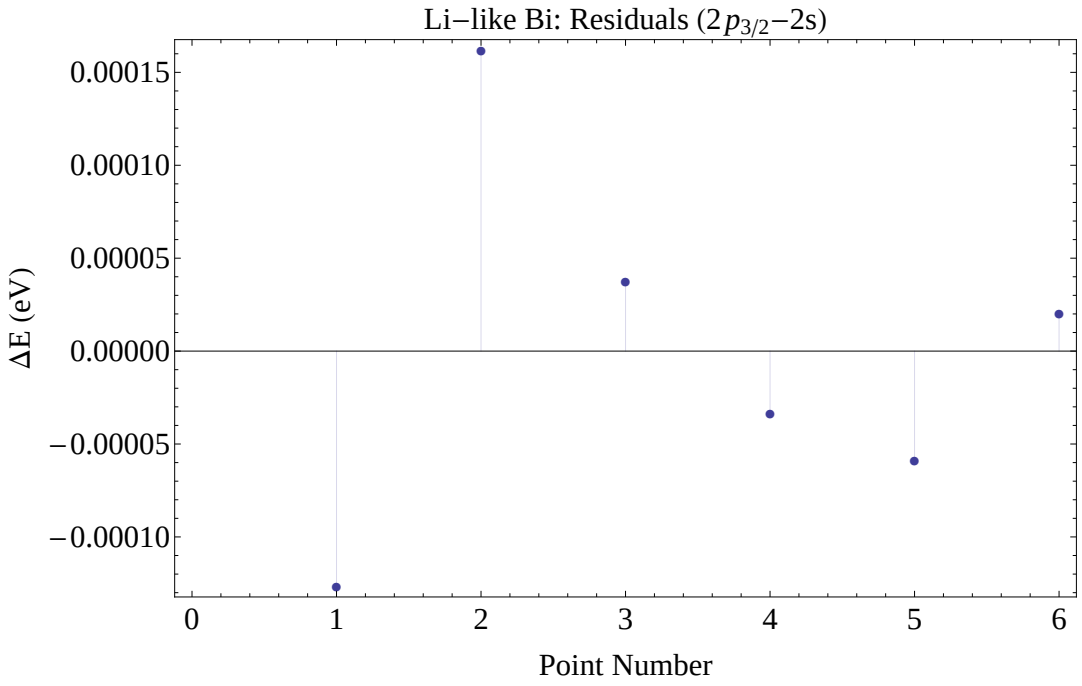

Figure 8.2: Residuals of the model for $2p_{3/2} - 2s$ transition in Bi.

The linear model has a non-zero slope, meaning that it can be inverted to give a phenomenological description of the variation of the nuclear charge radius as a function of the transition energy:

$$r_{rms} = 802.117 - 0.2857E \tag{8.12}$$

where the units of E is (eV) and r_{rms} is (fm). We can also obtain an expression for the uncertainty in r_{rms} via the derivative of the above equation:

$$\Delta r_{rms} = |\frac{\partial r_{rms}}{\partial E}|\Delta E = 0.2857\Delta E \tag{8.13}$$

With all this in place, we can obtain a value for the nuclear charge radius for bismuth using the spectroscopic data of Beiersdorfer et al. [15]. They measure a transition energy of 2788.14(4) eV. The total uncertainty in ΔE can be obtained from combining, in quadrature, the experimental uncertainty together with the theoretical uncertainty from the calculation, 0.07 eV [92], giving a final value for the charge

radius to be:

$$r_{rms} = 5.515(23) \text{ fm} \tag{8.14}$$

This compares very favourably with the current best experimental determination of 5.521(3) fm for bismuth [4].

8.2.2 Uranium (A = 238)

The second case that we will consider is the $2p_{1/2} - 2s$ transition in uranium; with experimental spectroscopic information is available Beiersdorfer et al. [14].

Table 8.4: First-order contributions to the transition energy for U in eV.

R (fm)	Dirac	PE	QED
5.82	-33.0164	368.822	-42.9312
5.83	-33.0991	368.826	-42.9306
5.84	-33.1818	368.829	-42.9300
5.85	-33.2646	368.831	-42.9295
5.86	-33.3473	368.834	-42.9289
5.87	-33.4303	368.836	-42.9283

The second-order and other processes do not shift with varying the nuclear charge radius, thus their value was calculated once for the particular transition, table 8.5.

Table 8.5: Second-order contributions to the transition energy for U in eV.

Second-order PE	-13.372
Third-order PE	0.147
Second-order QED	0.222
Screened QED	1.165
Nuclear Recoil	-0.071
Nuclear Polarization	0.038

This information can also be combined as points on an radius energy plane:

From this, we can perform a linear fit on the data using Mathematica's Linear-ModelFit function to extract a relationship between the transition energy and the

Table 8.6: Points for $2p_{1/2} - 2s$ transition in U.

R (fm)	E (eV)
5.82	281.003
5.83	280.924
5.84	280.845
5.85	280.766
5.86	280.686
5.87	280.607

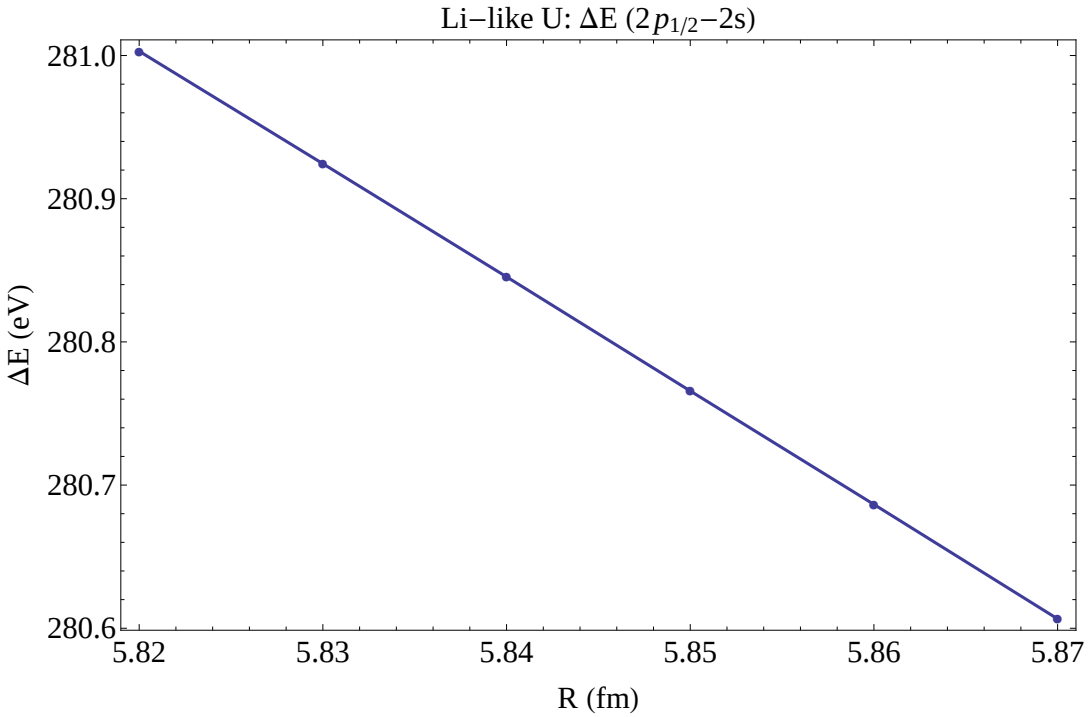

Figure 8.3: Energy variation vs. nuclear charge radius for $2p_{1/2} - 2s$ transition in U.

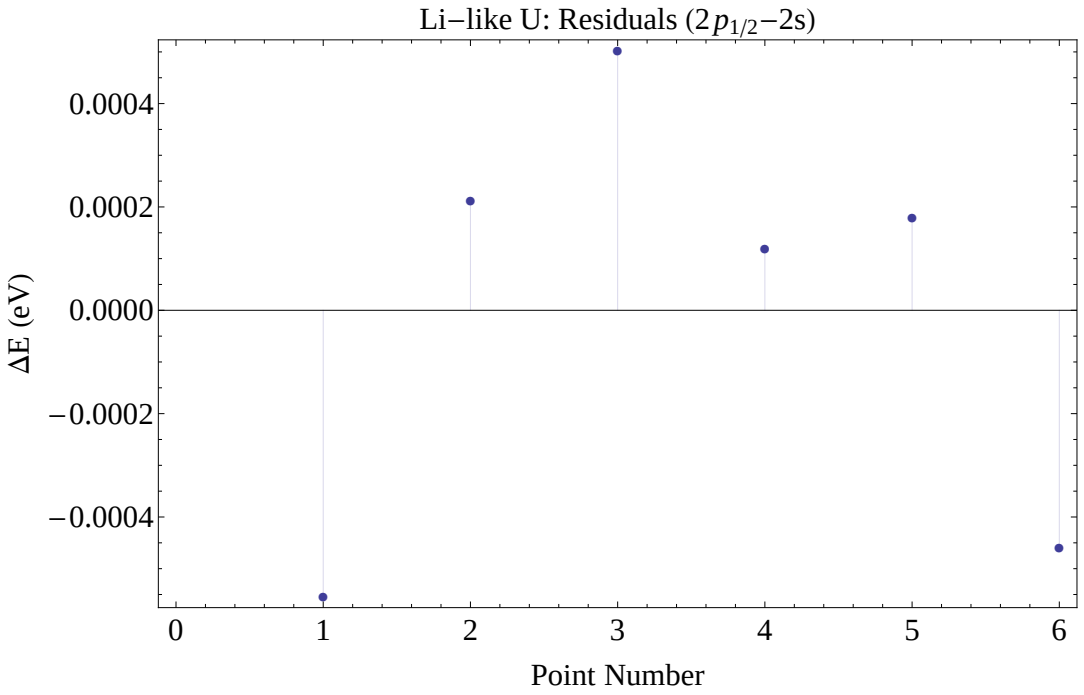

Figure 8.4: Residuals of the model for $2p_{1/2} - 2s$ transition in U

nuclear charge radius. This was performed on the bismuth data, with following equation obtained:

$$E = 327.162 - 7.931\ r_{rms} \tag{8.15}$$

To get an idea of how accurate our model is, we can calculate the residuals between the model and the data:

Thus we see that

Again, the above linear model has a non-zero slope, meaning that it can be inverted to give a phenomenological description of the variation of the nuclear charge radius as a function of the transition energy:

$$r_{rms} = 41.251 - 0.1261E \tag{8.16}$$

We can also obtain an expression for the uncertainty in r_{rms} via the derivative of the above equation:

$$\Delta r_{rms} = |\frac{\partial r_{rms}}{\partial E}|\Delta E = 0.1261\Delta E. \tag{8.17}$$

With all this in place, we can obtain a value for the nuclear charge radius for uranium using the spectroscopic data of Beiersdorfer et al. [14]. They measure a transition energy of 280.645(15) eV. The total uncertainty in ΔE can be obtained from combining, in quadrature, the experimental uncertainty together with the theoretical uncertainty, 0.14 eV [92], giving a final value for the charge radius to be:

$$r_{rms} = 5.865(18) \text{ fm}. \tag{8.18}$$

This again, compares very favourably with the current estimate of 5.851(7) fm [4].

8.3 The Remaining Cases

Having looked at the two elements where experimental data is actually available in order to explain and validate the method, in this section we will give the results for the remaining elements between $Z = 82 \rightarrow 92$. Of particular interest are the cases having no stable isotope. These cases will be indicated with a star. Furthermore, as a corollary, these cases lack experimental information for the nuclear polarization thus this contribution can only be based on Giant-Dipole Resonance (GDR) information thus introducing a large uncertainty into the calculation. For these cases, an uncertainty of 50% for the NP contribution will be used. The total theoretical uncertainty to the charge radius will be calculated by adding in quadrature the uncertainties to the higher-order contributions of the transition energies together with the nuclear polarization uncertainty, and then applying the uncertainty relations in each case. Thus the numerical uncertainty quoted in this section will be due to theoretical uncertainties only.

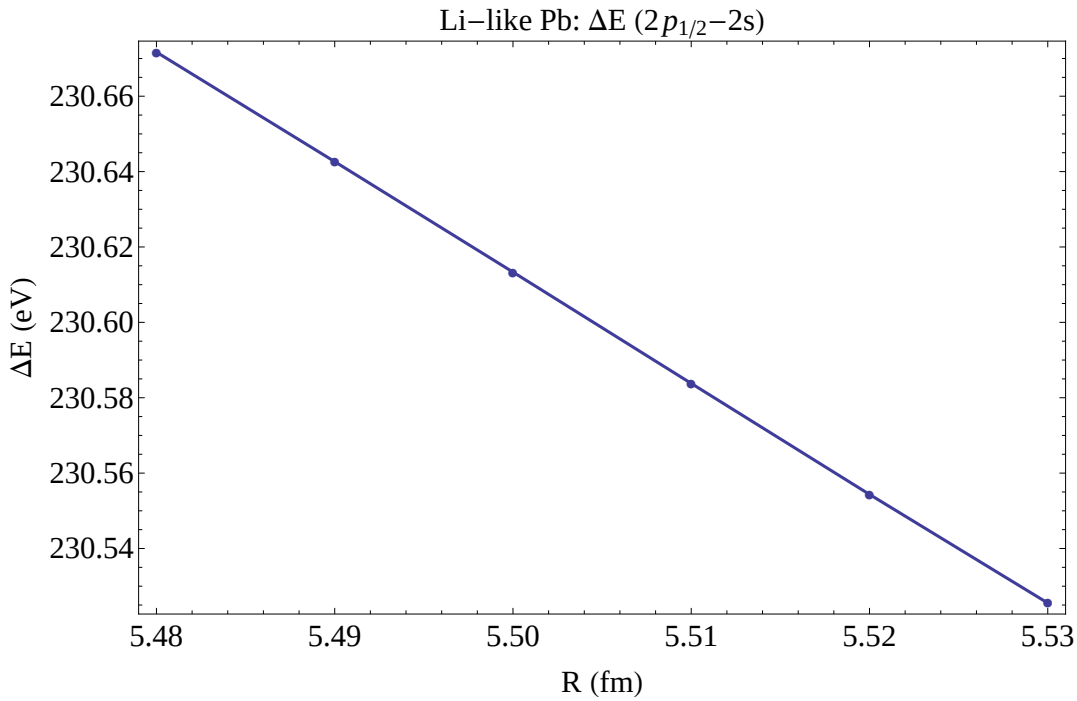

Figure 8.5: Energy variation vs. nuclear charge radius for $2p_{3/2} - 2s$ transition in Pb.

8.3.1 Lead (A = 208)

In this section we will produce the results for the $2p_{1/2} - 2s$ and $2p_{3/2} - 2s$ transitions for Li-like lead. The range chosen to vary the charge radius initially was $5.48 - 5.53$ fm, and the transition energy for each interval calculated. The results of these calculations for the $2p_{1/2} - 2s$ transition are shown in Table 8.7 and plotted in Figure 8.5.

Table 8.7: Points for $2p_{1/2} - 2s$ transition in Pb.

R (fm)	E (eV)
5.48	230.672
5.49	230.643
5.5	230.613
5.51	230.584
5.52	230.554
5.53	230.526

The model fit to the points is shown in (8.19),

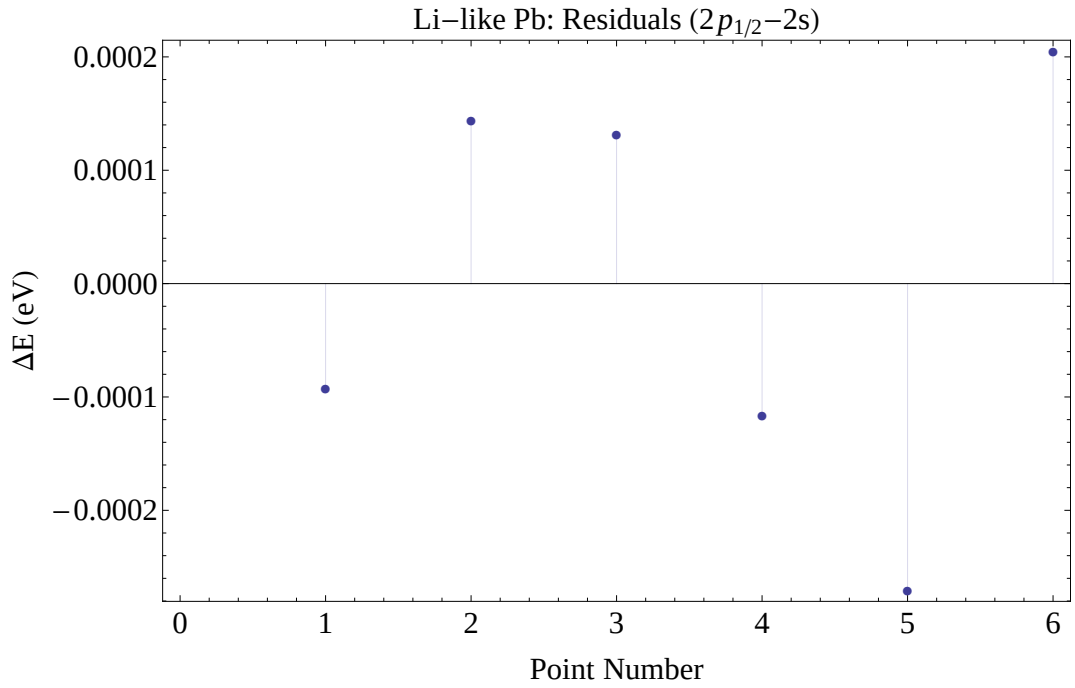

Figure 8.6: Residuals of the model for $2p_{1/2} - 2s$ transition in Pb.

$$E = 246.724 - 2.92917\ r_{rms}, \tag{8.19}$$

and the residuals of the model are shown in Figure 8.6. The model can be immediately inverted to obtain the relationship for the charge radius as a function of transition energy,

$$r_{rms} = 84.2298 - 0.3414E. \tag{8.20}$$

We can also obtain an expression for the uncertainty in r_{rms} via the derivative of the above equation:

$$\Delta r_{rms} = 0.3414\Delta E. \tag{8.21}$$

The theoretical uncertainty for the $2p_{1/2} - 2s$ transition of lead is $\Delta E = 0.101$ eV, leading to an uncertainty in the charge radius from theory to be:

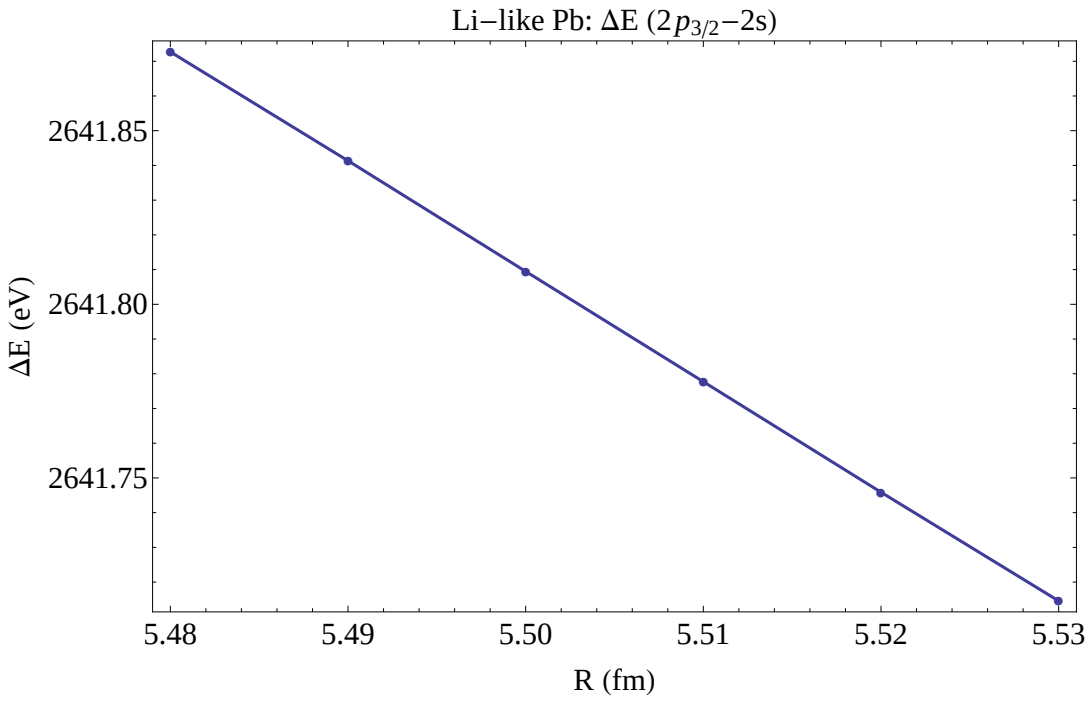

Figure 8.7: Energy variation vs. nuclear charge radius for $2p_{3/2} - 2s$ transition in Pb.

$$\Delta r_{rms}^{(theory)} = 0.034 \text{ fm}. \tag{8.22}$$

The results for the $2p_{3/2} - 2s$ transition are shown in Table 8.8, and graphed in figure 8.7.

Table 8.8: Points for $2p_{3/2} - 2s$ transition in Pb.

R (fm)	E (eV)
5.48	2641.87
5.49	2641.84
5.5	2641.81
5.51	2641.78
5.52	2641.75
5.53	2641.71

The model fit to the points is also shown in Figure 8.7 and the residuals of the model is shown in Figure 8.8.

The equation specifying the model is given as:

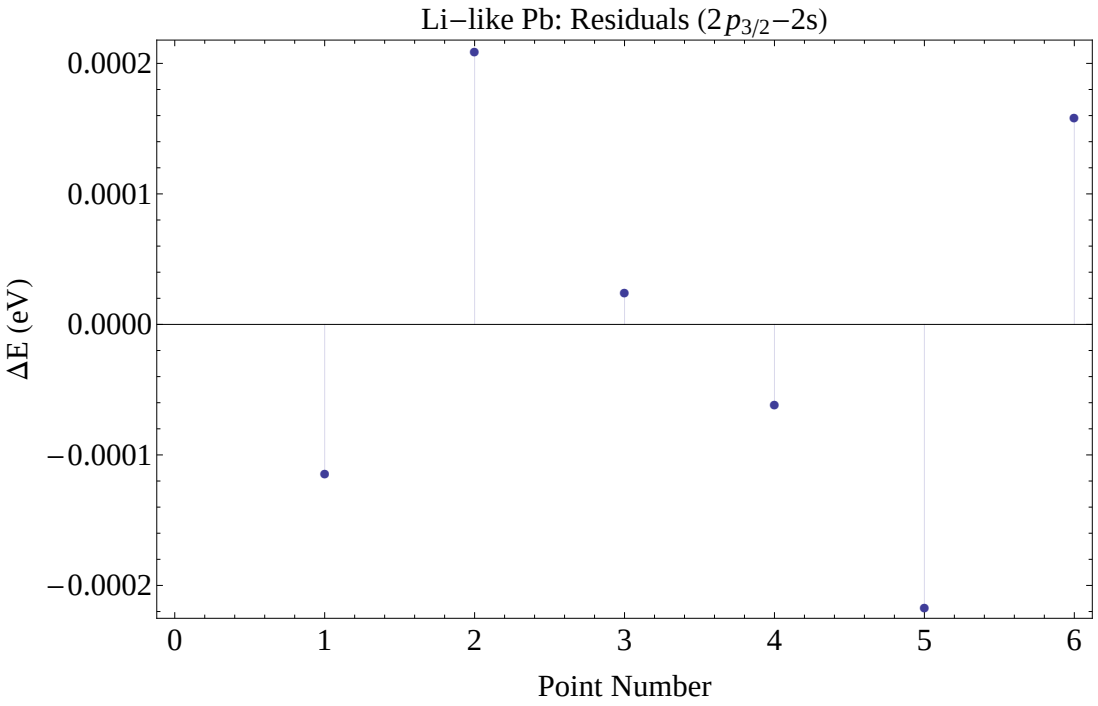

Figure 8.8: Residuals of the model for $2p_{3/2} - 2s$ transition in Pb.

$$E = 2659.23 - 3.1677\ r_{rms}, \tag{8.23}$$

which can be immediately inverted to obtain the relationship for the charge radius as a function of transition energy,

$$r_{rms} = 839.475 - 0.3157E. \tag{8.24}$$

We can also obtain an expression for the uncertainty in r_{rms} via the derivative of the above equation:

$$\Delta r_{rms} = 0.3157\Delta E. \tag{8.25}$$

The theoretical uncertainty for the $2p_{3/2} - 2s$ transition of lead is $\Delta E = 0.065$ eV, leading to an uncertainty in the charge radius from theory to be:

$$\Delta r_{rms}^{(theory)} = 0.021 \text{ fm}. \tag{8.26}$$

8.3.2 Bismuth (A = 209)

In this section we will produce the results for the $2p_{1/2} - 2s$ transition for Li-like bismuth. The range chosen to vary the charge radius initially was $5.48 - 5.53$ fm, and the transition energy for each interval calculated. The results of these calculations for the $2p_{1/2} - 2s$ transition are shown in Table 8.9.

Table 8.9: Points for $2p_{3/2} - 2s$ transition in Bi.

R (fm)	E (eV)
5.5	235.84
5.51	235.81
5.52	235.78
5.53	235.74
5.54	235.71
5.55	235.68

and can subsequently be plotted, as shown in Figure 8.9.

The model fit to the points is shown in (8.19),

$$E \text{ (eV)} = 253.624 - 3.23263 \; r_{rms} \tag{8.27}$$

and the residuals of the model are shown in Figure 8.6. The model can be immediately inverted to obtain the relationship for the charge radius as a function of transition energy,

$$r_{rms} = 78.458 - 0.309346E. \tag{8.28}$$

We can also obtain an expression for the uncertainty in r_{rms} via the derivative of the above equation:

$$\Delta r_{rms} = 0.3093 \Delta E. \tag{8.29}$$

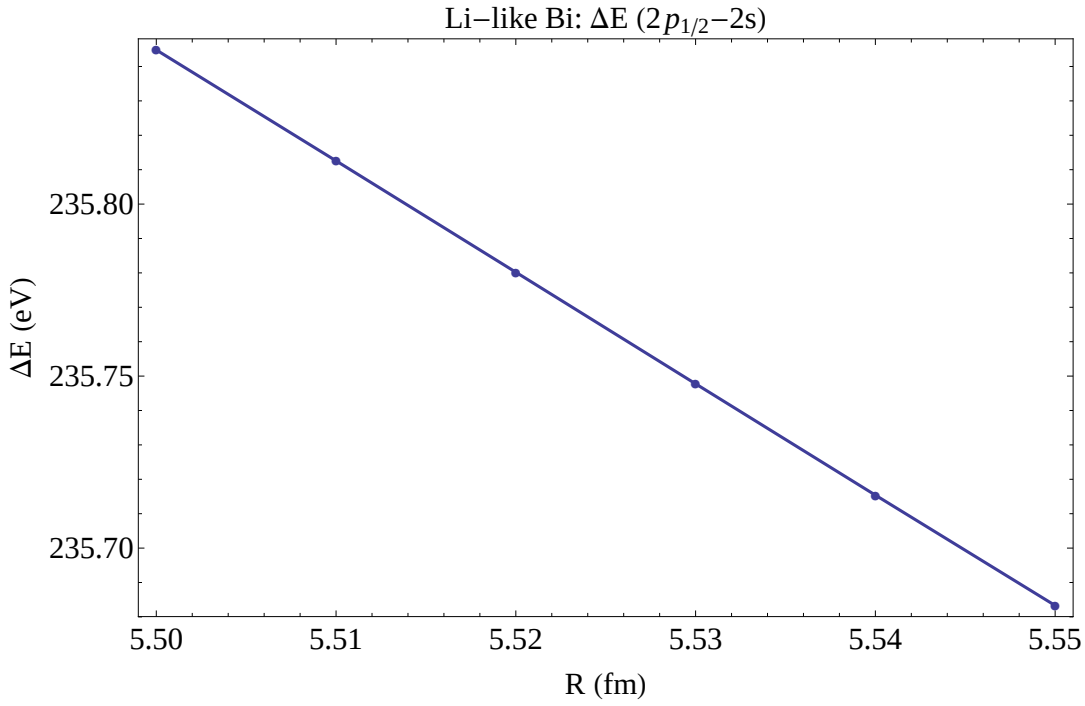

Figure 8.9: Energy variation vs. nuclear charge radius for $2p_{1/2} - 2s$ transition in Bi.

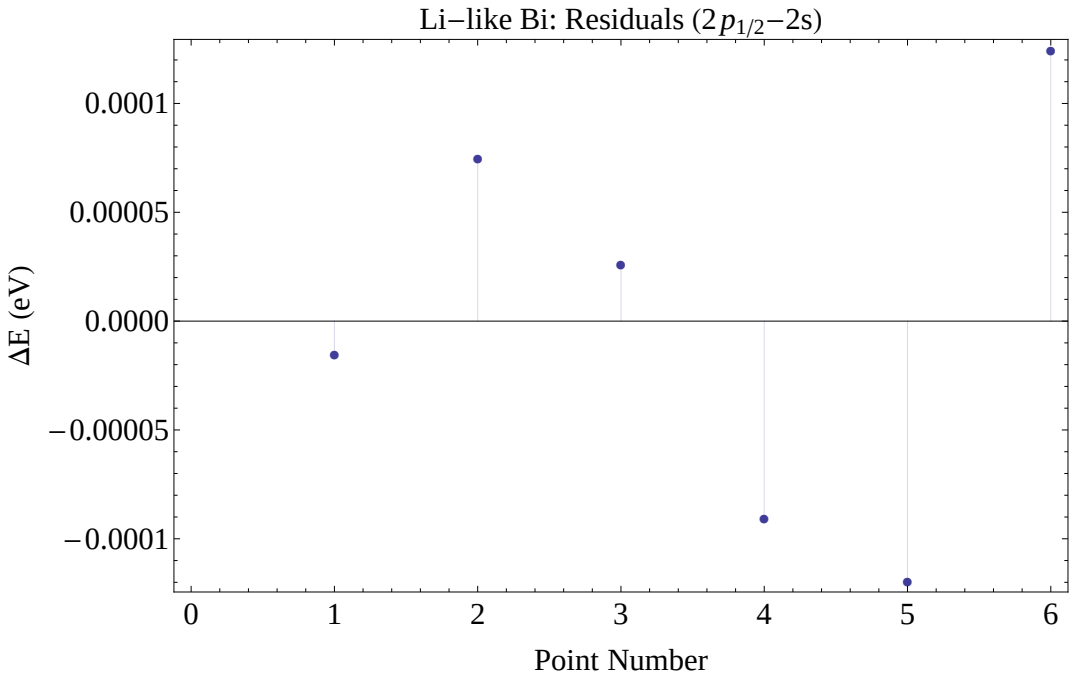

Figure 8.10: Residuals of the model for $2p_{3/2} - 2s$ transition in Bi.

The theoretical uncertainty for the $2p_{1/2} - 2s$ transition of bismuth is $\Delta E = 0.103$ eV, leading to an uncertainty in the charge radius from theory to be:

$$\Delta r_{rms}^{(theory)} = 0.03 \text{ fm}. \tag{8.30}$$

8.3.3 Polonium* (A = 209)

In this section we will produce the results for the $2p_{1/2} - 2s$ and $2p_{3/2} - 2s$ transitions for Li-like polonium. The range chosen to vary the charge radius initially was $5.50 - 5.55$ fm, and the transition energy for each interval calculated. The results of these calculations for the $2p_{1/2} - 2s$ transition are shown in Table 8.10, and graphed in figure 8.11.

Table 8.10: Points for $2p_{1/2} - 2s$ transition in Po.

R (fm)	E (eV)
5.50	240.955
5.51	240.92
5.52	240.884
5.53	240.849
5.54	240.813
5.55	240.777

The model fit to the points is also shown in Figure 8.11 and the residuals of the model is shown in Figure 8.12.

The equation specifying the model is given as:

$$E = 260.551 - 3.56283\ r_{rms}, \tag{8.31}$$

which when inverted obtain the relationship for the charge radius as a function of transition energy,

$$r_{rms} = 73.1304 - 0.2807E. \tag{8.32}$$

We can also obtain an expression for the uncertainty in r_{rms} via the derivative of the above equation:

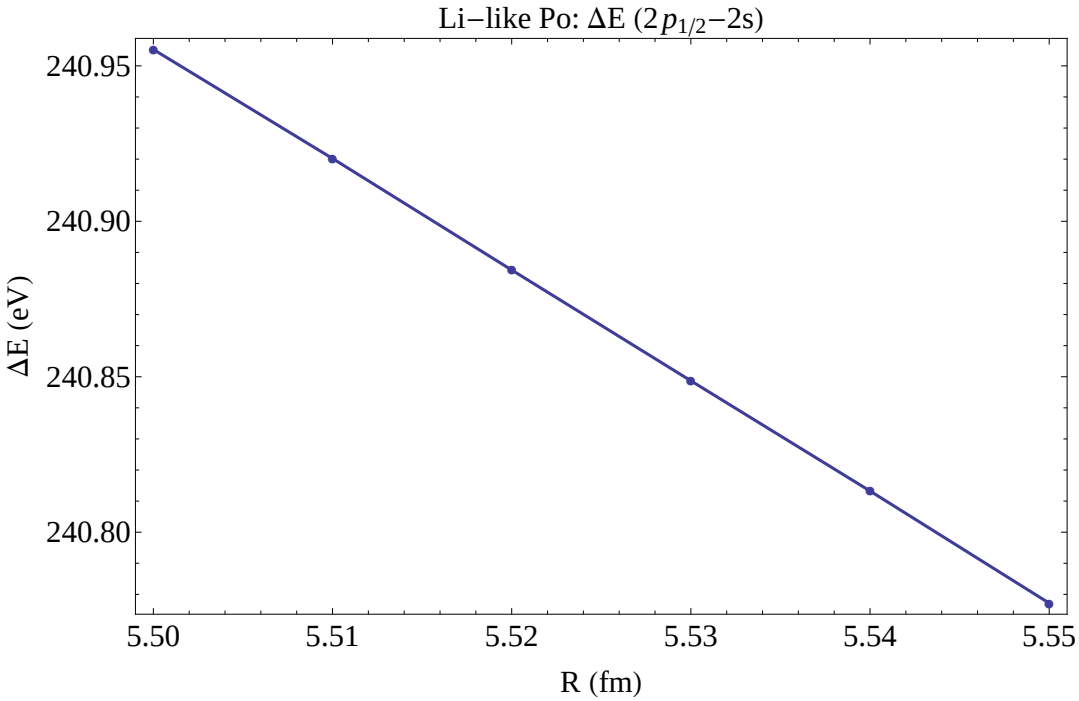

Figure 8.11: Energy variation vs. nuclear charge radius for $2p_{1/2} - 2s$ transition in Po.

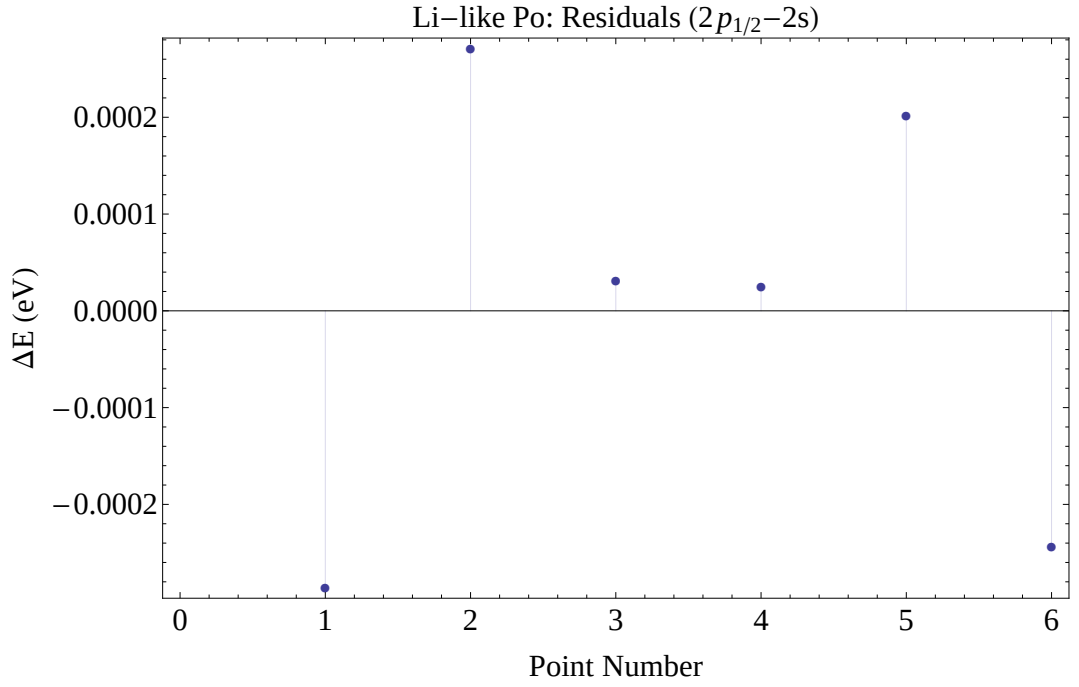

Figure 8.12: Residuals of the model for $2p_{1/2} - 2s$ transition in Po.

$$\Delta r_{rms} = 0.2807 \Delta E. \tag{8.33}$$

The theoretical uncertainty for the $2p_{1/2}-2s$ transition of polonium is $\Delta E = 0.125$ eV, leading to an uncertainty in the charge radius from theory to be:

$$\Delta r_{rms}^{(theory)} = 0.035 \text{ fm}. \tag{8.34}$$

The results for the $2p_{3/2} - 2s$ transition are shown in Table 8.11, and graphed in figure 8.13.

Table 8.11: Points for $2p_{3/2} - 2s$ transition in Po.

R (fm)	E (eV)
5.5	2941.
5.51	2940.96
5.52	2940.92
5.53	2940.88
5.54	2940.84
5.55	2940.8

The model fit to the points is also shown in Figure 8.13 and the residuals of the model is shown in Figure 8.14.

The equation specifying the model is given as:

$$E = 2962.31 - 3.87435 \; r_{rms}, \tag{8.35}$$

which can be immediately inverted to obtain the relationship for the charge radius as a function of transition energy,

$$r_{rms} = 764.594 - 0.2581 E. \tag{8.36}$$

We can also obtain an expression for the uncertainty in r_{rms} via the derivative of the above equation:

$$\Delta r_{rms} = 0.2581 \Delta E. \tag{8.37}$$

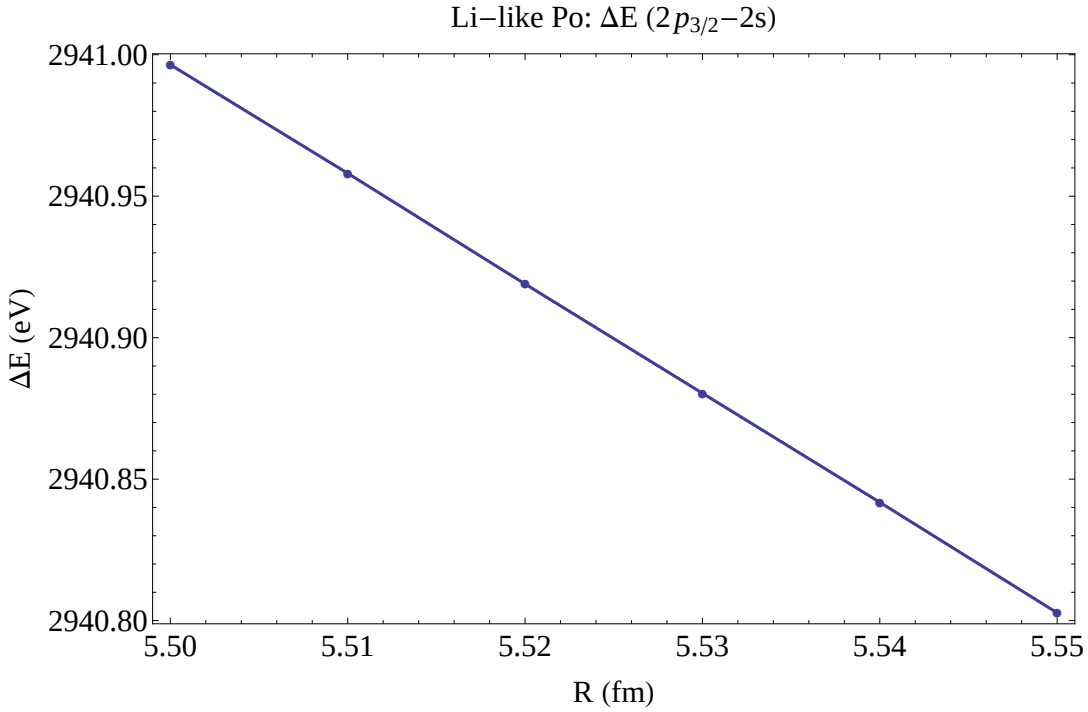

Figure 8.13: Energy variation vs. nuclear charge radius for $2p_{3/2} - 2s$ transition in Po.

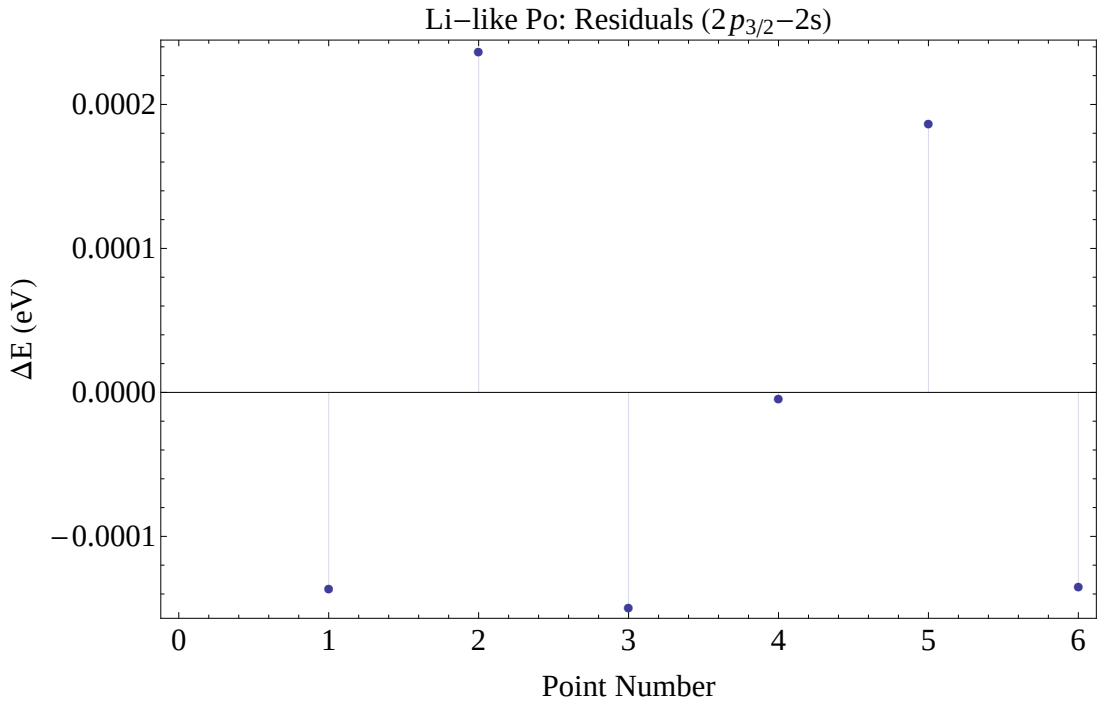

Figure 8.14: Residuals of the model for $2p_{3/2} - 2s$ transition in Po.

The theoretical uncertainty for the $2p_{3/2}-2s$ transition of polonium is $\Delta E = 0.086$ eV, leading to an uncertainty in the charge radius from theory to be:

$$\Delta r_{rms}^{(theory)} = 0.022 \text{ fm}. \tag{8.38}$$

8.3.4 Astatine* (A = 210)

In this section we will produce the results for the $2p_{1/2} - 2s$ and $2p_{3/2} - 2s$ transitions for Li-like astatine. The range chosen to vary the charge radius initially was $5.50 - 5.55$ fm, and the transition energy for each interval calculated. The results of these calculations for the $2p_{1/2} - 2s$ transition are shown in Table 8.12, and graphed in figure 8.15.

The model fit to the points is also shown in Figure 8.15 and the residuals of the model is shown in Figure 8.16.

The equation specifying the model is given as:

Table 8.12: Points for $2p_{1/2} - 2s$ transition in At

R (fm)	E (eV)
5.52	246.051
5.53	246.011
5.54	245.973
5.55	245.933
5.56	245.894
5.57	245.854

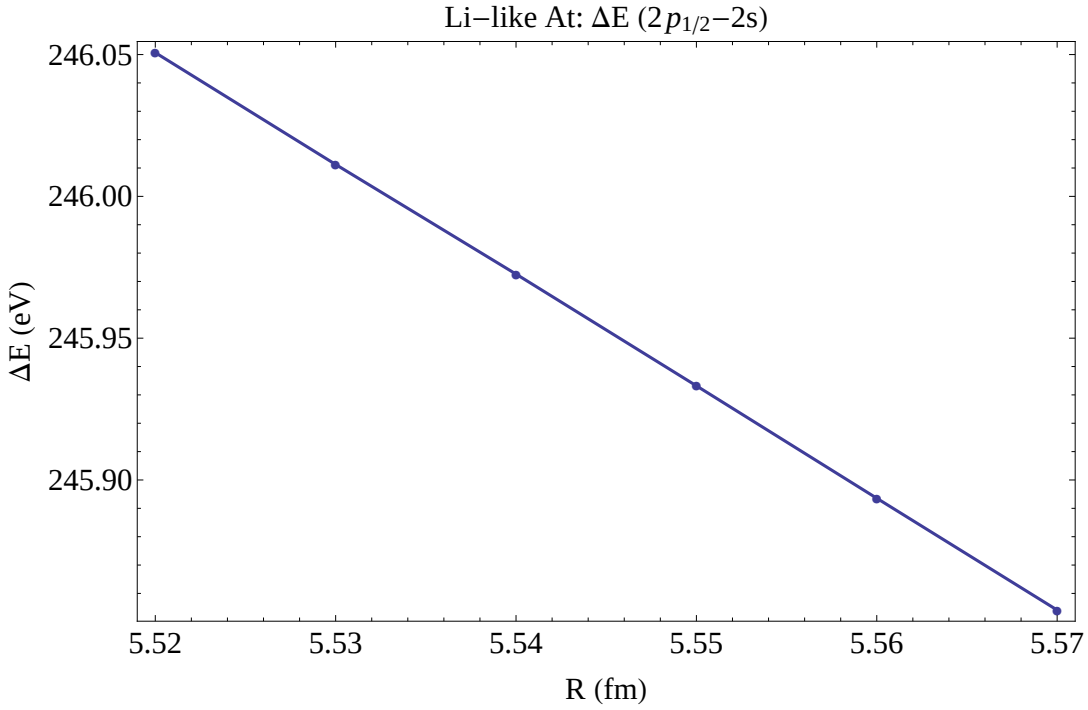

Figure 8.15: Energy variation vs. nuclear charge radius for $2p_{1/2} - 2s$ transition in At.

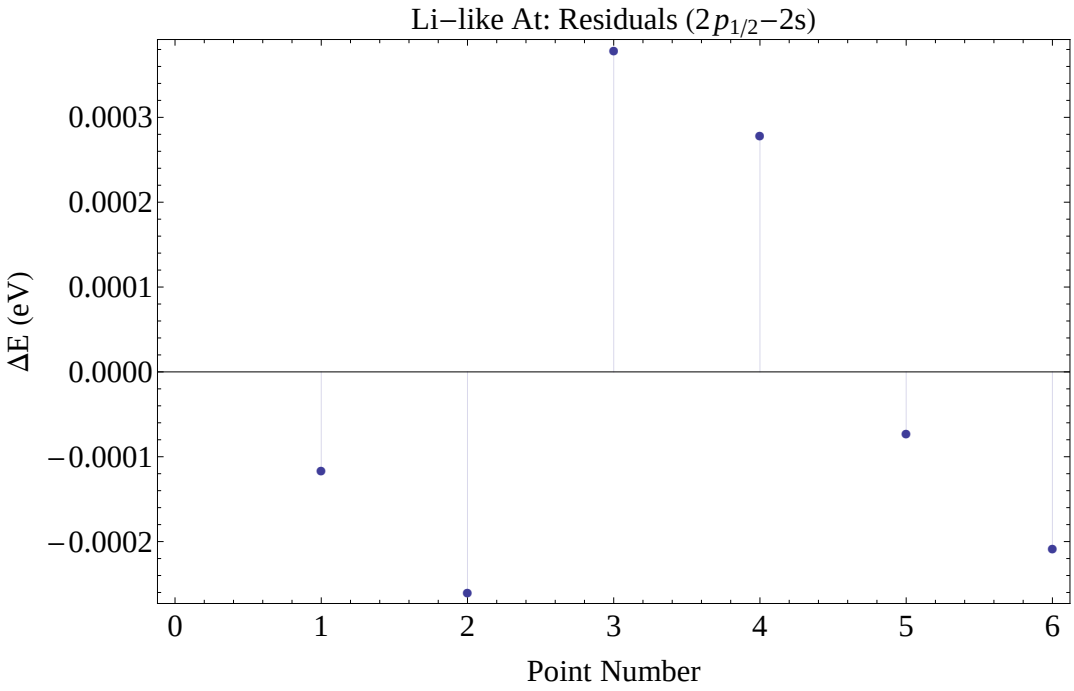

Figure 8.16: Residuals of the model for $2p_{1/2} - 2s$ transition in At.

$$E = 267.739 - 3.92904\ r_{rms}, \tag{8.39}$$

which when inverted obtain the relationship for the charge radius as a function of transition energy,

$$r_{rms} = 68.1437 - 0.2545E. \tag{8.40}$$

We can also obtain an expression for the uncertainty in r_{rms} via the derivative of the above equation:

$$\Delta r_{rms} = 0.2545\Delta E \tag{8.41}$$

The theoretical uncertainty for the $2p_{1/2} - 2s$ transition of astatine is $\Delta E = 0.275$ eV, leading to an uncertainty in the charge radius from theory to be:

$$\Delta r_{rms}^{(theory)} = 0.07 \text{ fm}. \tag{8.42}$$

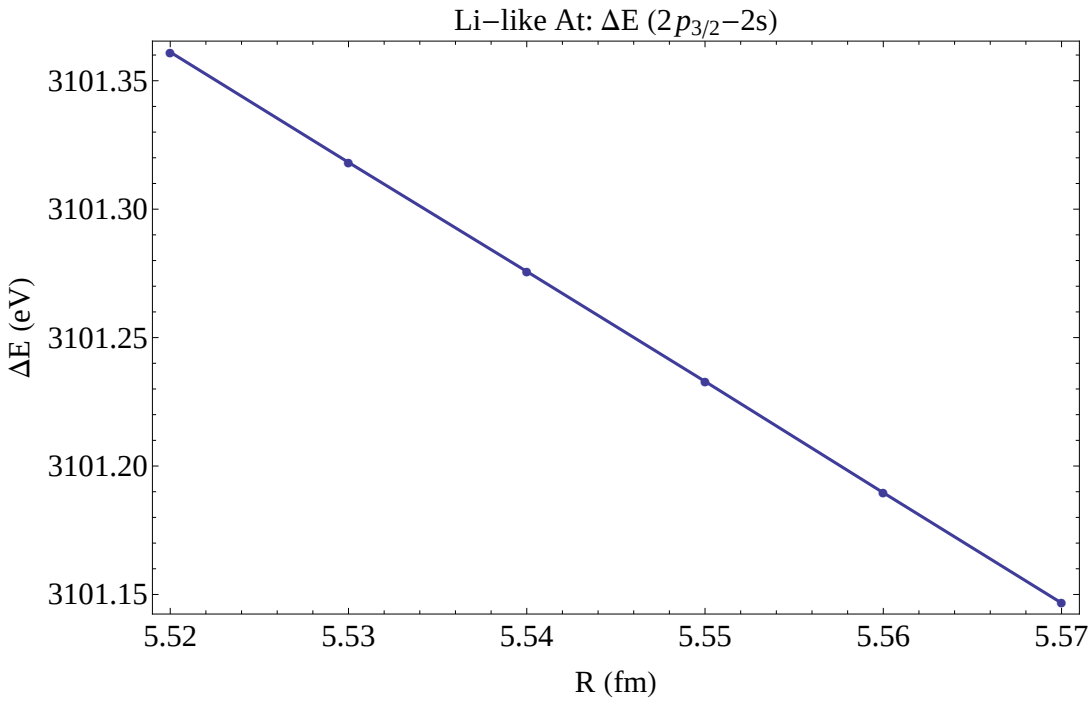

Figure 8.17: Energy variation vs. nuclear charge radius for $2p_{3/2} - 2s$ transition in At.

The results for the $2p_{3/2} - 2s$ transition are shown in Table 8.13, and graphed in figure 8.17.

Table 8.13: Points for $2p_{3/2} - 2s$ transition in At.

R (fm)	E (eV)
5.52	3101.36
5.53	3101.32
5.54	3101.28
5.55	3101.23
5.56	3101.19
5.57	3101.15

The model fit to the points is also shown in Figure 8.17 and the residuals of the model is shown in Figure 8.18.

The equation specifying the model is given as:

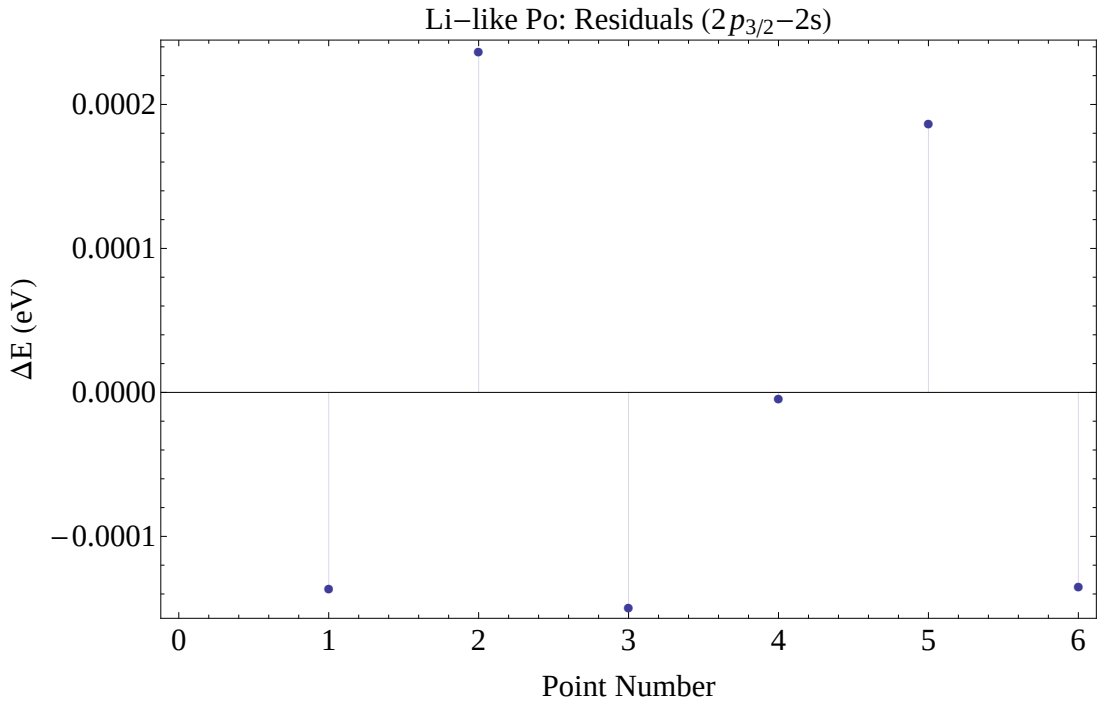

Figure 8.18: Residuals of the model for $2p_{3/2} - 2s$ transition in At.

$$E = 3125.03 - 4.28838\ r_{rms}, \tag{8.43}$$

which can be immediately inverted to obtain the relationship for the charge radius as a function of transition energy,

$$r_{rms} = 728.721 - 0.2332E. \tag{8.44}$$

We can also obtain an expression for the uncertainty in r_{rms} via the derivative of the above equation:

$$\Delta r_{rms} = 0.2332\Delta E. \tag{8.45}$$

The theoretical uncertainty for the $2p_{3/2} - 2s$ transition of astatine is $\Delta E = 0.263$ eV, leading to an uncertainty in the charge radius from theory to be:

$$\Delta r_{rms}^{(theory)} = 0.061 \text{ fm}. \tag{8.46}$$

8.3.5 Radon* (A = 222)

In this section we will produce the results for the $2p_{1/2} - 2s$ and $2p_{3/2} - 2s$ transitions for Li-like radon. The range chosen to vary the charge radius initially was $5.66 - 5.71$ fm, and the transition energy for each interval calculated. The results of these calculations for the $2p_{1/2} - 2s$ transition are shown in Table 8.14, and graphed in Figure 8.19.

Table 8.14: Points for $2p_{1/2} - 2s$ transition in Rn.

R (fm)	E (eV)
5.66	250.657
5.67	250.613
5.68	250.569
5.69	250.525
5.7	250.481
5.71	250.437

The model fit to the points is also shown in Figure 8.19 and the residuals of the model are shown in Figure 8.20.

The equation specifying the model is given as:

$$E = 275.506 - 4.39027\ r_{rms}, \tag{8.47}$$

which when inverted obtain the relationship for the charge radius as a function of transition energy,

$$r_{rms} = 62.7536 - 0.2278E. \tag{8.48}$$

We can also obtain an expression for the uncertainty in r_{rms} via the derivative of the above equation:

$$\Delta r_{rms} = 0.2278\Delta E. \tag{8.49}$$

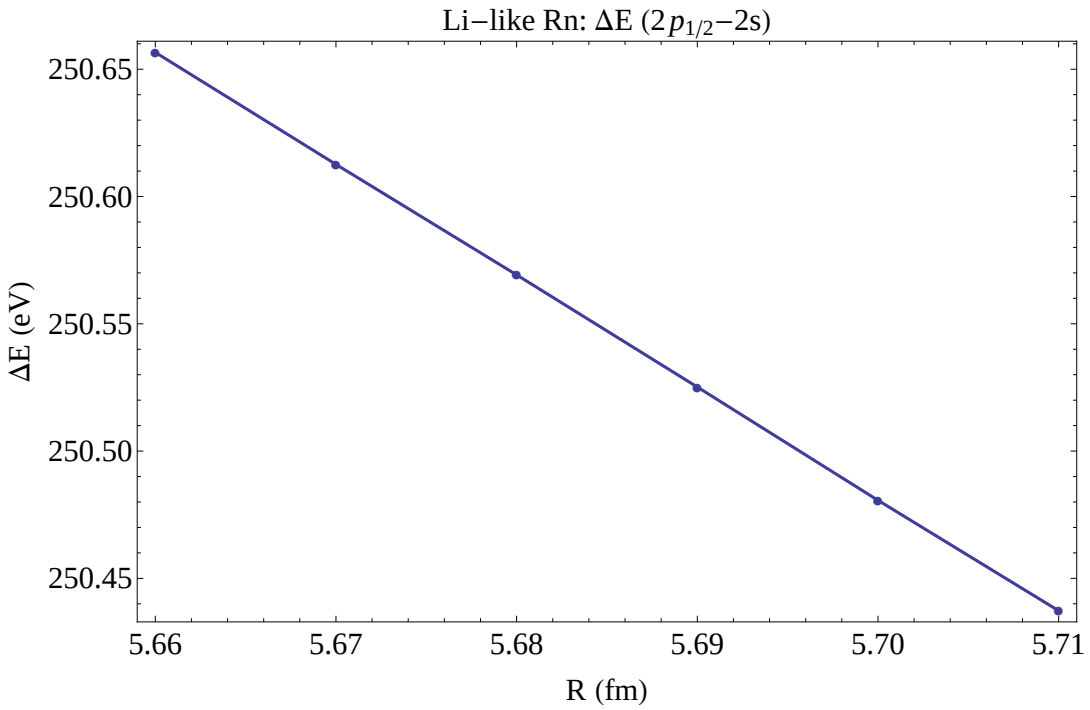

Figure 8.19: Energy variation vs. nuclear charge radius for $2p_{1/2} - 2s$ transition in Rn.

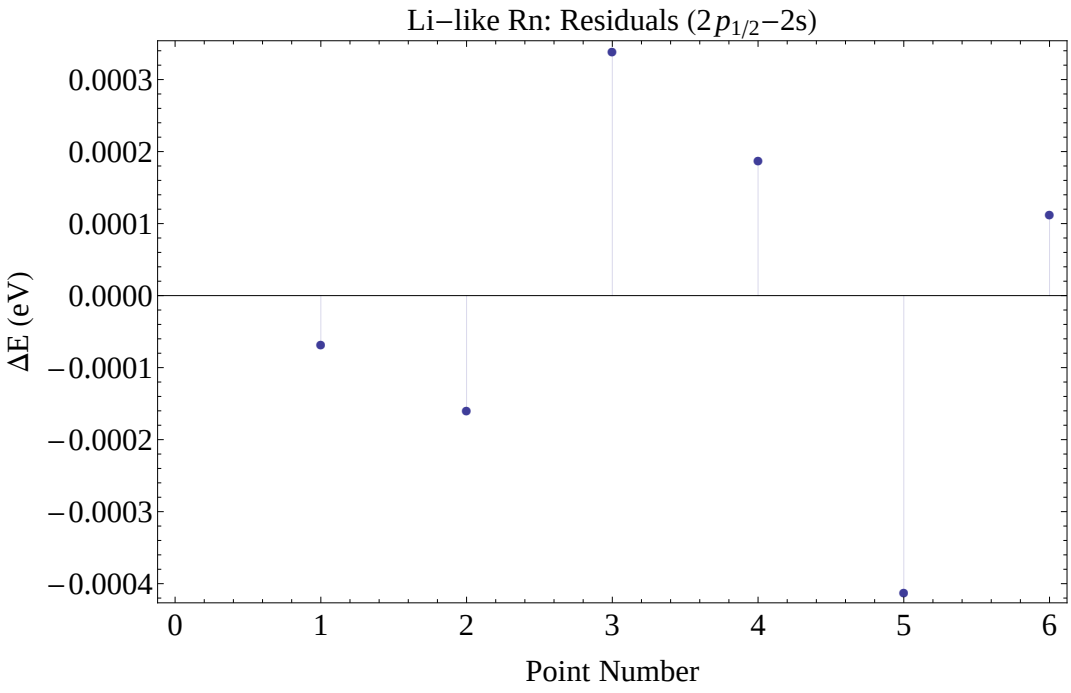

Figure 8.20: Residuals of the model for $2p_{1/2} - 2s$ transition in Rn

The theoretical uncertainty for the $2p_{1/2} - 2s$ transition of radon is $\Delta E = 0.133$ eV, leading to an uncertainty in the charge radius from theory to be:

$$\Delta r_{rms}^{(theory)} = 0.03 \text{ fm}. \tag{8.50}$$

The results for the $2p_{3/2} - 2s$ transition are shown in Table 8.15, and graphed in figure 8.21.

Table 8.15: Points for $2p_{3/2} - 2s$ transition in Rn

R (fm)	E (eV)
5.66	3268.89
5.67	3268.84
5.68	3268.79
5.69	3268.74
5.7	3268.69
5.71	3268.65

The model fit to the points is also shown in Figure 8.21 and the residuals of the model is shown in Figure 8.22.

The equation specifying the model is given as:

$$E = 3296.05 - 4.79972\ r_{rms}, \tag{8.51}$$

which can be immediately inverted to obtain the relationship for the charge radius as a function of transition energy,

$$r_{rms} = 686.718 - 0.2083E. \tag{8.52}$$

We can also obtain an expression for the uncertainty in r_{rms} via the derivative of the above equation:

$$\Delta r_{rms} = 0.2083\Delta E. \tag{8.53}$$

The theoretical uncertainty for the $2p_{3/2} - 2s$ transition of radon is $\Delta E = 0.109$ eV, leading to an uncertainty in the charge radius from theory to be:

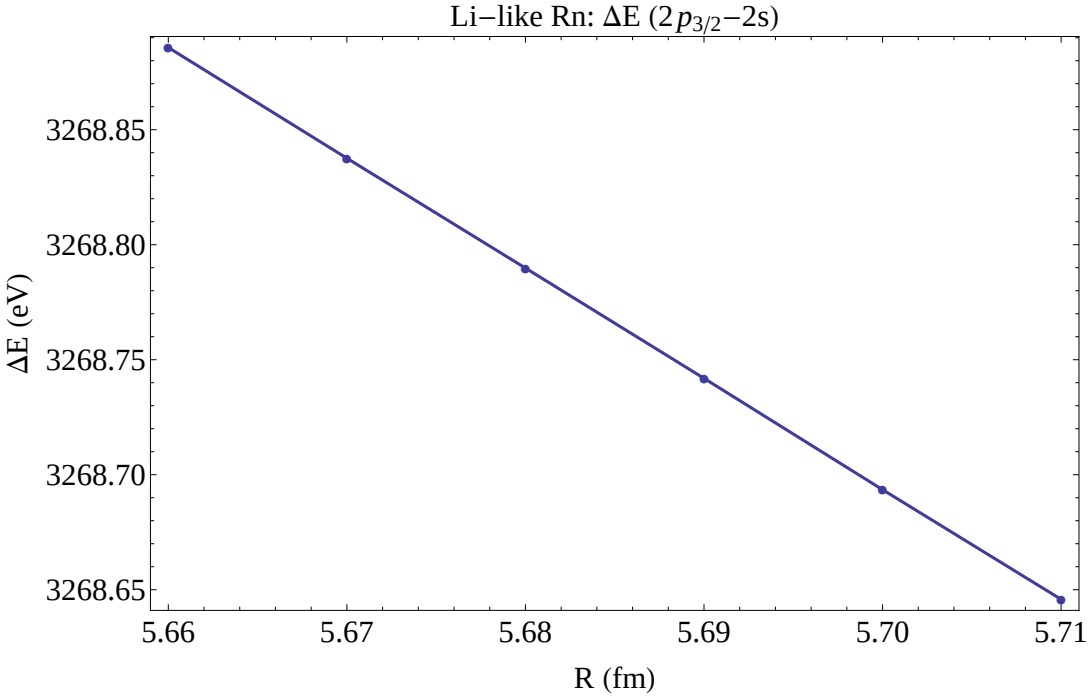

Figure 8.21: Energy variation vs. nuclear charge radius for $2p_{3/2} - 2s$ transition in Rn.

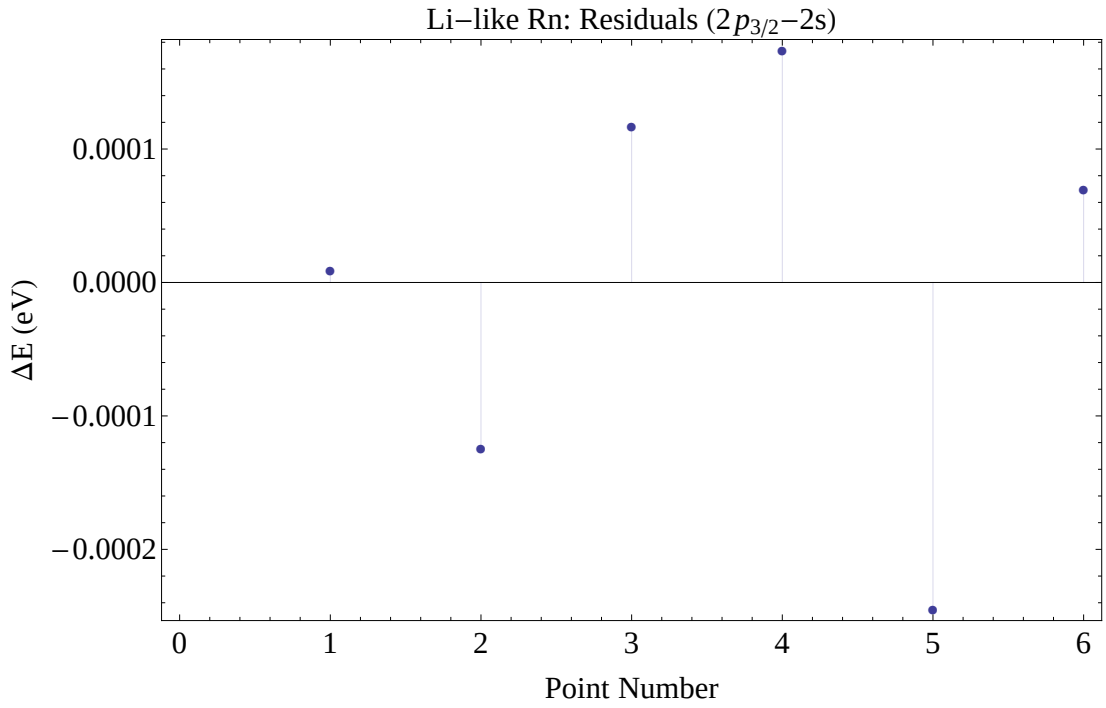

Figure 8.22: Residuals of the model for $2p_{3/2} - 2s$ transition in Rn.

$$\Delta r_{rms}^{(theory)} = 0.023 \text{ fm}. \tag{8.54}$$

8.3.6 Francium* (A = 223)

In this section we will present the results for the $2p_{1/2} - 2s$ and $2p_{3/2} - 2s$ transitions for Li-like francium. Again, it must be stressed that as of the time of this writing no spectroscopic information exists for francium. The range chosen to vary the charge radius initially was $5.65 - 5.71$ fm, and the transition energy for each interval calculated. The results of these calculations for the $2p_{1/2} - 2s$ transition are shown in Table 8.16, and graphed in figure 8.23.

The model fit to the points is also shown in Figure 8.23 and the residuals of the model is shown in Figure 8.24.

The equation specifying the model is given as:

Table 8.16: Points for $2p_{1/2} - 2s$ transition in Fr

R (fm)	E (eV)
5.65	255.929
5.66	255.88
5.67	255.833
5.68	255.784
5.69	255.736
5.7	255.688

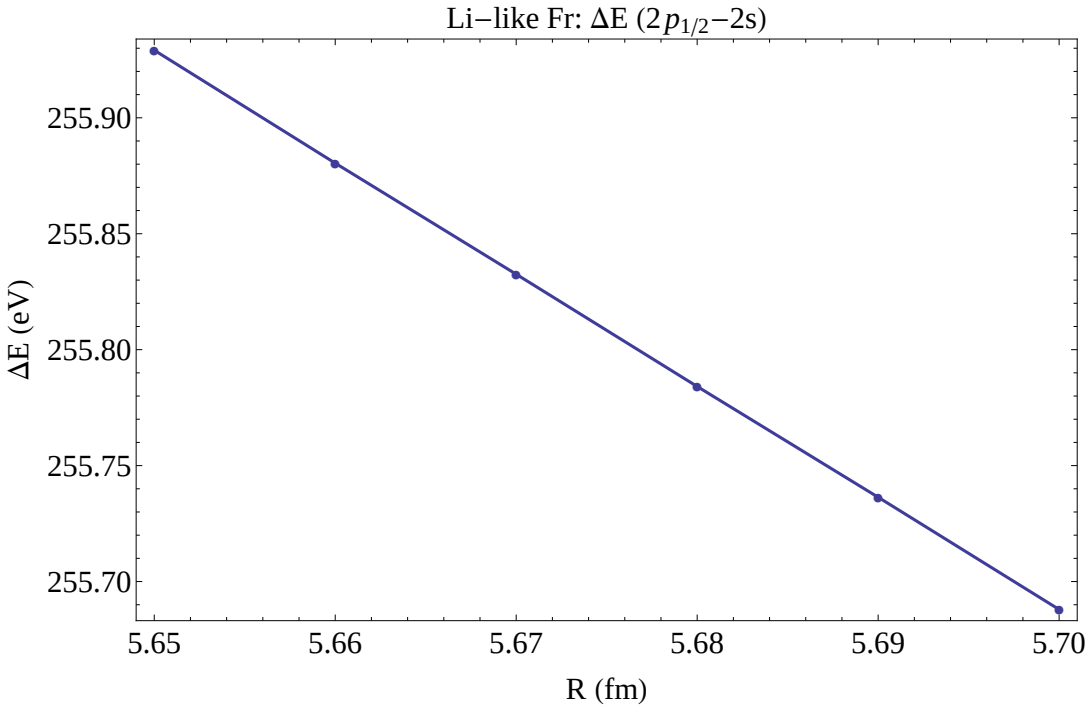

Figure 8.23: Energy variation vs. nuclear charge radius for $2p_{1/2} - 2s$ transition in Fr.

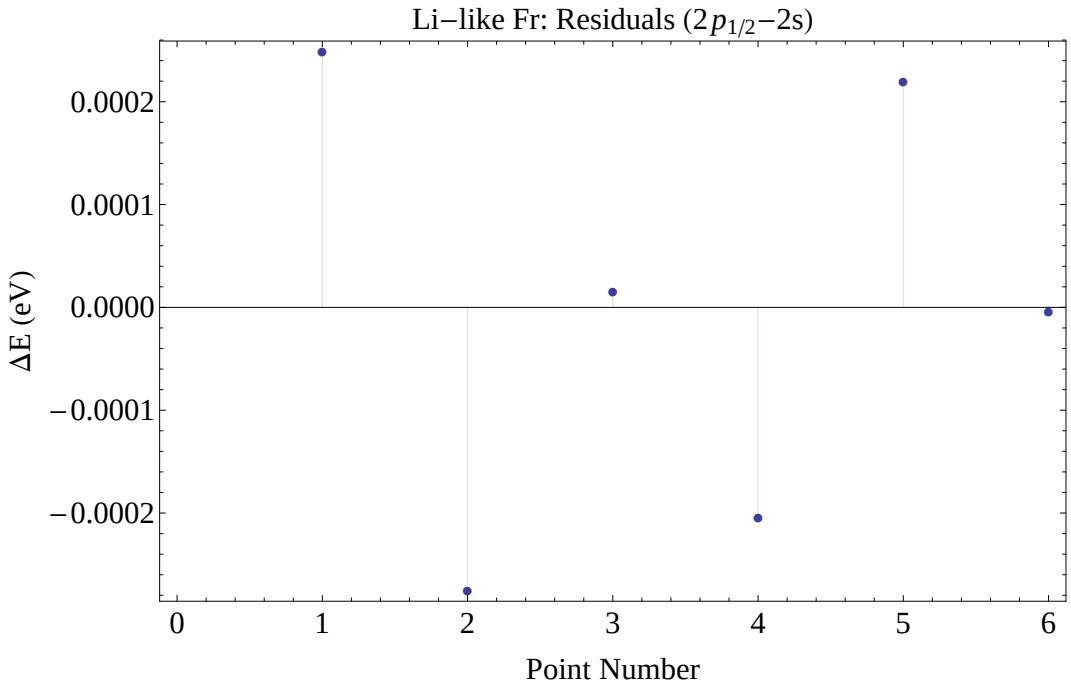

Figure 8.24: Residuals of the model for $2p_{1/2} - 2s$ transition in Fr.

$$E = 283.155 - 4.81881\ r_{rms}, \tag{8.55}$$

which when inverted obtain the relationship for the charge radius as a function of transition energy,

$$r_{rms} = 58.7604 - 0.2075E. \tag{8.56}$$

We can also obtain an expression for the uncertainty in r_{rms} via the derivative of the above equation:

$$\Delta r_{rms} = 0.2075\Delta E \tag{8.57}$$

The theoretical uncertainty for the $2p_{1/2}-2s$ transition of francium is $\Delta E = 0.129$ eV, leading to an uncertainty in the charge radius from theory to be:

$$\Delta r_{rms}^{(theory)} = 0.027 \text{ fm}. \tag{8.58}$$

The results for the $2p_{3/2} - 2s$ transition are shown in Table 8.17, and graphed in figure 8.25.

Table 8.17: Points for $2p_{3/2} - 2s$ transition in Rd

R (fm)	E (eV)
5.65	3445.14
5.66	3445.08
5.67	3445.03
5.68	3444.98
5.69	3444.92
5.7	3444.87

The model fit to the points is also shown in Figure 8.25 and the residuals of the model is shown in Figure 8.26.

The equation specifying the model is given as:

$$E = 3475.03 - 5.29008\ r_{rms}, \tag{8.59}$$

which can be immediately inverted to obtain the relationship for the charge radius as a function of transition energy,

$$r_{rms} = 656.894 - 0.1890E. \tag{8.60}$$

We can also obtain an expression for the uncertainty in r_{rms} via the derivative of the above equation:

$$\Delta r_{rms} = 0.1890\Delta E. \tag{8.61}$$

The theoretical uncertainty for the $2p_{3/2} - 2s$ transition of francium is $\Delta E = 0.104$ eV, leading to an uncertainty in the charge radius from theory to be:

$$\Delta r_{rms}^{(theory)} = 0.02 \text{ fm}. \tag{8.62}$$

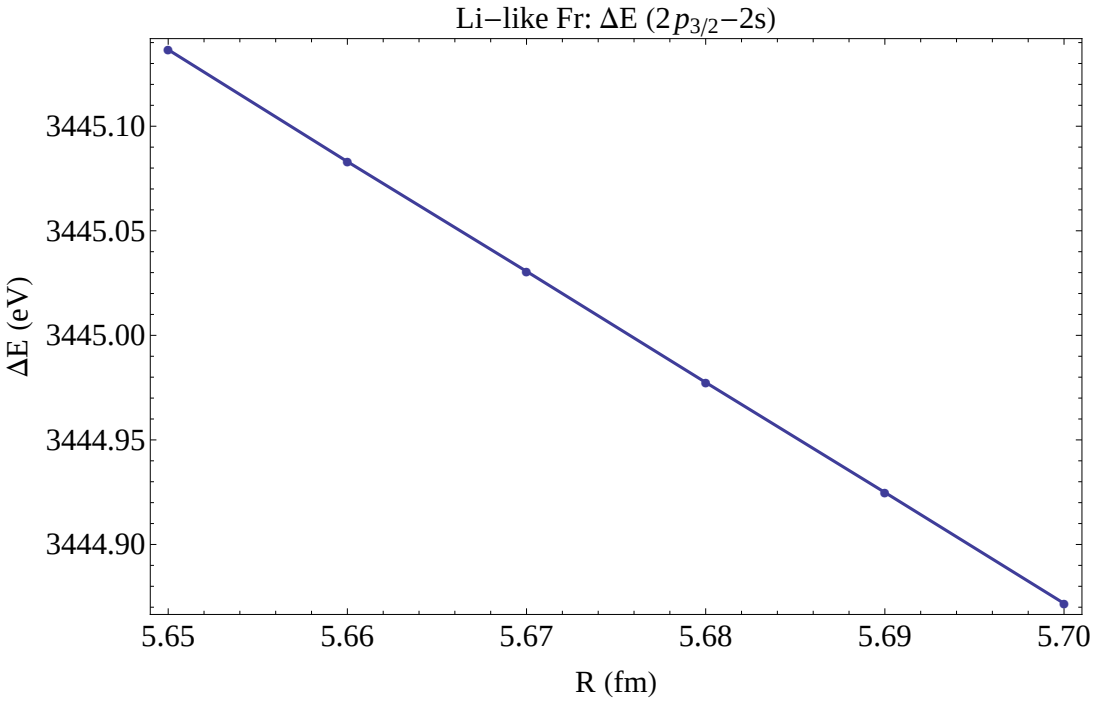

Figure 8.25: Energy variation vs. nuclear charge radius for $2p_{3/2} - 2s$ transition in Fr.

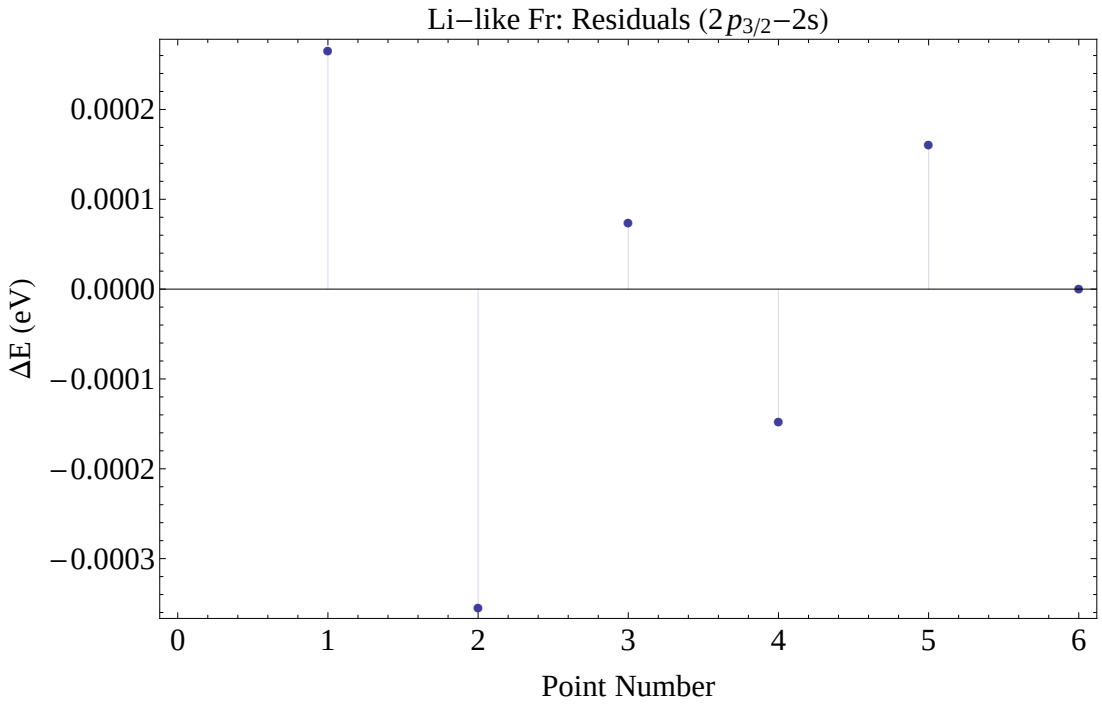

Figure 8.26: Residuals of the model for $2p_{3/2} - 2s$ transition in Fr.

8.3.7 Radium* (A = 226)

In this section we will produce the results for the $2p_{1/2} - 2s$ and $2p_{3/2} - 2s$ transitions for Li-like radium, of which no spectroscopic information exists. The range chosen to vary the charge radius initially was $5.7 - 5.75$ fm, and the transition energy for each interval calculated. The results of these calculations for the $2p_{1/2} - 2s$ transition are shown in Table 8.18, and graphed in figure 8.27.

Table 8.18: Points for $2p_{1/2} - 2s$ transition in Ra

R (fm)	E (eV)
5.7	260.932
5.71	260.879
5.72	260.825
5.73	260.772
5.74	260.719
5.75	260.665

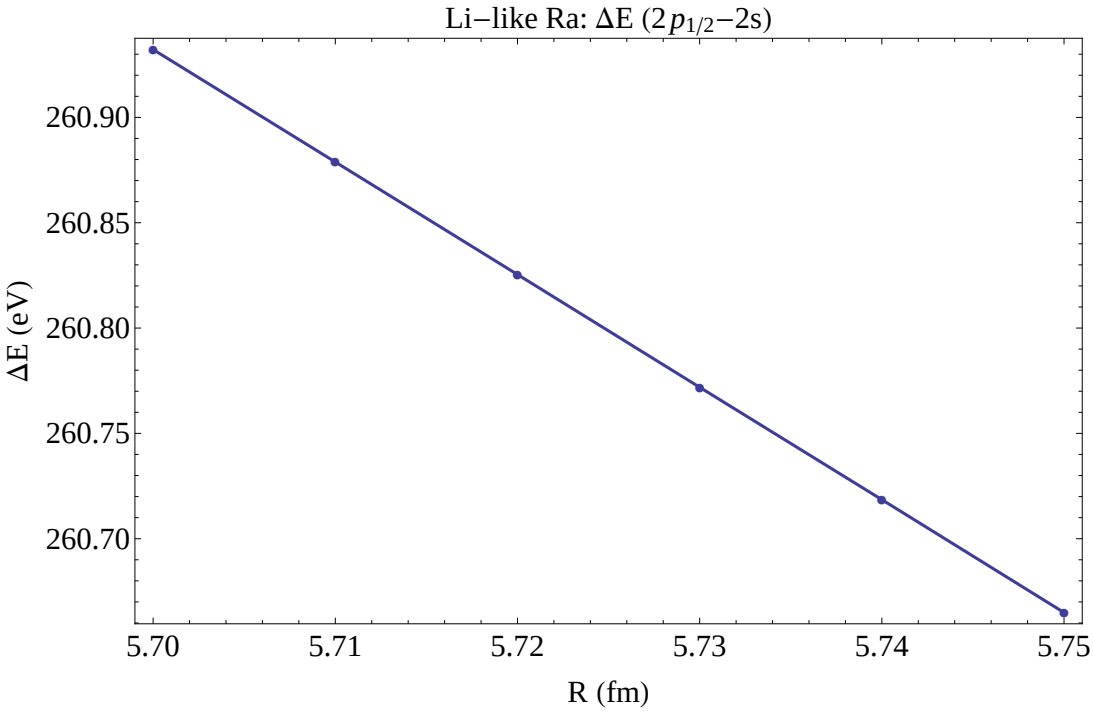

Figure 8.27: Energy variation vs. nuclear charge radius for $2p_{1/2} - 2s$ transition in Ra.

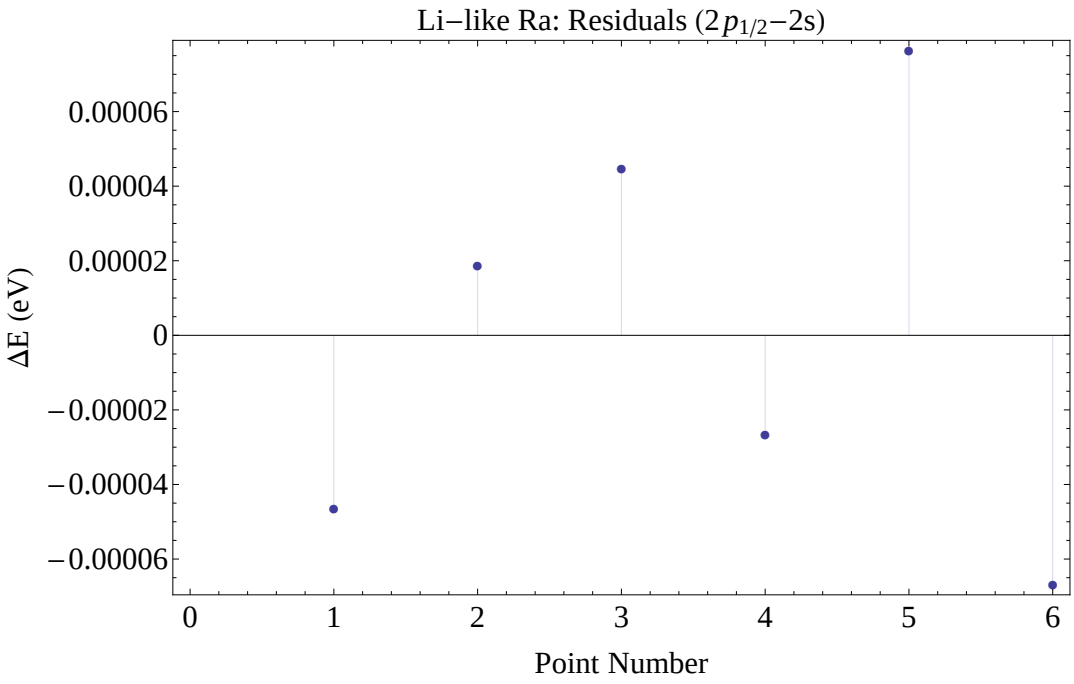

Figure 8.28: Residuals of the model for $2p_{1/2} - 2s$ transition in Ra.

The model fit to the points is also shown in Figure 8.27 and the residuals of the model is shown in Figure 8.28.

The equation specifying the model is given as:

$$E = 291.397 - 5.34465\ r_{rms}, \tag{8.63}$$

which when inverted obtain the relationship for the charge radius as a function of transition energy,

$$r_{rms} = 54.5175 - 0.1871E. \tag{8.64}$$

We can also obtain an expression for the uncertainty in r_{rms} via the derivative of the above equation:

$$\Delta r_{rms} = 0.1871\Delta E \tag{8.65}$$

The theoretical uncertainty for the $2p_{1/2} - 2s$ transition of radium is $\Delta E = 0.197$ eV,

leading to an uncertainty in the charge radius from theory to be:

$$\Delta r_{rms}^{(theory)} = 0.037 \text{ fm}. \tag{8.66}$$

The results for the $2p_{3/2} - 2s$ transition are shown in Table 8.19, and graphed in figure 8.29.

Table 8.19: Points for $2p_{3/2} - 2s$ transition in Ra

R (fm)	E (eV)
5.7	3629.52
5.71	3629.46
5.72	3629.40
5.73	3629.34
5.74	3629.28
5.75	3629.23

The model fit to the points is also shown in Figure 8.29 and the residuals of the model is shown in Figure 8.30.

The equation specifying the model is given as:

$$E = 3663.02 - 5.87683\ r_{rms}, \tag{8.67}$$

which can be immediately inverted to obtain the relationship for the charge radius as a function of transition energy,

$$r_{rms} = 623.298 - 0.1702E. \tag{8.68}$$

We can also obtain an expression for the uncertainty in r_{rms} via the derivative of the above equation:

$$\Delta r_{rms} = 0.1702\Delta E \tag{8.69}$$

The theoretical uncertainty for the $2p_{3/2} - 2s$ transition of radium is $\Delta E = 0.061$ eV, leading to an uncertainty in the charge radius from theory to be:

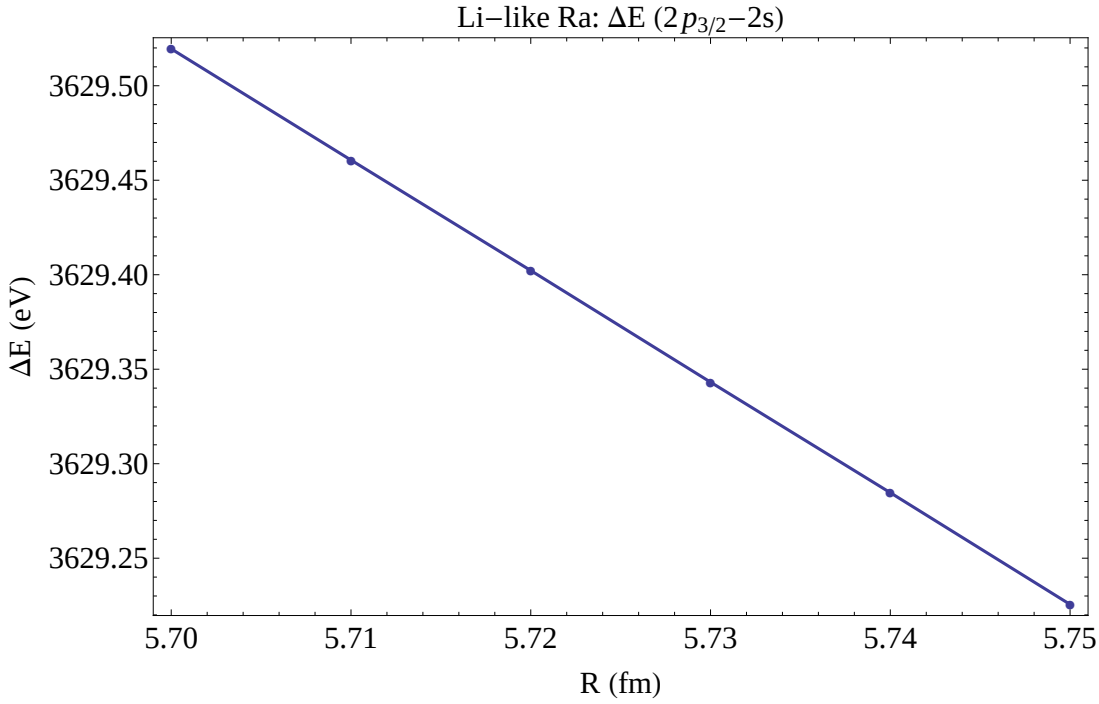

Figure 8.29: Energy variation vs. nuclear charge radius for $2p_{3/2} - 2s$ transition in Ra.

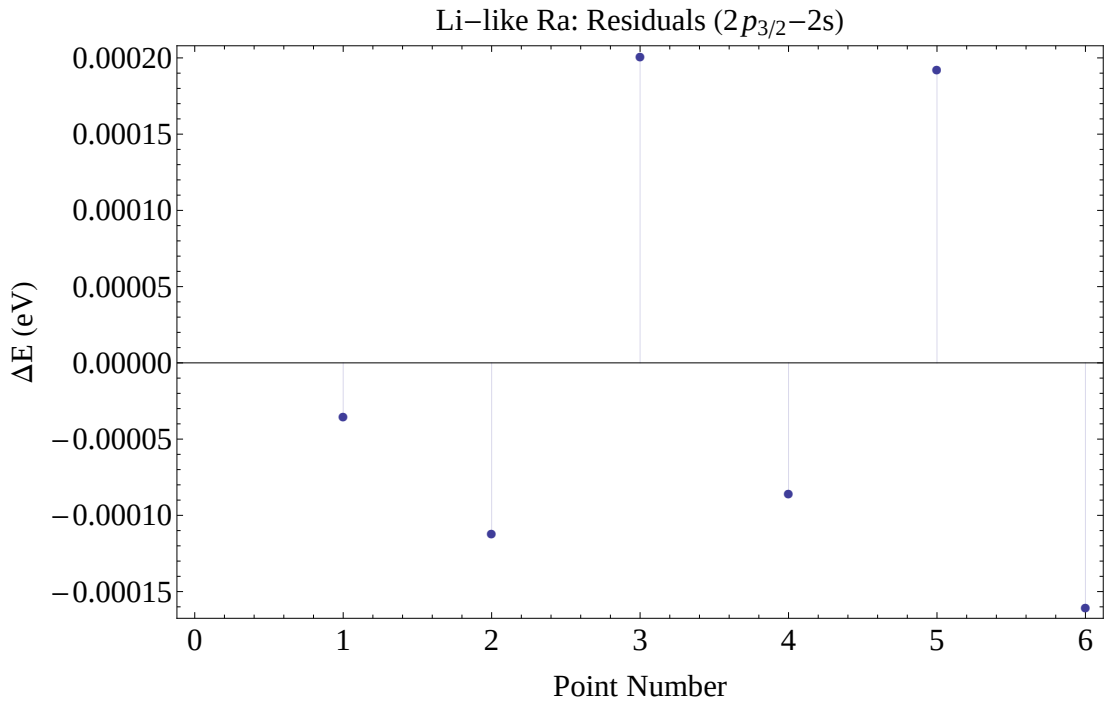

Figure 8.30: Residuals of the model for $2p_{3/2} - 2s$ transition in Ra.

$$\Delta r_{rms}^{(theory)} = 0.031 \text{ fm}. \tag{8.70}$$

8.3.8 Actinium* (A = 227)

In this section we will produce the results for the $2p_{1/2} - 2s$ and $2p_{3/2} - 2s$ transitions for Li-like actinium, of which no spectroscopic information exists. The range chosen to vary the charge radius initially was $5.65 - 5.71$ fm, and the transition energy for each interval calculated. The results of these calculations for the $2p_{1/2} - 2s$ transition are shown in Table 8.20, and graphed in figure 8.31.

The model fit to the points is also shown in Figure 8.31 and the residuals of the model is shown in Figure 8.32.

The equation specifying the model is given as:

$$E = 299.535 - 5.8536\ r_{rms}, \tag{8.71}$$

Table 8.20: Points for $2p_{1/2} - 2s$ transition in Ac.

R (fm)	E (eV)
5.65	266.453
5.66	266.394
5.67	266.336
5.68	266.277
5.69	266.219
5.7	266.16

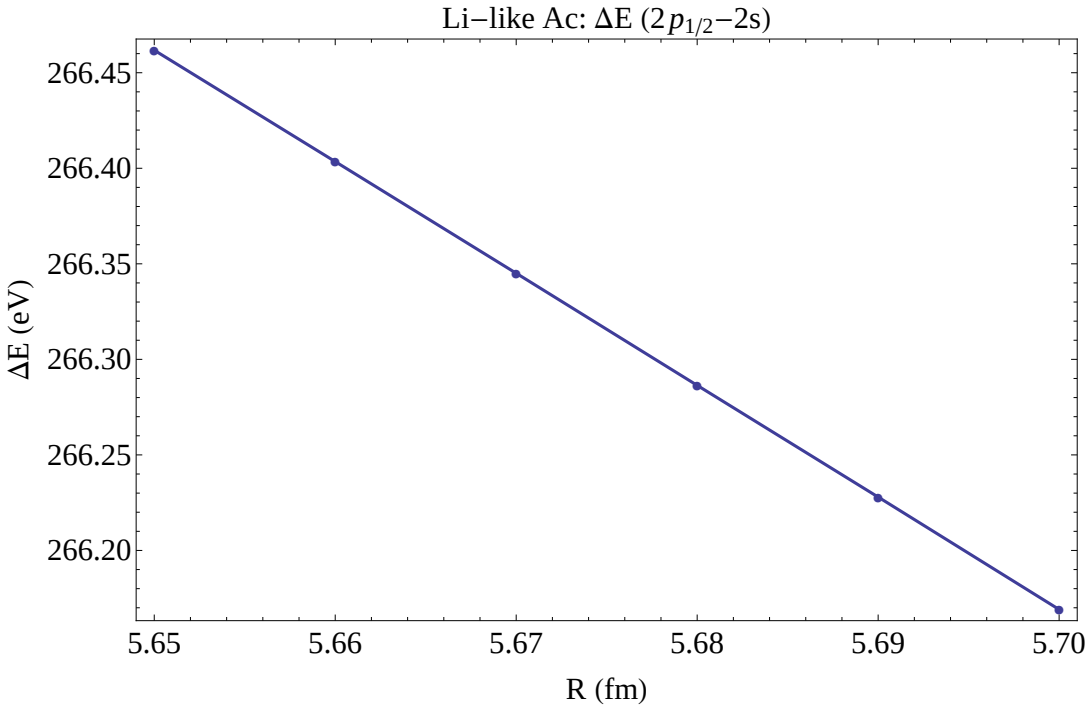

Figure 8.31: Energy variation vs. nuclear charge radius for $2p_{1/2} - 2s$ transition in Ac.

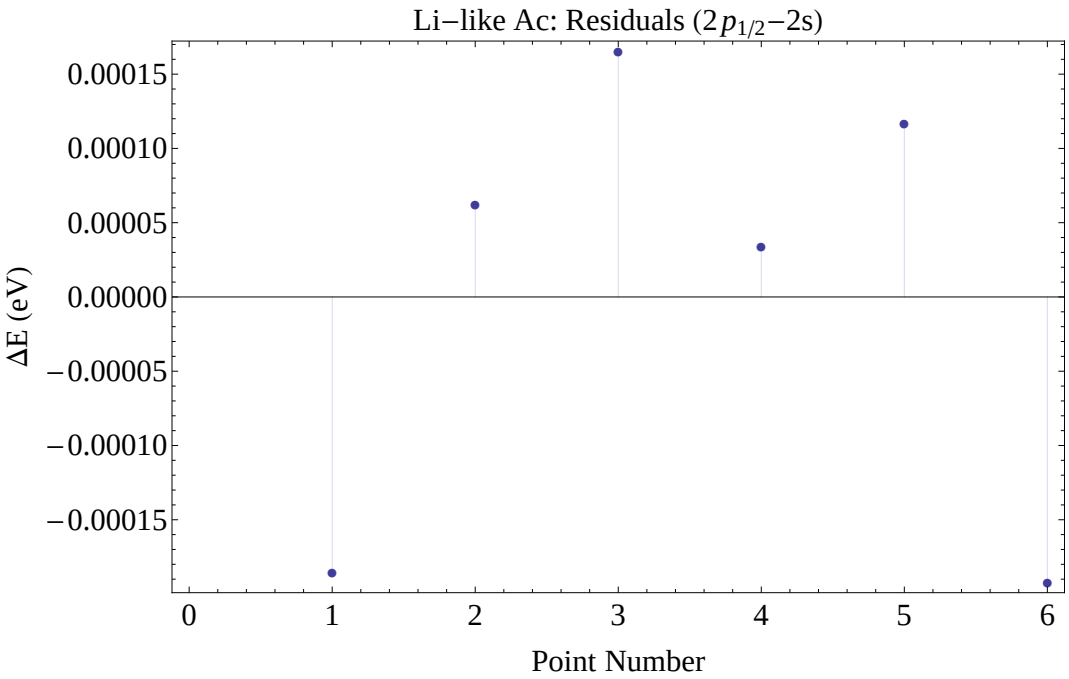

Figure 8.32: Residuals of the model for $2p_{1/2} - 2s$ transition in Ac.

which when inverted obtain the relationship for the charge radius as a function of transition energy,

$$r_{rms} = 51.1712 - 0.1708E. \tag{8.72}$$

We can also obtain an expression for the uncertainty in r_{rms} via the derivative of the above equation:

$$\Delta r_{rms} = 0.1708\Delta E. \tag{8.73}$$

The theoretical uncertainty for the $2p_{1/2} - 2s$ transition of actinium is $\Delta E = 0.394$ eV, leading to an uncertainty in the charge radius from theory to be:

$$\Delta r_{rms}^{(theory)} = 0.067 \text{ fm}. \tag{8.74}$$

The results for the $2p_{3/2} - 2s$ transition are shown in Table 8.21, and graphed in figure 8.33.

Table 8.21: Points for $2p_{3/2} - 2s$ transition in Ac.

R (fm)	E (eV)
5.65	3823.28
5.66	3823.21
5.67	3823.15
5.68	3823.09
5.69	3823.02
5.7	3822.96

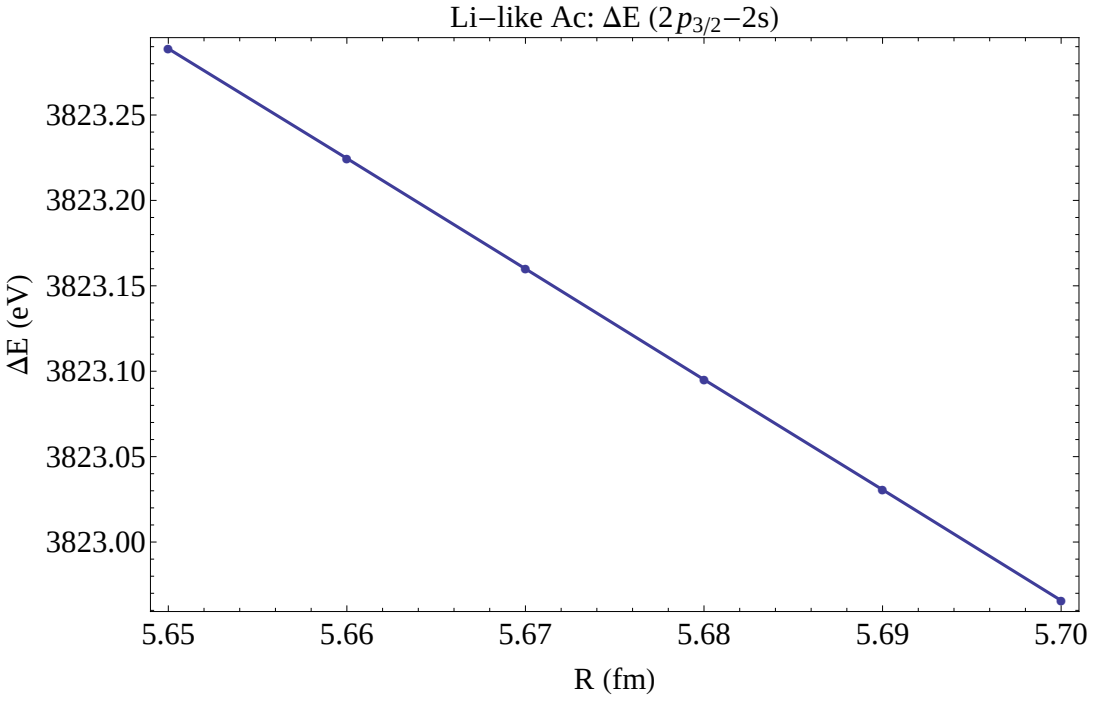

Figure 8.33: Energy variation vs. nuclear charge radius for $2p_{3/2} - 2s$ transition in Ac.

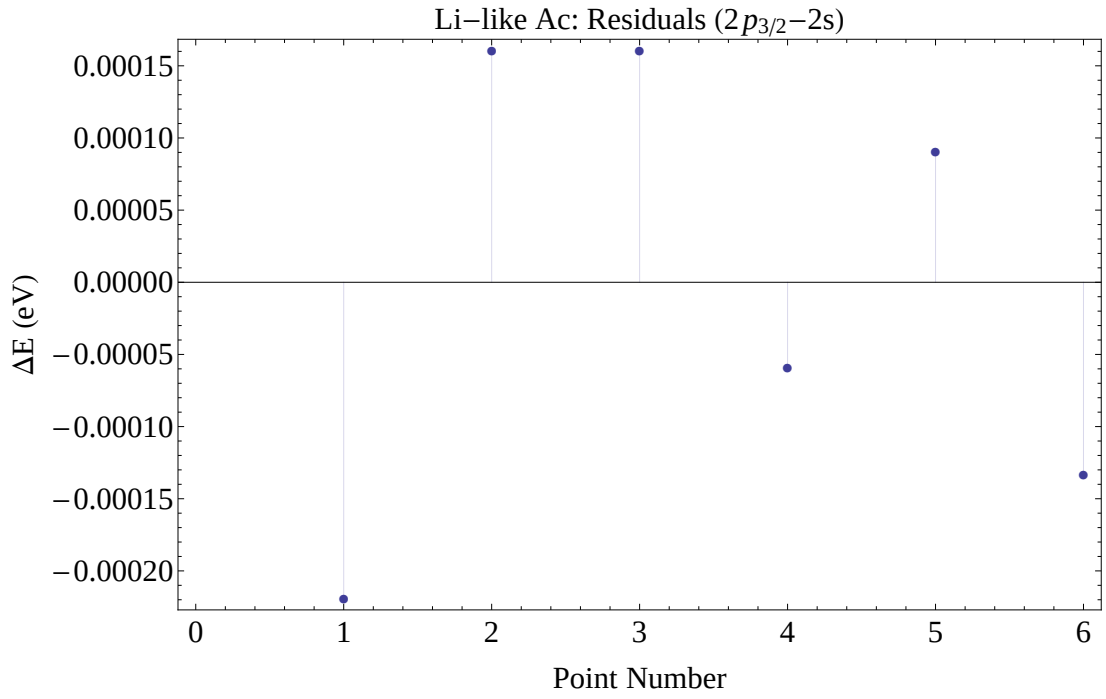

Figure 8.34: Residuals of the model for $2p_{3/2} - 2s$ transition in Ac.

The model fit to the points is also shown in Figure 8.33 and the residuals of the model is shown in Figure 8.34.

The equation specifying the model is given as:

$$E = 3859.8 - 6.4626\ r_{rms}, \tag{8.75}$$

which can be immediately inverted to obtain the relationship for the charge radius as a function of transition energy,

$$r_{rms} = 597.252 - 0.1547E. \tag{8.76}$$

We can also obtain an expression for the uncertainty in r_{rms} via the derivative of the above equation:

$$\Delta r_{rms} = 0.1547\Delta E. \tag{8.77}$$

The theoretical uncertainty for the $2p_{3/2} - 2s$ transition of actinium is $\Delta E = 0.385$ eV,

leading to an uncertainty in the charge radius from theory to be:

$$\Delta r_{rms}^{(theory)} = 0.06 \text{ fm}. \tag{8.78}$$

8.3.9 Thorium* (A = 232)

For thorium, the range chosen to vary the charge radius initially was 5.75−5.80 fm, and the transition energy for each interval calculated. The results of these calculations for the $2p_{1/2} - 2s$ transition are shown in Table 8.22, and graphed in figure 8.35.

Table 8.22: Points for $2p_{1/2} - 2s$ transition in Ac

R (fm)	E (eV)
5.75	271.122
5.76	271.057
5.77	270.992
5.78	270.927
5.79	270.862
5.8	270.797

The model fit to the points is also shown in Figure 8.35 and the residuals of the model is shown in Figure 8.36.

The equation specifying the model is given as:

$$E = 308.503 - 6.5011\ r_{rms}, \tag{8.79}$$

which when inverted obtain the relationship for the charge radius as a function of transition energy,

$$r_{rms} = 47.4543 - 0.1538E. \tag{8.80}$$

We can also obtain an expression for the uncertainty in r_{rms} via the derivative of the above equation:

$$\Delta r_{rms} = 0.1538\Delta E. \tag{8.81}$$

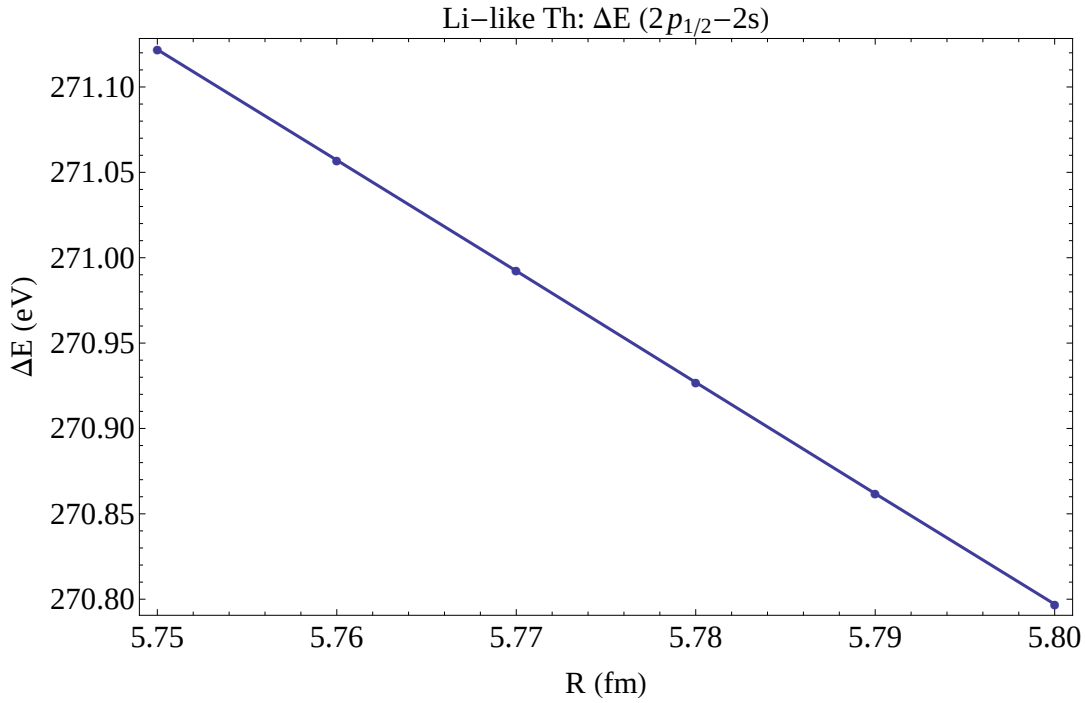

Figure 8.35: Energy variation vs. nuclear charge radius for $2p_{1/2} - 2s$ transition in Th.

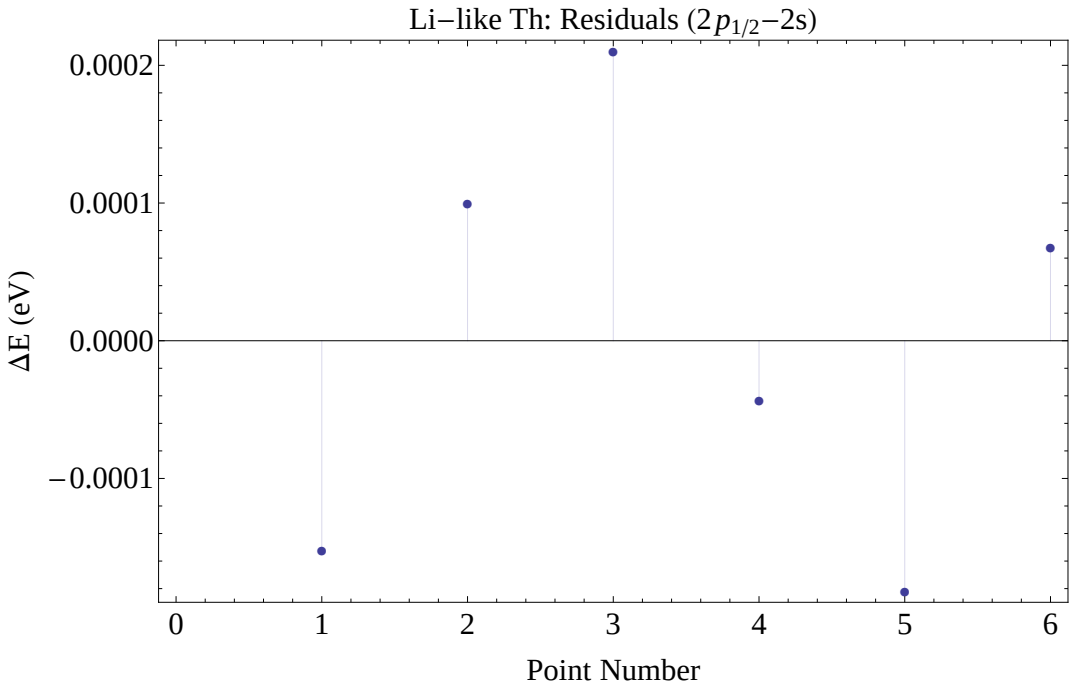

Figure 8.36: Residuals of the model for $2p_{1/2} - 2s$ transition in Th.

The theoretical uncertainty for the $2p_{1/2} - 2s$ transition of thorium is $\Delta E = 0.395$ eV, leading to an uncertainty in the charge radius from theory to be:

$$\Delta r_{rms}^{(theory)} = 0.061 \text{ fm}. \tag{8.82}$$

The results for the $2p_{3/2} - 2s$ transition are shown in Table 8.23, and graphed in figure 8.37.

Table 8.23: Points for $2p_{3/2} - 2s$ transition in Th.

R (fm)	E (eV)
5.75	4025.32
5.76	4025.25
5.77	4025.18
5.78	4025.11
5.79	4025.03
5.8	4024.96

The model fit to the points is also shown in Figure 8.37 and the residuals of the model is shown in Figure 8.38.

The equation specifying the model is given as:

$$E = 4066.75 - 7.2050\ r_{rms}, \tag{8.83}$$

which can be immediately inverted to obtain the relationship for the charge radius as a function of transition energy,

$$r_{rms} = 564.434 - 0.1388E. \tag{8.84}$$

We can also obtain an expression for the uncertainty in r_{rms} via the derivative of the above equation:

$$\Delta r_{rms} = 0.1388\Delta E. \tag{8.85}$$

The theoretical uncertainty for the $2p_{3/2} - 2s$ transition of thorium is $\Delta E = 0.385$ eV, leading to an uncertainty in the charge radius from theory to be:

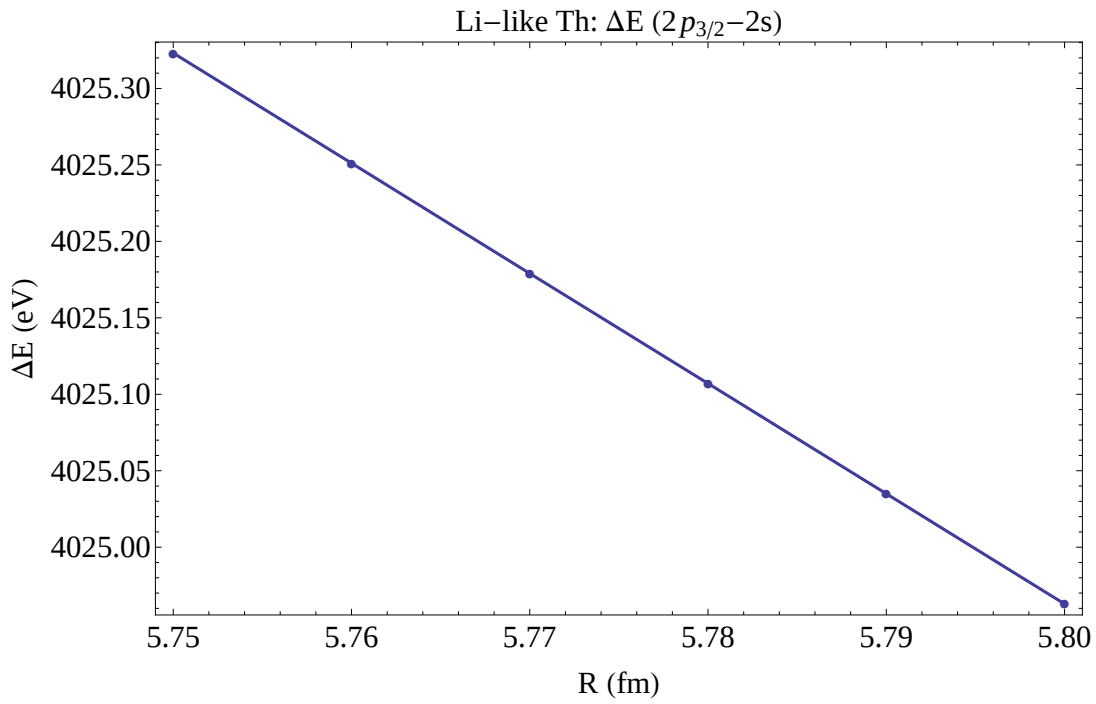

Figure 8.37: Energy variation vs. nuclear charge radius for $2p_{3/2} - 2s$ transition in Th.

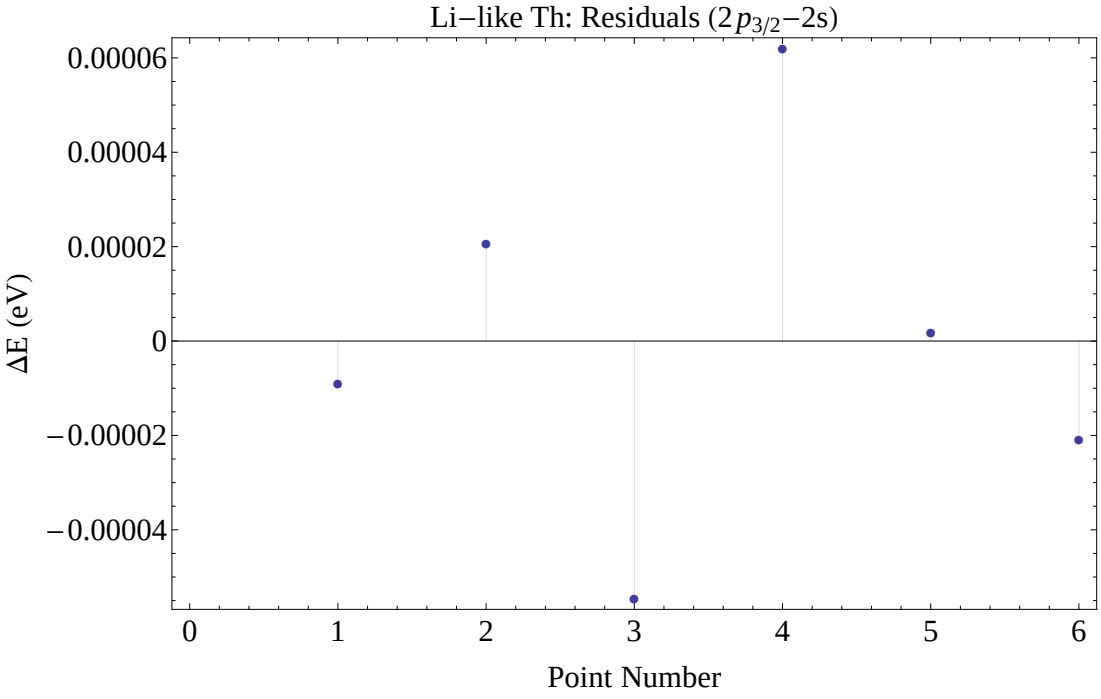

Figure 8.38: Residuals of the model for $2p_{3/2} - 2s$ transition in Th.

$$\Delta r_{rms}^{(theory)} = 0.053 \text{ fm}. \tag{8.86}$$

8.3.10 Protactinium* (A = 235)

For protactinium, the range chosen to vary the charge radius initially was 5.65 − 5.70 fm, and the transition energy for each interval calculated. The results of these calculations for the $2p_{1/2} - 2s$ transition are shown in Table 8.24, and graphed in figure 8.39.

Table 8.24: Points for $2p_{1/2} - 2s$ transition in Pa.

R (fm)	E (eV)
5.65	277.06
5.66	276.989
5.67	276.918
5.68	276.848
5.69	276.776
5.7	276.705

The model fit to the points is also shown in Figure 8.39 and the residuals of the model is shown in Figure 8.40.

The equation specifying the model is given as:

$$E = 317.205 - 7.1053\ r_{rms}, \tag{8.87}$$

which when inverted obtain the relationship for the charge radius as a function of transition energy,

$$r_{rms} = 44.6436 - 0.1407E. \tag{8.88}$$

We can also obtain an expression for the uncertainty in r_{rms} via the derivative of the above equation:

$$\Delta r_{rms} = 0.1407\Delta E. \tag{8.89}$$

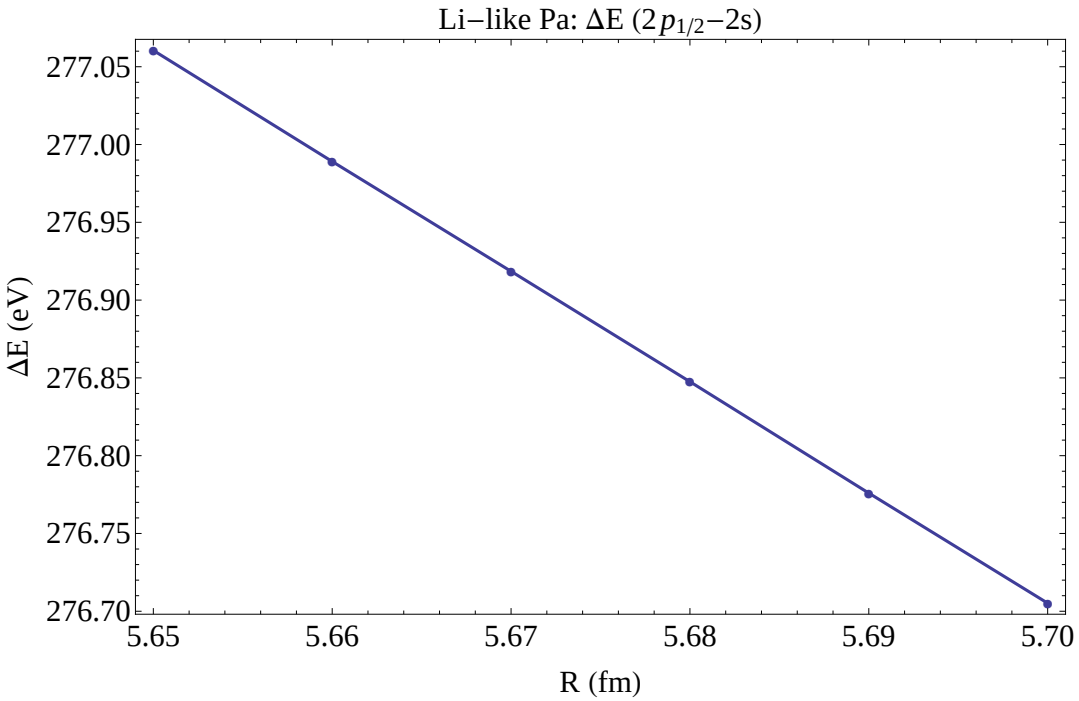

Figure 8.39: Energy variation vs. nuclear charge radius for $2p_{1/2} - 2s$ transition in Pa.

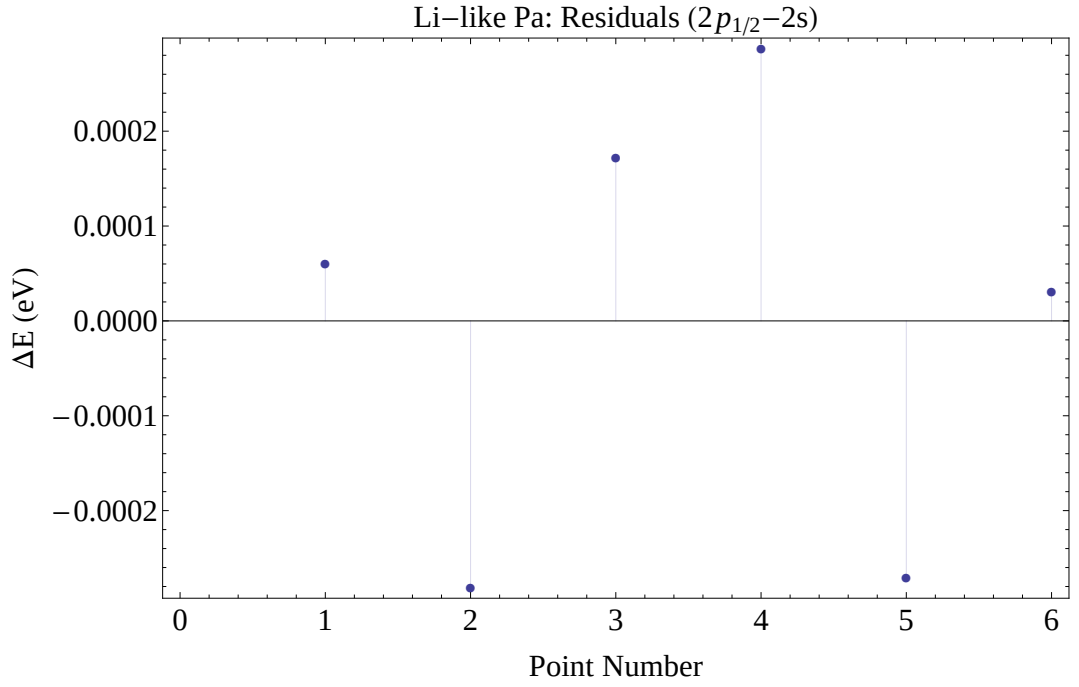

Figure 8.40: Residuals of the model for $2p_{1/2} - 2s$ transition in Pa.

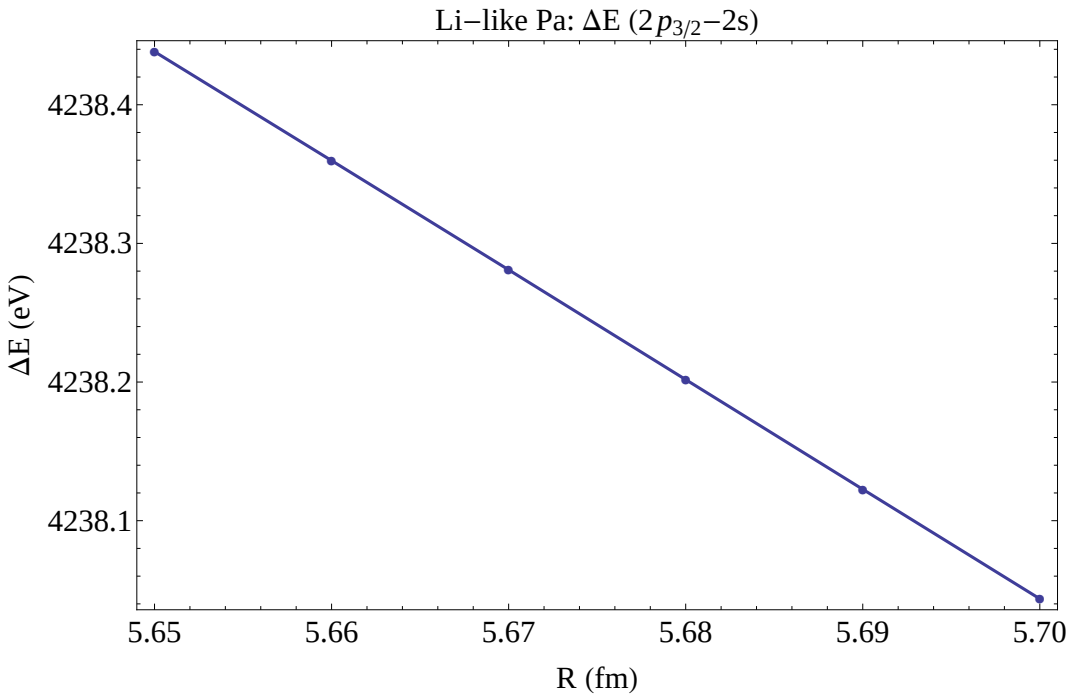

Figure 8.41: Energy variation vs. nuclear charge radius for $2p_{3/2} - 2s$ transition in Pa.

The theoretical uncertainty for the $2p_{1/2} - 2s$ transition of protactinium is $\Delta E = 0.503$ eV, leading to an uncertainty in the charge radius from theory to be:

$$\Delta r_{rms}^{(theory)} = 0.071 \text{ fm}. \tag{8.90}$$

The results for the $2p_{3/2} - 2s$ transition are shown in Table 8.25, and graphed in figure 8.41.

Table 8.25: Points for $2p_{3/2} - 2s$ transition in Pa

R (fm)	E (eV)
5.65	4238.44
5.66	4238.36
5.67	4238.28
5.68	4238.2
5.69	4238.12
5.7	4238.04

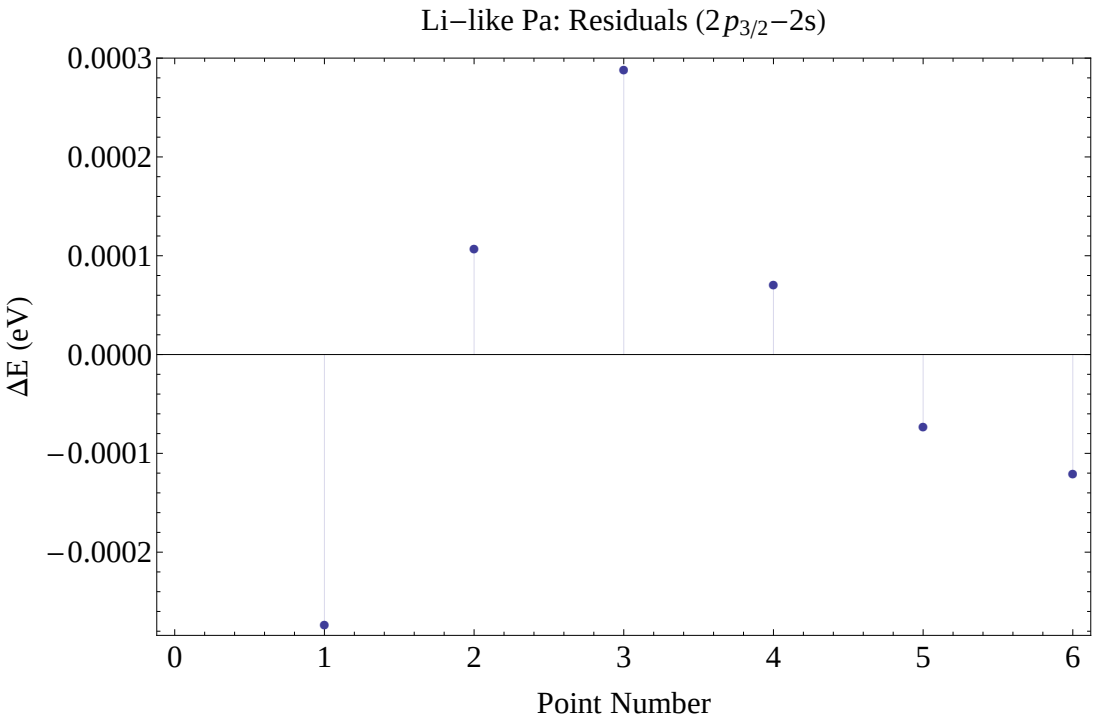

Figure 8.42: Residuals of the model for $2p_{3/2} - 2s$ transition in Pa

The model fit to the points is also shown in Figure 8.41 and the residuals of the model is shown in Figure 8.42.

The equation specifying the model is given as:

$$E = 4283.05 - 7.8961\ r_{rms}, \tag{8.91}$$

which can be immediately inverted to obtain the relationship for the charge radius as a function of transition energy,

$$r_{rms} = 542.424 - 0.1266E. \tag{8.92}$$

We can also obtain an expression for the uncertainty in r_{rms} via the derivative of the above equation:

$$\Delta r_{rms} = 0.1266\Delta E. \tag{8.93}$$

The theoretical uncertainty for the $2p_{3/2} - 2s$ transition of protactinium is $\Delta E = 0.494$ eV, leading to an uncertainty in the charge radius from theory to be:

$$\Delta r_{rms}^{(theory)} = 0.063 \text{ fm}. \tag{8.94}$$

8.3.11 Uranium (A = 238)

The results for the $2p_{3/2} - 2s$ transition in uranium are shown in Table 8.26, and graphed in figure 8.43.

Table 8.26: Points for $2p_{3/2} - 2s$ transition in U.

R (fm)	E (eV)
5.61	3445.67
5.62	3445.62
5.63	3445.57
5.64	3445.51
5.65	3445.46
5.66	3445.41
5.67	3445.35
5.68	3445.3

The model fit to the points is also shown in Figure 8.43 and the residuals of the model is shown in Figure 8.44.

The equation specifying the model is given as:

$$E = 4511.39 - 8.84836\ r_{rms}, \tag{8.95}$$

which can be immediately inverted to obtain the relationship for the charge radius as a function of transition energy,

$$r_{rms} = 509.856 - 0.1130E. \tag{8.96}$$

We can also obtain an expression for the uncertainty in r_{rms} via the derivative of the above equation:

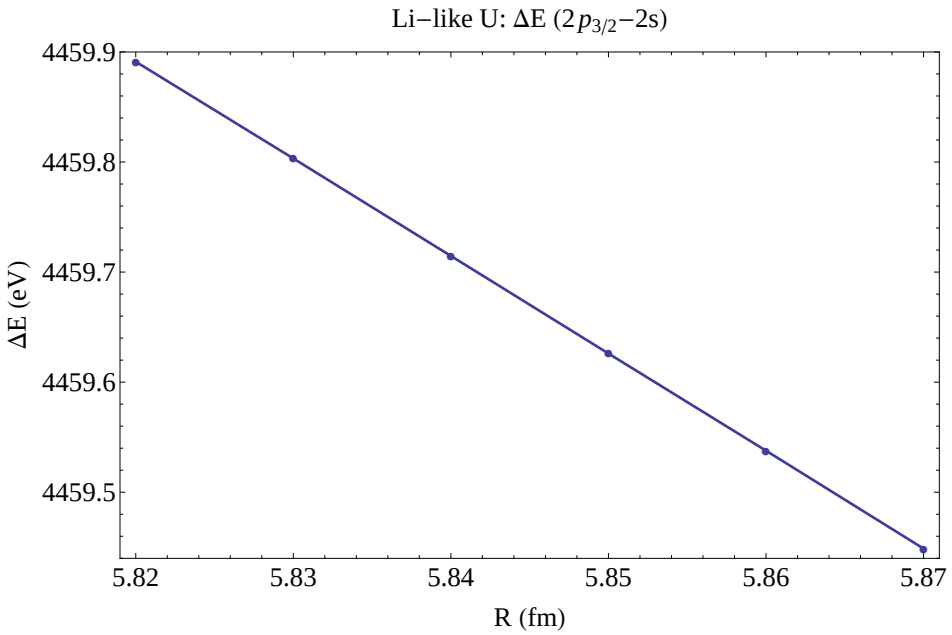

Figure 8.43: Energy variation vs. nuclear charge radius for $2p_{3/2} - 2s$ transition in U.

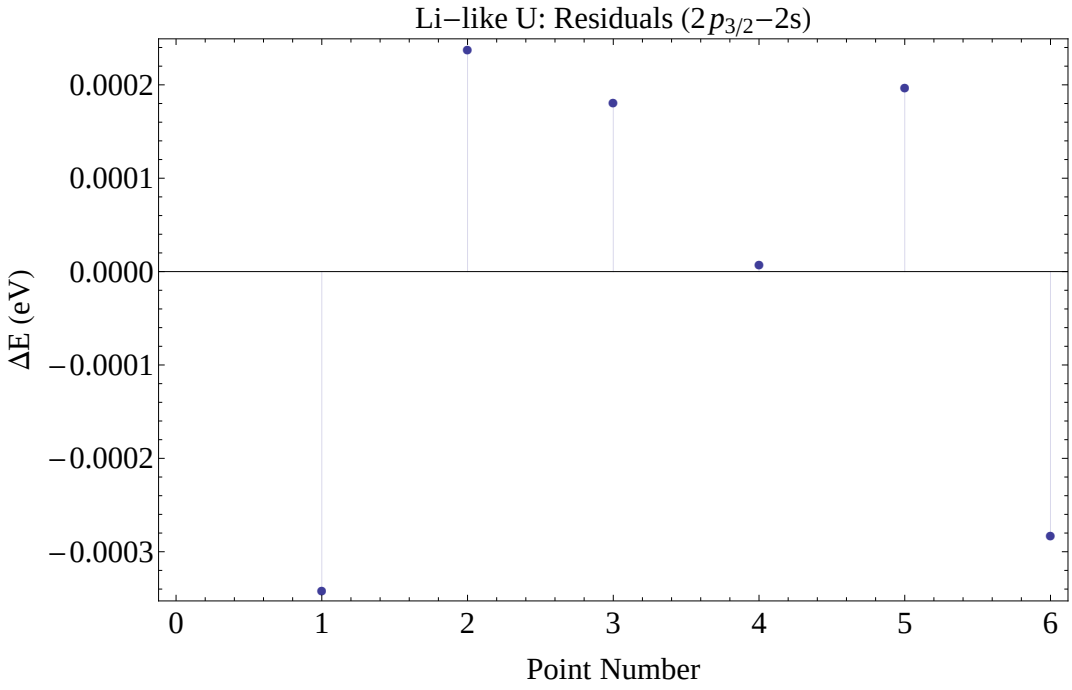

Figure 8.44: Residuals of the model for $2p_{3/2} - 2s$ transition in U.

$$\Delta r_{rms} = 0.1130 \Delta E. \tag{8.97}$$

The theoretical uncertainty for the $2p_{3/2} - 2s$ transition of uranium is $\Delta E = 0.065$ eV, leading to an uncertainty in the charge radius from theory to be:

$$\Delta r_{rms}^{(theory)} = 0.007 \text{ fm}. \tag{8.98}$$

Chapter 9

Conclusion

In this thesis we were able to obtain linear expressions relating the $2p_{1/2} - 2_s$ and $2p_{3/2} - 2_s$ transition energies for highly-charged ($Z = 82 \ldots 92$) Li-like ions and the nuclear charge radius of same said ions. The general method used was examining how the variation of the the nuclear charge radius effects the transition energy. From this it could be inferred that if a particular transition energy was experimentally obtained, this information would correspond to a particular nuclear charge radius, and thus the nuclear charge radius could be experimentally determined.

The main novelty of this technique comes in considering not only the leading contribution of the transition energy when performing our variation, the Dirac contribution, but also in considering the effect of changing the charge radius has on the leading radiative corrections: the one-loop QED and one-photon exchange contributions. This leads to a more accurate description of how the transition energy depends on the charge radius, and thus a more accurate charge radius should be extracted from a particular experimental transition energy.

Taking a broader view, we have learned that the current state of precision of atomic physics experiments in highly-charged ions together with the state of theoretical description can work together to provide information about a fundamental nuclear property, the charge radius. The relevance of this is two-fold: firstly, this scheme provides a new, complementary method of obtaining values of the nuclear charge radius, complementary to existing methods that probe the nucleus directly,

such as electron scattering. However, unlike the traditional methods, this scheme now opens up the possibility that radioactive nuclei, that heretofore have not had their nuclei measured via traditional techniques due to the necessity of collecting macroscopic amounts of the isotope into foils, can be studied experimentally via atomic physics experiments involving radioactive beam lines and EBITS. Secondly, the scheme now allows experiments involving heavy atoms that require accurate knowledge of their nuclear charge radius to be carried out and interpreted correctly. Several such high-profile experiments to study the fundamental symmetries of nature such as mirror symmetry and time reversal symmetry and their violation in heavy atoms have been proposed with the advent of powerful radioactive beam facilities, such as the TRIUMF facility in British Columbia. Candidate ions for such experiments are francium, radon, and radium – all elements with no stable isotopes and hence no nuclear charge radius information. For example, the Manitoba group working at TRIUMF is leading a mirror symmetry experiment in francium, which requires reliable knowledge of the nuclear charge radius in francium.

As was outlined in the Introduction, experiments of this type involve searches for electric dipole-moment transitions that are normally strictly forbidden by the symmetries of QED. However, interactions via the Weak force break these symmetries allowing these transitions to be accessed. Until the 1970s the current thought was that although possible, these now-allowed transitions would never actually be observed due to their low probability. The work of the Bouchiats in the mid 1970s showed conclusively that the experimental signatures of the aforementioned effects are actually enormously enhanced due to the strong electric field of the nucleus. Specifically, that the probability amplitudes of seeing forbidden transitions due to parity non-conservation were enhanced by about the third power of the nuclear charge, Z. Thus the strongest enhancement would be seen in highly charged ions, ions that in general are not stable. Furthermore, for highly-charged ions, a relativistic correction must be made in the calculation of the $s - p$ transition matrix, a correction that depends explicitly on value of the nuclear charge radius.

Until recently, techniques for performing these measurements did not exist. With their development, the timeliness of the results of this thesis are evident. Now exper-

imental groups have tools that will enable them to get a handle on the nuclear charge radius if spectroscopic information for the particular atom of interest is available. Currently, spectroscopic measurements of the required precision have been performed only for Bismuth and Uranium, thus it is only in these cases where we were able to test the viability of the method in this thesis.

The complete results of this analysis, for all elements between Lead and Uranium, are summarised in Table 9.1. It should be emphasised here that unlike the contributions to the transition energy mentioned above, the higher-order contributions: two-loop QED, two-photon exchange, three-photon exchange, screened-QED, and recoil, were not varied because, as in the case of two-loop QED and three-photon exchange effects the influence of a finite nuclear size itself is not completely understood, and secondly such a variation, at the two-loop order contributes at a level of $(\alpha/\pi)^2 \approx 5.4 \times 10^{-6}$, with respect to the Dirac finite nuclear size contribution, would come in at 20 eV $\times$ $(5.4 \times 10^{-6}) \approx 0.1$ meV level, a level well below both the current theoretical and experimental uncertainty. Thus the current published values for the energies due to these effects, using accepted nominal values for the charge radius where appropriate, were used to fill out the transition energies. Furthermore, the nuclear-polarization contribution was calculated explicitly for a nominal charge radius, but not varied. This was done because the lack of experimental knowledge of the nuclear polarization parameters introduces errors that overwhelm the effect of making small variations in the nuclear charge radius.
The method is also stable against experimental uncertainties, in that as experimental results improve the method should provide more accurate results.

9.1 Outlook

In this section some comments will be made about the future viability of this project, as well as directions for possible improvement. Two possible directions can be taken: firstly, the dependence of the second-order radiative corrections on the nuclear charge radius could be explicitly elucidated, in an analogous manner to the first-order corrections. However, the scaling problem still remains, with each new

Table 9.1: Table of final results obtained in this thesis together with their uncertainties. All uncertainties listed are due to uncertainties in the theory except those indicated with a *, where both theoretical and available experimental uncertainties are combined in quadrature. The units of E is eV.

Z	A	j $(2p_j - 2s_{1/2})$	$r_{rms}(E)$ (fm)	$\Delta r_{rms}(E)$ (fm)
82	208	1/2	$84.2298 - 0.3414E$	0.033
		3/2	$839.475 - 0.3157E$	0.019
83	209	1/2	$78.458 - 0.3093E$	0.03
		3/2	$802.117 - 0.2857E$	0.023*
84	209	1/2	$73.1304 - 0.2807E$	0.028
		3/2	$764.594 - 0.2581E$	0.016
85	210	1/2	$68.1437 - 0.2545E$	0.025
		3/2	$728.721 - 0.2332E$	0.014
86	222	1/2	$62.7536 - 0.2278E$	0.022
		3/2	$686.718 - 0.2083E$	0.013
87	223	1/2	$58.7604 - 0.2075E$	0.02
		3/2	$656.894 - 0.1890E$	0.012
88	226	1/2	$54.5175 - 0.1871E$	0.02
		3/2	$623.298 - 0.1702E$	0.011
89	227	1/2	$51.1712 - 0.1708E$	0.017
		3/2	$597.252 - 0.1547E$	0.01
90	232	1/2	$47.4543 - 0.1538E$	0.015
		3/2	$564.434 - 0.1388E$	0.009
91	231	1/2	$44.6436 - 0.1407E$	0.014
		3/2	$542.424 - 0.1266E$	0.008
92	238	1/2	$41.251 - 0.1261E$	0.018*
		3/2	$509.856 - 0.1130E$	0.007

order introducing a new factor of α/π. Thus, performing this type of analysis beyond second-order seems futile. Secondly it's clear that, for the foreseeable future, the nuclear polarization contribution will always be the final barrier to the precision of the method. The reduction of uncertainties in the QED and many-body contributions will not mitigate the uncertainties arising from the nuclear polarization contribution simply due to the lack of knowledge in this area. Thus the theoretical uncertainty in calculations of the transition energy will bottom out at about 0.05 eV, leading to the theoretical uncertainty for the charge radius to be those shown in Table 9.2. Thus until future work pins down the values of the "B" coefficients and their corresponding transition energies to a greater degree, the uncertainties arising from this effect will remain large.

A few final words should also be said about future experimental implementation to obtain the necessary spectroscopic information. Earlier we discussed that the recent advance of coupling EBIT/S devices with radioactive beam facilities have become available over the past decade (TITAN-EBIT at ISAC, REXEBIS at ISOLDE, ReA EBIT, NSCL) and more are coming online (e.g. CANREB/TRIUMF) However significant challenges still remain, these include the difficulty of breeding Li-like ions above bismuth, as well as achieving good optical access for the x-ray spectrometer. Furthermore, none of the current on-line breeders can achieve the 100 keV electron beams used for Bi^{80+} by Beiersdorfer et al. [15]. Once these experimental challenges are overcome, the potential of the work presented in this thesis can be fully realized.

Table 9.2: Table of uncertainties for the nuclear charge radius coming from the theoretical calculations.

Z	A	j $(2p_j - 2s_{1/2})$	$\Delta r_{rms}(E)$ (fm)
82	208	1/2	0.034
		3/2	0.021
83	209	1/2	0.023
		3/2	0.014
84	209	1/2	0.035
		3/2	0.022
85	210	1/2	0.070
		3/2	0.061
86	222	1/2	0.030
		3/2	0.023
87	223	1/2	0.027
		3/2	0.020
88	226	1/2	0.037
		3/2	0.031
89	227	1/2	0.067
		3/2	0.060
90	232	1/2	0.061
		3/2	0.053
91	231	1/2	0.071
		3/2	0.063
92	238	1/2	0.018
		3/2	0.007

Appendix A

Appendix 1: The RADIAL Program

This appendix summarizes the Fortran 77 package RADIAL used for calculating the "Dirac term" for the transition energy and wave-functions. All information described here is presented in more detail in Salvat et al. [72, 73], and is presented here for completeness of presentation. In its original form, RADIAL is able to calculate solutions to both the radial Schrödinger and Dirac equations for free and bound systems. However, only the bound-Dirac case was used in this thesis, thus only the bound-state Dirac equation solution will be discussed in any detail. Exceptions will be made if they pertain directly to the Dirac case.

An introduction to the bound-state Dirac equation was given in chapter 3, so those details will not be repeated here, thus we will begin our exposition with the potentials. RADIAL considers potentials of form $\mathcal{V}(r) \equiv rV(r)$ that are finite for all values of r, and reaches constant values when $r \to 0$ and $r \to \infty$. The function $\mathcal{V}(r)$ used in the calculations is the natural cubic spline that interpolates the values of a table provided by the user.

The radial wave equations for the cubic-spline are solved by using an exact power-series expansion of the radial functions, which are then summed up to the prescribed accuracy; thus truncation errors are completely controlled, while only round-off errors are of concern.

A.1 Power series solution of the radial equations

We will now look at the general approach RADIAL uses to calculate the wavefunctions and eigenvalues for bound states ($E \leqslant 0$) of the Dirac equation. It is important to note that RADIAL performs its calculations in generalized atomic units. In this system, the reduced Planck constant $\hbar$, the absolute value of the electron charge e, and mass of the electron m_e are equal to 1. In atomic units, energy and length are given by $E_0 = m_e e^4/\hbar^2$ (Hartrees) and $a_0 = \hbar^2/(m_e e^2)$ (Bohr radius). Furthermore, the speed of light is given by, $c = 1/\alpha$. In terms of more familiar units, $E_0 = 27.2114$ eV and $a_0 = 0.529177$ Å. As we saw in chapter 3, using these units leads to radial Dirac equations of the form

$$\begin{aligned} \frac{dP}{dr} &= \frac{-\kappa}{r}P + \frac{E - V + 2c^2}{c}Q, \\ \frac{dQ}{dr} &= \frac{E - V}{c}P + \frac{\kappa}{r}Q. \end{aligned} \tag{A.1}$$

To solve (A.1), one assumes that the values of the radial functions are known at a radial point r_a. The aim is to determine the functions in the interval between r_a and r_b, where the potential function is given by,

$$rV(r) = v_0 + v_1 r + v_2 r^2 + v_3 r^3. \tag{A.2}$$

At this point, we can introduce new variables:

$$x \equiv (r - r_a)/h, \qquad h \equiv r_b - r_a, \tag{A.3}$$

from which we can re-express equation (A.1) as

$$\begin{aligned} &(r_a + hx)\mathcal{P}' - \sigma|\kappa|h\mathcal{P} - \mathcal{U}h\mathcal{Q} + 2ch(r_a + hx)\mathcal{Q} = 0, \\ &(r_a + hx)\mathcal{Q}' + \sigma|\kappa|h\mathcal{Q} + \mathcal{U}h\mathcal{P} = 0, \end{aligned} \tag{A.4}$$

where

$$\mathcal{P}(x) \equiv P(r), \qquad \mathcal{Q}(x) \equiv Q(r), \tag{A.5}$$

and

$$\mathcal{U}(x) \equiv \frac{r[V(r) - E]}{c} = u_0 + u_1 x + u_2 x^2 + u_3 x^3. \tag{A.6}$$

We now introduce polynomial expansions for the functions $\mathcal{P}$ and $\mathcal{Q}$ in the form,

$$\mathcal{P}(x) = \sum_{n=0}^{\infty} a_n x^n, \qquad \mathcal{Q}(x) = \sum_{n=0}^{\infty} b_n x^n, \tag{A.7}$$

and substitute these results into (A.4). From this substitution we obtain the following recursion relations for the expansion coefficients a_n, and b_n,

$$\begin{aligned} a_n =& \frac{h}{nr_a}\left[-(n-1-\sigma|\kappa|)a_{n-1}\right. \\ &\left.+(u_0 - 2cr_a)b_{n-1} + (u_1 - 2ch)b_{n-2} + u_2 b_{n-3} + u_3 b_{n-4}\right], \\ b_n =& -\frac{h}{nr_a}\left[u_0 a_{n-1} + (n-1+\sigma|\kappa|)b_{n-1} + u_1 a_{n-2} + u_2 a_{n-3} + u_3 a_{n-4}\right]. \end{aligned} \tag{A.8}$$

Applying these relations together with the boundary conditions,

$$a_0 = P(r_a), \qquad b_0 = Q(r_a), \tag{A.9}$$

determines the a and b coefficients entirely.

Special series expansions must be used to start the solutions off at $r_a = 0$, given as

$$\mathcal{P}(x) = x^s \sum_{n=0}^{\infty} a_n x^n, \qquad \mathcal{Q}(x) = ^{s+t} \sum_{n=0}^{\infty} b_n x^n. \tag{A.10}$$

Applying these to (A.4) leads to the following recurrece relations for the expansion coefficents:

$$(s+n-\sigma|\kappa|)a_n - u_0 b_{n-t} + (u_1 - 2ch)b_{n-t-1} - u_2 b_{n-t-2} - u_3 b_{n-t-3} = 0,$$
$$(s+n+\sigma|\kappa|)b_{n-t} + u_0 a_n + u_1 a_{n-1} + u_2 a_{n-2} + u_3 a_{n-3} = 0. \quad \text{(A.11)}$$

The parameters s and t are determined by using the value of u_0 and the condition that the solutions be regular at the origin, $r = 0$. The wavefunctions are normalized at the second grid-point r_2 such that

$$P(r_2) = 1, \qquad Q(r_2) = \mathcal{Q}(1)/\mathcal{P}(1). \quad \text{(A.12)}$$

RADIAL uses the power-series expansion method above to solve the radial Dirac equations using a user specified accuracy parametrized by the variable ϵ. The user specifies a radial grid for which the values of the radial functions are given, but it should be pointed out that this radial grid may be different from the potential grid discussed above. If the two grids are different RADIAL merges them together and performs a sort so that the new grid points appear in strictly ascending order and $r_1 = 0$. Since we are ultimately dealing with bound-state solutions, the final point in the grid, r_{NT} must be made large enough so that the probability of finding the electron at a distance farther out than r_{NT} is negligible.

A.2 Bound State Eigenvalues

In this section we will discuss how bound-state energies ($E \leq 0$) are determined for specified quantum numbers. It turns out that many of the features of this method are quite similar to those given in Johnson [44] for their solution to the bound-Dirac problem.

For a given energy in the allowed interval, the power series method described above is used to extend the numerical solution outward from $r = 0$ up to a certain grid point r_m, which is further out than the outer turning point determined by the condition:

$$V(r_i) > E - \frac{l(l+1)}{2r_i^2} \qquad \text{if } i \geq m. \tag{A.13}$$

To obtain the solution, what must be done first is to ensure that for a given value of E, the outward solution from 0 to r_m, has the correct number of nodes given by the radial quantum number $n_r = n - (l+1)$ and n is the principal quantum number. To ensure that the correct number of nodes are found, a dense enough grid must be used so that there is at most a single node between two grid points; since the number of nodes of $P(r)$ are determined from its value at the grid points.

When the energy giving the correct number of nodes has been obtained for the outward solution, the solution is started at point r_{NT} and worked inwards to r_m. Then the inward solution is successively renormalized in order to satisfy the matching condition at r_m, that is $P_{in}(r_m) = P_{out}(r_m)$. Successive refinements are made to the solution ΔE from the discontinuity or $Q(r)$ at r_m as described by Mayers [55].

Specifically, for large enough radii the potential energy $V(r)$ becomes negligible when compared to the relativistic energy-momentum condition $E + 2c^2$. When this occurs, one can rewrite (A.1) by combining the two coupled equations into a single second-order differential equation for the large component P

$$P"(r) - \mu(r)P(r) = 0, \tag{A.14}$$

where,

$$\mu(r) \equiv \left[\frac{E+2c^2}{c^2}\left(V(r) - E\right) + \frac{l(l+1)}{r^2}\right]^{1/2}. \tag{A.15}$$

The inward solution is started at a point $r_\infty \gg r_m$, determined as the minimum grid point that satisfies the condition, $r_\infty\, \mu(r_\infty) > 75$, by applying equation (A.1) together with the following relation for the ratio of the large component to its derivative,

$$\frac{P'(r)}{P(r)} = -\frac{1}{2}\mu'\mu^{-1} - \mu. \tag{A.16}$$

This combination leads to the expression,

$$\frac{Q(r)}{P(r)} \approx -\frac{c}{E+2c^2}\left(\frac{\kappa}{r}+\frac{P'(r)}{P(r)}\right) = -\frac{c}{E+2c^2}\left(\frac{\kappa}{r}-\frac{1}{2}\mu'\mu^{-1}-\mu\right). \tag{A.17}$$

From this we obtain the formula for the eigenvalue correction, given by [55]:

$$\Delta E = cP(r_m)[Q_{in}(r_m) - Q_{out}(r_m)] \left\{ \int_0^\infty \left(P^2(r)+Q^2(r)\right) dr \right\}^{-1}. \tag{A.18}$$

As mentioned above, this summary highlights only the main points of the methods used by RADIAL. The interested reader is encouraged to go to the original manuals to fill in the missing steps.

Appendix B

Appendix 2: Mathematica Packages

B.1 Introduction

In this appendix we give the explicit Mathematica code used in this thesis. Three Mathematica "packages" were written and used together. The first two packages, "NRadius" and "NuclearPolarization" will be discussed here, while the third, "BSpline" will be described in Appendix C.

In Mathematica, packages are text files that contain Mathematica commands, designed to make it easy for users to distribute their programs to other users. In addition, packages provide a framework to write programs that can be integrated with Mathematica in a seamless manner. Importantly, this framework provides a name localizing construct, analogous to classes in other languages. This allows the programmer to define a collection of functions for export, called "public" functions, that are specific for users of the package to work with. Other auxiliary functions which are not for export, called "private", are not intended to be accessible to users [88, 86].

The basic template of a Mathematica package is the following [86]:

```
BeginPackage["package`"]

(* usage messages *)
package::usage = "usage message here...";

(* options *)
Options[package] = {opt1 → value1, opt2 → value2, ...}

(* private context *)
Begin["`Private`"]

(* function definitions *)
fun[] := ...
fun2[] := ...

(* end private context *)
End[]

EndPackage[]
```

The features mentioned above were the main motivating factors for using the package framework for writing the code for this thesis. In addition, Mathematica has very powerful numerical integration routines, all falling under the "NIntegrate[]" function framework, for evaluating integrands of all types [88]. This feature was also a motivating factor for the code having the form that it does.

B.2 "NRadius" Mathematica Package

The "NRadius" package brings together in one place all the tools developed for this PhD thesis; thus the codes gathered here allow for the calculation of the various

contributions to the 2p-2s transition energy as defined in the chapters of this thesis. The "NRadius" package is the "master" package as it were that calculates the main QED contributions. Currently the package uses the Fortran code RADIAL, called in Mathematica via the "MathLink" formalism, allowing external compiled code to be called as a Mathematica function, to calculate the energies and wavefunctions of the Dirac equation for hydrogenic ions using a Fermi nuclear charge distribution. The potential due to the Fermi nuclear charge distribution is calculated in NRadius as a private function.

To obtain the results shown in this thesis, a loop should be setup over an appropriate range of nuclear charge radii. Here the nominal charge radii as given in Angeli tables [4] were used as a guide in selecting the range. In the body of the loop, the energy components of the transition energy are evaluated sequentially for each radius value.

B.2.1 "NRadius" Functions

In this section we list the usable functions of the NRadius package, see the above comments for the meaning of "usable".

fermiPotential: generates the potential based on the Fermi two-parameter model. This procedure may take some time to evaluate for a large number of grid points.

Input:

- Ze : electron number (negative)
- Rr : RMS nuclear charge radius (fm)

diracPointEnergy: This procedure calculates the bound-state H-like Dirac equation assuming a point nucleus.

Input:

- Ze : electron number (negative)
- n : principal quantum number
- k : angular momentum

diracHSEnergy: This procedure calculates the bound-state H-like Dirac equation assuming a Hard-Sphere nuclear charge distribution.

Input:

- Ze : electron number (negative)
- RMS : root-mean-squared charge radius
- n : principal quantum number
- k : angular momentum

diracEnergy: This procedure calculates the bound-state H-like Dirac equation assuming a Fermi nuclear charge distribution.

Input:

- Ze : electron number (negative)
- RMS : root-mean-squared charge radius
- n : principal quantum number
- k : angular momentum

oneLoopQED: Calculates the complete one-loop correction to the Lamb shift in H-like ions s a function of Z for the 2p-2s transition.

Input:

- Z : nuclear charge
- r : rms radius (Fermi)
- j : angular momentum of p state

twoPhotonExchange: Calculates the two-photon exchange correction for lithium-like heavy ions for either $2p_{1/2}$ or $2p_{3/2}$ valence states.

Input:

- Zv : ion nuclear charge
- nv : valence principal quantum number
- lv : valence orbital state
- jv : valence total angular momentum

threePhotonExchange: Calculates the three-photon exchange correction for lithium like heavy ions (Z=83-92)for the $2p_{3/2} - 2s$ transition energy.

Input:
- Zv : ion nuclear charge

twoLoopQED: Calculates the complete two-loop QED correction to the Lamb shift in H-like ions as a function of Z.

Input:
- Z : nuclear charge
- n : principal quantum number
- kappa1: lower state angular momentum (s)
- kappa2: upper state angular momentum (p1/2, p3/2)

screenedQED: Calculates the QED contribution due to electron screening for the $2p_{3/2} - 2s$ transition energy (eV) in Li-like ions using the results of Optics and Spectroscopy, Vol. 99, No. 1, 2005.

Input:
- Z : charge number

nuclearRecoil: Calculates the nuclear recoil contribution to the $2p_{3/2} - 2s$ transition energy for highly-charged Li-like ions as a function of Z for the range (Z=83-92).

Input:
- Z : charge number

triangleCoefficient: Calculates the triangle condition, often encountered in angular momentum reduction calculations

nineJSymbol: nineJSymbol calculates the 9-J symbol occuring when four angular

momentum operators are combined; 3-J and 6-J symbols are part of native MATHEMATICA.

baseInfo: Exhibits information about the base states

B.2.2 "NRadius" Code

```
(* : Title : NRadius.m *)
(* :Context: NRadius` *)
(* :Author: Andrew S. M Senchuk *)
(* :Summary:
  This package contains all the functions required to evaluate the 2s-2p Lamb shift energy
      as a function of nuclear charge radius.
*)
(* :Copyright: 2017 by Andrew Senchuk *)
(* :Package Version: 1.0 *)
(* :Mathematica Version: 9.0 *)
(* :History: *)
(* :Keywords: Lamb shift, nuclear charge radius, highly charged ions, Quantum Electrodynamics
    *)
(* :Sources: *)
(* :Warnings: <description of global effects, incompatabilities > *)
(* : Limitations : <special cases not handled, known problems> *)
(* : Discussion : <description of algorithm, information for experts *)
(* :Requirements: RADIAL: a Fortran subroutine package for the solution of the radial dirac
    equation *)
(* :Examples: <sample input that demonstrates the features of this package> *)

(* set up package context, including public imports *)

BeginPackage["NRadius`"];

(* usage messages *)

```

```
25 NRadius::usage="The NRadius package brings together in one place all the MATHEMATICA tools
     developed by Andrew Senchuk for his PhD thesis. The topic of the thesis was the determination
     of absolute nuclear charge radii using x-ray spectroscopy in Li-like highly-charged ions;
     thus the codes gathered here allow for the calculation of the various contributions to the
     2S-2P transtition energy. (Note that curreclty the package must be used in conjunction
     with the Fortran code RADIAL, called in MATHEMATICA, which calculates the energies and
     wavefunctions of the Dirac equation for hydrogenic ions using a Fermi nuclear charge
     distribution ) Included functions: (for calculating transition energy) fermipotential ,
     diracPointEnergy, diracEnergy, onePhotonExchange, oneLoopQED, twoLoopQED,
     screenedQED, nuclearRecoil, nuclearPolarization, omegaL, bEL (for angular momentum
     calculation) triangularCoefficient , nineJSymbol";
26
27 fermiPotential :: usage="fermiPotential[Ze, Rr] generates the potential based on the Fermi two-
     parameter model. WARNING: This procedure may take some time to evaluate for a large number
     of grid points.
28   Input: Ze : electron number (negative)
29   Rr : RMS nuclear charge radius (fm)";
30
31 diracPointEnergy :: usage="This procedure calculates the bound-state H-like Dirac equation
     assuming a point nucleus.
32   Input: Ze : electron number (negative)
33   n : principal quantum number
34   k : angular momentum";
35
36 diracHSEnergy::usage="This procedure calculates the bound-state H-like Dirac equation assuming
     a Hard-Sphere nuclear charge distribution .
37   Input: Ze : electron number (negative)
38   RMS : root-mean-squared charge radius
39   n : principal quantum number
40   k : angular momentum";
41
42 diracEnergy :: usage="This procedure calculates the bound-state H-like Dirac equation assuming a
     Fermi nuclear charge distribution .
43   Input: Ze : electron number (negative)
44   RMS : root-mean-squared charge radius
45   n : principal quantum number
46   k : angular momentum";
```

```
47
48 onePhotonExchange::usage="onePhotonExchange[Zv,rms,nv,lv,jv] calculates the one-photon
       exchange correction in Li-like ions using the wavefunctions generated via the RADIAL
       program.
49   Input: Zv : nuclear charge
50   rms : nuclear charge radius
51   nv : valence principal quantum number
52   lv : valence orbital state
53   jv : valence total angular momentum";
54
55 oneLoopQED::usage="Calculates the complete one-loop correction to the Lamb shift in H-like ions
       s a function of Z for the 2p-2s transition.
56   Input: Z : nuclear charge
57   r : rms radius (Fermi)
58   j : angular momentum of p state";
59
60 twoPhotonExchange::usage="twoPhotonExchange[Zv,nv,lv,jv] calculates the two-photon exchange
       correction for lithium-like heavy ions for either 2p1/2 or 2p3/2 valence states.
61   Input: Zv : ion nuclear charge
62   nv : valence principal quantum number
63   lv : valence orbital state
64   jv : valence total angular momentum ";
65
66 threePhotonExchange::usage="threePhotonExchange[Zv] calculates the three-photon exchange
       correction for lithium like heavy ions (Z=83 - Z=92)for the 2p3/2-2s transition energy.
67   Input: Zv : ion nuclear charge";
68
69 twoLoopQED::usage="Calculates the complete two-loop QED correction to the Lamb shift in H-like
       ions as a function of Z.
70   Input:
71     Z : nuclear charge
72     n : principal quantum number
73     kappa1: lower state angular momentum (s)
74     kappa2: upper state angular momentum (p1/2, p3/2)";
75
76 screenedQED::usage="screenedQED[Z] calculates the QED contribution due to electron screening for
       the 2p3/2-2s transition energy (eV) in Li-like ions using the results of Optics and
```

```
    Spectroscopy, Vol. 99, No. 1, 2005.
77  Input: Z : charge number";
78
79  nuclearRecoil :: usage="nuclearRecoil[Z] calculates the nuclear recoil contribution to the 2S1
    /2-2P3/2 transition energy for highly-charged Li-like ions as a function of Z for the range
    (Z=83-92).
80  Input: Z : charge number";
81
82  triangleCoefficient :: usage="Calculates the triangle condition, often encountered in angular
    momentum reduction calculations";
83
84  nineJSymbol::usage="nineJSymbol calculates the 9-J symbol occuring when four angular momentum
    operators are combined; 3-J and 6-J symbols are part of native MATHEMATICA.";
85
86  baseInfo :: usage="Exhibits information about the base states";
87
88  (* error messages *)
89
90  (* options*)
91
92  (* private context *)
93  Begin["`Private`"];
94
95  ClearAll["Global`*"]
96
97  ClearMemory:=Module[{},Unprotect[In,Out];
98  Clear[In,Out];
99  Protect[In,Out];
100 ClearSystemCache[];]
101
102 ClearMemory;
103
104 (* Declarations *)
105
106 (* Initilaize atomic parameters *)
107 bohrRadius=5.2917721092*10^-11;
108 reducedComptonWavelength=3.8615926459*10^-13;
```

```
 alpha=0.0072973525376;
electronRestEnergy=QuantityMagnitude@UnitConvert[Quantity["ElectronMass"] Quantity["
    SpeedOfLight"]^2,"Electronvolts"];
energySommerfeld[Z_,n_,kappa_]:=(1+((0.007297352569800 Z)/(n-Abs[kappa]+Sqrt[kappa
    ^2-(0.007297352569800 Z)^2]))^2)^(-1/2)

(* Initialize RADIAL grid parameters *)
NV=6000;
RATIO=1.15;
RNN=0.65999;
STEP=RNN/(NV-100.0);

(* *)
Zpoints ={82,83,84,85,86,87,88,89,90,91,92};
MassRatio={379037,380866,380868,382699,404628,406454,411932,413758,422890,
          421063,433849};
SelfS12={2.077345,2.085316,2.094152,2.103876,2.11452,2.12610,2.13867,2.15225,
          2.166883,2.18262,2.199494};
UehlS12={-0.445583,-0.455731,-0.466384,-0.477573,-0.489332,-0.501701,-0.514721,
          -0.528436,-0.542896,-0.558156,-0.574274};
WkS12={0.029690,0.020497,0.021343,0.022230,0.023160,0.024138,0.025165,0.026245,
          0.027383,0.028581,0.029845};
SelfP12={0.206317,0.215830,0.225680,0.235886,0.2464700,0.257454,0.268864,
          0.280727,0.293072,0.305933,0.319341};
UehlP12={-0.057500,-0.060619,-0.063929,-0.067444,-0.071882,-0.075159,-0.079395,
          -0.083910,-0.088728,-0.093874,-0.099377};
WkP12={0.003588,0.003844,0.004120,0.004414,0.004731,0.005070,0.005434,0.005826,
          0.006246,0.006699,0.007186};
SelfP32={0.271861,0.274204,0.276550,0.278898,0.281249,0.283602,0.285956,
          0.288312,0.290668,0.293024,0.295380};
UehlP32={-0.003354,-0.003433,-0.003513,-0.003594,-0.003677,-0.003760,-0.003845,
          -0.003931,-0.004019,-0.004108,-0.004198};
WkP32={0.000497,0.000519,0.000542,0.000565,0.000590,0.000615,0.000642,0.000669,
          0.000697,0.000726,0.000756};

(* Define the core electron properties *)
nc=1;lc=0;jc=1/2;kappac=(lc-jc) (2 jc+1);kc=Abs[kappac]; Zc=Z;
```

```
144 gammac=(kappac^2-( alpha Zc)^2)^(1/2);
145 Enc= alpha^-2 (1+( alpha*Zc)^2/(gammac+nc-kc)^2)^(-1/2);
146 zTest=0;
147 rmsTest=0;
148
149 (* Galerkin method parameters *)
150 order=7;
151  splinebasiscnt =30;                (* Number of splines to form the basis *)
152 Np=splinebasiscnt+4-order;          (* Number of knots *)
153 numberofterms=2*splinebasiscnt;           (* total number of psuedo-states that will be generated
        for H-like Dirac equation *)
154
155 (* Private Functions *)
156
157 (* Dirac Energy - functions here link with F77 code RADIAL *)
158
159 grid[RATIO_,STEP_,RN_,NP_]:=Module[
160 {A,B,CC,CN,FR,FU, NDIM,R,RL,RR,RU},
161 (* This procedure sets up a radial grid R(N) (N=1,...,NP) *)
162 (* such that                                                *)
163 (*     1) R(1)=0, R(NP)=RN,                                 *)
164 (*     2) A*R(N)+B*Log[R(N)]-C=N (N>0)with                  *)
165 (*          A=1.0/STEP and B=1.0/Log[RATIO].                *)
166
167 (* declare local variables *)
168 (* define initial values *)
169 NDIM=8000;
170 R=Table[0.0,{1},{NP}];
171 A=(1.0)/STEP;
172 B=1.0/Log[RATIO];
173 CC=NP-A*RN-B*Log[RN];
174 R[[1,1]]=0.0;
175 RR=1.0*10^-35;
176 FR=A*RR+B*Log[RR]+CC-1;
177
178 (* test NP lower limit *)
179  If[NP<50,Return["*** ERROR IN GRID: NP =",NP," MUST BE LARGER THAN 50."]];
```

```
180
181 (* test NP upper limit *)
182 If[NP>NDIM,Return["*** ERROR IN GRID: NP =",NP," IS LARGER THAN NDIM."]];
183
184   (* test STEP and RATIO *)
185 (*If[(STEP<1.0*10^-10)\[Or]((RATIO-1.0)<1.0^-3),Return["*** ERROR IN GRID: STEP =",
      STEP ," OR RATIO =",RATIO ," ARE TOO SMALL"]];
186 *)
187 (* test R(2) of grid *)
188 If[FR>0.0, Return["*** ERROR IN GRID: R(2) is TOO SMALL."]];
189
190 (* calculate grid *)
191 Do[CN=CC-N;
192       RL=RR;
193       RU=RL;
194       RU=RU+RU;
195       FU=A*RU+B*Log[RU]+CN;
196       While[FU<0.0,RU=RU+RU;FU=A*RU+B*Log[RU]+CN;];
197       RR=0.5*(RU+RL);
198       FR=A*RR+B*Log[RR]+CN;
199        If[FR>0.0,RU=RR;,RL=RR;];
200       While[(RU-RL)>(1.0*10^-15)*RR, RR=0.5*(RU+RL);
201                         FR=A*RR+B*Log[RR]+CN;If[FR>0.0,RU=RR;,RL=RR;]];
202         R[[1,N]]=RR;,{N,2,NP}];
203
204 R=Transpose[R];
205 SetDirectory["c:\\f\\radial"];
206 Export["griddata.dat",R];
207 SetDirectory["C:\\Users\\Andrew\\Documents"];
208 Clear[R];Return["Grid calculation complete!"];]
209
210 fermiPotential[Ze_, Rr_]:=Module[{a=9.890591359557334` 10^-6,c,rad,R,distance,pot,potdata},
211 c=Sqrt[(5./3.)*Rr^2-(7./3.)(0.52338755*Pi)^2]*10^-15/bohrRadius;
212 R=Rr*10^-15/bohrRadius;
213 SetDirectory["c:\\f\\radial"];
214 rad=ReadList["griddata.dat",Real];
215 (* Define the inside and outside potential integrals *)
```

```
r\[CapitalPhi]I[r_,Z_]:=((4pi*Z)/1)NIntegrate[3/(4pi*c^3) (1+(pi^2 a^2)/c^2)^-1 rho^2/(1+E^((
    rho-c)/a)),{rho,0,r},MaxRecursion->12]+(4pi*Z*r)NIntegrate[3/(4pi*c^3) (1+(pi^2 a^2)/c^2)
    ^-1 rho/(1+E^((rho-c)/a)),{rho,r,c},MaxRecursion->12]+(4pi*Z*r)NIntegrate[3/(4pi*c^3)
    (1+(pi^2 a^2)/c^2)^-1 rho/(1+E^((rho-c)/a)),{rho,c,\[Infinity]},MaxRecursion->12];

r\[CapitalPhi]O[r_,Z_]:=((4pi*Z)/1)NIntegrate[3/(4pi*c^3) (1+(pi^2 a^2)/c^2)^-1 rho^2/(1+E^((
    rho-c)/a)),{rho,0,c},MaxRecursion->12]+((4pi*Z)/1)NIntegrate[3/(4pi*c^3) (1+(pi^2 a^2)/c
    ^2)^-1 rho^2/(1+E^((rho-c)/a)),{rho,c,r},MaxRecursion->12]+(4pi*Z*r)NIntegrate[3/(4pi*c
    ^3) (1+(pi^2 a^2)/c^2)^-1 rho/(1+E^((rho-c)/a)),{rho,r,\[Infinity]},MaxRecursion->12];

 DistributeDefinitions [a,c,distance,rad,r\[CapitalPhi]O,r\[CapitalPhi]I,R];

(* Generate the potential grid based on "Griddata" *)
pot=ParallelTable[If[rad[[i]]<= R,r\[CapitalPhi]I[rad[[i]],Ze],r\[CapitalPhi]O[rad[[i]],Ze]],{i
    ,1,NV},DistributedContexts:>{"NRadiusTest`Private`"}];

(* Combine the distance with corresponding potential value *)
potdata=Transpose[{rad,pot}];
MatrixForm[potdata];

(* Export the matrix of disatnce at potetial values *)
Export["potdata.dat",potdata];
SetDirectory["C:\\Users\\Andrew\\Documents"];
];


(* Define angular momentum reduction terms *)

(* Parity operator *)
parity[la_?NumericQ,lb_?NumericQ,L_?NumericQ]:=If[EvenQ[la+lb+L]==True,1,0];


(* Reduced matrix element for spherical harmonic *)
reducedCMatrix[J_?NumericQ,kappa1_?NumericQ,j1_?NumericQ,kappa2_?NumericQ,j2_?NumericQ
    ]:=(-1)^(j2+1/2) Sqrt[(2 j1+1) (2 j2 +1)]*ThreeJSymbol[{j1,1/2},{J,0},{j2,-1/2}] parity[(j1+
    kappa1/(2 j1+1)),(j2+kappa2/(2 j2+1)),J];

```

```
244
245
246 (* Triagular condition for angular momentum *)
247  triangleCoefficient [a_?NumericQ,b_?NumericQ,c_?NumericQ]:=If[Abs[a-b]<=c<=a+b,1,0];
248
249
250
251 (* Lambda function required for Coulomb part of one-photon exchange *)
252 lambda[k1_?NumericQ,j1_?NumericQ,k_?NumericQ,k2_?NumericQ,j2_?NumericQ]:= parity[(j1+k1/(2
       j1+1)),(j2+k2/(2 j2+1)),k]*ThreeJSymbol[{j1,-1/2},{j2,1/2},{k,0}]^2;
253
254
255 (* angular coefficents *)
256 S[J_?NumericQ,L_?NumericQ,k1_?NumericQ,j1_?NumericQ,k2_?NumericQ,j2_?NumericQ]:=If[J==0\[
       And]L==1,reducedCMatrix[0,k1,j1,-k2,j2],If[J!=0\[And]L==J+1,((J+1)/(2 J+1))^(1/2) (1+(
       k1+k2)/(J+1)) reducedCMatrix[J,k1,j1,-k2,j2],If[J!=0\[And]L==J,(k1-k2)/Sqrt[J(J+1)]
       reducedCMatrix[J,k1,j1,k2,j2],If[J!=0\[And]L==J-1,(J/(2 J+1))^(1/2) (-1+(k1+k2)/(J+1))
       reducedCMatrix[J,k1,j1,-k2,j2],0]]]];
257
258
259
260 J[j_,{ja_,ma_},{jb_,mb_},{jc_,mc_},{jd_,md_}]:=Sum[(-1)^(ja-ma+j-m+jb-mb) ThreeJSymbol[{
       ja,-ma},{j,m},{jc,mc}] ThreeJSymbol[{jb,-mb},{j,-m},{jd,md}],{m,-j,j}]//Quiet
261
262 (* This module calculates the 9-J symbol *)
263 nineJSymbol[{a_,b_,c_},{d_,e_,f_},{g_,h_,j_}]:=Module[{ alpha, alphamax,NJ},
264 (* Find largest value of alpha *)
265  alphamax=Max[{(a+j),(b+f),(d+h)}];
266 NJ=0;
267 Do[NJ=NJ+(-1)^(2 alpha) (2 alpha+1) SixJSymbol[{a,b,c},{f,j, alpha}]*SixJSymbol[{d,e,f},{b,
       alpha,h}]*SixJSymbol[{g,h,j},{ alpha,a,d}],{ alpha,0, alphamax,1/2}]//Quiet;
268 NJ
269 ];
270
271 (* Partial wave expansion *)
272 g[l_?NumericQ,w_?NumericQ,xa_?NumericQ,xb_?NumericQ]:=If[w==0,1/(2l+1) Min[xa,xb]^l/Max[xa
       ,xb]^(l+1),I w SphericalBesselJ[l,w Min[xa,xb]] SphericalHankelH1[l,w Max[xa,xb]]];
```

```
273
274
275
276 (* Radial Integrals *)
277
278 RInt[J_?NumericQ,\[Omega]_?NumericQ,Pa_,Qa_,Pb_,Qb_,Pc_,Qc_,Pd_,Qd_,ja_?NumericQ,ka_?
       NumericQ,jb_?NumericQ,kb_?NumericQ,jc_?NumericQ,kc_?NumericQ,jd_?NumericQ,kd_?
       NumericQ]:=(2J+1) NIntegrate[(-1)^J reducedCMatrix[J,ka,ja,kc,jc] reducedCMatrix[J,kb,jb,kd,
       jd] g[J,\[Omega],x1,x2](Pa[x1]*Pc[x1]+Qa[x1]*Qc[x1])*(Pb[x2]*Pd[x2]+Qb[x2]*Qd[x2])
279 +If[J==0,reducedCMatrix[0,ka,ja,kc,jc] reducedCMatrix[0,kb,jb,kd,jd] g[1,\[Omega],x1,x2] (Pa[x1]
       Qc[x1]-Qa[x1]Pc[x1]) (Pb[x2]Qd[x2]-Qb[x2]Pd[x2]),(-1)^J reducedCMatrix[J,ka,ja,kc,jc]
       reducedCMatrix[J,kb,jb,kd,jd] ((J+1)/(2J+1))g[J+1,\[Omega],x1,x2] (Pa[x1]Qc[x1]-Qa[x1]Pc[
       x1]+(ka-kc)/(J+1) (Pa[x1]Qc[x1]+Qa[x1]Pc[x1])) (Pb[x2]Qd[x2]-Qb[x2]Pd[x2]+(kb-kd)/(J+1)
        (Pb[x2]Qd[x2]+Qb[x2]Pd[x2]))+(-1)^J reducedCMatrix[J,ka,ja,kc,jc] reducedCMatrix[J,kb,jb,kd,
       jd] (J/(2J+1))g[J-1,\[Omega],x1,x2] (Pa[x1]Qc[x1]-Qa[x1]Pc[x1]+(kc-ka)/J (Pa[x1]Qc[x1]+Qa
       [x1]Pc[x1])) (Pb[x2]Qd[x2]-Qb[x2]Pd[x2]+(kd-kb)/J (Pb[x2]Qd[x2]+Qb[x2]Pd[x2]))+(-1)^(J
       +1) reducedCMatrix[J,-ka,ja,kc,jc] reducedCMatrix[J,-kb,jb,kd,jd] (((ka+kc)(kb+kd))/(J(J+1))
       )g[J,\[Omega],x1,x2] (Pa[x1]Qc[x1]+Qa[x1]Pc[x1]) (Pb[x2]Qd[x2]+Qb[x2]Pd[x2])],{x2,0.,pVPoints
       [[NV,1]]},{x1,0.,pVPoints[[NV,1]]},Method->{"GlobalAdaptive","SymbolicProcessing"->0}]//
       Quiet;
280
281
282 (* These functions calculate the One-Loop QED contribution to the Lamb-Shift using the point
       results of Yerokhin and Shabaev (2015) *)
283 beta[Ze_]:= Interpolation [MapThread[List,{Zpoints,MassRatio}],Ze, InterpolationOrder ->3];
284 SELF[Ze_,l_, jj_]:=Which[(l==1&&jj==1/2),Interpolation[MapThread[List,{Zpoints,SelfP12}],Ze,
       InterpolationOrder->3],
285             (l==1&&jj==3/2),Interpolation[MapThread[List,{Zpoints,SelfP32}],Ze,
                 InterpolationOrder->3],
286             True, Interpolation [MapThread[List,{Zpoints,SelfS12}], Ze, InterpolationOrder ->3]];
287 UEHL[Ze_,l_, jj_]:=Which[(l==1&&jj==1/2),Interpolation[MapThread[List,{Zpoints,UehlP12}],Ze,
       InterpolationOrder->3],
288             (l==1&&jj==3/2),Interpolation[MapThread[List,{Zpoints,UehlP32}],Ze,
                 InterpolationOrder->3],
289             True, Interpolation [MapThread[List,{Zpoints,UehlS12}],Ze, InterpolationOrder ->3]];
290 WK[Ze_,l_, jj_]:=Which[(l==1&&jj==1/2),Interpolation[MapThread[List,{Zpoints,WkP12}],Ze,
       InterpolationOrder->3],
```

```
291              (l==1&&jj==3/2),Interpolation[MapThread[List,{Zpoints,WkP32}],Ze,
                     InterpolationOrder->3],
292              True, Interpolation [MapThread[List,{Zpoints,WkS12}],Ze,InterpolationOrder->3]];
293
294 pointOneLoopQEDSE[Ze_,n_,l_,jj_]:=( alpha/pi)((Ze  alpha)^4/n^3)(beta[Ze]/(1+beta[Ze]))^3 SELF[
        Ze,l,jj ]  ;
295 pointOneLoopQEDVP[Ze_,n_,l_,jj_]:=( alpha/pi)((Ze  alpha)^4/n^3)(beta[Ze]/(1+beta[Ze]))^3 (
        UEHL[Ze,l,jj]+WK[Ze,l,jj]) ;
296
297 DeltaEND[n_,l_, j_ ,Ze_,Rsph_]:=((diracEnergy[Ze,Sqrt[3/5]  alpha  Rsph,n,(l-j)(2j+1)]-
        diracPointEnergy [Ze,n,(l-j)(2j+1)])*27.21138386);
298
299  ff [Z_,Rsph_]:=Module[{gamma},
300              gamma=Sqrt[1-(Z alpha)^2];
301 (1/(3 (Z  alpha)^2))*(-2*Log[Rsph]-5/3+pi*Tan[pi gamma]+(2/(3+2 gamma))+2*PolyGamma
        [-1-2 gamma]-((pi^(3/2) *(3+2 gamma)*Gamma[gamma+1])/(40*Sin[2 pi gamma]*(gamma
        -1)*Gamma[-1-2 gamma]*Gamma[gamma+3/2]))*(2 Rsph)^(2(1-gamma)))
302  ];
303
304 GNSE[n_,l_, j_ ,Z_,Rsph_]:=Module[{a01,a00, a10,alog,a22,a21,b,gamma},
305    a01=N[8/9];
306    a00 =Which[j==3/2,(0.808879967-1),
307            True,0.808879967];
308    a10 =Which[l==1&&j==1/2,N[pi(379/432-16Log[2]/3)],
309           l==1 && j==3/2,N[pi(559/432-4Log[2])],
310           True,N[pi(-23/4+4Log[2])]];
311    alog=N[pi^2/6-15/4];
312    a22=N[-2/3];
313    a21=N[-2(n^2-1)/n^2];
314    gamma=Sqrt[1-(Z alpha)^2];
315    b=E^(1/(2 gamma)-EulerGamma-5/6);
316
317    Which[l==1,a01*Log[1/(Z alpha)^2]+a00+(Z alpha)*a10+(Z alpha)^2*(alog*KroneckerDelta[j
          ,1/2]*Log[b/Rsph]+a21*KroneckerDelta[j,1/2]*(Log[1/(Z alpha)^2])
318         +Which[j==1/2,141.838-4.78895Z+0.0552297Z^2-0.000214623Z^3,
319                                                 True,99.7534-3.68213Z+0.0450514Z^2-0.00017817Z^3]),
```

```
320       True,(Z  alpha)*a10+(Z alpha)^2*(alog*Log[b/Rsph]+a22*(Log[1/(Z alpha)^2])
              ^2+(-110.044+3.94841Z-0.0466387Z^2+0.000180466Z^3))]
321 ];
322
323 GNVP[n_,l_,j_,Z_,Rsph_]:=Module[{a00, a10,a21,b,gamma},
324   a00 =Which[True,-8/45];
325   a10 =Which[l==1&&j==1/2,N[23Pi/72],
326         l==1 && j==3/2,N[5Pi/72],
327         True,N[3Pi/4]];
328   a21=4/15;
329   gamma=Sqrt[1-(Z alpha)^2];
330   b=E^(1/(2 gamma)-EulerGamma-5/6);
331   Which[l==1,a00+(Z alpha)*a10+(Z alpha)^2*(2/(3gamma)*KroneckerDelta[j,1/2]*Log[b/Rsph
          ]^2+ff[Z,Rsph]*KroneckerDelta[j,1/2]
332     +Which[j==1/2,-4.92417+0.076397Z,
333                                          True,0.194751-0.00197697Z]),
334       True,(Z  alpha)*a10+(Z alpha)^2*(2/(3gamma) (Log[b/Rsph])^2+a21 Log[1/(Z alpha)^2]+ff[Z
              ,Rsph]+(-5.6409+0.0818693Z))]
335 ];
336
337 (* Define NQED correction using Radial Dirac*)
338 DeltaEnseD[n_,l_,j_,Z_,Rsph_]:=If[l==0,DeltaEND[n,0,1/2,-Z,Rsph],DeltaEND[n,1,1/2,-Z,Rsph]] (
        alpha/pi) GNSE[n,l,j,Z,Rsph];
339 DeltaEnvpD[n_,l_,j_,Z_,Rsph_]:=If[l==0,DeltaEND[n,0,1/2,-Z,Rsph],DeltaEND[n,1,1/2,-Z,Rsph]] (
        alpha/pi) GNVP[n,l,j,Z,Rsph];
340
341 (* Nuclear Recoil Function Definitions *)
342 E1[Z_,A_,n_,l_,j_]:=Block[{alpha=0.007297352569800,kappa,gamma,me,mn=939.565 10^6,mp
        =938.272 10^6,M,ElectronRestEnergy},
343 (*
344 alpha: fine-structure constant;
345 kappa: angular momentum;
346 gamma: gamma term;
347 me: electron mass in eV;
348 mn: neutron mass in eV;
349 mp: proton mass in eV;
350 M: nuclear mass in eV;
```

```
351 *)
352
353 ElectronRestEnergy=UnitConvert[Quantity["ElectronMass"] Quantity["SpeedOfLight"]^2,"
        Electronvolts"];
354 me=QuantityMagnitude@ElectronRestEnergy;
355 M=Z*(mp)+(A-Z)*mn;
356 kappa=((-1)^(j+l+1/2))(j+1/2);
357 gamma=Re@Sqrt[kappa^2-(alpha Z)^2];
358
359 (me/M)*(alpha Z)^2/(2.(n^2-2.(n-Abs[kappa])*(Abs[kappa]-gamma)))*me];
360
361 E2[Z_,A_,n_, l_, j_]:=Block[{alpha=0.007297352569800,kappa,gamma,me,mn=939.565 10^6,mp
        =938.272 10^6,M,ElectronRestEnergy,P1sPoints,P2sPoints,P2p12Points,P2p32Points,P1s,P2s,
        P2p12,P2p32},
362 (*
363 alpha: fine-structure constant;
364 kappa: angular momentum;
365 gamma: gamma term;
366 me: electron mass in eV;
367 mn: neutron mass in eV;
368 mp: proton mass in eV;
369 M: nuclear mass in eV;
370 *)
371 ElectronRestEnergy=UnitConvert[Quantity["ElectronMass"] Quantity["SpeedOfLight"]^2,"
        Electronvolts"];
372 me=QuantityMagnitude@ElectronRestEnergy;
373 M=Z(mp)+(A-Z)mn;
374
375 (* Define P-point matrices *)
376 P1sPoints=Transpose@ {{1,5,10,15,20,25,30,35,40,45,50,55,60,65,70,75,80,85,90,
377   92,95,100},{5.43,4.3033,3.795,3.4973,3.294,3.1483,3.0437,2.9714,2.9268,2.9077,2.9137,
378   2.9456,3.0061,3.0997,3.2334,3.4183,3.672,4.022,4.519,4.77,5.25,6.4}};
379
380 P2sPoints=Transpose@ {{1,5,10,15,20,25,30,35,40,45,50,55,60,65,70,75,80,85,90,
381   92,95,100},{6.155,5.0335,4.5383,4.2599,4.0825,3.9691,3.9037,3.8785,3.89,3.9376,4.0228,
382   4.1498,4.3248,4.5584,4.8656,5.2698,5.807,6.537,7.557,8.08,9.05,11.4}};
383
```

```
P2p12Points=Transpose@ {{1,5,10,15,20,25,30,35,40,45,50,55,60,65,70,75,80,85,90,
92,95,100},{−0.3011,−0.2692,−0.2277,−0.1845,−0.1393,−0.092,−0.0421,0.0122,0.0685,0.131,
  0.2,0.2774,0.3655,0.468,0.5894,0.737,0.9214,1.1598,1.481,1.643,1.937,2.63}};

P2p32Points=Transpose@ {{1,5,10,15,20,25,30,35,40,45,50,55,60,65,70,75,80,85,90,
92,95,100},{−0.3013,−0.2724,−0.2379,−0.2047,−0.1726,−0.1413,−0.1107,−0.0081,−0.0517,
 −0.023,0.005,0.0326,0.0597,0.0863,0.1125,0.1384,0.1638,0.1889,0.2138,0.2236,
0.2383,0.2623}};

(* Define P−point interpolation functions *)
P1s[Zz_]:= Interpolation [P1sPoints,Zz];
P2s[Zz_]:= Interpolation [P2sPoints,Zz];
P2p12[Zz_]:=Interpolation [P2p12Points,Zz];
P2p32[Zz_]:=Interpolation [P2p32Points,Zz];

(* Define Case construct to pick the correct P function *)
(me/M)*(alpha Z)^5/(Pi*n^3) (
Which[
(n==1&&l==0&&j==1/2),P1s[Z],
(n==2&&l==0&&j==1/2),P2s[Z],
(n==2&&l==1&&j==1/2),P2p12[Z],
(n==2&&l==1&&j==3/2),P2p32[Z],
True ,0.]) *me];

Eint[Z_,A_,n_, l_ , j_]:=Block[{alpha=0.007297352569800,kappa,gamma,me,mn=939.565 10^6,mp
    =938.272 10^6,M,ElectronRestEnergy,Q2p12Points,Q2p32Points,Q2p12,Q2p32},
(*
alpha: fine−structure constant;
kappa: angular momentum;
gamma: gamma term;
me: electron mass in eV;
mn: neutron mass in eV;
mp: proton mass in eV;
M: nuclear mass in eV;
*)
ElectronRestEnergy=UnitConvert[Quantity["ElectronMass"] Quantity["SpeedOfLight"]^2,"
    Electronvolts"];
```

```
me=QuantityMagnitude@ElectronRestEnergy;
M=Z(mp)+(A-Z)mn;

(* Define Q-point matrices *)
Q2p12Points=Transpose@{{5,10,15,20,25,30,35,40,45,50,55,60,65,70,75,80,85,90,
 92,95,100},{0.99935,0.99741,0.99416,0.98959,0.9837,0.97645,0.96782,0.95776,0.94622,
 0.93313,0.91841,0.90195,0.88361,0.8632,0.84052,0.81529,0.78716,0.7557,
0.74206,0.72035,0.68041}};

Q2p32Points=Transpose@{{5,10,15,20,25,30,35,40,45,50,55,60,65,70,75,80,85,90,
 92,95,100},{0.99953,0.9981,0.99573,0.99239,0.98809,0.98281,0.97653,0.96926,0.96097,
 0.95165,0.94129,0.92988,0.91742,0.9039,0.8893,0.87362,0.85686,0.83896,
0.83148,0.81988,0.79951}};

(* Define P-point interpolation functions *)
Q2p12[Zz_]:=Interpolation[Q2p12Points,Zz];
Q2p32[Zz_]:=Interpolation[Q2p32Points,Zz];

(* Define Case construct to pick the correct P function *)
-(2.^9/3.^8)*(me/M)*(alpha Z)^2(
Which[
(n==2&&l==1&&j==1/2),Q2p12[Z],
(n==2&&l==1&&j==3/2),Q2p32[Z],
True,0.])*me];

(* Public Functions *)

diracPointEnergy[Ze_,n_,k_]:=Module[{inputdata,energy},
SetDirectory["c:\\f\\radial"];
inputdata={{Ze,n,k}};
Export["inputdata2.dat",inputdata];
energy=ReadList["!pointdirac<inputdata2.dat",Number];
SetDirectory["C:\\Users\\Andrew\\Documents"];
energy [[1]]]

diracHSEnergy[Ze_,n_,k_]:=Module[{inputdata,energy},
SetDirectory["c:\\f\\radial"];
```

```
inputdata={{Ze,n,k}};
Export["inputdata3.dat",inputdata];
energy=ReadList["!sphere<inputdata3.dat",Number];
SetDirectory["C:\\Users\\Andrew\\Documents"];
energy [[1]]


diracEnergy[Ze_,RMS_,n_,k_]:=Module[{inputdata,energy,rms},
SetDirectory["c:\\f\\radial "];
rms=RMS*10^-15/bohrRadius;
inputdata={{Ze,rms,n,k}};
Export["inputdata.dat",inputdata];
energy=ReadList["!fermidirac<inputdata.dat",Number];
SetDirectory["c:\\users\\andrew\\documents"];
energy [[1]]

onePhotonExchange[Zv_,Rms_,nv_,lv_,jv_]:=Module[{onephotonEnergy,rms=Rms*10^-15/bohrRadius
    },
kappav=(lv-jv)*(2 jv+1);
kv=Abs[kappav];
Ze=-Zv;
gammav=(kappav^2-( alpha Zv)^2)^(1/2);
nPrimed=nv-kv;
Env= alpha^-2 (1+(( alpha Zv)/(gammav+nv-kv))^2)^(-1/2);
\[Lambda]= (( alpha^-4-Env^2)^(1/2))/ ( alpha^-1);
nwaves = NV;
diracEnergy [Ze,rms,nc,kappac];
waves=Import["waves.dat"];

pCPoints =Table[{waves[[x,2]], waves[[x,3]]},{x,1,NV}];
qCPoints =Table[{waves[[x,2]], waves[[x,4]]},{x,1,NV}];

diracEnergy [Ze,rms,nv,kappav];
waves=Import["waves.dat"];

pVPoints =Table[{waves[[x,2]],(-1)^lv waves[[x,3]]},{x,1,NV}];
qVPoints =Table[{waves[[x,2]],(-1)^lv waves[[x,4]]},{x,1,NV}];
```

```
492
493 Pc=Evaluate@Interpolation[pCPoints, Method->"Spline",InterpolationOrder->3];
494 Qc=Evaluate@Interpolation[qCPoints, Method->"Spline",InterpolationOrder->3];
495
496 Pv=Evaluate@Interpolation[pVPoints, Method->"Spline",InterpolationOrder->3];
497 Qv=Evaluate@Interpolation[qVPoints, Method->"Spline",InterpolationOrder->3];
498
499 Delta=Abs[diracEnergy [Ze,rms,nv,kappav]-diracEnergy [Ze,rms,nc,kappac]]  alpha;
500
501 onephotonEnergy=Sqrt[(2jc+1)/(2jv+1)]RInt[0,0,Pv,Qv,Pc,Qc,Pv,Qv,Pc,Qc,jv,kappav,jc,kappac,jv,
      kappav,jc,kappac]-\!\(
502 \*UnderoverscriptBox[\(\[Sum]\), \(J = Abs[jc - jv]\), \(jc + jv\)]\(
503 \*FractionBox[
504 SuperscriptBox[\((\(-1\))\), \(jv - jc + J\)], \(2  jv + 1\)] RInt[J, Delta, Pv, Qv, Pc, Qc, Pc,
      Qc, Pv, Qv, jv, kappav, jc, kappac, jc, kappac, jv, kappav]\)\);
505 onephotonEnergy]
506
507 twoPhotonExchange[Zv_,jv_]:=Block[{dE2sList,dE2p12List,dE2p32List,tPE12,tPE32,zPoints,zPoints2},
508 (* References:
509   Yerokhin et. al., Phys. Rev. Lett. 85 (2000)
510   Artemyev et. al., Phys. Rev. A, 67 (2003)
511 *)
512 zPoints={80,82,83,90,92};
513 zPoints2=Select[zPoints,(Mod[#,10]==0||#==83||#==92)&];
514 dE2sList={-11.1458,-11.5948,-12.8220,-13.2247};
515 dE2p12List={-20.8276,-22.0439,-25.4481,-26.5964};
516 dE2p32List={-12.9736,-13.2027,-13.7788,-13.9543};
517
518 tPE12=Interpolation[MapThread[List,{zPoints2,(dE2p12List-dE2sList)}], InterpolationOrder->3];
519 tPE32=Interpolation[MapThread[List,{zPoints2,(dE2p32List-dE2sList)}], InterpolationOrder->3];
520
521 If[jv==1/2,Return[tPE12[Zv]],Return[tPE32[Zv]]]
522
523 threePhotonExchange[Zv_,jv_]:=Module[{tPEData12,zPoints12,tPEData32,zPoints32},
524 zPoints12={80,83,90,92,100};
525 tPEData12={0.076,0.087,0.118,0.132,0.183};
526 zPoints32={80,83,90,92};
```

```
tPEData32={-.02,-.02,-.02,-.02};
 If [jv==1/2,Return[Interpolation[MapThread[List,{zPoints12,tPEData12}],InterpolationOrder->3][Zv
    ]],
Return[ Interpolation [MapThread[List,{zPoints32,tPEData32}],InterpolationOrder->3][Zv]]]]

(* One-loop QED correction *)
oneLoopQED[Z_,r_,j_]:=Module[{DeltaEn,DeltaEpnt,Rsph},

Rsph=Sqrt[5/3]*r*(10^-15)/reducedComptonWavelength;

DeltaEpnt=((pointOneLoopQEDSE[Z,2,1,j]+pointOneLoopQEDVP[Z,2,1,j])-(pointOneLoopQEDSE[Z
    ,2,0,1/2]+pointOneLoopQEDVP[Z,2,0,1/2])) electronRestEnergy;
DeltaEn=(DeltaEnseD[2,1,j,Z,Rsph]+DeltaEnvpD[2,1,j,Z,Rsph])-(DeltaEnseD[2,0,1/2,Z,Rsph]+
    DeltaEnvpD[2,0,1/2,Z,Rsph]);

Return[DeltaEpnt+DeltaEn]
 ];

twoLoopQED[Z_,n_,kappa2_,kappa1_]:=Module[{DE,energy,F,SESE2sPoints,SESE2p12Points,
    SESE2p32Points,SEVP2sPoints,SEVP2p12Points,SEVP2p32Points,VPVP2sPoints,
    VPVP2p12Points,VPVP2p32Points,VPVPKS2sPoints,VPVPKS2p12Points,VPVPKS2p32Points,
    SVPE2sPoints,SVPE2p12Points,SVPE2p32Points,SESE2s,SESE2p12,SESE2p32,SEVP2s,
    SEVP2p12,SEVP2p32,VPVP2s,VPVP2p12,VPVP2p32,VPVPKS2s,VPVPKS2p12,VPVPKS2p32,
    SVPE2s,SVPE2p12,SVPE2p32,ZPoints},

ZPoints={60,65,70,75,80,83,90,92,100};

SESE2sPoints={{60,-1.976},{70,-2.453},{83,-3.296},{92,-4.218},{100,-5.455}};
SESE2p12Points={{60,0.222},{70,0.192},{83,0.133},{92,0.012},{100,-0.214}};
SESE2p32Points={{60,0.02},{70,-0.082},{83,-0.175},{92,-0.241},{100,-0.282}};
SEVP2sPoints=MapThread[List,{ZPoints
    ,{0.9854,1.1463,1.34094,1.5827,1.8834,2.1010,2.751,2.9786,4.224}}];
SEVP2p12Points=MapThread[List,{ZPoints
    ,{0.01477,0.02653,0.04384,0.069408,0.107174,0.138236,0.2488,0.2940,0.5871}}];
SEVP2p32Points=MapThread[List,{ZPoints
    ,{0.010449,0.015548,0.0217,0.029019,0.037514,0.043186,0.05798,0.06251,0.08183}}];
```

```
552 VPVP2sPoints=MapThread[List,{ZPoints
        ,{−0.10566,−0.1342,−0.1713,−0.2212,−0.2880,−0.3393,−0.505,−0.566,−0.935}}];
553 VPVP2p12Points=MapThread[List,{ZPoints
        ,{−0.003233,−0.005518,−0.008238,−0.01313,−0.02094,−0.02778,−0.0543,−0.0658,−0.1482}}];
554 VPVP2p32Points=MapThread[List,{ZPoints
        ,{−0.000029,−0.000039,−0.000051,−0.0000067,−0.000085,−0.000099,−0.000136,
555       −0.000149,−0.000209}}];
556 VPVPKS2sPoints=MapThread[List,{ZPoints
        ,{−1.04561,−1.1053,−1.17895,−1.27069,−1.38369,−1.4642,−1.6988,−1.7791,−2.201}}];
557 VPVPKS2p12Points=MapThread[List,{ZPoints
        ,{−0.069624,−0.08862,−0.112569,−0.143102,−0.182409,−0.21150,−0.30171,−0.33488,−0.5202}}];

558 VPVPKS2p32Points=MapThread[List,{ZPoints
        ,{−0.008931,−0.010259,−0.011673,−0.013175,−0.014770,−0.015775,−0.018267,
559       −0.019020,−0.022227}}];
560 SVPE2sPoints=MapThread[List,{ZPoints
        ,{0.16851,0.18271,0.20042,0.22260,0.25059,0.27097,0.33285,0.35535,0.47842}}];
561 SVPE2p12Points=MapThread[List,{ZPoints
        ,{0.00098,0.00314,0.00603,0.00994,0.01528,0.01943,0.03322,0.03863,0.07124}}];
562 SVPE2p32Points=MapThread[List,{ZPoints
        ,{0.00226,0.00220,0.00213,0.00205,0.00197,0.00191,0.00177,0.00172,0.00152}}];
563
564 SESE2s[Zz_]:=Interpolation[SESE2sPoints,Zz];
565 SESE2p12[Zz_]:=Interpolation[SESE2p12Points,Zz];
566 SESE2p32[Zz_]:=Interpolation[SESE2p32Points,Zz];
567 SEVP2s[Zz_]:=Interpolation[SEVP2sPoints,Zz];
568 SEVP2p12[Zz_]:=Interpolation[SEVP2p12Points,Zz];
569 SEVP2p32[Zz_]:=Interpolation[SEVP2p32Points,Zz];
570 VPVP2s[Zz_]:=Interpolation[VPVP2sPoints,Zz];
571 VPVP2p12[Zz_]:=Interpolation[VPVP2p12Points,Zz];
572 VPVP2p32[Zz_]:=Interpolation[VPVP2p32Points,Zz];
573 VPVPKS2s[Zz_]:=Interpolation[VPVPKS2sPoints,Zz];
574 VPVPKS2p12[Zz_]:=Interpolation[VPVPKS2p12Points,Zz];
575 VPVPKS2p32[Zz_]:=Interpolation[VPVPKS2p32Points,Zz];
576 SVPE2s[Zz_]:=Interpolation[SVPE2sPoints,Zz];
577 SVPE2p12[Zz_]:=Interpolation[SVPE2p12Points,Zz];
578 SVPE2p32[Zz_]:=Interpolation[SVPE2p32Points,Zz];
```

```
579
580 F[Zz_,k_]:=Which[k==1,SESE2p12[Zz],k==-2,
581 SESE2p32[Zz],True,SESE2s[Zz]]+Which[k==1,SEVP2p12[Zz],k==-2,
582 SEVP2p32[Zz],True,SEVP2s[Zz]]+Which[k==1,VPVP2p12[Zz],k==-2,
583 VPVP2p32[Zz],True,VPVP2s[Zz]]+Which[k==1,VPVPKS2p12[Zz],k==-2,
584 VPVPKS2p32[Zz],True,VPVPKS2s[Zz]]+Which[k==1,SVPE2p12[Zz],k==-2,
585 SVPE2p32[Zz],True,SVPE2s[Zz]];
586
587 energy[Zz_,k_]:=( alpha/pi)^2 (Zz  alpha)^4/(n^3  alpha^2) F[Zz,k];
588 (energy[Z,kappa2]-energy[Z,kappa1]) 27.21138]
589
590 screenedQED[Z_,j_]:=Module[{SE12,SE32,VP12,VP32,ZPoints},
591 ZPoints={80,83,90,92,100};
592 SE12={1.1322,1.2335,1.4639,1.5243,1.6834};
593 SE32={1.37206,1.57902,2.19887,2.41964,3.58486};
594 VP12={-0.2149,-0.2471,-0.3332,-0.3598,-0.460};
595 VP32={-0.3553,-0.4314,-0.6803,-0.776,-1.329};
596 Return@If[j==1/2,Interpolation[MapThread[List,{ZPoints,(SE12+VP12)}],Z,InterpolationOrder->3],
        Interpolation[MapThread[List,{ZPoints,(SE32+VP32)}],Z,InterpolationOrder->3]]
597 ]
598
599  nuclearRecoil [Z_,A_,n1_, l1_ , j1_ , n2_, l2_ , j2_]:=(*
600 Z: Nuclear charge;
601 A: Mass number;
602 n1:  principle  quantum number excited state;
603 l1 :  orbital  angular  momentum excited state;
604 j1 :  total  angular  momentum excited state;
605 n2:  principle  quantum number base state;
606 l2 :  orbital  angular  momentum base state;
607 j2 :  total  angular  momentum base state;
608 *)(E1[Z,A,n1,l1 , j1]+E2[Z,A,n1,l1 , j1]+Eint[Z,A,n1,l1 , j1 ]) -(E1[Z,A,n2,l2, j2]+E2[Z,A,n2,l2 , j2]+Eint
        [Z,A,n2,l2 , j2 ])
609
610 (* end  private  context *)
611 End [];
612
613 EndPackage[]
```

B.3 "NuclearPolarization" Mathematica Package

"NuclearPolarization" calculates the nuclear polarization contribution by calling the "BSpline" package to generate a spectrum of B-splines. Due to the uncertainty of the nuclear polarization contribution a nominal nuclear charge radius is calculated via a hard-sphere extended nuclear charge model of the nucleus with a radius R_0 given by $R_0 = 1.2A^{1/3}$ (fm), as explained in Chapter 7. The results of using this package are then added to the results of using the NRadius package to obtain final transition energies.

B.3.1 "NuclearPolarization" Functions

bEL: Function generates the B(EL) values for the giant multipole resonance states which are estimated by the phenomenological energy weighted sum rule as shown in Chapter 7.

Input:

- L : nuclear multipole moment (L=0,1,2,3)
- tau : isospin of excitation (tau=0,1)
- A : atomic mass number
- Z : nuclear charge

nuclearPolarization: This function acts as a wrapper for the two methods of calculating the nuclear polarization correction, the numerical and analytical, as shown in Chapter 7. The numerical method uses a spline basis set to generate the states that are summed over. Because the spline method is rather slow in comparison to the analytical method, the analytical form will be used when appropriate and the spline method invoked when needed.

Input:

- L : nuclear multipole moment (L=0,1,2,3)
- B : isospin of excitation (tau=0,1)

- wL : nuclear excitation energy (MeV)
- Z : nuclear charge
- A : atomic mass number
- n : principal electron quantum number
- l : electron orbital angular momentum quantum number
- j : electron total angular momentum quantum number

omegaL: Function generates the excitation energies (in MeV) for the giant multipole resonance states which are assumed to be concentrated in a single resonant state for each ($L\tau$).

Input:
- L : nuclear multipole moment (L=0,1,2,3)
- tau : isospin of excitation (tau=0,1)
- A : atomic mass number

B.3.2 "NuclearPolarization" Code

```
(* : Title : NuclearPolarization .m *)
(* :Context: ProgrammingInMathematica`Skeleton` *)
(* :Author: Andrew S. M. Senchuk *)
(* :Summary:
  This package calculates the nuclear polarization correction to the Lamb shift of H-like atoms
      /ions using the
  Galerkin method with B-splines to generate the intermediate states that are summed over in
      the calculation
  of the energy correction .
*)
(* :Copyright: <year> by <name or institution> *)
(* :Package Version: 1.0 *)
(* :Mathemtica Version: 9.0 *)
(* :Keywords: template, skeleton , package *)
(* :Sources: *)
(* :Requirements: *)

(* set up the package context, including public imports *)
BeginPackage["ASMSThesis`NuclearPolarization`",{"ASMSThesis`AtomicConstants`"}];

```

```
19 (* usage messages for the exported functions and the context itself *)
20
21 NuclearPolarization::usage="NuclearPolarization.m is a package that calculates the nuclear
       polarization correction to the Lamb shift of H-like atoms/ions using the Galerkin method
       with B-splines to generate the intermediate states that are summed over in the calculation
       of the energy correction.";
22
23 GaussLegendreQuadrature::usage="GaussLegendreQuadrature[f_,{x_,a_,b_},n_Integer,prec_]
       numerically calculates the integral of f over the limits a and b using the method of
       Gaussian-Legendre quadrature (Guassian integration), where n is the order of the integration
       (the default is 10), and to a given precision (the default is MachinePrecison)";
24
25 nuclearPolarization::usage = " nuclearPolarization[L, B, wL, Z, Rms, n, l, j] calculates the
       nuclear-polarization energy shifts for one-electron highy-charged ions. Two methods are
       employed in the calculation based on which states are requested.
26   Input:
27     L  : nuclear multipole moment
28     B  : reduced electric transition probability
29     wL : nuclear excitation energy in MeV
30     Z  : charge of ion
31     n  : principle quantum number for ion
32     l  : orbital state of ion
33     j  : total angular momentum state of ion";
34
35 omegaL::usage = "Function generates the excitation energies (in MeV) for the giant multipole
       resonance states which are assumed to be concentrated in a single resonant state for eact (
       L\[Tau])
36   Input:
37     L   : nuclear multipole moment (L=0,1,2,3).
38     tau : isospin of excitation (tau=0,1).
39     A   : atomic mass number.";
40
41 bEL::usage = "Function generates the B(EL) values for the giant multipole resonance states which
       are estimated by the phenomenological energy weighted sum rule, see Hoffmann (1984) and
       Rinker (1978)
42   Input:
43     L   : nuclear multipole moment (L=0,1,2,3).
```

```
44      tau : isospin of excitation (tau=0,1).
45      A   : atomic mass number.
46      Z   : nuclear charge.";
47
48 (* error messages for the exported functions *)
49 (*  NuclearPolarization :: badarg= *)
50
51 Begin["`Private`"]    (* begin the private context (implementaion part) *)
52
53  ClearAll ["Global`*"]
54 ClearMemory:=Module[{},Unprotect[In,Out];
55  Clear[In,Out];
56  Protect[In,Out];
57  ClearSystemCache[];]                (* Buffer cleaner *)
58
59  CloseKernels [];                                (* Initialize all available kernels *)
60 Unprotect[$ProcessorCount];
61 $ProcessorCount=4;
62 LaunchKernels[4];
63
64 ClearMemory;
65
66 (* Define electron rest energy in eV *)
67 (* Sommerfeld energy *)
68 energySommerfeld[Z_,n_,\[Kappa]_]:=(1+((fineStructureConstant Z)/(n-Abs[\[Kappa]]+Sqrt[\[Kappa
       ]^2-(fineStructureConstant Z)^2]))^2)^(-1/2);
69
70 (* Radial dependance operators incorporating nuclear distribution *)
71 (*F[0, r_]:=(5Sqrt[\[Pi]]) /(2Rsph^3) (1-(r/Rsph)^2)HeavisideTheta[(Rsph-r)];
72 F[L_, r_]:=((4\[Pi])/(2L+1))Piecewise[{{r^L/Rsph^(2 L+1),r<Rsph},{1/r^(L+1),r>= Rsph}}];
73 *)
74 F[L_,Rsph_,r_]:= If [L==0,(5Sqrt[\[Pi]])/(2Rsph^3) (1-(r/Rsph)^2)HeavisideTheta[(Rsph-r)],((4\[Pi
       ] )/((2L+1)Rsph^L)) Piecewise[{{r^L/Rsph^(L+1),r<Rsph},{Rsph^L/r^(L+1),r>= Rsph}}]];
75
76 (* Gaussian-Legendre integration function *)
77 GaussLegendreQuadrature[f_,{x_,a_,b_}, n_Integer : 10, prec_: MachinePrecision]:=
78   Module[{nodes,weights},
```

```
79      {nodes,weights}=Most[NIntegrate`GaussRuleData[n,prec]];(b-a) weights.Map[Function[x,f],
            Rescale[nodes,{0,1},{a,b}]]];
80
81  (* base-state grid generating function *)
82  makeGrid[nsplines_,order_,rmax_,dr0_]:=
83    Module[{ipow=nsplines-order+1,t0,h},
84      (* Generate the t0 and h parameters *)
85      {t0,h}=step[ipow,rmax,dr0];
86      (*Print[{t0,h}];*)
87      (* Generate the grid *)
88      Join[ConstantArray[0.0,{order}],Table[t0 (Exp[(i-order) h]-1.),{i,order+1,nsplines}],
            ConstantArray[rmax,{order}]]];
89
90  step[ipow_,rmax_,dr_]:=
91    Module[{small=10.^-10, nmax=54,a,b,c, dx,f,fa,fb,fc,t0,h,i},
92      f[x_]:=1.0+(rmax/dr)*x-(1.0+x)^ipow;
93      fa=f[small]; a=small;
94      If[fa<= 0.0,Print["fa !!!"]; Abort []];
95      fb=f[1.0];  b=1.0;
96      If[fb>= 0.0,Print["Problem with fb!  Increase the number of splines ..."]; Abort []];
97      dx=1.0;i=1;c=0.5*(a+b);fc=f[c];
98      While[fc!=0.0&&i<nmax,
99        If[fb*fc>0.0,b=c;fb=fc;,a=c;fa=fc;];
100       c=0.5*(a+b);
101       fc=f[c];
102       ++i;];
103     (*Print[{dr/c,Log[1.0+c]}];*)
104     {dr/c,Log[1.0+c]}];
105
106 (* intermediate state grid generating function *)
107 CFFGrid[order_,r1_,rmax_,h_,hm_]:=
108   Module[{i=0,j=1,rgrid={},rexp,rlin},
109     (* r1 is the first internal knot point *)
110     (* rmax is the outside value of the *)
111     (* h is the parameter for the exponenetial portion *)
112     (* hm is the max value for the linear portion of the grid *)
113
```

```
114     (* Define recursive functions for the exponential and linear portions *)
115     rexp[0]=0.0;
116     rexp[1]=r1;
117     rexp[i_]:=(1+h) rexp[i-1]/;i>1;
118      rlin [i_]:= rlin [i-1]+hm/;i>1;
119
120     (* Evaluate the grid *)
121     While[(rexp[i+1]-rexp[i])<=hm,rgrid=Append[rgrid,rexp[i+1]];i++;];
122      rlin [1]= rgrid //Last;
123     While[ rlin [j+1]<rmax,rgrid=Append[rgrid,rlin[j+1]];j++];
124     (* add beginning and ending points *)
125     Join[Table[0,{order}], rgrid ,Table[Last[ rgrid ],{order-1}]]//N];
126
127  linearExponentialGrid [rmin_,rmax_,n_, order_, i0_]:=Module[{\[Alpha],\[Beta],h=1/4,r0},
128 (* rmin: minimum value for the grid *)
129 (* rmax: maximum value for the grid *)
130 (* n: number of grid points *)
131 (* order: order of the splines used *)
132 (* i0: points at which linear region begins *)
133  If[i0>= n,Print["ERROR: i0 too big. Reduce i0 or increase number of splines ."];,
134 r0=(rmax (Exp[h(i0-1)]-1)+h rmin Exp[h(i0-1)](n-i0))/(h Exp[h(i0-1)](n-i0)+Exp[h(i0-1)]-1);
135 \[Alpha]=(r0-rmin)/(Exp[h(i0-1)]-1);
136 \[Beta]=(rmax-r0)/(n-i0);
137  Join[ConstantArray[0,{order-1}],Table[rmin+\[Alpha] (Exp[h(i-1)]-1),{i,1, i0-1}],Table[r0+\[Beta
        ] (i-i0),{i , i0 , n}], ConstantArray[rmax,{order -1}]]]];
138 Options[galerkinHS]={
139 MaxRecursion:>$RecursionLimit,
140  PrecisionGoal->Automatic,
141 WorkingPrecision->Automatic};
142
143 galerkinHS[Z_?NumericQ,R0_?NumericQ,{l_?NumericQ,j_?NumericQ},{order_?NumericQ,nsplines_?
        NumericQ,base_?NumericQ},opts:OptionsPattern[]]:=
144 Module[{\[Alpha],\[Beta]=10^5,aPrime,cSplineMat,diagnostic=False,dr,dSplineMat,\[Epsilon ],
        hardSphere,k=(l-j)(2j+1),knots, knotslength , kSplineMat,mataPrime,matA,matB,matv,matkappa,
        matc,matd,maxRecursion,Np,precisionGoal,R0x,Rmaxx,Rsphx,scal,sortEigensystem,t,V,vSplineMat,
        workingPrecision},
145
```

```
146 {maxRecursion,precisionGoal , workingPrecision }=OptionValue[{MaxRecursion,PrecisionGoal,
        WorkingPrecision}];
147 If [ precisionGoal ===Automatic,precisionGoal=MachinePrecision];
148 If [ workingPrecision ===Automatic,workingPrecision=precisionGoal+10];
149
150 (* Convert R0 to natural units where length is in units of the reduced Compton wavelength *)
151 {R0x,Rmaxx,Rsphx,\[Alpha],\[Epsilon], scal }=SetPrecision[{R0,(80/Z),(*Sqrt[5/3]**)(R0*10^-15)/
        bohrRadius,fineStructureConstant,10^-35,(2/ Z)},workingPrecision];
152
153 (* define the basis functions: *)
154 Np=nsplines+1-order;
155 dr=Which[Abs[k]==1,SetPrecision[0.0001scal,workingPrecision ],
156       Abs[k]==2,SetPrecision[0.001 scal , workingPrecision ],
157       True, SetPrecision [0.01  scal , workingPrecision ]];
158 knots=Which[base==1,SetPrecision[makeGrid[nsplines,order,Rmaxx,dr], workingPrecision ],
159         True, SetPrecision [ linearExponentialGrid [0,(80/ Z)(* Au *)/fineStructureConstant , Np+1,order
                ,20], workingPrecision ]];
160 grid =Append[grid,knots];
161 knotslength=Length[knots]-order-2;
162 t=Table[knots[[order+i ]],{ i ,0, Np}];
163 If [ diagnostic ==True,Print["\n"];
164 Print [" The grid is :"]; Print [knots ];
165 Print [" The differences are :"]; Print [ Differences [knots ]];
166 Print [" t = ",t ];
167 Print [" The number of splines used: ", nsplines ];
168 Print [Plot [Evaluate [Table [BSplineBasis [{ order-1,knots},i ,x],{ i ,0, knotslength+1}]],{x ,0.0, Last [
        knots ]}, PlotRange->All]];
169 ];
170
171 (* define a sorting function *)
172 sortEigensystem [ eigsys_ ]:=Transpose[Sort [Transpose[ eigsys ]]];
173
174 (* define the appropriate potential function *)
175 (*V[x_]:= -Z/ x;*)
176 V[x_]:= Piecewise[{{((-Z)/(2 Rsphx) (3-x^2/Rsphx^2)),x<Rsphx},{((-Z)/ x),x>= Rsphx}}];
177 (* Generate respective matricies *)
178
```

```
179 matc=Block[{upper,lower},upper=PadLeft@ParallelTable[Sum[GaussLegendreQuadrature[BSplineBasis
      [{order-1,knots},ii,x]*BSplineBasis[{order-1,knots},ij,x],
180                 {x,t[[n]],t[[n+1]]},2 order,workingPrecision],{n,1,Np}]//Quiet,{ii,0,knotslength
                        +1},{ij,ii,knotslength+1}];
181     lower=ReplacePart[Transpose[upper],{i_,i_}->0];
182     lower+upper];
183
184 matd=Block[{upper,lower}, upper=PadLeft@ParallelTable[If[ii!=ij,Sum[GaussLegendreQuadrature[
      BSplineBasis[{order-1,knots},ii,x]*D[BSplineBasis[{order-1,knots},ij,x],x],{x,t[[n]],t[[n
      +1]]},2 order,workingPrecision],{n,1,Np}]//Quiet,0],{ii,0,knotslength+1},{ij,ii,knotslength
      +1}];
185     lower=ReplacePart[Transpose[-upper],{i_,i_}->0];
186     lower+upper];
187
188 (*matd=Block[{upper,lower}, upper=PadLeft@ParallelTable[Sum[GaussLegendreQuadrature[
      BSplineBasis[{order-1,knots},ii,x]*D[BSplineBasis[{order-1,knots},ij,x],x],{x,t[[n]],t[[n
      +1]]},2 order,workingPrecision],{n,1,Np}]//Quiet,{ii,0,knotslength+1},{ij,ii,knotslength
      +1}];
189     lower=ReplacePart[Transpose[-upper],{i_,i_}->0];
190     lower+upper];*)
191
192 matkappa=Block[{upper,lower},upper=PadLeft@ParallelTable[Sum[GaussLegendreQuadrature[(k/x)
      BSplineBasis[{order-1,knots},ii,x]*BSplineBasis[{order-1,knots},ij,x],{x,t[[n]],t[[n+1]]},2
      order,workingPrecision],{n,1,Np}]//Quiet,{ii,0,knotslength+1},{ij,ii,knotslength+1}];
193       lower=ReplacePart[Transpose[upper],{i_,i_}->0];
194       lower+upper];
195
196 matv=Block[{upper,lower}, upper=PadLeft@ParallelTable[Sum[GaussLegendreQuadrature[(V[x])
      BSplineBasis[{order-1,knots},ii,x]*BSplineBasis[{order-1,knots},ij,x],{x,t[[n]],t[[n+1]]},2
      order,workingPrecision],{n,1,Np}]//Quiet,{ii,0,knotslength+1},{ij,ii,knotslength+1}];
197     lower=ReplacePart[Transpose[upper],{i_,i_}->0];
198     lower+upper];
199
200 mataPrime=Table[If[k<0,((1/fineStructureConstant)KroneckerDelta[ii,1] KroneckerDelta[jj,1]-
201         (1/(2 fineStructureConstant)) KroneckerDelta[ii,1] KroneckerDelta[jj,(knotslength+2)
                +1]-
202         (1/(2 fineStructureConstant)) KroneckerDelta[ii,(knotslength+2)+1] KroneckerDelta[jj,1]+
```

```
203          (1/(2  fineStructureConstant ))  KroneckerDelta[ ii , knotslength+2] KroneckerDelta[ jj ,
                 knotslength+2]-
204          (1/(2  fineStructureConstant ))  KroneckerDelta[ ii ,2( knotslength+2)] KroneckerDelta[ jj ,2(
                 knotslength+2)]),
205          ((2/ fineStructureConstant ^2)   KroneckerDelta[ ii ,1]  KroneckerDelta[ jj ,1]-
206          (1/(2 fineStructureConstant ))  KroneckerDelta[ ii ,1]  KroneckerDelta[ jj ,( knotslength+2)
                 +1]-
207          (1/(2 fineStructureConstant ))  KroneckerDelta[ ii ,( knotslength+2)+1] KroneckerDelta[jj,1]+
208          (1/(2 fineStructureConstant ))  KroneckerDelta[ ii , knotslength+2] KroneckerDelta[ jj ,
                 knotslength+2]-
209          (1/(2 fineStructureConstant ))  KroneckerDelta[ ii ,2 knotslength+4] KroneckerDelta[ jj ,2
                 knotslength+4])],
210            { ii ,1,2 knotslength+4},{jj ,1,2 knotslength+4}];
211
212  If [ diagnostic ==True,Print[matc//MatrixForm];
213       Print [matd//MatrixForm];
214       Print [matkappa//MatrixForm];
215       Print [matv//MatrixForm];
216  ];
217  (* Combine matricies to form matrix A and B *)
218  matA=ArrayFlatten[{{matv,(matd-matkappa)/fineStructureConstant},{(-matd-matkappa)/
         fineStructureConstant,-(2/fineStructureConstant^2) matc+matv}}]+mataPrime;
219  matB=ArrayFlatten[{{matc,ConstantArray[0,{knotslength+2,knotslength+2}]},{ConstantArray[0,{
         knotslength+2,knotslength+2}],matc}}];
220  (*
221  Print [matA//MatrixForm];
222  Print [matB//MatrixForm];
223  *)
224
225  (*Print [" The condition  number for matA is: ",Norm[matA] Norm[Inverse[matA]]];*)
226  (* Export the matrix b and splinegrid  for  later  use *)
227  (*
228  Export[" matrixB.m",matB];
229  Export[" knots.m",knots];
230  *)
231  matrixB=Append[matrixB,matB];
232  (* calculate  the  generalized  eigenvalues  and  eigenvectors  from the above matricies *)
```

```
(* Evaluate eigenvalues *)
SetPrecision [sortEigensystem@Eigensystem[{matA,matB}],precisionGoal]
(*Chop@sortEigensystem[Eigensystem[{matA,matB}]][[1]]*)];

(* Define base states *)
pBase[x_?NumericQ,{kappa_?NumericQ,eigenVector_?ListQ,j_?NumericQ}]:=Sum[eigenVector[[splines+
    j,i]]BSplineBasis[{order-1,gridb},i-1,x],{i,1, splines }];
qBase[x_?NumericQ,{kappa_?NumericQ,eigenVector_?ListQ,j_?NumericQ}]:=Sum[eigenVector[[splines+
    j,i+splines]] BSplineBasis[{order-1,gridb},i-1,x],{i,1, splines }];

(* Define intermediate states *)
pMp[x_?NumericQ,{eigenVector_?ListQ},m_?NumericQ]:=Sum[eigenVector[[splines+m,ii]]BSplineBasis
    [{order-1,gridint},ii-1,x],{ii,1, splines }];
qMp[x_?NumericQ,{eigenVector_?ListQ},m_?NumericQ]:=Sum[eigenVector[[splines+m,ii+splines]]
    BSplineBasis[{order-1,gridint},ii-1,x],{ii,1, splines }];
pMn[x_?NumericQ,{eigenVector_?ListQ},m_?NumericQ]:=Sum[eigenVector[[(splines+1)-m,ii]]
    BSplineBasis[{order-1,gridint},ii-1,x],{ii,1, splines }];
qMn[x_?NumericQ,{eigenVector_?ListQ},m_?NumericQ]:=Sum[eigenVector[[(splines+1)-m,ii+splines]]
    BSplineBasis[{order-1,gridint},ii-1,x],{ii,1, splines }];

pListp[x_?NumericQ,{eigenVector_?ListQ,i_?NumericQ},m_?NumericQ]:=Sum[eigenVector[[i,splines+
    m,ii]]BSplineBasis[{order-1,grid[[i]]}, ii-1,x],{ii,1, splines }];
qListp[x_?NumericQ,{eigenVector_?ListQ,i_?NumericQ},m_?NumericQ]:=Sum[eigenVector[[i,splines+
    m,ii+splines]]BSplineBasis[{order-1,grid[[i]]}, ii-1,x],{ii,1, splines }];
pListn[x_?NumericQ,{eigenVector_?ListQ,i_?NumericQ},m_?NumericQ]:=Sum[eigenVector[[i,(splines
    +1)-m,ii]]BSplineBasis[{order-1,grid[[i]]}, ii-1,x],{ii,1, splines }];
qListn[x_?NumericQ,{eigenVector_?ListQ,i_?NumericQ},m_?NumericQ]:=Sum[eigenVector[[i,(splines
    +1)-m,ii+splines]]BSplineBasis[{order-1,grid[[i]]}, ii-1,x],{ii,1, splines }];

(* Define matrix elements *)
Options[matPositive]={
MaxRecursion:>$RecursionLimit,
PrecisionGoal->Automatic,
WorkingPrecision->Automatic};
Options[matNegative]={
MaxRecursion:>$RecursionLimit,
PrecisionGoal->Automatic,
```

```
260 WorkingPrecision->Automatic};
261 Options[ matPositiveList ]={
262 MaxRecursion:>$RecursionLimit,
263  PrecisionGoal->Automatic,
264 WorkingPrecision->Automatic};
265 Options[matNegativeList]={
266 MaxRecursion:>$RecursionLimit,
267  PrecisionGoal->Automatic,
268 WorkingPrecision->Automatic};
269
270 matPositive[{n_?NumericQ,k_?NumericQ,Rsp_?NumericQ,L_?NumericQ},{intereigenValues_?ListQ,
       intereigenVectors_?ListQ},{baseeigenValues_?ListQ,baseeigenVector_?ListQ,w_?NumericQ},mm_?
       NumericQ,opts:OptionsPattern[]]:=Module[{baseChoice,maxRecursion,precisionGoal,
       workingPrecision},
271 (* Control precision *)
272 {maxRecursion,precisionGoal, workingPrecision }=OptionValue[{MaxRecursion,PrecisionGoal,
       WorkingPrecision}];
273  If [ precisionGoal ===Automatic,precisionGoal=MachinePrecision];
274  If [ workingPrecision ===Automatic,workingPrecision=precisionGoal+10];
275 (* Select base state *)
276 Which[(k==-1&&n==1),baseChoice=1,
277    (k==-1&&n==2),baseChoice=2,
278    k==1,baseChoice=2,
279    k==-2,baseChoice=1];
280 (* Evaluate matrix element *)
281 (Quiet@NIntegrate[F[L,Rsp,r]( pBase[r,{k, baseeigenVector, baseChoice}] pMp[r,{ intereigenVectors },
       mm]+qBase[r,{k,baseeigenVector,baseChoice}]qMp[r,{intereigenVectors},mm]),{r,0,Rsp
       ,0.002,0.2,1}, WorkingPrecision->workingPrecision,PrecisionGoal->precisionGoal]*
       fineStructureConstant^3)^2/(( intereigenValues [[ splines +mm]]-baseeigenValues[[splines+
       baseChoice]]+w)fineStructureConstant^2)
282 ];
283 matNegative[{n_?NumericQ,k_?NumericQ,Rsp_?NumericQ,L_?NumericQ},{intereigenValues_?ListQ,
       intereigenVectors_?ListQ},{baseeigenValues_?ListQ,baseeigenVector_?ListQ,w_?NumericQ},mm_?
       NumericQ,opts:OptionsPattern[]]:=Module[{baseChoice,maxRecursion,precisionGoal,
       workingPrecision},
284 {maxRecursion,precisionGoal, workingPrecision }=OptionValue[{MaxRecursion,PrecisionGoal,
       WorkingPrecision}];
```

```
285 If [ precisionGoal ===Automatic,precisionGoal=MachinePrecision];
286 If [ workingPrecision ===Automatic,workingPrecision=precisionGoal+10];
287 (* Select base state *)
288 Which[(k==-1&&n==1),baseChoice=1,
289   (k==-1&&n==2),baseChoice=2,
290   k==1,baseChoice=2,
291   k==-2,baseChoice=1];
292 (* Evaluate matrix element *)(Quiet@NIntegrate[F[L,Rsp,x] (pBase[x,{k,baseeigenVector,baseChoice
        }] pMn[x,{intereigenVectors},mm]+qBase[x,{k,baseeigenVector,baseChoice}]qMn[x,{
        intereigenVectors},mm]),{x,0,Rsp,0.002,0.2,1}, WorkingPrecision->workingPrecision,
        PrecisionGoal->precisionGoal]*fineStructureConstant^3)^2/(( intereigenValues [[ splines +1-mm
        ]]-baseeigenValues[[splines+baseChoice]]-w)fineStructureConstant^2)
293 ];
294
295 matPositiveList [{n_?NumericQ,k_?NumericQ,Rsp_?NumericQ,L_?NumericQ},{intereigenValues_?ListQ,
        intereigenVectors_?ListQ,jj_},{baseeigenValues_?ListQ, baseeigenVector_?ListQ,w_?NumericQ},\[
        Lambda]_?NumericQ,mm_?NumericQ,opts:OptionsPattern[]]:=Module[{baseChoice,maxRecursion,
        precisionGoal,workingPrecision},
296 {maxRecursion,precisionGoal, workingPrecision }=OptionValue[{MaxRecursion,PrecisionGoal,
        WorkingPrecision}];
297 If [ precisionGoal ===Automatic,precisionGoal=MachinePrecision];
298 If [ workingPrecision ===Automatic,workingPrecision=precisionGoal+10];
299 (* Select base state *)
300 Which[(k==-1&&n==1),baseChoice=1,
301   (k==-1&&n==2),baseChoice=2,
302   k==1,baseChoice=2,
303   k==-2,baseChoice=1];
304 (* Evaluate matrix element *)(Quiet@NIntegrate[F[L,Rsp,r](pBase[r,{k,baseeigenVector,baseChoice
        }] pListp[r,{ intereigenVectors , jj },mm]+qBase[r,{k,baseeigenVector,baseChoice}]qListp[r,{
         intereigenVectors , jj },mm]),{r,0,Rsp,0.002,0.2,1}, WorkingPrecision->workingPrecision,
        PrecisionGoal->precisionGoal]*fineStructureConstant^(\[Lambda]+1))^2/((intereigenValues[[jj ,
         splines +mm]]-baseeigenValues[[splines+baseChoice]]+w)fineStructureConstant^2)
305 ];
306 matNegativeList[{n_?NumericQ,k_?NumericQ,Rsp_?NumericQ,L_?NumericQ},{intereigenValues_?ListQ,
        intereigenVectors_?ListQ,jj_},{baseeigenValues_?ListQ, baseeigenVector_?ListQ,w_?NumericQ},\[
        Lambda]_?NumericQ,mm_?NumericQ,opts:OptionsPattern[]]:=Module[{baseChoice,maxRecursion,
        precisionGoal,workingPrecision},
```

```
307 {maxRecursion,precisionGoal , workingPrecision }=OptionValue[{MaxRecursion,PrecisionGoal,
        WorkingPrecision}];
308 If [ precisionGoal ===Automatic,precisionGoal=MachinePrecision];
309 If [ workingPrecision ===Automatic,workingPrecision=precisionGoal+10];
310 (* Select base state *)
311 Which[(k==-1&&n==1),baseChoice=1,
312   (k==-1&&n==2),baseChoice=2,
313   k==1,baseChoice=2,
314   k==-2,baseChoice=1];
315 (* Evaluate matrix element *)(Quiet@NIntegrate[F[L,Rsp,x] (pBase[x,{k,baseeigenVector,baseChoice
        }] pListn [x,{ intereigenVectors , jj },mm]+qBase[x,{k,baseeigenVector,baseChoice}]qListn[x,{
        intereigenVectors , jj },mm]),{x,0,Rsp ,0.002,0.2,1}, WorkingPrecision->workingPrecision,
        PrecisionGoal->precisionGoal]*fineStructureConstant^(\[Lambda]+1))^2/((intereigenValues[[jj ,
        splines +1-mm]]-baseeigenValues[[splines+baseChoice]]-w)fineStructureConstant^2)
316 ];
317
318 Options[ nuclearPolarizationSpline ]={
319 MaxRecursion:>$RecursionLimit,
320 PrecisionGoal->Automatic,
321 WorkingPrecision->Automatic};
322  nuclearPolarizationSpline [{Z_?NumericQ,A_?NumericQ},{n_?NumericQ,l_?NumericQ,j_?NumericQ},{
        B_?NumericQ,L_?NumericQ,wL_?NumericQ},opts:OptionsPattern[]]:=
323 Module[{\[Alpha],baseSystem,baseValues, baseVectors,Bx, diagnostic=False,diagnosticB=False,
        diagnosticI =False,diagnosticN=False,\[Epsilon ],\[ Gamma],intermediateSystem,
        intermediateValues,intermediateVectors , jrange , jrangelength , k=(l-j)(2j+1),knots,knotslength ,\[
        Lambda],lp,maxRecursion,Np,precisionGoal , Rmax,R0x,Rsphx,RspAUx,RspNUx,wLx,
        workingPrecision},
324
325 {maxRecursion,precisionGoal , workingPrecision }=OptionValue[{MaxRecursion,PrecisionGoal,
        WorkingPrecision}];
326 If [ precisionGoal ===Automatic,precisionGoal=MachinePrecision];
327 If [ workingPrecision ===Automatic,workingPrecision=precisionGoal+10];
328
329 (* Convert R0 to natural units where length is in units of the reduced Compton wavelength *)
330 {Rsphx,RspNUx,RspAUx,\[Alpha],\[Epsilon],wLx}=SetPrecision[{1.2 A^(1/3)*10^-15,(1.2 A^(1/3)
        *10^-15)/reducedCompton,(1.2 A^(1/3)*10^-15)/bohrRadius,fineStructureConstant,10^-35,wL
        /27.211385},workingPrecision];
```

```
331
332 If [ diagnostic==True,
333 Print[" Diagnostic-Output: Constants"];
334 Print[" Rsph (fm) = ",Rsphx];
335 Print[" Rsph (NU) = ",RspNUx];
336 Print[" Rsph (AU) = ",RspAUx];
337 Print["          \[Alpha] = ",\[Alpha]];
338 Print["          \[Epsilon] = ",\[Epsilon]];
339 Print["         \[Omega]L = ",wLx];];
340
341 (* nuclear state properties *)
342 \[Lambda]=If[L==0,2,L];

      (* *)
343 \[Gamma]=Sqrt[1-(fineStructureConstant Z)^2];
344
345 (* Calculate the base-states *)
346 matrixB={};
347 grid={};
348 baseSystem=galerkinHS[Z,Rsphx,{l,j},{order, splines ,1}, WorkingPrecision->workingPrecision,
      PrecisionGoal->precisionGoal];
349 Print[" Base states does!"];
350 BaseVectors=baseSystem[[2]];
351 BaseValues=baseSystem[[1]];
352 gridb=grid [[1]];
353 BaseNorms=1/Sqrt[Map[BaseVectors[[#]].matrixB[[1]].BaseVectors[[#]]&,Range[2*splines ]]];
354 NBaseVectors=BaseVectors*BaseNorms;
355
356 (* Diagnostic - Check base values *)
357 If [diagnosticB==True,
358 Pcore[1,-1,r_]:=Sqrt[(1+\[Gamma])/2] Sqrt[(2 Z)/Gamma[2 \[Gamma] +1]] (2 Z r)^\[Gamma] Exp
      [-Z r];
359 Qcore[1,-1,r_]:=Sqrt[(1-\[Gamma])/2] Sqrt[(2 Z)/Gamma[2 \[Gamma] +1]] (2 Z r)^\[Gamma] Exp
      [-Z r];
360 Print[" Diagnostic-Output: Base-state check"];
361 Print[BaseValues[[ splines +1]]]; Print["\[CapitalDelta]En = ",Map[Abs@(energySommerfeld[Z,#,k
      ]-1-(BaseValues[[splines+#]]*fineStructureConstant^2))&,{1,2,3,4,5,6}] ];
```

```
362 Print["Before normalization of base states: ",Map[BaseVectors[[#]].matrixB[[1]].BaseVectors
        [[#]]&,Range[2 splines ]]];
363 Print["Normalization of base states: ",Map[NBaseVectors[[#]].matrixB[[1]].NBaseVectors[[#]]&,
        Range[2 splines ]]];
364 (* Plot base wavefunctions *)
365 Print[Plot[Evaluate[{pBase[r,{k,NBaseVectors,1}],qBase[r,{k,NBaseVectors,1}]/(
        fineStructureConstant Z)}],{r,0,0.2}, PlotRange->All]];
366 Print[Plot[Evaluate[Abs[pBase[r,{k,NBaseVectors,1}]]-Pcore[1,-1,r]],{r,0,0.2}, PlotRange->All]];
367 Print[Plot[Evaluate[Abs[qBase[r,{k,NBaseVectors,1}]]-Qcore[1,-1,r]],{r,0,0.2}, PlotRange->All
        ]];];
368
369 (* Calculate the intermediate states *)
370 matrixB={};
371 grid={};
372 jrange=Range[Abs[L-j],L+j];
373 jrangelength=Length[jrange];
374 lp=Flatten@Pick[Map[{#-1/2,#+1/2}&,jrange],Map[EvenQ,Map[{#-1/2,#+1/2}&,jrange]+L+l
        ,{2}]];
375 If[diagnostic==True,
376 Print["\nDiagnostic-Output: Allowed Intermediate States"];
377 Print["Allowed jp = ",jrange];
378 Print["Allowed lp = ",lp];
379 Print["Number on intermediate states = ", jrangelength];];
380
381 intermediateSystem=MapThread[galerkinHS[Z,Rsphx,{#1,#2},{order,splines,1},WorkingPrecision->
        workingPrecision,PrecisionGoal->precisionGoal]&,{lp,jrange}];
382 Print["\nIntermediate states done!"];
383 IntermediateValues=Table[intermediateSystem[[i,1]],{i,jrangelength}];
384 IntermediateVectors=Table[intermediateSystem[[i,2]],{i,jrangelength}];IntermNorms=Table[(Sqrt[
        Map[IntermediateVectors[[i,#]].matrixB[[i]].IntermediateVectors[[i,#]]&,Range[2*splines ]]])
        ^-1,{i,jrangelength}];
385 NIntermediateVectors=IntermediateVectors*IntermNorms;
386
387 (* positive continuum range *)
388 urange=Table[Select[Range[splines], IntermediateValues[[jj, splines+#]]>0&],{jj,jrangelength}];
389
390 (* Diagnostic - Check intermediate values *)
```

```
391 If [ diagnosticI ==True,Print["\nDiagnostic-Output: Intermediate-state check"];
392 Print[IntermediateValues];
393 Print["\[CapitalDelta]En = ",Map[(energySommerfeld[Z,#+1,(lp[[1]]-jrange[[1]])(2jrange[[1]]+1)
      ]-1-(IntermediateValues[[1, splines +#]]*fineStructureConstant^2)) &,{1,2,3,4,5,6}]];
394 Print["\[CapitalDelta]En = ",Map[(energySommerfeld[Z,#+2,(lp[[2]]-jrange[[2]])(2jrange[[2]]+1)
      ]-1-(IntermediateValues[[2, splines +#]]*fineStructureConstant^2)) &,{1,2,3,4,5,6}]];
395 Print["urange:",urange];
396 Print["Normalization of intermediate states: ",{Map[NIntermediateVectors[[1,#]].matrixB [[1]].
      NIntermediateVectors[[1,#]]&,Range[2 splines ]], Map[NIntermediateVectors[[2,#]].matrixB
      [[2]]. NIntermediateVectors[[2,#]]&,Range[2 splines ]]}];
397 Print[Plot[Evaluate[{pListp[r,{NIntermediateVectors,1},2], qListp[r,{NIntermediateVectors,1},2]/(
      fineStructureConstant Z)}],{r,0,0.15}, PlotRange->All]];
398 Print[Plot[Evaluate[{pListp[r,{NIntermediateVectors,2},1], qListp[r,{NIntermediateVectors,2},1]/(
      fineStructureConstant Z)}],{r,0,0.15}, PlotRange->All]];];
399 (*
400 Print[Map[Plot[{pMp[r,{NIntermediateVectors,1},urange [[1,#]]], qMp[r,{NIntermediateVectors,1},
      urange [[1,#]]]/( fineStructureConstant Z)},{r,0,10}, PlotRange->All]&,Range[1,5]]];
401 Print[Map[Plot[{pMp[r,{NIntermediateVectors,2},urange [[2,#]]], qMp[r,{NIntermediateVectors,2},
      urange [[2,#]]]/( fineStructureConstant Z)},{r,0,10}, PlotRange->All]&,Range[1,5]]];
402 *)
403
404 (* Evaluate nuclear polarization *)
405 ;
406 If[diagnosticN==True,
407 (* Diagnostic - Plot matrix element integrands *)
408 Print["\nDiagnostic-Output: Integrand check"];
409 Print[Plot[F[L,RspAUx,r],{r,0,0.001}, PlotRange->All]];
410 Print[Map[Plot[F[L,RspAUx,r]*(pBase[r,{k,NBaseVectors,1}]*pListp[r,{NIntermediateVectors,1},
      urange[[1,#]]]+qBase[r,{k,NBaseVectors,1}]*qListp[r,{NIntermediateVectors,1},urange
      [[1,#]]]) ,{r,0,0.001}, PlotRange->All]&,Range[1,3]]];
411 Print[Map[Plot[F[L,RspAUx,r]*(pBase[r,{k,NBaseVectors,1}]*pListp[r,{NIntermediateVectors,2},
      urange[[2,#]]]+qBase[r,{k,NBaseVectors,1}]*qListp[r,{NIntermediateVectors,2},urange
      [[2,#]]]) ,{r,0,0.001}, PlotRange->All]&,Range[1,3]]];
412 ];
413 (* Calculate NP correction *)
414 DE=-\[Alpha]^2 B (0.000670605)^\[Lambda] ((2L+1)/(4\[Pi]))ParallelSum[(2jrange[[i]]+1)
      ThreeJSymbol[{jrange[[i]],1/2},{j,-1/2},{L,0}]^2 (Total[Map[matPositiveList[{n,k,RspAUx,L},{
```

```
IntermediateValues,NIntermediateVectors,i},{BaseValues,NBaseVectors,wLx},\[Lambda],#,
WorkingPrecision->workingPrecision,PrecisionGoal->precisionGoal]&,urange[[i]]]]+Total[Map[
matNegativeList[{n,k,RspAUx,L},{IntermediateValues,NIntermediateVectors,i},{BaseValues,
NBaseVectors,wLx},\[Lambda],#,WorkingPrecision->workingPrecision,PrecisionGoal->
precisionGoal]&,Range[splines]]]),{i,jrangelength}]QuantityMagnitude@electronRestEnergy;
DE
];

nuclearPolarization [L_?NumericQ,B_?NumericQ,wL_?NumericQ,Z_?NumericQ,A_?NumericQ,n_?
NumericQ,l_?NumericQ,j_?NumericQ]:=Module[{BeL,r0=1.2 A^(1/3),\[Mu],\[Kappa],\[Gamma],
Nn,\[Epsilon],R,Cc,range,mat,jrange,jrangelength,\[Kappa]range,lrange},
(* This function acts as a wrapper for the two methods of calculating the nuclear polarization
correction. Since the method does not really matter, and because the spline method is
rather slow, the analytical form will be used when appropriate and the spline method
invoked when needed *)

(* Analytical portion *)
If[j==1/2 && L>=2,
\[Mu][jp_]:=Sqrt[(jp+1/2)^2-(fineStructureConstant*Z)^2];
\[Kappa]=l*(l+1)-j*(j+1)-1/4;
\[Gamma]=Sqrt[\[Kappa]^2-(fineStructureConstant*Z)^2];
Nn=Sqrt[((n-Abs[\[Kappa]])+\[Gamma])^2+(fineStructureConstant*Z)^2];

\[Epsilon]=(1+((fineStructureConstant*Z)/(n-j-1/2+\[Mu][j]))^2)^(-1/2);

R[jp_]:=1/(\[Mu][jp]*(\[Gamma]+\[Mu][jp]+L+1))*(1/(\[Gamma]+L+1)+2/(\[Mu][jp]-\[Gamma
]+L))+1/(\[Mu][jp]*(\[Gamma]+\[Mu][jp]-L))*(1/(L-\[Gamma])+2/(\[Gamma]-\[Mu][jp]-L)
);

Cc=(((n-Abs[\[Kappa]])^2-2*\[Epsilon]*(n-Abs[\[Kappa]])*(Nn-\[Kappa])+(Nn-\[Kappa])^2)*
Gamma[2*\[Gamma]+(n-Abs[\[Kappa]])+1])/(Gamma[2\[Gamma]+1]^2*Nn^2*(Nn-\[Kappa])
*(n-Abs[\[Kappa]])!);

Return[-2*Pi*(B*fineStructureConstant*(10^-28)^L)*(fineStructureConstant*(fineStructureConstant
*Z)^2*Cc)/((2L+1)*(r0*10^-15)^(2L))*((2*Z*r0*10^-15)/(Nn*bohrRadius))^(2*\[Gamma])*
Sum[(2jp+1)*ThreeJSymbol[{jp,1/2},{j,-1/2},{L,0}]^2*R[jp],{jp,Abs[L-j],L+j}]*
electronRestEnergy]];
```

```
435
436 (* Numerical portion *)
437
438 (* Input *)
439  splines =40;
440 order=8;
441 nuclearParams={Z,A};
442 atomicParams={n,l,j};
443  polarizationParams={B,L,wL*10^6};
444
445 Return[ nuclearPolarizationSpline [nuclearParams,atomicParams,polarizationParams]]
446  ];
447
448 omegaL[L_?NumericQ,\[Tau]_?NumericQ,A_?NumericQ]:=
449 Which[
450 (* Function generates the excitation energies (in MeV) for the giant multipole resonance states
       which are assumed to be concentrated in a single resonant state for eact (L\[Tau])
451 Input:
452   L - nuclear multipole moment (L=0,1,2,3).
453  \[Tau] - isospin of excitation (\[Tau]=0,1).
454  A - atomic mass number. *)
455
456 L==0,N@(100.*(1-\[Tau])+200.*\[Tau])*(1-A^(-1/3))*A^(-1/3),
457 L==1,N@95.*(1-A^(-1/3))*A^(-1/3),
458 True,N@(75.*(1-\[Tau])+160.*\[Tau])(1-A^(-1/3))*A^(-1/3)];
459
460 bEL[L_?NumericQ,\[Tau]_?NumericQ,Z_?NumericQ,A_?NumericQ]:=
461 Which[
462 (* Function generates the B(EL) values for the giant multipole resonance states which are
       estimated by the phenomenological energy weighted sum rule, see Hoffmann (1984) and Rinker
       (1978)
463 Input:
464   L - nuclear multipole moment (L=0,1,2,3).
465  \[Tau] - isospin of excitation (\[Tau]=0,1).
466  A - atomic mass number.
467  Z - nuclear charge. *)
468
```

```
469 L==0,(25./(4.*\[Pi]))*Z*(0.0035857574)*(A^(2/3)/omegaL[L,\[Tau],A])*(Z/A*(1-\[Tau])+(A-Z)/
        A*\[Tau]),
470 True ,(3./(4.*\[ Pi]) )*Z*(20.7509113)*(L /omegaL[L,\[Tau],A])*(0.01)^L*(1.2*A^(1/3))^(2L-2)*(Z/
        A*(1-\[Tau])+(A-Z)/A*\[Tau])];
471
472 End[];          (* end the private context *)
473 Protect [];     (* protect exported symbols *)
474 EndPackage[]    (* end the package context *)
```

Appendix C

Appendix 4: Finite Basis Sets

In Chapter 7 of this thesis, where we dealt with the nuclear polarization correction, we saw that we needed to perform a sum over intermediate electron states to obtain the final value of the energy. In this thesis, the technique of finite basis sets was chosen to address the problem. The basic idea is to replace the summation and integration over the real spectrum with a single finite summation over a psuedospectrum. Although there are many ways of doing this, we will follow the approach of Johnson et al. [43], Sapirstein and Johnson [77] and Sapirstein [75].

C.1 Forming the basis set

The first step in forming a finite basis set is to confine the atom (or ion) in a finite box of radius R, which discretizes the continuum and limits the number of bound states. The radius is chosen sufficiently large so that the resulting states are not distorted. Typically a value of $40/Z_{nuc}$ is chosen [75]. Because the problem under consideration is relativistic, special care is required in implementing appropriate boundary conditions. The problem arises when attempting to confine an electron in a potential that goes to infinity at $r > R$. This problem is the well known Klein Paradox [11, 82], and leads to oscillatory solutions. The same problem occurs in nuclear physics when hadrons are treated as bound states of quarks; and the solution implemented is the the same, letting the mass of the hadron become large for $r > R$.

This is the celebrated "MIT bag model" [43]. When the representation of the Dirac wavefunction defined in (2.18) is used:

$$\phi_{n\kappa m}(\vec{r}) = \frac{1}{r}\begin{pmatrix} \imath P_\kappa(r)\ \Omega_{\kappa m}(\hat{r}) \\ Q_\kappa(r)\ \Omega_{-\kappa m}(\hat{r}) \end{pmatrix}, \tag{C.1}$$

the boundary conditions become $P(r) = Q(r)$.

The above represent a denumerable infinity of states, the task is to convert this to a finite number. The conversion will be carried out via a Galerkin method as described in [33]; the equations are expressed in terms of an action principle and the action integral is expanded in terms of basis functions. The variation of the action leads to the radial Dirac equation

$$\begin{aligned} S = \frac{1}{2}\int_0^R dr \Bigg[& cP_\kappa(r)\left(\frac{d}{dr} - \frac{\kappa}{r}\right) Q_\kappa(r) - cQ_\kappa(r)\left(\frac{d}{dr} - \frac{\kappa}{r}\right) P_\kappa(r) \\ & + V(r)\left(Q_\kappa^2(r) + P_\kappa^2(r)\right) - 2mc^2 Q_\kappa^2(r)\Big] - \frac{\epsilon}{2}\int_0^R dr\left[P_\kappa^2(r) + Q_\kappa^2(r)\right] \\ & + S_{boundary}, \end{aligned} \tag{C.2}$$

where $S_{boundary}$ is given as

$$S_{boundary}(\kappa < 0) = \frac{c}{4}\left[P_\kappa^2(r) - Q_\kappa^2(r)\right] + \frac{c}{2}P_\kappa^2(0) - \frac{c}{2}P_\kappa(0)Q_\kappa(0) \tag{C.3}$$

and

$$S_{boundary}(\kappa > 0) = \frac{c}{4}\left[P_\kappa^2(r) - Q_\kappa^2(r)\right] + c^2 P_\kappa^2(0) - \frac{c}{2}P_\kappa(0)Q_\kappa(0). \tag{C.4}$$

The requirement $\delta S = 0$ force $P_\kappa(R) = Q_\kappa(R)$ and $P_\kappa(0) = 0$; the latter constraint comes from the term in $S_{boundary}$ involving $P_\kappa^2(0)$. Furthermore, the larger constant multiplying the $P_\kappa^2(0)$ term in the $\kappa > 0$ case is chosen empirically in order to prevent spurious states. Spurious states are parts of the pseudospectrum that have non-physical energies and lie in the bound-state region; typically at the position of the

lowest-bound state. These states can be moved to the end of the set in order for the first members of the set to correspond to physical bound states [43].

C.2 Definition of basis splines

The basis chosen will be a set of n B-splines of order k as described in de Boor [29]. We divide the interval $[0, R]$ into segments where the endpopints of the segments are given by a knot sequence $\{t_i\},\ i = 1, 2, ..., n+k$. The B-splines of order k, $B_{i,k}(r)$, on this knot sequence are defined by the recursive relation [29],

$$B_{i,1}(r) = \begin{cases} 1, & t_i \leq r \leq t_{i+1} \\ 0, & \text{otherwise} \end{cases} \tag{C.5}$$

and

$$B_{i,k}(r) = \frac{r - t_i}{t_{i+k-1} - t_i} B_{i,k-1}(r) + \frac{t_{i+k} - r}{t_{i+k} - t_{i+1}} B_{i+1,k-1}(r). \tag{C.6}$$

The function is a piecewise polynomial of degree $k-1$ inside the interval $t_i \leq r \leq t_{i+1}$ which vanishes outside the interval. The set of B-splines of order k of the knot sequence t_i forms a complete basis for piecewise polynomials of degree $k-1$ on the interval spanned by the knot sequence. The sum at any point r of all the B-splines that do not vanish at the point equals one. The knots defining the grid have k-fold multiplicity at the endpoints 0 and R, that is $t_1 = t_2 = \cdots = t_k = 0$ and $t_{n+1} = t_{n+2} = \cdots = t_{n+k} = R$. For $k > 1$, the B-splines usually vanish at the endpoints, except the first B-spline equals 1 at $r = 0$ and the last B-spline equals 1 at $r = R$. This fact will be used to implement appropriate boundary conditions. In general there is no restriction how the knots are defined, provided that they are monotonically increasing.

Expansions are made for P and Q in terms of the B-splines:

$$P(r) = \sum_{i=1}^{n} p_i B_i, \qquad Q(r) = \sum_{i=1}^{n} q_i B_i, \tag{C.7}$$

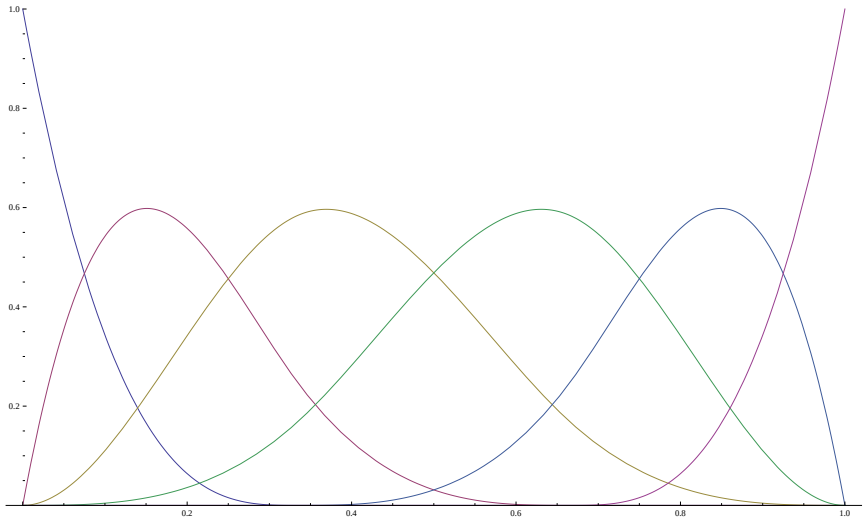

Figure C.1: Basis set of B-splines of order 3 over the knot sequence $\{0, 0, 0, 0, 1/3, 2/3, 1, 1, 1, 1\}$.

and together with the variational principle, can be applied to (C.2) to obtain a system of equations which can be written as a generalized $2n \times 2n$ eigenvalue problem

$$Av = \epsilon Bv \tag{C.8}$$

where the vector of length 2n is given by $v = (pl, p2, \cdots, pn, ql, q2, \cdots, qn)$. A and B are symmetric $2n \times 2n$ matrices,

$$A = \begin{pmatrix} (V) & c[(D) - (\kappa/r)] \\ -c[(D) + (\kappa/r)] & -2mc^2(C) + (V) \end{pmatrix} + A', \tag{C.9}$$

$$B = \begin{pmatrix} (C) & 0 \\ 0 & (C) \end{pmatrix}. \tag{C.10}$$

The contribution from the boundary conditions come in through the matrix A', given

as,

$$A' = \begin{cases} c\delta_{i,1}\delta_{j,1} - \frac{c}{2}\delta_{i,1}\delta_{j,n+1} - \frac{c}{2}\delta_{i,n+1}\delta_{j,1} & \\ +\frac{c}{2}\delta_{i,n}\delta_{j,n} - \frac{c}{2}\delta_{i,2n}\delta_{j,2n}, & \text{for } \kappa < 0, \\ 2c^2\delta_{i,1}\delta_{j,1} - \frac{c}{2}\delta_{i,1}\delta_{j,n+1} - \frac{c}{2}\delta_{i,n+1}\delta_{j,1} & \\ +\frac{c}{2}\delta_{i,n}\delta_{j,n} - \frac{c}{2}\delta_{i,2n}\delta_{j,2n}, & \text{for } \kappa > 0. \end{cases} \tag{C.11}$$

The $n \times n$ matrices forming (C.9) and (C.10) can be written as,

$$(C)_{ij} = \int B_i(r)B_j(r)dr, \tag{C.12a}$$

$$(D)_{ij} = \int B_i(r)dB_j(r)dr, \tag{C.12b}$$

$$(V)_{ij} = \int B_i(r)V(r)B_j(r)dr, \tag{C.12c}$$

$$(\kappa/r)_{ij} = \int B_i(r)\kappa/rB_j(r)dr. \tag{C.12d}$$

It is interesting to note that the matrices (C), (D), (V), and (κ/r) are diagonally dominant banded matrices, allowing one to evaluate the solution to the generalized eigenvalue equation to very high accuracy, even when the basis sets become large. The orthonormalty condition of the solution if given by:

$$\sum_{i,j} v_i^\alpha (B)_{ij} v_j^\beta = \delta_{\alpha\beta} \tag{C.13}$$

where v^α is the eigenvector associated with the eigenvalue ϵ_α

C.3 Mathematica Implementation - "BSpline" Package

In this section we give the code for the implementation of the above theory in the Mathematica package "BSpline.m".

```
(* : Title : BSpline.m -- *)
(* :Context: ASMSThesis`BSpline` *)
(* :Author: Andrew S. M. Senchuk *)
(* :Summary:
  This package uses the Galerkin method together with the BSplineBasis[] function to generate
  a pseudo-spectrum to the Dirac equation for a H-like ion.
*)
(* :Copyright:     2017 by Andrew S. M. Senchuk *)
(* :Package Version: 1.0 *)
(* :Mathemtica Version: 9.0 *)
(* :Keywords: Bsplines, Galerkin, Dirac, H-ion *)
(* :Sources:
  W. R. Johnson, S. A. Blundell, and J. Sapirstein, Phys. Rev. A, 37, 2, (1988)
  J. Sapirstein, W. R. Johnson, J. Phys. B: At. Mol. Opt. Phys. 29 (1996)*)
(* :Warnings:
  <description of global effects, incompatibilities >
*)
(* : Limitations :
  <special cases not handled, known problems>
*)
(* : Discussion :
  <description of algorithm, information for experts>
*)
(* :Requirements:
  ASMSThesis/AtomicConstants.m
  ASMSThesis/ArrayOfFunctionsRule.m *)
(* :Examples:

  <sample input>
  Z=2; rms=1.671; nsplines=40; order=7;
  TRKSumRule[Z,{0,1/2},1,PrecisionGoal->20]

  <sample output>
  TRK Sum-Rule: -1.278657752317*10^-7
*)

```

```
(* set up the package context, including public imports *)
BeginPackage["ASMSThesis`BSpline`","ASMSThesis`AtomicConstants`"]

(* usage messages for the exported functions and the context itself *)
BSpline::usage = "BSpline.m is a package that allows the user to generate a pseudo-spectrum for
    the H-ion Dirac equation in Atomic units. The algorithm uses B-Splines incorporated into
    the Galerkin method to generate both eigenvalues and eigenvectors. The package also allows
    the user to check the quality of the spectrum by calculating the relativistic TRK Sum-
    Rule. Options in the function definitions allows the user to specify the WorkingPrecision and
    PrecisionGoal of the various algorithms."

galerkinHS::usage = "galerkinHS[Z,R0,{l,j},{order, nsplines,base},opts] "

TRKSumRule::usage = "TRKSumRule[Z,{l0,j0},l,opts]"

Begin["`Private`"]  (* begin the private context (implementation part) *)

CloseKernels[];                          (* Initialize all available kernels *)

Unprotect[$ProcessorCount];
$ProcessorCount=4;
LaunchKernels[4];

(* definitions of auxiliary functions and local (static) variables *)

(* Sommerfeld energy *)
energySommerfeld[Z_,n_,kappa_]:=(fineStructureConstant^-2)(1+((fineStructureConstant Z)/(n-Abs
    [kappa]+Sqrt[kappa^2-(fineStructureConstant Z)^2]))^2)^(-1/2);

GaussLegendreQuadrature[f_,{x_,a_,b_}, n_Integer: 10, prec_: MachinePrecision]:=
  Module[{nodes,weights},
    {nodes,weights}=Most[NIntegrate`GaussRuleData[n,prec]];
    (b-a) weights.Map[Function[x,f], Rescale[nodes,{0,1},{a,b}]]
  ];

(* base-state grid generating function *)
makeGrid[nsplines_, order_, rmax_,dr0_]:=
```

```
68 Module[{ipow=nsplines-order+1,t0,h},
69
70 (* Generate the t0 and h parameters *)
71 {t0,h}=step[ipow,rmax,dr0];
72 (*Print[{t0,h}];*)
73 (* Generate the grid *)
74 Join[ConstantArray[0.0,{order}], Table[t0 (Exp[(i-order) h]-1),{i,order+1,nsplines}],
       ConstantArray[rmax,{order}]]
75 ];
76 step[ipow_,rmax_,dr_]:=
77 Module[{small=10.^-10, nmax=54,a,b,c, dx,f,fa,fb,fc,t0,h,i},
78
79 f[x_]:=1.0+(rmax/dr)*x-(1.0+x)^ipow;
80
81  fa=f[small]; a=small;
82 If[fa<= 0.0,Print["fa !!!"]; Abort []];
83 fb=f[1.0]; b=1.0;
84 If[fb>= 0.0,Print["Problem with fb! Increase the number of splines ..."]; Abort []];
85
86 dx=1.0;i=1;c=0.5*(a+b);fc=f[c];
87 While[fc!=0.0&&i<nmax,
88 If[fb*fc>0.0,b=c;fb=fc;,a=c;fa=fc;];
89 c=0.5*(a+b);
90 fc=f[c];
91 ++i;];
92
93 (*Print[{dr/c,Log[1.0+c]}];*)
94 {dr/c,Log[1.0+c]}
95 ];
96
97 linearExponentialGrid[rmin_?NumericQ,rmax_?NumericQ,n_?NumericQ,order_?NumericQ,i0_?
       NumericQ,h0_?NumericQ]:=Module[{alpha,beat,h=h0,r0},
98 (* rmin: minimum value for the grid *)
99 (* rmax: maximum value for the grid *)
100 (* n: number of grid points *)
101 (* order: order of the splines used *)
102 (* i0: points at which linear region begins *)
```

```
103 If [i0>= n,Print["ERROR: i0 too big. Reduce i0 or  increase  number of splines ."];,
104 r0=(rmax (Exp[h(i0−1)]−1)+h rmin Exp[h(i0−1)](n−i0))/(h Exp[h(i0−1)](n−i0)+Exp[h(i0−1)]−1);
105 alpha=(r0−rmin)/(Exp[h(i0−1)]−1);
106 beat=(rmax−r0)/(n−i0);
107 Join[ConstantArray[0,{order−1}],Table[rmin+alpha (Exp[h(i−1)]−1),{i,1,i0−1}],Table[r0+beat (i−
        i0),{i,i0,n}],ConstantArray[rmax,{order−1}]]];
108
109 (* Define base states *)
110 pBase[x_?NumericQ,{order_?NumericQ,eigenVector_?ListQ,j_?NumericQ}]:=Sum[eigenVector[[splines+j
        ,ii]] BSplineBasis[{order−1,gridb}, ii −1,x],{ ii ,1, splines }];
111 qBase[x_?NumericQ,{order_?NumericQ,eigenVector_?ListQ,j_?NumericQ}]:=Sum[eigenVector[[splines+j
        ,ii+splines]]  BSplineBasis[{order−1,gridb}, ii −1,x],{ ii ,1, splines }];
112
113 (* Define intermediate states *)
114 pMp[x_?NumericQ,{order_?NumericQ,eigenVector_?ListQ,grid_?ListQ,i_?NumericQ},m_?NumericQ]:=
        Sum[eigenVector[[i,splines+m,ii]]BSplineBasis[{order−1,grid}, ii −1,x],{ ii ,1, splines }];
115 qMp[x_?NumericQ,{order_?NumericQ,eigenVector_?ListQ,grid_?ListQ,i_?NumericQ},m_?NumericQ]:=
        Sum[eigenVector[[i,splines+m,ii+splines]]BSplineBasis[{order−1,grid}, ii −1,x],{ ii ,1, splines }];
116 pMn[x_?NumericQ,{order_?NumericQ,eigenVector_?ListQ,grid_?ListQ,i_?NumericQ},m_?NumericQ]:=
        Sum[eigenVector[[i,(splines+1)−m,ii]]BSplineBasis[{order−1,grid}, ii −1,x],{ ii ,1, splines }];
117 qMn[x_?NumericQ,{order_?NumericQ,eigenVector_?ListQ,grid_?ListQ,i_?NumericQ},m_?NumericQ]:=
        Sum[eigenVector[[i,(splines+1)−m,ii+splines]]BSplineBasis[{order−1,grid}, ii −1,x],{ ii ,1, splines
        }];
118
119 parity [l1_?NumericQ,l2_?NumericQ,l3_?NumericQ]:=If[EvenQ[l1+l2+l3],Return[1],Return[0]];
120
121 (* definition  of the exported functions *)
122 Options[galerkinHS]={
123 MaxRecursion:>$RecursionLimit,
124 PrecisionGoal−>Automatic,
125 WorkingPrecision−>Automatic};
126
127 galerkinHS[Z_?NumericQ,R0_?NumericQ,{l_?NumericQ,j_?NumericQ},{order_?NumericQ,nsplines_?
        NumericQ,base_?NumericQ},opts:OptionsPattern[]]:=
128 Module[{alpha,aPrime,cSplineMat,diagnostic=False,dr,dSplineMat,epsilon,hardSphere,k=(l−j)(2j+1),
        knots,knotslength,kSplineMat,mataPrime,matA,matB,matv,matkappa,matc,
129 matd,maxRecursion,Np,precisionGoal,R0x,Rmaxx,Rsphx,scal,sortEigensystem,t,V,vSplineMat,
```

```
      workingPrecision },
130
131 {maxRecursion,precisionGoal , workingPrecision }=OptionValue[{MaxRecursion,PrecisionGoal,
      WorkingPrecision}];
132 If [ precisionGoal ===Automatic,precisionGoal=MachinePrecision];
133 If [ workingPrecision ===Automatic,workingPrecision=precisionGoal+10];
134
135 (* Convert R0 to natural units where length is in units of the reduced Compton wavelength *)
136 {R0x,Rmaxx,Rsphx,alpha,epsilon, scal }=SetPrecision[{R0,(80/Z)(* Au *),Sqrt[5/3]*(R0*10^-15)/
      bohrRadius,fineStructureConstant,10^-150,(2/Z)},workingPrecision];
137
138 (* define the basis functions: *)
139 Np=nsplines+1-order;
140
141 If [base==1,dr=Which[Abs[k]==1,SetPrecision[0.0001scal,workingPrecision],
142             Abs[k]==2,SetPrecision[0.001scal , workingPrecision ],
143             True, SetPrecision [0.08  scal , workingPrecision ]],
144     dr=Which[Abs[k]==1,SetPrecision[0.265,workingPrecision],
145         Abs[k]==2,SetPrecision[0.26, workingPrecision ],
146         True, SetPrecision [0.27, workingPrecision ]]];
147
148 knots=Which[base==1,SetPrecision[makeGrid[nsplines,order,Rmaxx,dr], workingPrecision ],
149       True, SetPrecision [ linearExponentialGrid [0, Rmaxx,Np+1,order,Np,dr],workingPrecision ]];
150 grid=knots;
151 splines =nsplines;
152 knotslength=Length[knots]-order-2;
153 t=Table[knots[[order+i ]],{ i ,0, Np}];
154 (*Print [t ];
155 Print["The number of linear points used: ", knotslength-34];*)
156 Print["\n"];
157 Print["The grid is :"]; Print [ grid ];
158 Print["The differences are :"]; Print [ Differences [ grid ]];
159 Print["The number of splines used: ", nsplines ];
160 (*Print [Plot [Evaluate [Table [BSplineBasis [{ order-1,knots},i ,x],{ i ,0, knotslength+1}]],{x ,0.0, Last [
      knots ]}, PlotRange->All]];*)
161
162 (* define a sorting function *)
```

```
163 sortEigensystem[ eigsys_]:=Transpose[Sort[Transpose[eigsys ]]];
164
165 (* define the appropriate potential function *)
166 V[x_]:= Piecewise[{{((-Z/(2 Rsphx)) *(3-x^2/Rsphx^2)),x<Rsphx},{((-Z)/ x),x>= Rsphx}}];
167 (*V[x_]:= (-Z)/x;*)
168 (* Generate respective matricies *)
169
170 matc=Block[{upper,lower},
171     upper=PadLeft@ParallelTable[Sum[GaussLegendreQuadrature[BSplineBasis[{order-1,knots},ii,x]*
          BSplineBasis[{order-1,knots}, ij ,x],
172                 {x,t[[n]], t[[n+1]]},2 order, workingPrecision ],{ n,1, Np}]//Quiet,{ii ,0, knotslength
                    +1},{ij, ii , knotslength+1},
173                 DistributedContexts -> {"ASMSThesis`BSpline`Private`"}];
174     lower=ReplacePart[Transpose[upper],{ i_, i_}->0];
175     lower+upper];
176
177 matd=Block[{upper,lower},
178     upper=PadLeft@ParallelTable[If[ ii !=ij ,Sum[GaussLegendreQuadrature[BSplineBasis[{order-1,
          knots},ii,x]*D[BSplineBasis[{order-1,knots}, ij ,x],x],{x,t[[n]], t[[n+1]]},2 order,
          workingPrecision ],{ n,1, Np}]//Quiet,0],{ ii ,0, knotslength+1},{ij, ii , knotslength+1},
          DistributedContexts -> {"ASMSThesis`BSpline`Private`"}];
179     lower=ReplacePart[Transpose[-upper],{i_, i_}->0];
180     lower+upper];
181
182 matkappa=Block[{upper,lower},
183       upper=PadLeft@ParallelTable[Sum[GaussLegendreQuadrature[(k/x)BSplineBasis[{order-1,knots
            },ii,x]*BSplineBasis[{order-1,knots}, ij ,x],{x,t[[n]], t[[n+1]]},2 order, workingPrecision
            ],{ n,1, Np}]//Quiet,{ii ,0, knotslength+1},{ij, ii , knotslength+1},DistributedContexts ->
             {"ASMSThesis`BSpline`Private`"}];
184       lower=ReplacePart[Transpose[upper],{ i_, i_}->0];
185       lower+upper];
186
187 matv=Block[{upper,lower},
188     upper=PadLeft@ParallelTable[Sum[GaussLegendreQuadrature[(V[x])BSplineBasis[{order-1,knots},
          ii,x]*BSplineBasis[{order-1,knots}, ij ,x],{x,t[[n]], t[[n+1]]},2 order, workingPrecision ],{
          n,1, Np}]//Quiet,{ii ,0, knotslength+1},{ij, ii , knotslength+1},DistributedContexts -> {"
          ASMSThesis`BSpline`Private`"}];
```

```
189     lower=ReplacePart[Transpose[upper],{i_,i_}->0];
190     lower+upper];
191
192 mataPrime=Table[If[k<0,((1/fineStructureConstant)KroneckerDelta[ii,1] KroneckerDelta[jj,1]-
193         (1/(2 fineStructureConstant)) KroneckerDelta[ii,1] KroneckerDelta[jj,(knotslength+2)
                +1]-
194         (1/(2 fineStructureConstant)) KroneckerDelta[ii,(knotslength+2)+1] KroneckerDelta[jj,1]+
195         (1/(2 fineStructureConstant)) KroneckerDelta[ii,knotslength+2] KroneckerDelta[jj,
                knotslength+2]-
196         (1/(2 fineStructureConstant)) KroneckerDelta[ii,2(knotslength+2)] KroneckerDelta[jj,2(
                knotslength+2)]),
197         ((2/fineStructureConstant^2) KroneckerDelta[ii,1] KroneckerDelta[jj,1]-
198         (1/(2fineStructureConstant)) KroneckerDelta[ii,1] KroneckerDelta[jj,(knotslength+2)
                +1]-
199         (1/(2fineStructureConstant)) KroneckerDelta[ii,(knotslength+2)+1] KroneckerDelta[jj,1]+
200         (1/(2fineStructureConstant)) KroneckerDelta[ii,knotslength+2] KroneckerDelta[jj,
                knotslength+2]-
201         (1/(2fineStructureConstant)) KroneckerDelta[ii,2knotslength+4] KroneckerDelta[jj,2
                knotslength+4])],
202           {ii,1,2knotslength+4},{jj,1,2knotslength+4}];
203
204 If[diagnostic==True,Print[matc//MatrixForm];
205 Print[matd//MatrixForm];
206 Print[matkappa//MatrixForm];
207 Print[matv//MatrixForm];];
208
209
210 (* Combine matricies to form matrix A and B *)
211 matA=ArrayFlatten[{{matv,(matd-matkappa)/fineStructureConstant},{(-matd-matkappa)/
        fineStructureConstant,-(2/fineStructureConstant^2) matc+matv}}]+mataPrime;
212 matB=ArrayFlatten[{{matc,ConstantArray[0,{knotslength+2,knotslength+2}]},{ConstantArray[0,{
        knotslength+2,knotslength+2}],matc}}];
213 (*
214 Print[matA//MatrixForm];
215 Print[matB//MatrixForm];
216 *)
217
```

```
(*Print["The condition number for matA is: ",Norm[matA] Norm[Inverse[matA]]];*)
(* Export the matrix b and splinegrid for later use *)
(*
Export["matrixB.m",matB];
Export["knots.m",knots];
*)
matrixB=matB;
(* calculate the generalized eigenvalues and eigenvectors from the above matricies *)
(* Evaluate eigenvalues *)
SetPrecision [sortEigensystem@Eigensystem[{matA,matB}],precisionGoal]
(*Chop@sortEigensystem[Eigensystem[{matA,matB}]][[1]]*)
]

Options[TRKSumRule]={
MaxRecursion:>$RecursionLimit,
PrecisionGoal->Automatic,
WorkingPrecision->Automatic}

TRKSumRule[Z_?NumericQ,rms_?NumericQ,order_?NumericQ,nsplines_?NumericQ,{l0_?NumericQ,j0_?
    NumericQ},opts:OptionsPattern[]]:=
Module[{alpha,base=1,baseSystem,baseValues, baseVectors,Bx, epsilon ,intermediateSystem1,
    intermediateSystem2, intermediateValues , intermediateVectors , jrange ,
jrangelength , knots, knotslength ,\[Lambda],lp,maxRecursion,Np,pos1,pos2,neg1,neg2,precisionGoal ,
    Rmax,R0x,Rsphx,RspNUx,t,tb,ti,total=0.0,
wLx,workingPrecision },

{maxRecursion,precisionGoal , workingPrecision }=OptionValue[{MaxRecursion,PrecisionGoal,
    WorkingPrecision}];
If [ precisionGoal ===Automatic,precisionGoal=MachinePrecision];
If [ workingPrecision ===Automatic,workingPrecision=precisionGoal+10];

Np=nsplines+1-order;
knots;
knotslength=Length[knots]-order-2;

(* Convert R0 to natural units where length is in units of the reduced Compton wavelength *)
{alpha, epsilon }=SetPrecision[{ fineStructureConstant ,10^-35},workingPrecision ];
```

```
251
252 Print[" Diagnostic-Output: Constants"];
253 Print["            alpha  = ",alpha];
254 Print["            epsilon  = ",epsilon ];
255
256 (* Calculate the base-states *)
257 baseSystem=galerkinHS[Z,rms,{l0,j0},{order, nsplines ,base},WorkingPrecision->workingPrecision,
        PrecisionGoal->precisionGoal];
258 Print[" Base states does !"];
259 gridb=grid;
260
261 BaseValues=baseSystem[[1]];
262 BaseVectors=baseSystem[[2]];
263 Print["\n",BaseValues];
264 BaseNorms=1/Sqrt[Map[BaseVectors[[#]].matrixB.BaseVectors[[#]]&,Range[2nsplines]]];
265 NBaseVectors=BaseVectors*BaseNorms;
266
267 Print[" Normalization of base states : ",Map[NBaseVectors[[#]].matrixB.NBaseVectors[[#]]&,Range
        [2nsplines]]];
268 Print[Plot[{Evaluate@pBase[r,{order,NBaseVectors,1}],Evaluate@qBase[r,{order,NBaseVectors,1}]/(
        fineStructureConstant  Z)},{r ,0,0.1}, PlotRange->All]];
269
270
271 (* Calculate the intermediate-states *)
272 (* Must include all states allowed by the selection rules given by Parity and 3JSymbol. Parity
        allows l0+1 and l0-1*)
273 Do[
274  If [l<0,Continue []];
275 intermediateSystem1=galerkinHS[Z,rms,{l,l-1/2},{order, nsplines ,base},WorkingPrecision->
        workingPrecision,PrecisionGoal->precisionGoal];
276 matrixB1=matrixB;
277 grid1=grid;
278 intermediateSystem2=galerkinHS[Z,rms,{l,l+1/2},{order, nsplines ,base},WorkingPrecision->
        workingPrecision,PrecisionGoal->precisionGoal];
279 matrixB2=matrixB;
280 grid2=grid;
281 Print["\nIntermediate states done!"];
```

```
282 IntermediateValues={intermediateSystem1[[1]], intermediateSystem2[[1]]};
283 IntermediateVectors={intermediateSystem1[[2]], intermediateSystem2[[2]]};
284 Print["\n", IntermediateValues];
285 IntermNorms={1/Sqrt[Map[IntermediateVectors[[1,#]].matrixB1.IntermediateVectors[[1,#]]&,Range[2
      nsplines]]],1/ Sqrt[Map[IntermediateVectors[[2,#]]. matrixB2. IntermediateVectors[[2,#]]&,
      Range[2nsplines]]]};
286 NIntermediateVectors=IntermediateVectors*IntermNorms;
287 (*
288 Print["Normalization of intermediate states: ",{Map[NIntermediateVectors[[1,#]].matrixB1.
      NIntermediateVectors[[1,#]]&,Range[2nsplines]], Map[NIntermediateVectors[[2,#]].matrixB2.
      NIntermediateVectors[[2,#]]&,Range[2nsplines]]}];
289 *)
290
291 (* Calculate the positive and negative matrix elements *)
292 If[Quiet@ThreeJSymbol[{l-1/2,-1/2},{j0,1/2},{1,0}]==0,pos1=0.,pos1=(-1)^(2j0+1) (2 l)
      ThreeJSymbol[{l-1/2,-1/2},{j0,1/2},{1,0}]^2 parity[l,1,l0]
293   ParallelSum[( IntermediateValues[[1, nsplines+i]]-BaseValues[[nsplines+1]])(Abs@NIntegrate[r
        (pBase[r,{order,NBaseVectors,1}] pMp[r,{order,NIntermediateVectors,grid1,1}, i]+qBase
        [r,{order,NBaseVectors,1}]qMp[r,{order,NIntermediateVectors,grid1,1}, i]),{r,0,80/Z},
294     Method->{"GaussKronrodRule","SymbolicProcessing"->0},WorkingPrecision->
          workingPrecision,PrecisionGoal->precisionGoal]//Quiet)^2,{i,1,nsplines},
          DistributedContexts -> {"ASMSThesis`BSpline`Private`"}]];
295 Print[pos1];
296 If[Quiet@ThreeJSymbol[{l+1/2,-1/2},{j0,1/2},{1,0}]==0,pos2=0.,pos2=(-1)^(2j0+1) (2 l+2)
      ThreeJSymbol[{l+1/2,-1/2},{j0,1/2},{1,0}]^2 parity[l,1,l0]
297   ParallelSum[( IntermediateValues[[2, nsplines+i]]-BaseValues[[nsplines+1]])(Abs@NIntegrate[r
        (pBase[r,{order,NBaseVectors,1}] pMp[r,{order,NIntermediateVectors,grid2,2}, i]+qBase
        [r,{order,NBaseVectors,1}]qMp[r,{order,NIntermediateVectors,grid2,2}, i]),{r,0,80/Z},
298     Method->{"GaussKronrodRule","SymbolicProcessing"->0},WorkingPrecision->
          workingPrecision,PrecisionGoal->precisionGoal]//Quiet)^2,{i,1,nsplines},
          DistributedContexts -> {"ASMSThesis`BSpline`Private`"}]];
299 Print[pos2];
300 If[Quiet@ThreeJSymbol[{l-1/2,-1/2},{j0,1/2},{1,0}]==0,neg1=0.,neg1=(-1)^(2j0+1) (2 l)
      ThreeJSymbol[{l-1/2,-1/2},{j0,1/2},{1,0}]^2 parity[l,1,l0]
301   ParallelSum[( IntermediateValues[[1, nsplines+1-i]]-BaseValues[[nsplines+1]])(
        Abs@NIntegrate[r (pBase[r,{order,NBaseVectors,1}] pMn[r,{order,NIntermediateVectors,
        grid1,1}, i]+qBase[r,{order,NBaseVectors,1}]qMn[r,{order,NIntermediateVectors,grid1
```

```
            ,1},i]),{r,0,80/Z},
302         Method->{"GaussKronrodRule","SymbolicProcessing"->0},WorkingPrecision->
              workingPrecision,PrecisionGoal->precisionGoal]//Quiet)^2,{i,1,nsplines},
              DistributedContexts -> {"ASMSThesis`BSpline`Private`"}]];
303 Print[neg1];
304 If[Quiet@ThreeJSymbol[{l+1/2,-1/2},{j0,1/2},{1,0}]==0,neg2=0.,neg2=(-1)^(2j0+1) (2 l+2)
      ThreeJSymbol[{l+1/2,-1/2},{j0,1/2},{1,0}]^2 parity[l,1,l0]
305       ParallelSum[( IntermediateValues [[2, nsplines+1-i]]-BaseValues[[nsplines+1]])(
            Abs@NIntegrate[r (pBase[r,{order,NBaseVectors,1}] pMn[r,{order,NIntermediateVectors,
            grid2,2},i]+qBase[r,{order,NBaseVectors,1}]qMn[r,{order,NIntermediateVectors,grid2
            ,2},i]),{r,0,80/Z},
306         Method->{"GaussKronrodRule","SymbolicProcessing"->0},WorkingPrecision->
              workingPrecision,PrecisionGoal->precisionGoal]//Quiet)^2,{i,1,nsplines},
              DistributedContexts -> {"ASMSThesis`BSpline`Private`"}]];
307 Print[neg2];
308 total = total + (pos1+pos2+neg1+neg2);,
309     {l,l0-1,l0+1,2}];
310 Print["\nTRK Sum-Rule: ",total];
311
312 ]
313
314 End[]     (* end the private context *)
315
316 Protect[galerkinHS,TRKSumRule]  (* protect exported symbols *)
317
318 EndPackage[]  (* end the package context *)
```

C.4 "BSpline" Package Results

In this section we will list some of the results of tests done on the generated spectrum. One standard indicator of the quality of the spectrum generated by the B-Spline method is how well it satisfies certain quantum mechanical sum-rules [43]. In particular, for the Dirac spectrum, the relativistic TRK sum-rule [31, 36].

$$\left[\frac{l}{2l+1} \sum_n \omega_{n0} | < n = 0, \kappa = -1 | r | n, \kappa = l > |^2 \right. \tag{C.14}$$

$$\left. + \frac{l+1}{2l+1} \sum_n \omega_{n0} | < n = 0, \kappa = -1 | r | n, \kappa = -l-1 > |^2 \right] = 0 \tag{C.15}$$

To test the sum-rule a spectrum was generated for Uranium using a basis set of 40 splines of order $k = 7$, for orbital angular momentum states $l = 0 \cdots 4$ and $j = 1/2 \cdots 9/2$, the results of which are shown in Table C.1.

Table C.1: Values of the relativistic Thomas-Reich-Khun sum-rule for the four lowest angular momentum states in uranium.

State (Z = 92)	**TRK**
l=0, j=1/2	6.7×10^{-8}
l=1, j=3/2	1.3×10^{-8}
l=2, j=5/2	3.3×10^{-9}
l=3, j=7/2	3.5×10^{-13}
l=4, j=9/2	1.4×10^{-12}

Thus we see that the spectra generated satisfies the TRK sum-rule to at least one part in 10^8, and this improves as one goes higher in l and j. However, for our application of calculating the nuclear polarization correction we are dealing with only the lowest angular momentum states.

Appendix D

Appendix 5: Vector Spherical Harmonics

To facilitate the reduction of the matrix elements $\psi_a \vec{\alpha} \psi_b$ it is useful to recall some results from the theory of vector spherical harmonics. Our treatment will mirror that of Johnson [44] and Brink and Satchler [25]. When one combines the spherical harmonics with spherical basis vectors via an expansion, one obtains the definition of a vector spherical harmonic:

$$\vec{Y}_{JLM}(\hat{r}) = \sum_{\sigma} \langle L, M-\sigma; 1, \sigma | JM \rangle \, Y_{L,M-\sigma}(\hat{r}) \vec{\xi}_{\sigma}. \tag{D.1}$$

The vector spherical harmonics are eigenfunctions of angular momentum operators J^2andJ_z with eigenvalues J^2, $J(J+1)$ respectively where J is a member of the set of integers. With the value of J set, L takes on the following values:

$$\text{for } J > 0: \qquad L = J \pm 1, J \tag{D.2}$$

$$\text{for } J = 0: \qquad L = 0, 1. \tag{D.3}$$

Furthermore, the VSH obey the following orthogonality relations

$$\int_0^{2\pi} d\phi \int_0^{\pi} sin(\theta) d\theta \; Y^{\dagger}_{JLM}(\hat{r}) Y_{J'L'M'}(\hat{r}) = \delta_{JJ'}\delta_{LL'}\delta_{MM'}. \tag{D.4}$$

The most useful property, for us at least, of vector spherical harmonics is they can be used as an expansion basis for vector functions. For instance let us consider the vector function $\hat{r}Y_{LM}(\hat{r})$. We can expand this in a series of vector spherical harmonics:

$$\hat{r}Y_{LM}(\hat{r}) = \sum_{JLM} a_{JLM} Y_{JLM}(\hat{r}), \tag{D.5}$$

and apply the orthogonality relation to isolate the expansion coefficients:

$$\int d\Omega Y^{\dagger}_{JLM} \hat{r} Y_{LM}(\hat{r}) = \sum_{JLM} a_{JLM} \int d\Omega Y^{\dagger}_{JLM} Y_{JLM}, \tag{D.6}$$

so,

$$a_{JLM} = \int d\Omega Y^{\dagger}_{JLM} \hat{r} Y_{LM}(\hat{r}). \tag{D.7}$$

Using the spherical representation of the axial vector [25],

$$\hat{r} = \sqrt{\frac{4\pi}{3}} \sum_{\nu} Y^{*}_{1\nu} \; \xi_{\nu}, \tag{D.8}$$

and employing the expansion definition of the VSH, we can express the expasion coefficients as:

$$a_{JLM} = \sum_{\mu\nu} C(L, 1, J; M-\mu, \mu, M) \xi^{\dagger}_{\mu} \xi_{\nu} \tag{D.9}$$

$$\times \int d\Omega Y^{*}_{L \; M-\mu}(\hat{r}) \sqrt{\frac{4\pi}{3}} Y^{*}_{1\nu}(\hat{r}) Y_{lm}(\hat{r}) \tag{D.10}$$

$$= \sum_{\mu\nu} C(L, 1, J; M-\mu, \mu, M) \; \xi^{\dagger}_{\mu} \xi_{\nu} \; \left\langle l, m | C^{1}_{\nu} | L, M-\nu \right\rangle. \tag{D.11}$$

We can now make use of standard relations for the orbital angular momentum matrix elements:

$$\left\langle l_1, m_1 | C_q^k | l_2, m_2 \right\rangle = (-1)^{l_1 - m_1} \begin{pmatrix} l_1 & k & l_2 \\ -m_1 & q & m_2 \end{pmatrix} \left\langle l_1 || C_q^k || l_2 \right\rangle, \tag{D.12}$$

$$\left\langle l_1 || C_q^k || l_2 \right\rangle = (-1)^{l_1} \sqrt{(2l_1+1)(2l_2+1)} \begin{pmatrix} l_1 & k & l_2 \\ 0 & 0 & 0 \end{pmatrix}, \tag{D.13}$$

and,

$$C(j_2, k, j_1; m_2, q, m_1) = (-1)^{j_1 - m_1} \sqrt{2j_1 + 1} \begin{pmatrix} j_1 & k & j_2 \\ -m_1 & q & m_2 \end{pmatrix}. \tag{D.14}$$

Thus, the expansion coefficients can be re-expressed as

$$\begin{aligned} a_{JLM} = & \sum_{\mu\nu} (-1)^{J-M+2l-m} \sqrt{[J, l, L]} \begin{pmatrix} J & 1 & L \\ -M & \mu & M-\mu \end{pmatrix} \\ & \times \begin{pmatrix} l & 1 & L \\ -m & \nu & M-\nu \end{pmatrix} \begin{pmatrix} l_1 & k & l_2 \\ 0 & 0 & 0 \end{pmatrix} \xi_\mu^\dagger \xi_\nu. \end{aligned} \tag{D.15}$$

Since $\xi_\mu^\dagger \xi_\nu = \delta_{\mu\nu}$, our expression becomes:

$$\begin{aligned} a_{JLM} = & \sum_{\mu} (-1)^{J-M+2l-m} \sqrt{[J, l, L]} \begin{pmatrix} J & 1 & L \\ -M & \mu & M-\mu \end{pmatrix} \\ & \times \begin{pmatrix} l & 1 & L \\ -m & \mu & M-\mu \end{pmatrix} \begin{pmatrix} l_1 & k & l_2 \\ 0 & 0 & 0 \end{pmatrix}, \end{aligned} \tag{D.16}$$

and we can now sum over the magnetic quantum numbers,μ using the relation:

$$\sum_{\alpha\beta} \begin{pmatrix} a & b & c \\ \alpha & \beta & \gamma \end{pmatrix} \begin{pmatrix} a & b & k \\ \alpha & \beta & \kappa \end{pmatrix} = \frac{\delta_{ck} \delta_{\gamma\kappa}}{2c+1}. \tag{D.17}$$

Thus we obtain,

$$\sum_{\mu} \begin{pmatrix} 1 & L & J \\ \mu & M-\mu & -M \end{pmatrix} \begin{pmatrix} 1 & L & l \\ \mu & M-\mu & -m \end{pmatrix} = \frac{\delta_{Jl}\delta_{Mm}}{2l+1}, \tag{D.18}$$

and

$$a_{JLM} = (-1)^l \sqrt{[L]} \begin{pmatrix} l_1 & k & l_2 \\ 0 & 0 & 0 \end{pmatrix} \delta_{Jl}\delta_{Mm}. \tag{D.19}$$

Using the symmetry properties of the 3j symbol [25]

$$\begin{pmatrix} l & 1 & L \\ 0 & 0 & 0 \end{pmatrix} = (-1)^{L+1+l} \begin{pmatrix} L & 1 & l \\ 0 & 0 & 0 \end{pmatrix}, \tag{D.20}$$

together with the equivalence between 3j and Clebsch-Gordan coefficents, we obtain:

$$\begin{pmatrix} l & 1 & L \\ 0 & 0 & 0 \end{pmatrix} = \frac{(-1)^{2L+l}}{\sqrt{2l+1}} C(L,1,l;0,0,0). \tag{D.21}$$

Therefore we finally obtain a simple expression for the expansion coefficients in terms of C-G coefficients:

$$a_{JLM} = \sqrt{\frac{2L+1}{2l+1}}\ C(L,1,l;0,0,0)\ \delta_{Jl}\ \delta_{Mm}. \tag{D.22}$$

Now we can obtain a simple expression for the above C-G coefficent [44]:

$$C(L,1,l;0,0,0) = \sqrt{\frac{l}{2L+1}}\delta_{L,l-1} - \sqrt{\frac{l+1}{2L+1}}\delta_{L,l+1}, \tag{D.23}$$

so our expression for a_{JLM} becomes,

$$a_{JLM} = \left(\sqrt{\frac{l}{2L+1}}\delta_{L,l-1} - \sqrt{\frac{l+1}{2L+1}}\delta_{L,l+1} \right) \delta_{Jl}\ \delta_{Mm}. \tag{D.24}$$

Thus we may write for the expression $\hat{r}Y_{JM}(\hat{r})$

$$\hat{r}\ Y_{JM}(\hat{r}) = \sqrt{\frac{J}{2J+1}}Y_{JJ-1M}(\hat{r}) - \sqrt{\frac{J+1}{2J+1}}Y_{JJ+1M}(\hat{r}). \tag{D.25}$$

This vector is in the direction $\hat{r}$ and is referred to as a longitudinal spherical harmonic [44]. We can now introduce the spherical form of the above vector function:

$$Y_{JM}^{(-1)}(\hat{r}) = \hat{r}Y_{JM}(\hat{r}). \tag{D.26}$$

The vector spherical harmonic $Y_{JJM}(\hat{r})$ is orthogonal to $Y_{JM}^{(-1)}(\hat{r})$ and is transverse. The combination below is also orthogonal to $Y_{JM}^{(-1)}(\hat{r})$ and gives a second spherical vector:

$$\sqrt{\frac{J+1}{2J+1}}Y_{JJ-1M}(\hat{r}) + \sqrt{\frac{J}{2J+1}}Y_{JJ+1M}(\hat{r}). \tag{D.27}$$

Thus we have the the following components,

$$Y_{JM}^{(-1)}(\hat{r}) = \sqrt{\frac{J}{2J+1}}Y_{JJ-1M}(\hat{r}) - \sqrt{\frac{J+1}{2J+1}}Y_{JJ+1M}(\hat{r}) \tag{D.28}$$

$$Y_{JM}^{(0)}(\hat{r}) = Y_{JJM}(\hat{r}) \tag{D.29}$$

$$Y_{JM}^{(1)}(\hat{r}) = \sqrt{\frac{J+1}{2J+1}}Y_{JJ-1M}(\hat{r}) + \sqrt{\frac{J}{2J+1}}Y_{JJ+1M}(\hat{r}), \tag{D.30}$$

satisfying the orthonormality condition:

$$\int d\Omega \; Y_{JM}^{(\lambda)\,\dagger}(\Omega)Y_{J'M'}^{(\lambda')}(\Omega) = \delta_{JJ'}\delta_{MM'}\delta_{\lambda\lambda'}. \tag{D.31}$$

Inverting the expressions gives,

$$Y_{JJ-1M}(\hat{r}) = \sqrt{\frac{J}{2J+1}}Y_{JM}^{(-1)}(\hat{r}) + \sqrt{\frac{J+1}{2J+1}}Y_{JM}^{(1)}(\hat{r}) \tag{D.32}$$

$$Y_{JJM}(\hat{r}) = Y_{JM}^{(0)}(\hat{r}) \tag{D.33}$$

$$Y_{JJ+1M}(\hat{r}) = -\sqrt{\frac{J+1}{2J+1}}Y_{JM}^{(-1)}(\hat{r}) + \sqrt{\frac{J}{2J+1}}Y_{JM}^{(1)}(\hat{r}), \tag{D.34}$$

which leads to the following expressions:

$$Y_{JM}^{(-1)}(\hat{r}) = \hat{r}Y_{JM}(\hat{r}) \tag{D.35}$$

$$Y_{JM}^{(0)}(\hat{r}) = \frac{1}{\sqrt{J(J+1)}}\vec{L}Y_{JM}(\hat{r}) \tag{D.36}$$

$$Y_{JM}^{(1)}(\hat{r}) = \frac{r}{\sqrt{J(J+1)}}\vec{\nabla}Y_{JM}(\hat{r}). \tag{D.37}$$

These are used in evaluating matrix elements of vector operators $\vec{r}$, $\vec{L}$ and $\vec{p}$ for evaluating matrix elements in chapter 5.

Bibliography

[1] A. D. Alhaidari. Dirac equation with coupling to 1/r singular vector potentials for all angular momenta. *Foundations of Physics*, 40(8):1088–1095, 2010.

[2] I Angeli. Evaluation Procedure for Nuclear rms Charge Radii. *Acta Physics Hungaria*, 69(July 1990):233–247, 1991.

[3] I. Angeli. A consistent set of nuclear rms charge radii: Properties of the radius surface R(N,Z). *Atomic Data and Nuclear Data Tables*, 87(2):185–193, 2004.

[4] I Angeli, Yu P Gangrsky, K P Marinova, I N Boboshin, S Yu Komarov, B S Ishkhanov, and V V Varlamov. N and Z Dependence of Nuclear Charge Radii. *Journal of Physics G: Nuclear and Particle Physics*, 36:085102, 2009.

[5] A. N. Artemyev, V. M. Shabaev, and V. A. Yerokhin. Relativistic nuclear recoil corrections to the energy levels of hydrogenlike and high-Z lithiumlike atoms in all orders in αz, 1995.

[6] A N Artemyev, V M Shabaev, and V A Yerokhin. Nuclear recoil corrections to the 2p3p state energy of hydrogen-like and high-2 lithium-like atoms in all orders in a2. *J. Phys. B: At. Mol. Opt. Phys. Phys. B At. Mol. Opt. Phys*, 28 (28):5201–5206, 1995.

[7] A N Artemyev, T Beier, G Plunien, V M Shabaev, G Soff, and V A Yerokhin. Vacuum-polarization screening corrections to the energy levels of lithiumlike ions. *Phys. Rev. A*, 60(1):45–49, 1999.

[8] A. N. Artemyev, V. M. Shabaev, M. M. Sysak, V. A. Yerokhin, T. Beier, G. Plunien, and G. Soff. Evaluation of the two-photon exchange diagrams for the (1s^2)2p3/2 electron configuration in Li-like ions. *Physical Review A*, 67(6): 062506, 2003.

[9] L M Barkov and M S Zolotorev. Observation of Parity Non-Conservation in Atomic Transitions. *Letters to J. E. T. P.*, 26:379–383, 1978.

[10] L M Barkov and M S Zolotorev. Parity Violation in Atomic Bismuth. *Physics Letters*, 85(2):308–313, 1979.

[11] G. Baym. *Lectures on Quantum Mechanics*. W. A. Benjamin, Inc., New York, 1969.

[12] J. Behr and G. Gwinner. Standard model tests with trapped radioactive atoms. *J. Phys. G: Nucl. Part. Phys.*, 36:033101, 2009.

[13] T. Beier, P. Mohr, H. Persson, and G. Soff. Influence of nuclear size on QED corrections in hydrogenlike heavy ions. *Physical Review A*, 58(2):954–963, 1998.

[14] P. Beiersdorfer, D. Knapp, R. E. Marrs, S. R. Elliott, and M. H. Chen. Structure and Lamb shift of 2s1/2-2p levels in lithiumlike U89+ through neonlike U82+. *Physical Review Letters*, 71(24):3939–3942, dec 1993. URL `https://link.aps.org/doi/10.1103/PhysRevLett.71.3939`.

[15] P. Beiersdorfer, A. Osterheld, J. Scofield, J. Crespo López-Urrutia, and K. Widmann. Measurement of QED and Hyperfine Splitting in the 2s1/2- 2p3/2 X-Ray Transition in Li-like B209i80+. *Physical Review Letters*, 80(14):3022–3025, 1998.

[16] H. A. Bethe and E. E. Salpeter. *Quantum Mechanics of One- and Two-Electron Atoms*. Dover, Mineola, New York, 2008.

[17] J. Billowes and P Campbell. High-resolution laser spectroscopy for the study of nuclear sizes and shapes High-resolution laser spectroscopy for the study of nuclear sizes and shapes. *J. Phys. G: Nucl. Part. Phys.*, 21:707, 1995.

[18] James D. Bjorken and D. Drell, Sidney. *Relativistic Quantum Mechanics*. McGraw-Hill Book Company, Inc., 1998.

[19] S. A. Blundell, D. S. Guo, W. R. Johnson, and J. Sapirstein. Formulas from First-, Second-, and Third-Order Perturbation Theory for Atoms with One Valence Electron. *Atomic Data and Nuclear Data Tables*, 37:103–119, 1987.

[20] Steven. A. Blundell. Accurate screened QED calculations in high-Z many-electron ions. *Physical Review A*, 46(7):3762–3775, 1992.

[21] M. A. Bouchiat and C. Bouchiat. I. Parity violation induced by weak neutral currents in atomic physics. *J. Phys. France*, 35:899–927, 1974.

[22] M. A. Bouchiat and C. Bouchiat. Parity violation induced by weak neutral currents in atomic physics: part II. *J. Phys. France*, 36:493–509, 1975.

[23] M. A. Bouchiat and C. C. Bouchiat. Weak neutral currents in atomic physics. *Physics Letters B*, 48(2):111–114, 1974.

[24] M. A. Bouchiat and C. C. Bouchiat. Parity violation in Atoms. *Reports in the Progress of Physics*, 60:1351–1396, 1997.

[25] D. M. Brink and G. R. Satchler. *Angular Momentum*. Oxford University Press, Oxford, 3rd edition, 1993.

[26] P. H. Bucksbaum, E. D. Commins, and L. R. Hunter. Observation pf parity nonconservation in atomic thallium. *Physical Review D*, 24(5):1134–1148, 1981.

[27] E. D. Commins and P. H. Bucksbaum. *Weak Interactions of Leptons and Quarks*. Cambridge University Press, London, 1983.

[28] Andrzej Czarnecki, Ulrich D. Jentschura, and Krzysztof Pachucki. Calculation of the one- and two-loop lamb shift for arbitrary excited hydrogenic states. *Physical Review Letters*, 95(18):1–4, 2005.

[29] Carl de Boor. *A Practical Guide to Splines*. Springer-Verlag, New York, 1978.

[30] A Derevianko and S G Porsev. Theoretical overview of atomic parity violation. *The European Physical Journal A*, 32(4):517–523, jun 2007.

[31] G. W F Drake and S. P. Goldman. Application of discrete-basis-set methods to the Dirac equation. *Physical Review A*, 23(5):2093–2098, 1981.

[32] V A Dzuba, W R Johnson, and M S Safronova. Calculation of isotope shifts for cesium and francium. pages 1–9, 2005.

[33] C. A. J. Fletcher. *Computational Galerkin Methods*. Springer-Verlag, New York, 1984.

[34] Thomas Franosch and Gerhard Soff. The influence of the nuclear shape and of the muonic vacuum polarization on strongly bound electrons. *Z. Phys. D*, 18: 219–222, 1991.

[35] J. D. Gillaspy, D. Osin, Yu Ralchenko, J. Reader, and S. A. Blundell. Transition energies of the D lines in Na-like ions. *Physical Review A - Atomic, Molecular, and Optical Physics*, 87(6):1–13, 2013. ISSN 10502947. doi: 10.1103/PhysRevA.87.062503.

[36] S. P. Goldman and G. W F Drake. Relativistic sum rules and integral properties of the Dirac equation. *Physical Review A*, 25(6):2877–2881, 1982.

[37] I. P. Grant. *Relativistic Quantum Theory of Atoms and Molecules*. Springer-Verlag, 2007.

[38] Walter Greiner. *Relativistic Quantum Mechanics: wave equations*. Springer-Verlag, Berlin, second edition, 1997.

[39] Robert Hofstadter. Electron scattering and nuclear structure. *Reviews of Modern Physics*, 28(3):214–254, 1956.

[40] D. J. Hylton. Finite-nuclear-size corrections to the Uehling potential. *Physical Review A*, 32(3):1303–1309, sep 1985.

[41] Michael I. Eides, Howard Grotch, and Valery A Shelyuto. Theory of light hydrogenlike atoms. *Physics Reports*, 342(2-3):63–261, 2001.

[42] W. R. Johnson, S. A. Blundell, and J. Sapirstein. Many-body perturbation-theory calculations of energy levels along the lithium isoelectronic sequence. *Physical Review A*, 37(8):2764–2777, 1988.

[43] W. R. Johnson, S. A. Blundell, and J. Sapirstein. Finite basis sets for the Dirac equation constructed from B splines. *Physical Review A*, 37(2):307–315, 1988.

[44] Walter R. Johnson. *Atomic Structure Theory*. Springer-Verlag, Berlin, 2007.

[45] Walter R. Johnson and Gerhard Soff. No Title. *Atomic Data and Nuclear Data Tables*, 33(405), 1985.

[46] I. B. Khriplovich. *Parity Nonconservation in Atomic Phenomena*. CRC Press, 1991.

[47] S. Klarsfeld. Analytical expressions for the evaluation of vacuum-polarization potentials in muonic atoms. *Physics Letters B*, 66(1):86–88, 1977.

[48] H. Jürgen Kluge and Wilfried Nörtershäuser. Lasers for nuclear physics. *Spectrochimica Acta - Part B Atomic Spectroscopy*, 58(6):1031–1045, 2003.

[49] Kenneth S. Krane. *Introductory Nuclear Physics*. John Wiley and Sons, New York, 1988.

[50] L. N. Labzowsky and A. V. Nefiodov. Analytic evaluation of the nuclear polarization contribution to the energy shift in heavy ions. *Physics Letters A*, 188 (4-6):371–375, 1994.

[51] Ingvar Lindgren and J Morisson. *Atomic Many-Body Theory*. Springer-Verlag, Berlin, second edition, 2009.

[52] Z Lu, P Mueller, G W F Drake, and Steven C Pieper. Colloquium : Laser probing of neutron-rich nuclei in light atoms. 85(December), 2013.

[53] Roman Maeder. *Programming in Mathematica*. Addison-Wesley, Reading, Massachusetts, 3rd edition, 1997.

[54] Joseph B Mann and R Johnson. 1971 Breit Interaction. 4(1), 1971.

[55] D. F. Mayers. Relativistic self-consistent field calculation for mercury. *Proceedings of the Royal Society A*, 241(1224):93–109, 1957.

[56] Peter Mohr. Quantum Electrodynamics of high-Z few-electron atoms. *Physical Review A*, 32(4):1949–1957, 1985.

[57] Peter J. Mohr. Quantum Electrodynamics Calculations in Few-Electron Systems. *Physica Scripta*, T46:44–51, 1993.

[58] Peter J. Mohr, Günter Plunien, and Gerhard Soff. QED corrections in heavy atoms. *Physics Reports*, 293(5-6):227–369, 1998.

[59] Gudrid Moortgat-Pick. The Furry picure. *Journal of Physics: Conference Series*, 198:012002, 2009.

[60] Cédric Nazé. Relativistic ab initio calculations of isotope shifts. 2013.

[61] A. V. Nefiodov, G. Pluniena, and G. Soff. Nuclear-polarization effect to the hyperfine structure in heavy multicharged ions. *Physics Letters, Section B: Nuclear, Elementary Particle and High-Energy Physics*, 552(1-2):35–40, 2003.

[62] Andrei V. Nefiodov, Leonti N. Labzowsky, Günter Plunien, and Gerhard Soff. Nuclear polarization effects in spectra of multicharged ions. *Physics Letters, Section A: General, Atomic and Solid State Physics*, 222(4):227–232, 1996.

[63] R Neugart. Lasers in nuclear physics A review. *Eur. Phys. J. A*, 15:35–39, 2002.

[64] W.E. Otten. Nuclear Radii and Moments of Unstable Isotopes. In D. A. Bromley, editor, *Treatise on Heavy Ion Science*, pages 517–638. Springer, Boston, 1989.

[65] Krzysztof Pachucki. Contributions to the binding, two-loop correction to the Lamb shift. *Physical Review A*, 48(4):2609–2614, 1993.

[66] Adriana Pálffy. Nuclear effects in atomic transitions. *Contemporary Physics*, 51 (6):471–496, 2010.

[67] Michael E. Peskin and Daniel V. Schrodeder. *An Introduction to Quantum Field Theory*. 1995.

[68] Günter Plunien and Gerhard Soff. Nuclear-polarization contribution to the Lamb shift in actinide nuclei. *Physical Review A*, 51(2):1119–1131, 1995.

[69] Günter Plunien and Gerhard Soff. Erratum: Nuclear-polarization contribution to the Lamb shift in actinide nuclei. *Physical Review A*, 53(6):4614–4616, 1996.

[70] Günter Plunien, Berndt Muller, and Walter Greiner. Nuclear polarization contribution to the Lamb shift in heavy atoms. *Physical Review A*, 39(10):5428–5431, 1989.

[71] Günter Plunien, Berndt Muller, Walter Greiner, and Gerhard Soff. Nuclear polarization in heavy atoms and superheavy quasiatoms. *Physical Review A*, 43 (11):5853–5866, 1991.

[72] F Salvat, J M Fernfindez-varea, and W Williamson Jr. Accurate numerical solution of the radial Schrodinger and Dirac wave equations. *Computer Physics Communications*, 90(1):151–168, 1995.

[73] F Salvat, J M Fernandez-Varea, and W Williamson. RADIAL: a FORTRAN subroutine package for the solution of the radial Schr odinger and Dirac wave equations. *RADIAL Manual*, 2011.

[74] J Sapirstein. Quantum Electrodynamics of Many-Electron Atoms. *Physica Scripta*, 36:801–808, 1987.

[75] J. Sapirstein. Theoretical methods for the relativistic atomic many-body problem. *Reviews of Modern Physics*, 70(1):55–76, 1998.

[76] J. Sapirstein and K. T. Cheng. Determination of the two-loop Lamb shift in lithiumlike bismuth. *Physical Review A. Atomic, Molecular, and Optical Physics*, 64(2):1–9, 2001.

[77] J Sapirstein and W R Johnson. The use of basis splines in theoretical atomic physics. *Journal of Physics B: Atomic, Molecular and Optical Physics*, 29(22): 5213–5225, 1996.

[78] J. Sapirstein and D. Yennie. Theory of Hydrogenic Bound States. In T. Kinoshita, editor, *Quantum Electrodynamics*. World Scientific, 1990.

[79] Jonathan Sapirstein. Theory of Many-Electron Atoms. *Physica Scripta*, T46: 52–60, 1993.

[80] Leonard I. Schiff. *Quantum Mechanics*. McGraw-Hill Book Company, Inc., New York, second edition, 1955.

[81] V M Shabaev and A N Artemyev. Relativistic Nuclear Recoil Corrections to the Energy Levels of Multicharged Ions. *J. Phys. B: At. Mol. Opt. Phys.*, 27:1307, 1994.

[82] R Shankar. *Principles of Quantum Mechanics*. Springer-Verlag, second edition, 1994.

[83] A P Stone. Nuclear and Relativistic Effects in Atomic Spectra. *Proc. Phys. Soc.*, 77(3):786, 1961.

[84] K. Tsukada, A. Enokizono, T. Ohnishi, K. Adachi, T. Fujita, M. Hara, M. Hori, T. Hori, S. Ichikawa, K. Kurita, K. Matsuda, T. Suda, T. Tamae, M. Togasaki, M. Wakasugi, M. Watanabe, and K. Yamada. First Elastic Electron Scattering from Xe132 at the SCRIT Facility. *Physical Review Letters*, 118(26):262501, 2017.

[85] L M Wang, Chun Li, Z Yan, and G W F Drake. Isotope shifts and transition frequencies for the S and P states of lithium : Bethe logarithms and second-order relativistic recoil. 032504:1–10, 2017.

[86] Paul Wellin. *Programming with Mathematica: An Introduction*. Cambridge University Press, Cambridge, 2013.

[87] C E Wieman, M C Noecker, B P Masterson, and J Cooper. No Title. *Physical Review Letters*, 58:1738, 1987.

[88] Stephen Wolfram. *The Mathematica Book*. Wolfram Media Inc, 5th revise edition, 2003.

[89] V. A. Yerokhin and V. M. Shabaev. Lamb shift of n = 1 and n = 2 states of hydrogen-like atoms, 1 < Z < 110. *Journal of Physical and Chemical Reference Data*, 44(3):1–53, 2015.

[90] V. A. Yerokhin, A. N. Artemyev, V. M. Shabaev, M. M. Sysak, O. M. Zherebtsov, and G. Soff. Two-photon exchange corrections to the 2p1/2-2s transition energy in Li-like high-Z ions. *Physical Review Letters*, 85(22):4699–4702, 2000.

[91] V. A. Yerokhin, A. N. Artemyev, V. M. Shabaev, G. Plunien, and G. Soff. Screened Self-energy Correction to the 2p3/2-2s Transition Energy in Li-like Ions. *Optics and Spectroscopy*, 99(1):12–17, 2005.

[92] V. A. Yerokhin, P. Indelicato, and V. M. Shabaev. Nonperturbative calculation of the two-loop lamb shift in Li-like ions. *Physical Review Letters*, 97(25):13–16, 2006.

[93] V. A. Yerokhin, P. Indelicato, and V. M. Shabaev. Nonperturbative calculation of the two-loop lamb shift in Li-like ions. *Physical Review Letters*, 97(25):13–16, 2006.

[94] V. A. Yerokhin, A. N. Artemyev, and V. M. Shabaev. QED treatment of electron correlation in Li-like ions. *Physical Review A - Atomic, Molecular, and Optical Physics*, 75(6):1–21, 2007.

[95] V A Yerokhin, P Indelicato, and V M Shabaev. Two-loop QED corrections in few-electron ions. *Can. J. Phys.*, 85(June 2006):521–529, 2007.

[96] V. A. Yerokhin, P. Indelicato, and V.M. Shabaev. Two-loop QED corrections with closed fermion loops. *Physical Review A - Atomic, Molecular, and Optical Physics*, 77(062510):1–12, 2008.

[97] Vladimir A. Yerokhin. Nuclear-size correction to the Lamb shift of one-electron atoms. *Physical Review A - Atomic, Molecular, and Optical Physics*, 83(1):1–10, 2011.

[98] O. M. Zherebtsov, V. M. Shabaev, and V. A. Yerokhin. Third-order interelectronic-interaction correction to the 2p(1/2)-2s transition energy in lithiumlike ions. *Physics Letters, Section A: General, Atomic and Solid State Physics*, 277(4-5):227–232, 2000.